

# UC Berkeley

## UC Berkeley Electronic Theses and Dissertations

### Title

The Study of Disorder in Amorphous Silica, Alkali-Silica Reaction Gel and Fly Ash

### Permalink

<https://escholarship.org/uc/item/0n101652>

### Author

Meral, Cagla

### Publication Date

2012

Peer reviewed|Thesis/dissertation

The Study of Disorder in Amorphous Silica, Alkali-Silica Reaction Gel and Fly Ash

By

Çağla Meral

A dissertation submitted in partial satisfaction of the

requirements for the degree of

Doctor of Philosophy

in

Engineering – Civil and Environmental Engineering

in the

Graduate Division

of the

University of California, Berkeley

Committee in charge:

Professor Paulo J. M. Monteiro, Co-Chair

Professor Claudia P. Ostertag, Co-Chair

Professor Hans-Rudolf Wenk

Professor Garrison Sposito

Fall 2012



## Abstract

The Study of Disorder in Amorphous Silica, Alkali-Silica Reaction Gel and Fly Ash

by

Çağla Meral

Doctor of Philosophy in Civil and Environmental Engineering

University of California, Berkeley

Professor Paulo J. M. Monteiro, Co-Chair

Professor Claudia P. Ostertag, Co-Chair

Significant progress was achieved with the application of Rietveld method to characterize the crystalline, and nanocrystalline phases in portland cement concrete. However, to obtain detailed information on the amorphous phases present in concrete, it is necessary to analyze the total scattering data. The pair distribution function (PDF) method, that takes the Sine Fourier transform of the measured structure factor over a wide momentum transfer range, has been successfully utilized in the study of liquids and amorphous solids. The method provides a direct measure of the probability of finding an atom surrounding a central atom at a radial distance away. The obtained experimental characteristic distances can be used to validate the predictions by the theoretical models, such as, molecular dynamics simulations. This research focuses on obtained results of PDF analysis on silica fume, rice husk ash, fly ash, alkali-silica reaction gel, and opals.



# Acknowledgements

This thesis would not have come about without the help, cooperation and support of many people. First of all, I would like to thank to my principal advisor, Professor Paulo Monteiro for the insightful discussions we had, his guidance during my graduate studies, his patience and support. This thesis would not have been possible without his suggestions, feedbacks and encouragements. I am also grateful to my co-advisor Professor Claudia Ostertag for being a great role model, both as a scientist and as a woman. Her scientific vision and her words on the importance of a balanced life allowed me to grow, and find my path. I would like to extend my thanks to my mentor Professor Hans-Rudolf Wenk. His enthusiasm towards science is infectious; and he is like a sea of knowledge. Working with him has been a privilege for me; and I am truly grateful for this opportunity.

I am also thankful to Professor Garrison Sposito for his constructive criticism and proofreading of my thesis. His books and his lectures were extremely useful while writing this thesis. I want to convey special thanks to my grandadvisor (my advisor's advisor!) Professor Povindar Kumar Mehta. He has a very clear vision on sustainable construction materials; and one of his seminars I attended more than a decade ago is one of the reasons that I came to Berkeley.

Special thanks are due to Dr. Chris Benmore. The total scattering experiments I conducted with him is the basis of this thesis. He is an amazing scientist; and I am very grateful to have the chance of working with him. His guidance and suggestions were very critical for completion of his thesis. I am also very thankful to another total scattering expert, Dr. Lawrie Skinner, for his insightful discussions, and suggestions. He is one of the most hard-working scientists that I have ever met. I also want to thank Dr. Petek Yener and Professor Arpad Horvath. Collaborating with them was one of the highlights of my research; and allowed me to look at my research from a different angle. I am grateful to Professor Haroldo de Mayo Bernardes as he is the one who kindly provided some of the samples studied in this thesis. I extend my thanks to Dr. Abdul Hamid Emwas and Dr. Rae Taylor for their help with NMR measurements; and to Dr. Silvina Cerveny for her help with some of the TGA measurements. These inter-continental collaborations were a critical part of my thesis. I am thankful to Dula Parkinson; working with him on micro-tomography was great. He is one of the most efficient scientists I had a chance to work with. I also convey thanks to Dr. Sven Vogel, Dr. Thomas Proffen, Dr. Rex Hjelm, Dr. Juergen Eckert, Dr. Monika Hartl and Dr. Luke Daemen. Using neutrons in my research was a very unique opportunity; and it was a great experience to be able to work with such inspiring scientists.

I am also grateful to my fellow Group Monteiro students and researchers. Working with them has been one of my most rewarding experiences. I also thank to 115 MatCave residents. Our office might not have any windows; but, it has a great spirit. They have made my research life much richer. Group Wenk is also very special for me; I will miss the weekly "heated, high pressure" discussions.

Last but not least, I would like to thank my family. They have been extremely supportive, and always believed I could. My very special thanks are due to my parents and my brother who taught me the value of kindness, hard work and to stay strong.

# Contents

<b>Acknowledgements .....</b>	<b>i</b>
<b>Chapter 1 Introduction.....</b>	<b>1</b>
<b>Chapter 2 Methods.....</b>	<b>7</b>
2.1 Total Scattering.....	9
2.2 Small Angle Scattering.....	17
2.3 Scanning X-ray Transmission Microscopy (STXM) .....	21
2.4 Conclusion.....	25
<b>Chapter 3 Amorphous Silica .....</b>	<b>26</b>
3.1 Materials.....	27
3.1.1 Silica fume and rice husk ash.....	27
3.1.2 Opal.....	28
3.2 Results and discussions .....	29
3.2.1 Scanning Electron Microscopy (SEM) and X-ray Diffraction (XRD) .....	29
3.2.2 Nuclear Magnetic Resonance (NMR) Spectroscopy .....	31
3.2.3 Fourier Transform Infrared (FTIR) Spectroscopy .....	33
3.2.4 Thermal Analysis .....	34
3.2.5 Total Scattering.....	36
3.2.5.1 Silica fume and rice husk ash .....	39
3.2.5.2 Opal .....	41
3.3 Conclusions.....	57
<b>Chapter 4 Alkali Silica Reaction.....</b>	<b>58</b>
4.1 Reaction mechanisms.....	62
4.1.1 Dissolution of silica .....	62
4.1.2 Polymerization of silica and gelling.....	67
4.1.3 Alkali silica reaction .....	72
4.2 Scanning Electron Microscopy (SEM) Investigations .....	75
4.2.1 ASR damaged concrete samples .....	76
4.2.2 Results and discussions.....	77
4.3 Conclusions.....	85
<b>Chapter 5 Alkali Silica Reaction Gel.....</b>	<b>86</b>
5.1 Previous experimental literature on alkali-silica reaction at molecular and nanometer scale.....	86
5.1.1.1 Nuclear Magnetic Resonance (NMR) Spectroscopy .....	86

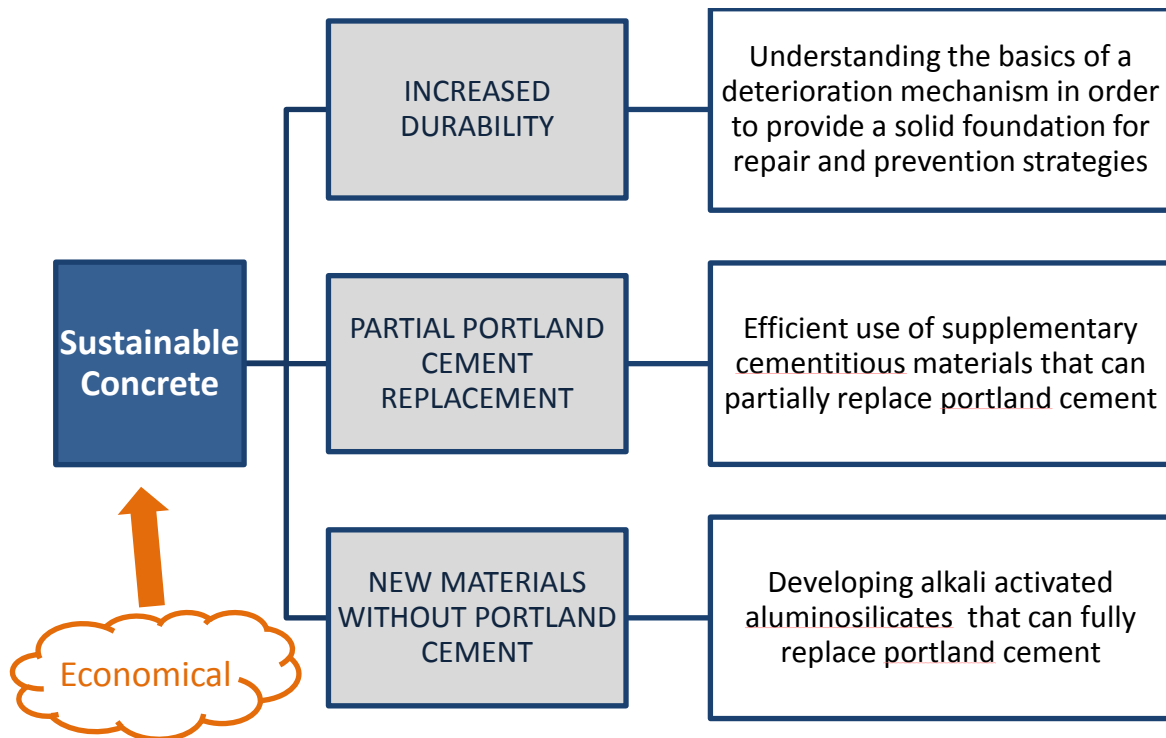
5.1.1.2	X-ray absorption near edge structure (XANES) and extended x-ray absorption fine structure (EXAFS) spectroscopy.....	90
5.1.1.3	Small Angle Scattering.....	91
5.2	Experimental program.....	95
5.2.1	Materials.....	95
5.2.1.1	Alkali silica reaction gel.....	97
5.2.1.2	Na-Kanemite.....	98
5.2.2	Characterization Experiments on the Field Gels.....	103
5.2.2.1	Thermogravimetric analysis.....	103
5.2.2.2	Vibrational spectroscopy.....	105
5.2.2.2.1	Fourier Transform Infrared Spectroscopy.....	105
5.2.2.2.2	Incoherent inelastic neutron scattering.....	107
5.2.2.3	Nuclear Magnetic Resonance (NMR) Spectroscopy.....	109
5.2.2.4	Scanning x-ray transmission microscopy (STXM).....	117
5.2.2.5	Total scattering investigations.....	120
5.2.2.6	Small angle neutron scattering.....	125
5.3	Conclusions.....	128
<b>Chapter 6</b>	<b>Fly Ash.....</b>	<b>130</b>
6.1	Using fly ash in cement and concrete industry.....	131
6.1.1	Using fly ash as a portland cement replacement.....	132
6.1.2	Using alkali activated fly ash as a binder in concrete.....	134
6.2	Characterization of the glass phase in Class F fly ash.....	135
6.2.1	Nuclear Magnetic Resonance (NMR) Spectroscopy.....	138
6.2.2	MD Model.....	141
6.2.3	Total scattering investigations.....	143
6.2.4	Scanning Transmission X-ray Microscopy (STXM).....	148
6.3	Conclusions.....	151
<b>Chapter 7</b>	<b>Conclusions.....</b>	<b>152</b>
<b>References</b>	<b>.....</b>	<b>154</b>

# 1

## Introduction

The word concrete comes from *concretus* (compact, condensed) in Latin, a conjunction of *con* (together) and the past participle of *cresco* (to grow) [1]. Thus, the word can be translated as ‘grown solid together’ [1]. From the time of ancient Romans, who mixed volcanic ash and lime with fist sized rocks, till today’s modern plants, concrete has been one of the most durable and popular building materials. According to 2011 data [2], the global production of portland cement is about 3.4 billion tons per year, almost all being used in construction projects. Considering typical concrete proportions [3], this amount of cement is incorporated into approximately 27.9 billion tons of concrete, which also requires some 22.3 billion tons of aggregates and 2.2 billion tons of fresh water, leading to an incredible global average consumption of 4.1 tons of concrete per person/year. This makes portland cement concrete the most widely used manmade material. The reasons for concrete’s domination are diverse. Among the most critical are its flexibility and adaptability as proven by various types of constructions it is used; its low maintenance requirements during the service life of the structures; and the economic and widespread accessibility of its constituents [3]. However, the massive production and consumption cycle of concrete has significant environmental impacts making the current concrete industry unsustainable [4]. Being able to meet the high volumes of future concrete demand without placing too much burden on the environment is a major challenge. Currently, portland cement concrete production accounts for 5-7% ( $2.1 \times 10^9$  tons) of anthropogenic carbon dioxide ( $\text{CO}_2$ ) emissions annually [4] (the greenhouse gas responsible for an estimated 64% of the enhanced greenhouse effect [5]). Most of the emissions are attributable to the production of cement clinker, the active ingredient in concrete [6]. Approximately half of these emissions are through combustion of fossil fuels; as portland cement is one of the most energy-intensive materials, 4-5 GJ per ton [4]. The remaining portion is due to calcination of the limestone. Overall, for 1 kg of portland cement clinker 0.87 kg of  $\text{CO}_2$  is released to the atmosphere [6]. As a result, on average  $\text{CO}_2$  emissions from cement production add up to almost 2 billion metric tons annually, slightly more than 6% of the global fossil-fuel emissions. This number corresponds to direct emissions only, i.e., those generated in the cement factory. The threat of climate change presents one of the major environmental challenges for today’s society, and the rising atmospheric  $\text{CO}_2$  concentration is alarming. Thus, the cement and concrete industry plays a key role in  $\text{CO}_2$ -emission mitigation strategies [7]. The pressure to develop advanced alternatives that are more ecological, and yet with the necessary strength, durability and economics is building up.

The need for enlarging the built environment is inevitable due to the increasing population. In addition, we are faced with an aging civil infrastructure that requires constant maintenance, and in some severe cases complete replacement of the structures. Therefore, setting a road map to sustainability is of vital importance. Three different approaches on achieving sustainable and economical concrete are summarized in Figure 1-1. The microscopic- and macroscopic scale knowledge on these alternatives is growing at a rapid pace. In this research, the focus is looking at some of these alternatives from a different light in order to broaden the existing knowledge on atomic - and nanometer - scale. Study at these levels is essential to understand the basic properties of materials and reaction mechanisms, providing researchers with the tools to create solutions to pressing problems that have previously been dealt with on an ad hoc basis because of a fundamental lack of knowledge.



**Figure 1-1. Road map to sustainable concrete**

The ability to determine the atomic structure of complex materials increased exponentially within the last century. The periodicity, extended symmetry, and long-range order of crystalline materials provided the basis for the development of systematic and quantitative structural analysis methods [8]. From the mid-1930s, x-ray and neutron diffraction has been used for quantitative phase analysis of crystalline materials. The Rietveld method [9] developed in 1970's opened a new chapter in structural refinement of crystalline structures. The method uses the whole profile of the powder diffraction pattern, and utilizes the unit-cell dimensions for determining the peak positions, and the atomic positional and thermal displacement parameters as a model for the peak intensities [10]. This method has been successfully applied in characterization of anhydrous cements and hydrated cement paste [11,12]. Rietveld method was also successfully used in understanding nano structure of calcium silicate hydrates [13].

The structurally disordered materials lack long-range periodic order, and yet, their structure is not random; and they still contain significant and varied local atomic structural arrangements on the length scales up to several tens of nearest neighbors [14]. The traditional structure refinements yield only long-range average structures of the materials, but neglect the diffuse scattering part of the diffraction patterns which contains information on the local disorder [15]. Therefore, of the traditional structural refinement methods in structurally disorder materials are not very effective. Experimental determination of the complete atomic structure of an amorphous or a poorly crystalline material is almost impossible, as this requires a precise determination of the coordinates of all of the atoms. Yet, the material properties are not determined by the absolute position of each atom, rather by the relative positions of the atoms which are close enough to interact [16], making the knowledge of the local atomic environment and the relative positions of near neighbor atoms extremely valuable for both amorphous and nanocrystalline materials.

**Chapter 2** focuses on introducing some of the synchrotron x-ray and neutron based characterization techniques used in this research to probe structurally disordered or poorly ordered materials including total scattering, small angle scattering, and scanning x-ray transmission microscopy. Total scattering uses both the Bragg and diffuse scattering. The pair distribution function obtained via Fourier transform of the normalized total scattering can be used directly to determine the bond lengths within a structure, or to distinguish between different models for structural disorder. Small-angle scattering is used in probing structures at length scales from 10 to 1000 Å. The method is based on passing an intense x-ray or neutron beam through a sample, and measuring the beam scattered out due to the interactions with the material. The resulting profile inverted back to real space or fitted to models describing structures in reciprocal space [17]. Scanning transmission X-ray microscopy (STXM) is a transmission microscopy technique with a monochromatic x-ray beam produced by synchrotron radiation [18]. The energy of the beam can be varied in the beamline over a wide energy. This unique feature allows us to obtain morphological and element-specific information on a variety of materials.

In **chapter 3**, the focus is on amorphous silicas. These have been of importance to civil engineers for several reasons. Silica fume and rice husk ash, both almost pure amorphous silicas, are amongst the most well-known, and effective mineral admixtures used in modern cement and concrete industry. Opals, also an example of amorphous silica, can be found as impurities in the concrete aggregates; however, opals can lead to durability problems. **Chapter 3** broadens the atomic level knowledge on these amorphous silicas using x-ray and neutron based total scattering.

Modern portland cement concrete is a composite consisting of aggregate and hydrated cement matrix with highly alkaline pore solution. The highly alkaline environment is not a friendly environment for certain reactive aggregates with amorphous or poorly-crystalline silica phases causing them to corrode, such as opals. The reaction forms a gel that swells inside the concrete mass, generating tensile stresses that can over time crack the structure. **Chapter 4** discusses the alkali-silica reaction mechanism.

Alkali-silica reaction (ASR) has been known for decades. However, there is a lack of a firm understanding at molecular and nanometer scales of the reaction product and of its expansion when exposed to moisture. It is well-accepted that the swelling is caused by gel adsorbing water however there is only limited understanding of the location of the water inside the gel. This information is critical to find methods to minimize or even eliminate the reaction in affected structures. In **chapter 5**, the existing experimental results on ASR gel at molecular- and nanometer-scale are reviewed. Then, results of this study on the field alkali-silica gels are summarized. The atomic structure of the gel was analyzed by total scattering methods at Advanced Photon Source located at Argonne National Laboratory. The presence of nano-confined water was studied by incoherent inelastic neutron scattering, and, finally, small angle neutron scattering revealed critical information about the pore structure of the gel showing distinct length scales.

Achieving durable concretes is one of the three approaches to the road to sustainability. However, eliminating a large portion of annual CO<sub>2</sub> emissions due to the concrete sector is just as important. In order to eliminate an annual 1 billion tons of CO<sub>2</sub> emissions through the concrete sector requires approximately 50 wt% portland cement replacement with a low carbon alternative. This would require 1.7 billion tons of alternative materials worldwide. Hence, pozzolanic supplementary cementitious materials such as fly ash, silica fume, rice husk ash and natural pozzolans [19] play a very significant role on the road to sustainability. These siliceous or siliceous and aluminous materials in themselves possess little to no cementitious value. But, in finely divided form and in the presence of moisture, they react with calcium hydroxide (Ca(OH)<sub>2</sub>) available in concrete to form highly cementitious compounds. Fly ash is an amorphous aluminosilicate rich [20] byproduct of coal industry with global production of approximately 650 million tons annually. The US 2010 fly ash production is around 68 million tons [21]. 62% of it is placed in landfills; and only the remaining 38% is utilized [22]. Almost half of the utilized fly ash is used in concrete related applications such as pozzolanic cement and concrete production. For decades, pozzolanic concrete and cements with fly ash as a portland cement replacement have been effectively used to produce sustainable and durable products.

Another alternative approach to achieve sustainability in concrete sector is developing new materials that do not utilize portland cement. Within the last decade, alkali activated aluminosilicates are being used to produce environmentally friendly concretes with favorable mechanical and engineering properties [23] creating new opportunities in the field of structural and construction material. Alkali-activation of aluminosilicates results in a high performance binder that can be an alternative to portland cement based systems at certain projects allowing the elimination of a large portion of CO<sub>2</sub> emissions associated with concrete production. The capability of using industrial waste materials rich in aluminosilicates such as fly ash and slag as source material eliminates the need for additional landfills. The reaction products of alkali activation are mainly amorphous with a few aluminosilicate crystalline phases, depending on the synthesizing environment, *i.e.* pH value of alkali-activator, Si/Al ratio, and curing temperature, etc [24,25].

However, the understanding of fly ash at atomic level is limited. Specifically the glassy portion, which is most reactive phase of the fly ash, is not well studied. Therefore, in **chapter 6**, focus is on investigating the glassy portion of fly ash at the atomic level. The glassy fly ash is



probed with x-ray total scattering, and a molecular dynamics model that can be used in a variety of simulations is provided.

To sum up, many mineral admixtures for concrete (*i.e.* silica fume, rice husk ash and fly ash), reactive aggregates (*i.e.* opal), and alkali silica reaction gel have often varying degrees of disorder. Classical crystallographic characterization typically only determines the average structure of the material, while total scattering methods can provide insightful information about their local atomic arrangements. Overall in this research, focus is on looking at these disordered materials at atomic- and nanometer- scale.

The structure of the dissertation is summarized in Figure 1-2.

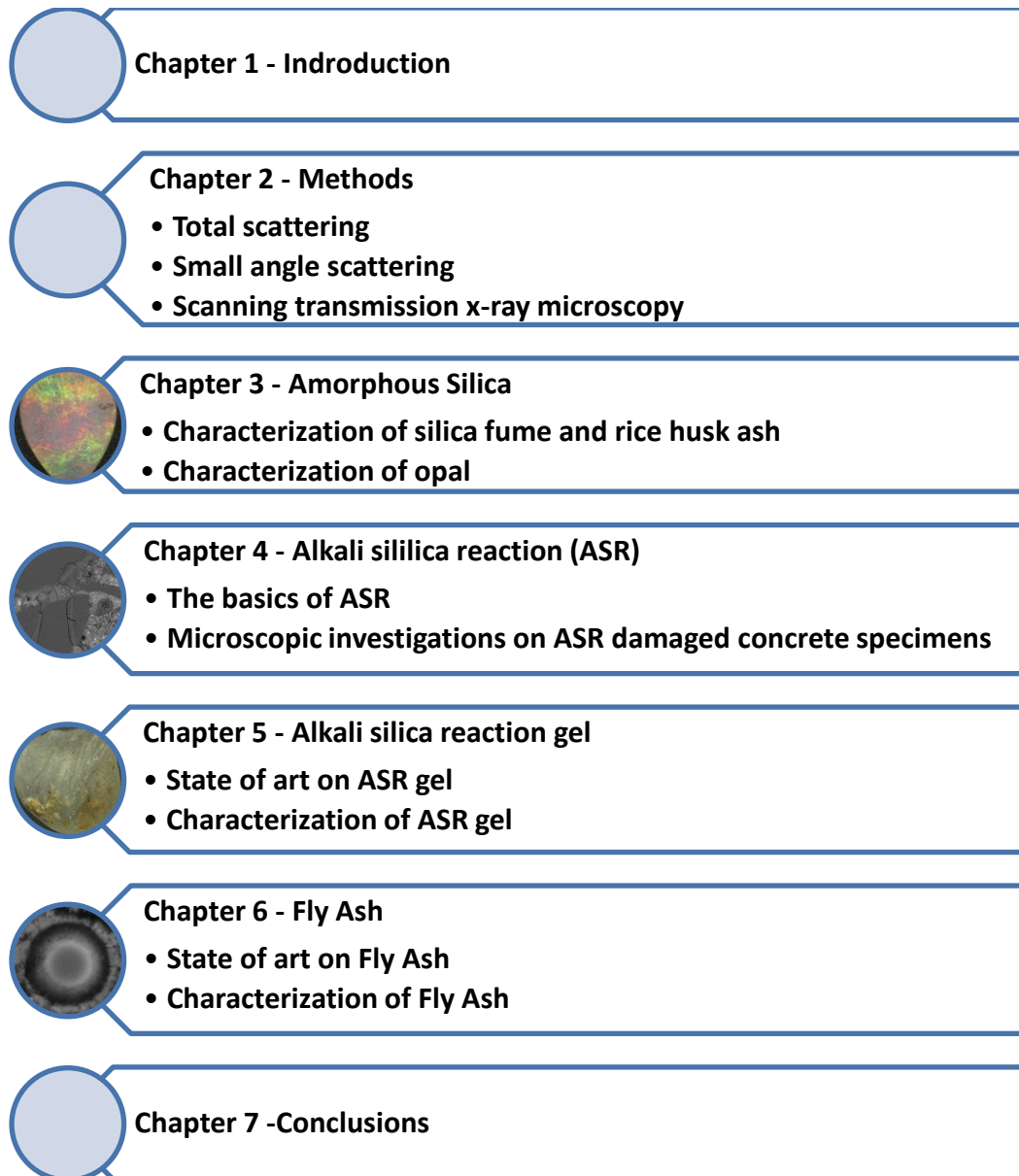


Figure 1-2. Structure of the dissertation



# 2

## Methods

The main limitation of traditional crystal structure refinements is the fact that they yield only long-range average structures of the material but neglect the diffuse scattering part of the diffraction pattern, which contains information on the local disorder [15]. In contrast to crystalline solids, structurally disordered materials (Figure 2-1) lack long-range periodic order, and yet, their structure is not random. They still contain significant and varied local atomic structural motifs on the length scales up to several tens of nearest neighbors [14]. Their lack of long-range order (LRO) severely restricts the utility of traditional structure refinement methods.

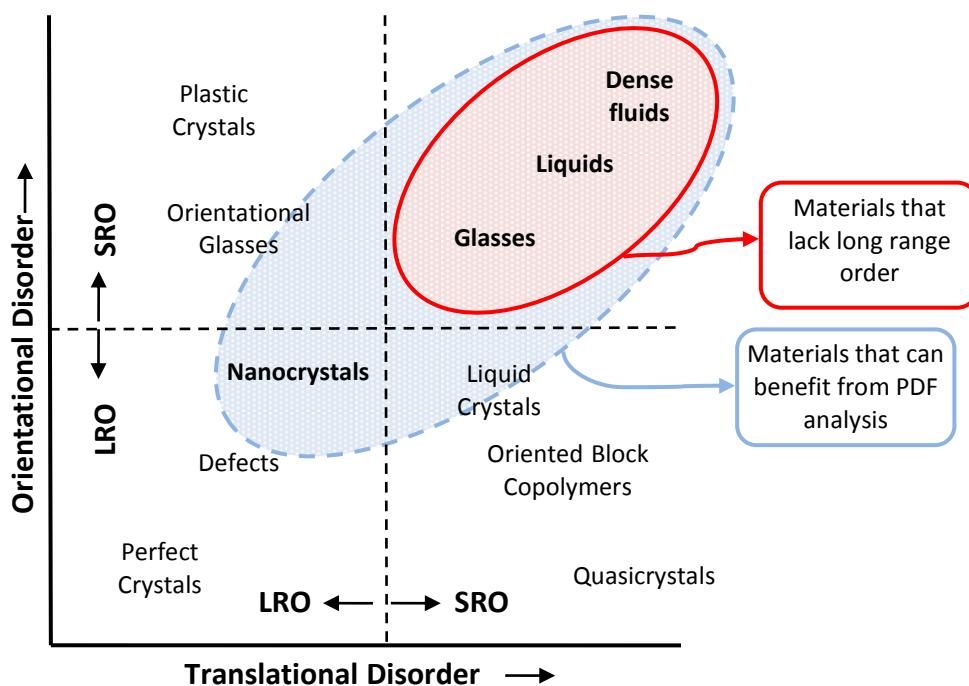
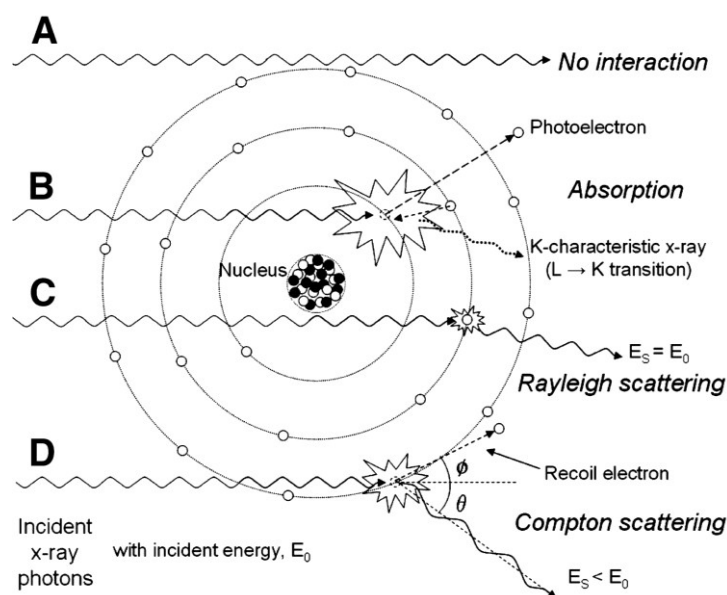


Figure 2-1. Schematic plot of translational and orientational order and disorder in materials, adapted from [26]. LRO, long range order. SRO, short range order.

Experimental determination of the complete atomic structure of an amorphous (*i.e.* glasses and liquids) or a poorly crystalline (*i.e.* nanocrystals, and gels) material is nearly

impossible, as it would require a precise determination of the coordinates of all of the atoms. Material properties are not determined by the absolute position of each atom, but by the relative positions of the atoms which are close enough to interact [16]. Therefore, the knowledge of the local atomic environment and the relative positions of near neighbor atoms is extremely valuable both for an amorphous and a nanocrystalline material.

At synchrotron light sources intense beams of X-rays are produced from accelerators, and directed into experimental stations hosting instruments that utilize different types of interaction of photons with matter: X-rays can be transmitted through a sample without any interaction (Figure 2-2A), can interact with the sample in various ways (see Figure 2-2B-C). The ratio of absorption/fluorescence, Compton and Rayleigh scattering and transmission depends on the sample thickness, density and composition, and the incident X-ray energy.



**Figure 2-2. Schematic of X-ray interactions, adapted from [27]. (A) Unattenuated beam does not interact with material, and gets transmitted. (B) Photoelectric absorption results in total removal of incident X-ray photon with energy greater than binding energy of electron in its shell, with excess energy distributed to kinetic energy of photoelectron. (C) Rayleigh scattering is an elastic interaction with electron (or whole atom) in which no energy is exchanged and incident X-ray energy equals scattered X-ray energy with small angular change in direction. (D) Compton scattering interactions occur with essentially unbound electrons, with transfer of energy shared between recoil electron and scattered photon, with energy exchange described by Klein–Nishina formula. Compton scattering is inelastic.**

In this chapter, some of the synchrotron based characterization experiments used throughout this research will be introduced: total scattering, small angle scattering (SAS) and scanning X-ray transmission microscopy (STXM). As their names suggest, the total scattering and small angle scattering utilize the scattered beam from the sample, whereas STXM takes advantage of the transmitted beam. The total scattering experiments are conducted at Advanced

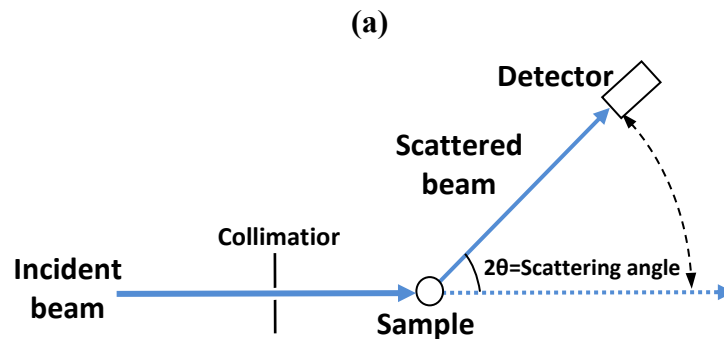
Photon Source (APS), IL. The small angle scattering and STXM experiments are conducted at Advanced Light Source (ALS), Berkeley.

In this research, total scattering and small angle scattering experiments at neutron facilities are also conducted at the Los Alamos Neutron Scattering Centre (LANSCE). Unlike electrons and photons (X-rays) which are scattered by electrons, neutrons undergo extremely weak electromagnetic interactions allowing them to pass through the matter largely unimpeded, and interact only with the atomic nuclei. Like the case in X-rays and photons, if a neutron passing through a sample is scattered with no loss of energy, the scattering is elastic [28]. The scattered neutron waves may undergo interference. When the scattered waves from different nuclei of the same type interfere, coherent scattering arises which is measured in diffraction experiments. When the natural isotropic and spin mixture of the sample destroys the local order, and reduces the interference between the scattered waves (sometimes completely), incoherent scattering arises [29]. If the neutron exchanges energy with the sample, then the scattering is inelastic [29]. In this chapter, we will briefly describe neutron based total scattering, and small angle scattering.

## 2.1 Total Scattering

Neutron and X-ray diffraction techniques measure the differential scattering cross-section (see Figure 2-3). The measurements are generally represented in momentum transfer ( $Q$ ) space, or commonly known as reciprocal space.  $Q$ , the momentum transfer vector, is the difference between the wave vectors of the incident and scattering neutrons or X-rays. For elastic scattering, the magnitude of  $Q$  is given by  $4\pi \sin \theta / \lambda$  where  $\lambda$  is the wavelength, and  $2\theta$  is the angle of scattering. The  $\lambda$  can be calculated from  $\lambda = E/hc$  where  $E$  is the energy of the beam  $E$ ,  $c$  is the speed of light and  $h$  is the Planck constant.

The maximum experimental  $Q$ -range is limited to  $4\pi/\lambda$ , since  $\sin \theta \leq 1$ . For example,  $\text{Cu K}\alpha$  radiation, having a wavelength of  $1.54 \text{ \AA}$ , has a  $Q$ -range limit of about  $8 \text{ \AA}^{-1}$  [16]. High energy synchrotron sources, such as beamline 11-ID-C at APS operating around  $115\text{keV}$  use wavelengths around  $0.1 \text{ \AA}$ , allowing a much wider  $Q$ -range compared to a standard laboratory X-ray diffraction instrument using  $\text{Cu K}\alpha$  radiation.



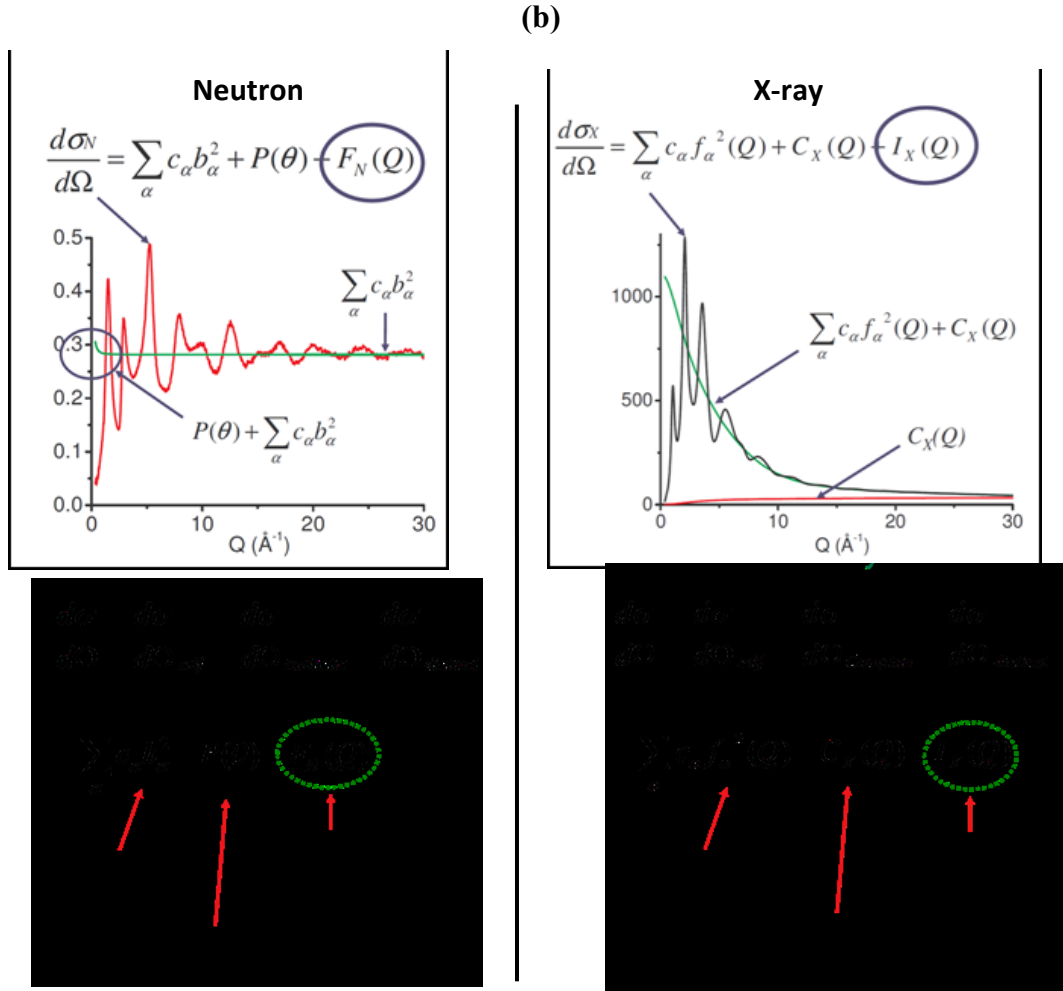


Figure 2-3. (a) Schematic for a typical scattered intensity from a sample using a monochromatic incident beam. (b) Examples of spallation neutron and X-ray differential scattering cross sections,  $d\sigma/d\Omega$ , where  $Q$  is the magnitude of the momentum transfer vector,  $c_{\alpha}$  is the atomic concentration of atoms of species  $\alpha$ ,  $b_{\alpha}$  is the coherent neutron scattering length,  $f_{\alpha}(Q)$  is the X-ray (usually atomic) form factor for species  $\alpha$ .

The differential scattering cross-section is proportional to the structure factor,  $S(Q)$ , of a monatomic system, or to a weighted sum of partial structure factors,  $S_{\alpha\beta}(Q)$ , for a polyatomic system, as shown in Figure 2-4a [30]. For example, vitreous germania ( $\text{GeO}_2$ ) has three partial structure factors, namely Ge-Ge, Ge-O and O-O (see Figure 2-4-b). By identifying each species or element specific group of the contributing atom-atom correlations explicitly, the X-ray weighted total structure factor can be written as:

$$S_X(Q) - 1 = \sum_{\alpha, \beta=1}^n c_{\alpha} c_{\beta} f_{\alpha\beta}(Q) [S_{\alpha\beta}(Q) - 1] = \rho_0 \sum_{i=1}^n c_{\alpha} c_{\beta} f_{\alpha\beta} \int_0^{\infty} 4\pi r^2 [g_{\alpha\beta}(r) - 1] \frac{\sin Qr}{Qr} dr \quad (2.1)$$

where  $\rho_o=N/V$  is the atomic number density (in atoms/ $\text{\AA}^3$ ),  $c_\alpha$  is the atomic concentration of atoms of species  $\alpha$ ,  $S_{\alpha\beta}(Q)$  are the partial structure factors,  $g_{\alpha\beta}(r)$  are the corresponding partial pair distribution functions,  $r$  is the distance in real space and

$$f_{\alpha\beta}(Q) = f_\alpha(Q)f_\beta(Q) / \sum_{\alpha=1}^n c_\alpha f_\alpha^2(Q) \quad (2.2)$$

where  $f_\alpha(Q)$  is the X-ray form factor for atomic species  $\alpha$  [31].

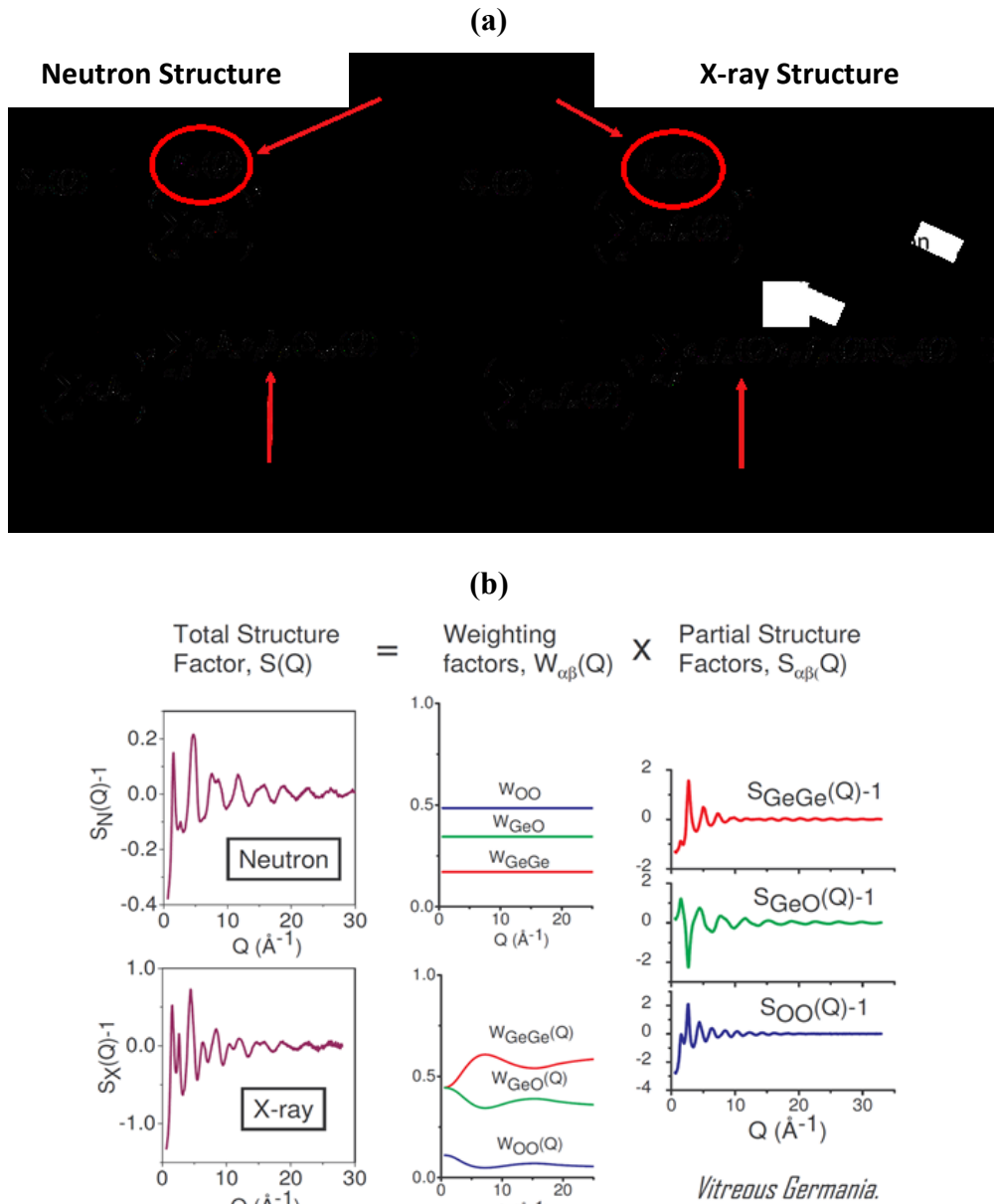


Figure 2-4. (a) Neutron and X-ray structure factors,  $S(Q)$ . (b) Partial neutron and X-ray structure factors for vitreous germania [32].

When neutrons are used,  $f_\alpha(Q)$  is replaced by the Q-independent coherent neutron scattering length,  $b_\alpha$  [31]. The interactions of neutrons and X-rays with matter are very different. X-rays are more sensitive to heavier elements (i.e. have a higher Z value); whereas the neutron cross sections tend to be more similar, displaying variation from isotope to isotope in a complex pattern. Therefore, combining neutron and X-ray diffraction techniques often provides complementary information [30]. A review of notations for representing  $S(Q)$  in terms of distribution functions is given in [33].

In order to obtain an accurate  $S(Q)$ , a multitude of experimental effects need to be minimized and/or corrected for (container scattering, sample absorption, multiple scattering, detector efficiency etc.) before normalization. There are various computer programs available for these X-ray and/or neutron specific corrections, depending on the type of measurement. For example PDFgetX2 is commonly used for analysis of X-ray PDF measurements [34]. A summary of data treatment and corrections for neutron PDF scattering measurements of liquids and glasses can be found in [35].

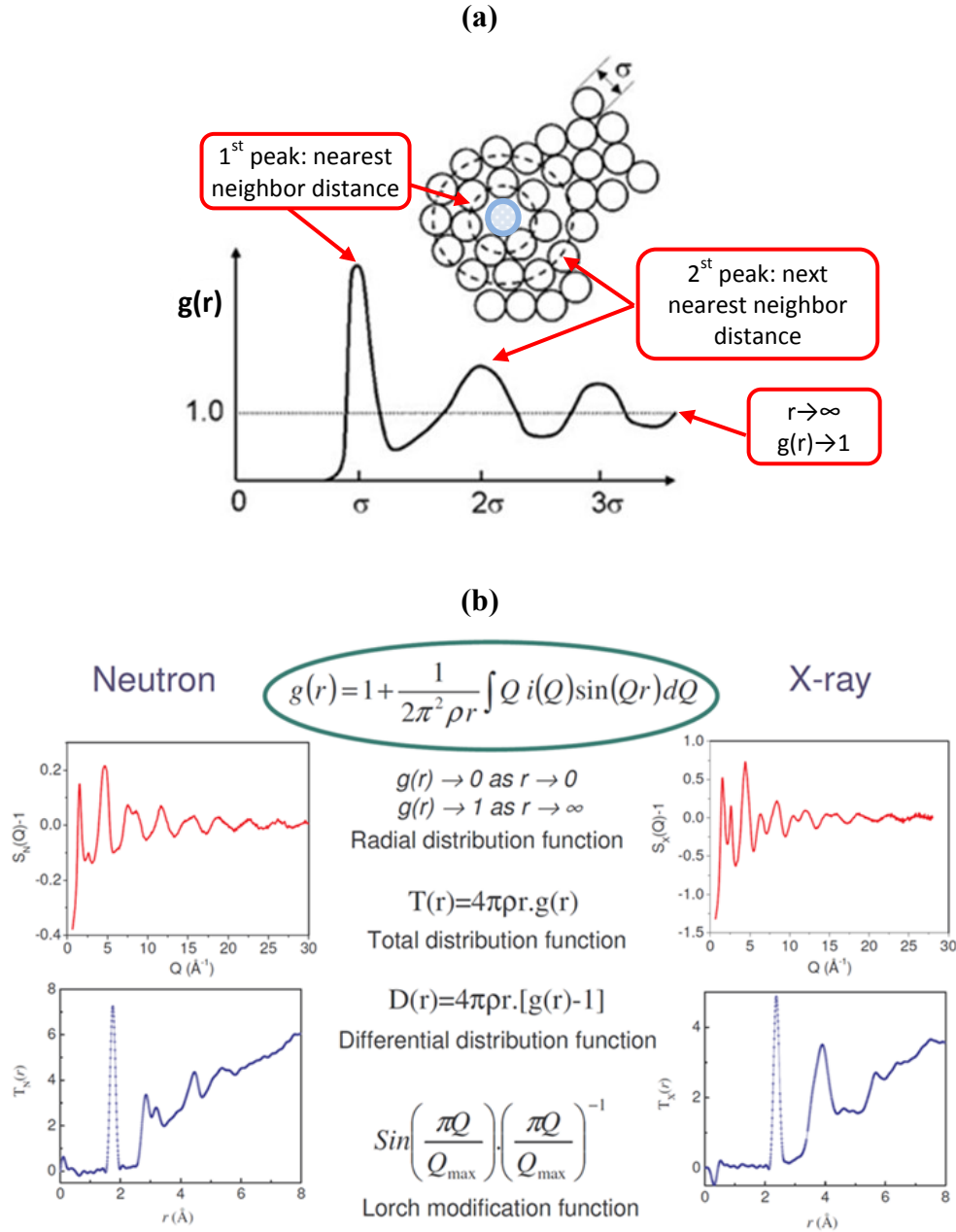
$S(Q)$  can be directly studied in reciprocal space; because the low-Q peaks are highlighted in this representation and are dominated by intermediate or extended range ordering, whereas the high-Q oscillations are primarily related to the local bond distributions. However, the local structure is more easily visualized by (partial) Fourier transforming  $S(Q)$  into real space and studying the (total or partial) pair-distribution functions (PDF) (see Figure 2-5). As in structure factors, for a material containing  $n$  different atom types, there are  $n(n+1)/2$  partial PDFs contributing to the measured total, each weighted by the concentration and scattering strength of the involved pair of species. Theoretically, the integral in the Fourier transformation is performed over the Q-range from zero to infinity, but in practice, the finite value of maximum accessible  $Q_{\max}$  in the Sine-Fourier transform leads to peak broadening and non-physical oscillations (also called truncation ripples) at low- $r$  values in real space [36]. This can be minimized by damping  $S(Q)$  at high-Q values (e.g. by Lorch modification function [37]) before the Fourier transformation. The total X-ray pair distribution function,  $G_X(r)$ ,

$$G_X(r) = \frac{f_\alpha(Q)f_\beta(Q)}{(2\pi)^3\rho_0} \int_0^\infty 4\pi Q^2 S_X(Q) \frac{\sin Qr}{Qr} dQ \quad (2.3)$$

represents the weighted sum of the partial PDFs,  $g_{\alpha\beta}(Q)$ , emphasizing the local structural correlations and is commonly used in the studies of liquids and computed as an output from Molecular Dynamics or Monte Carlo simulations [38]. In calculations, both the sharp Bragg peaks (as a result of LRO), and diffuse components (as a result of disordered local structure) are taken into consideration. Therefore, the PDF method is also referred to as the total scattering method.

It is sometimes useful to emphasize the medium- or long-range correlations by using the differential distribution function,  $D_x(r) = 4\pi r \rho_0 (G_X(r) - 1)$ , [31]. Also, the representation  $N_x(r) = rT_x(r) = 4\pi r^2 \rho_0 G_X(r)$  has a direct physical interpretation to actual coordination numbers, since  $N(r)d(r)$  represents the number of atoms lying within a range  $(r + dr)$  from any given atom [30].



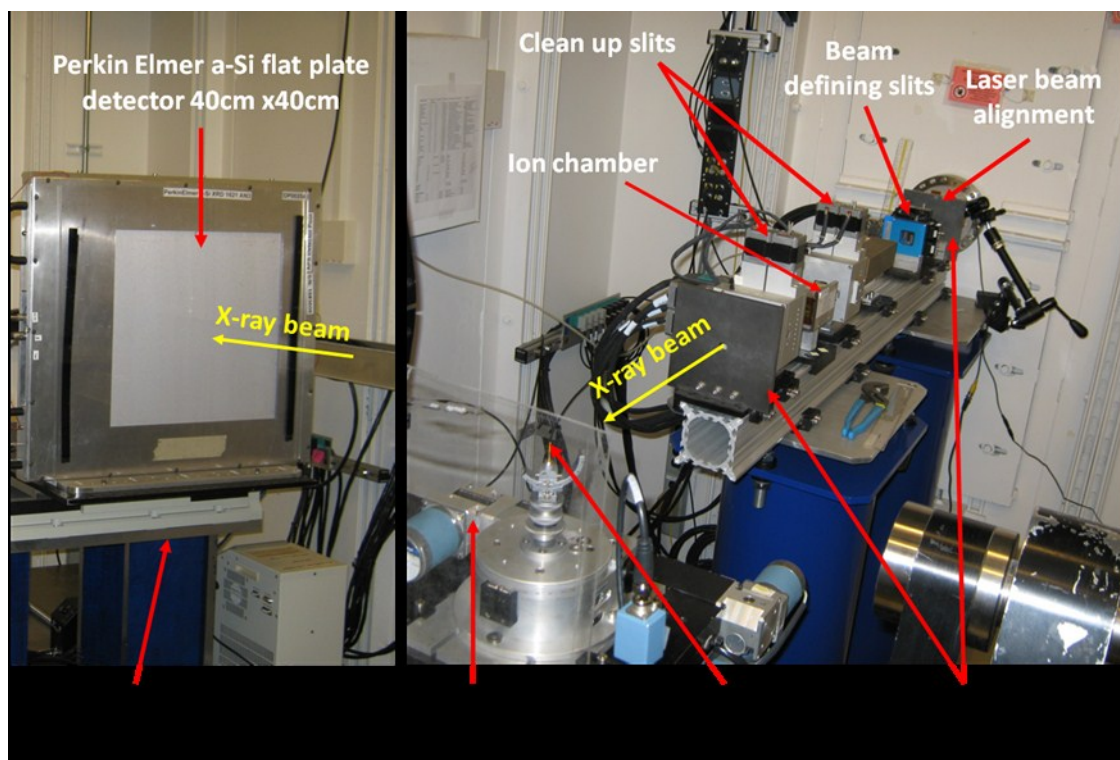


**Figure 2-5. (a) Pair Distribution Function,  $G(r)$ , for a monatomic system.  $G(r)$  allows us to visualize the probability of finding another atom at a given distance  $r$  in real space, adopted from [39]. (b) Calculating  $G(r)$  from  $S(Q)$  for neutrons and X-rays.**

The PDF technique was pioneered by Warren [40] in the 1930s using X-rays to study non-crystalline forms of matter. However, it gained popularity first in the field of neutron scattering -- especially in the 1980s -- with the development of high flux spallation neutron sources, providing access to high momentum transfers [41]. With the development of 3<sup>rd</sup> generation synchrotrons in the mid-1990s and the production of hard X-ray beams, PDF analysis using high energy X-rays became popular as a research tool for studying disordered materials.

During this time, PDF was increasingly applied to characterize nanocrystalline systems as well as amorphous and liquid materials.

In a PDF experiment utilizing an X-ray probe, a monochromatic beam of high energy X-rays ( $E > 60 \text{ keV}$ ,  $\lambda < 0.2068 \text{ \AA}^{-1}$ ) scatters in transmission geometry, passing through the sample into a detector in the forward direction (see Figure 2-3a). The combination of high energy and low angle compress a wide momentum transfer ( $Q$ ) range into a small angular solid angle, minimizing attenuation and multiple scattering effects on millimeter-sized samples. Today, there are a handful of high energy X-ray PDF beamlines around the world and a large boost to the versatility of this technique has been the use of large area detectors, which allow for much shorter measurement times, but lack energy discrimination. For example, the high energy X-ray beamline at 11-ID-C at the APS operates at 115 keV (see Figure 2-6).

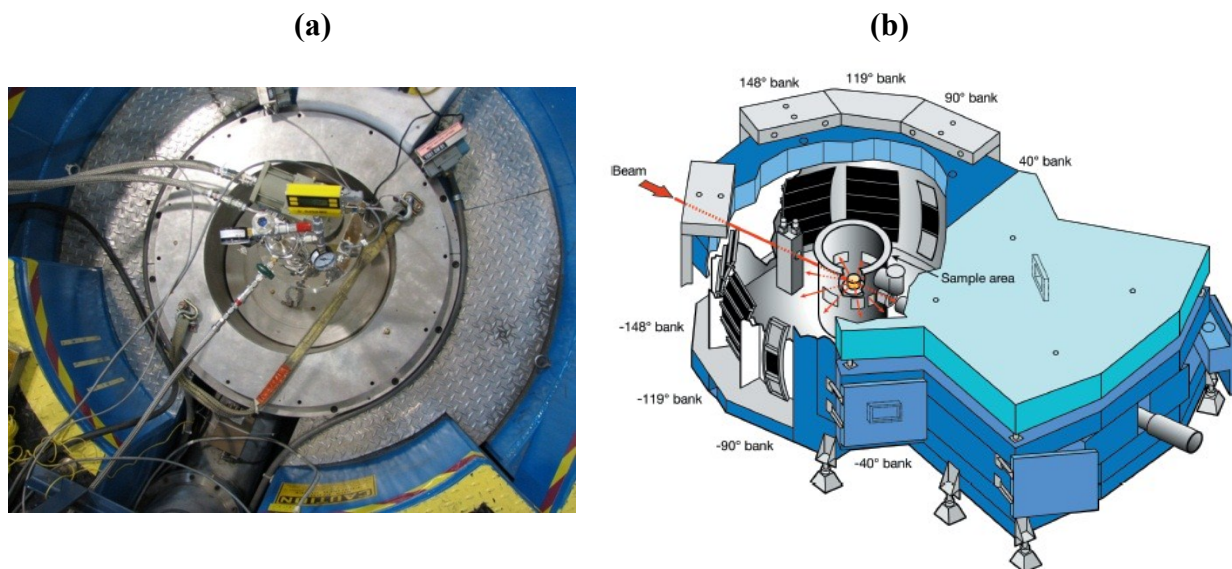


**Figure 2-6. Beamline 11-ID-C, APS. Fixed incident energy 115 KeV (wavelength 0.108 Å). Sample-detector distance: 25-300 cm; Q-range: 0.2-40 Å<sup>-1</sup>; detector pixel size: 0.2 mm x 0.2 mm.**

Beamline 11-ID-C has three pairs of horizontal and vertical collimating slits. An ion chamber measures the incident flux and the direct beam that is not scattered or absorbed by the sample. The incident beam is blocked with short length of 3 mm diameter tungsten rod, mounted in front of the area detector. The sample is positioned on a goniometer with three-dimensional motor control. Alignment is initially performed using an optical telescope and laser beam system, and precise adjustments (to within 10 microns) are made using the X-ray beam and a moveable photodiode detector. The detector distance can be varied depending on the aimed Q-range. In this research, was used at positioned at different distances. For measurements with fly

ash is located at 426.5mm, for opal measurements it is located at 657.87 mm. Regular dark current measurements are performed between area detector scans to minimize the effects of electronic drift. In this study, for accurate local and intermediate range order structure determination of a sample, several measurement with count times of 5-6 minutes are averaged providing good statistics over a wide  $Q$ -range. However, the speed of the measurement depends on the sample, and the detector and the computers available; thus, may be much shorter or longer.

Some of the PDF experiments in this study were conducted with neutrons at NPDF Beamline (Figure 2-7) at LANSCE. The NPDF is a total-scattering powder diffractometer, with high neutron flux and backscattering detector modules that provide high resolution. This permits access to a wide range of momentum transfer with sufficient counting statistics. It is located 32 meters from the spallation neutron target, and comprises 20 detector panels with a total 160 position sensitive detectors [42].



**Figure 2-7. (a) The lid of the NPDF beamline experimental chamber at Los Alamos Neutron Scattering Center; (b) the schematic of the beamline [42].**

The PDF method is most powerful when interpreted along with information from other methods, both experimental and computational. Partial structure factor information may be extracted by using both X-ray PDF and neutron PDF data sets together, and also through the techniques of anomalous scattering, isomorphic substitution and isotopic neutron diffraction substitution experiments [30,43]. Combining PDF data with X-ray or neutron small angle scattering, nanotomography, high-resolution TEM, or reflectivity measurements is very useful to interpret the collected data [44]. Although these methods do not provide any atomic structure information, they give important supplementary data such as particle size, density fluctuations and homogeneity of the sample.

PDF gives an overview of the structure of the material over a wide range of length-scales and places constraints on atomistic models. Widely used methods to model PDF data are Reverse Monte Carlo (RMC) modeling [45], and Empirical Potential Structural Refinement (EPSR) [46]. The RMC method iteratively refines a three-dimensional atomistic model of the material that is consistent with PDF data sets [30], analogous to a Rietveld refinement in crystallography. An important advantage of using RMC modeling is its flexibility in combining different data types into the same model. The main disadvantage of this (or any similar) technique is the lack of a unique structure solution. Additionally, in RMC modeling the starting configuration has to be chosen carefully, since the method lacks inherent chemical and thermodynamic constraints. EPSR is, in concept, a similar method compared to RMC or Rietveld refinement, targeting mainly molecular systems, whereby it refines an interatomic potential until the three-dimensional atomic model for the system is in agreement with the PDF data [46].

Classical molecular dynamics (MD) predicts the PDF by moving atoms in a limited simulation box according to predefined inter-atomic potentials and force fields. The used potentials are often derived from known crystal structures and do not always represent the investigated system. MD simulations do not always reproduce the  $S(Q)$  data precisely. However, they predict trends well, as information on both structure and dynamics of the system as chemical bonding information is assigned to atoms.

*Ab initio* molecular dynamics simulations combine the advantages of MD and density functional theory, and generally provide more accurate models than MD simulations with the added cost of computational time. Simulations on disordered materials usually require thousands of atoms for useful statistical averaging and information on intermediate range ordering. This large requirement prevents the application of *ab initio* MD simulations in many cases.

The two most common X-ray absorption methods, the extended X-ray absorption fine structure (EXAFS) and the X-ray absorption near-edge structure (XANES), are also used in combination with PDF data. EXAFS is an element-specific bulk probe that is sensitive to dilute species. EXAFS reveals information about the ligation, coordination number and bond distance in the local molecular environment of the investigated element [30,44]. The information obtained from EXAFS complements PDF analysis. XANES, similar to EXAFS, provides only near neighbor distance distributions and coordination numbers, but it is much more sensitive to bond angles compared to EXAFS [44]. In cement research, most of the applications of EXAFS and XANES are in the study of immobilization of species by the hydration products [47–49]. Details of this method are discussed in section 2.3.

Raman spectroscopy in solids utilizes the inelastic or Raman scattering of monochromatic light usually from a laser. The extreme sensitivity of Raman spectra to local deviations from the average periodicity makes it valuable in exploring local structure [44], providing supplementary information for PDF analysis. Recent applications of Raman spectroscopy to study calcium silicate hydrates (C-S-H) have been reported by Garbev *et al.* [50] and Black *et al.* [51]. Solid state NMR is another powerful technique that could be used in combination with PDF analysis. It is sensitive to local structure in disordered materials and yields information on local symmetry and the speciation distribution of the probe atom [52,53], whereas PDF only gives average coordination numbers.

## 2.2 Small Angle Scattering

Small-angle scattering (SAS) is a powerful method used in probing structures at length scales from 10 to 1000 Å with applications ranging from polymers, and biological molecules to microemulsions, Figure 2-8 [17].

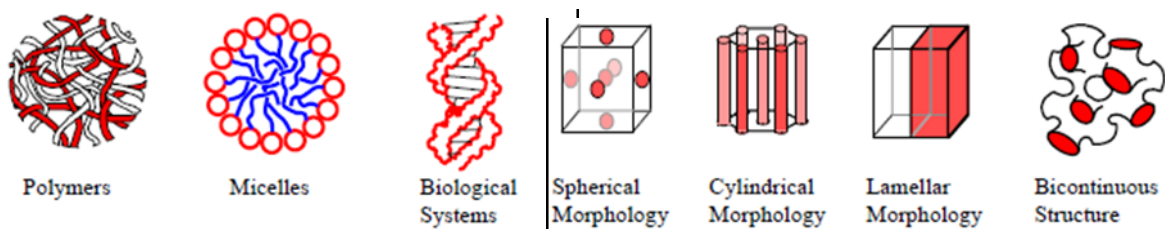


Figure 2-8. Various classes of samples and morphologies investigated by SANS [17]

The method is based on passing an intense X-ray (SAXS) or neutron (SANS) beam through a sample, and measuring the beam scattered out due to the interactions with the material, Figure 2-9. The resulting profile, the intensity of scattered neutrons or X-rays as a function of scattering angle, is in the reciprocal space, not in real space like microscopy. Therefore, the profile has to be inverted back to real space or fitted to models describing structures in reciprocal space [17].

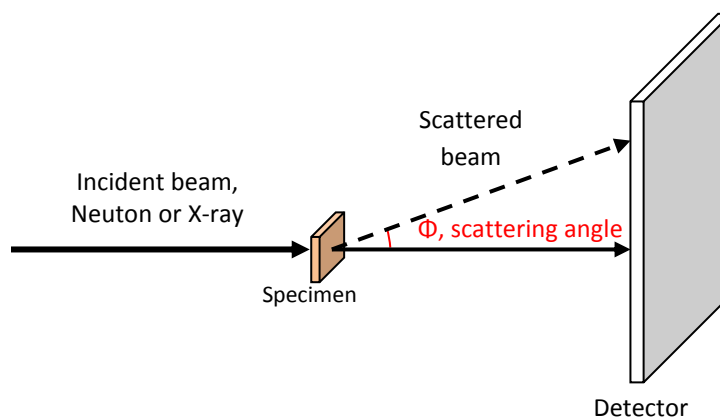


Figure 2-9. Schematic of a small-angle scattering experiment. This is not to scale with vertical dimensions are in centimeters whereas horizontal dimensions are in meters.

Choosing between SANS and SAXS is also critical. The X-ray-scattering length of an atom, a measure of the interaction of an X-ray with an atom, depends on the atomic number, so SAXS is dominated by the heavier elements in the sample. However, the neutron-scattering lengths of most elements are similar, making it more convenient for hydrogen-related studies. The possibility of deuteration (using deuterium to replace hydrogen) to enhance the contrast, further eases water related studies. ASR, as being a hygroscopic gel, is capable of expanding by adsorbing large amounts of water. Using the deuteration might allow a better understanding of

ASR's expansion mechanism. The disadvantage of choosing SANS is the long measurement times due to the low flux of neutron sources compared to higher fluxes of X-ray sources [17].

SANS instruments can be either reactor-based using monochromated neutron beams or time-of-flight instruments at pulsed neutron sources with a range of wavelengths. A low-Q configuration covers the first order of magnitude (0.2° to 2°) and a high-Q configuration covers the second one (2° to 20°). The scattering vector is defined as  $Q = (4\pi/\lambda) \sin(\theta/2)$  where  $\lambda$  is the neutron wavelength, and  $\theta$  is the scattering angle. The small-angle approximation ( $\sin(\theta/2) \approx \theta/2$ ) simplifies this equation to  $Q = 2\pi\theta/\lambda$ .

The scattering curve of a homogeneous sample can be derived from the electron distribution of the particle:

$$I(Q) = 4\pi \int_0^{D_{max}} g(r) \frac{\sin(Qr)}{Qr} dr \quad (2.4)$$

where  $D_{max}$  is the maximum distance present in the scattering particle,  $g(r)$  is the pair distribution function. From a practical standpoint, the lowest resolution portion of the SAS curve is dictated by a single size parameter [54]. This size parameter, the radius of gyration ( $R_g$ ), is the square root of the average squared distance of each scatterer from the particle center.  $R_g$  represents the effective size of the scattering object whether it is a polymer chain, part of a protein, a micelle, or a domain in a multiphase system [17]. For example, a sphere of radius  $r$  with uniform electron density, for example, has a  $R_g = \sqrt{3/5} r$ .  $R_g$  is shape-dependent and a poor measure of the actual molecular weight (volume) of the molecule of interest. Instrumental smearing as well as polydispersity and multiple scattering appear to decrease the effective  $R_g$ . Inter-particle effects also contribute to  $R_g$  except at the infinite dilution limit (case of an isolated particle) [17].

Guinier first observed that the correlation range for dilute particles was simply the average particle radius of gyration [55]; and from then on, Guinier factorization became a useful method for analysis of the overall scattering function to determine the shape of the pore or particle. The radius of gyration ( $R_g$ ), also known as Guinier radius, is extracted from the initial curvature of the scattering profile [56]:

$$I(Q) = \text{constant} \times \left( 1 - \frac{Q^2 R_g^2}{3} + \dots \right) \quad (2.5)$$

At low-Q region, the scattering intensity from isolated and not strongly correlated particles or fractal aggregates do not depend on the shape of the particles. Instead, it depends only on contrast, number and volume of particles and the radius of gyration ( $R_g$ ), as expanded below:

$$I(Q) = I_0 \exp\left(-\frac{Q^2 R_g^2}{3}\right), \quad \text{Ln}[I(Q)] = \text{Ln}[I_0] - \frac{Q^2 R_g^2}{3} \quad (2.6)$$

where  $I_0$  is the intensity at  $Q=0$ . There are three types of pore shapes: spherical, elongated (tubular) and lamellar. Guinier plot of  $\text{Ln}[I(Q)]$  against  $Q^2$  will give a straight line from which



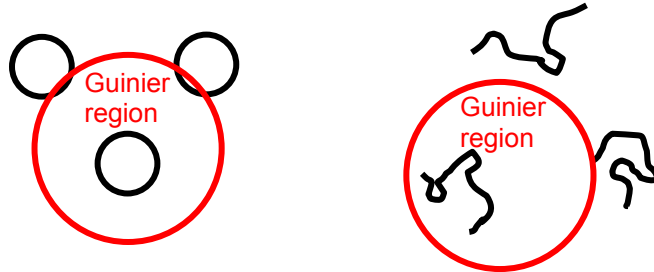
$R_g$  and  $I_0$  can be extracted. The Q-range over which the Guinier approximation is valid ( $QR_g < 1.3$  for globular, and  $QR_g < 0.8$  for elongated objects) is much larger for particles with small  $R_g$  than larger particles, as the probed range ( $2\pi/Q$ ) should be larger than the particle size, Figure 2-10. Beyond this range the particle shape plays an important role, hence this approximation is not valid. The Guinier plot is modified when the scattering objects are elongated. For instance, for a cylinder of length  $L$  and radius  $r$ , the low-Q Guinier approximation remains the same where  $R_g^2 = L^2/12 + r^2/2$ . The intermediate-Q Guinier approximation is different:

$$I(Q) = \frac{I_0}{Q} \exp\left(-\frac{Q^2 R_g^2}{2}\right) \quad (2.7)$$

where  $R_g^2 = r^2/2$  [17]. To investigate the possibility of elongated pores or particles, intermediate-Q Guinier plot becomes  $\ln[I(Q).Q]$  against  $Q^2$ . Similarly for a lamella (flat object) of thickness  $T$ , the intermediate-Q Guinier approximation becomes:

$$I(Q) = \frac{I_0}{Q^2} \exp\left(-\frac{Q^2 R_g^2}{2}\right) \quad (2.8)$$

where  $R_g^2 = T^2/12$ . Thus, the intermediate-Q Guinier plot becomes  $\ln[I(Q).Q^2]$  against  $Q^2$  [17].



**Figure 2-10. Scattering particles are smaller than the probed range in the Guinier region shown for isolated particles and for single polymer coils [17]. The range of a Guinier plot corresponds to  $QR_g < \sqrt{3}$  for globular objects which is obtained if the probed range ( $2\pi/Q$ ) is larger than the particle size. Taken from [17].**

Another well-known method is the Zimm approximation. It provides a shape-independent radius, and like the Guinier approximation. It is valid in the  $Q.R_g < \sqrt{3}$  region. The assumption is that the scattering intensity has a Lorentzian form:

$$I(Q) = \frac{I_0}{1 + Q^2 \xi^2} \quad (2.9)$$

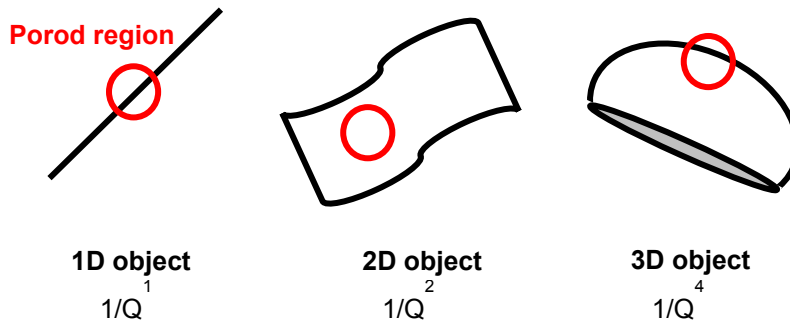
where  $\xi$  is the correlation length characteristic of the system of inhomogenities. Following this equation, a Zimm plot of  $1/I(Q)$  against  $Q^2$  yields  $1/I_0$  as intercept, and  $\xi^2/I_0$  as slope. In the high-Q region, where  $Q^2 \xi^2 > 1$ , radius of gyration can be calculated with  $\xi = R_g/\sqrt{2}$ .

When the probed range is smaller than the scattering object, the radiation is actually probing the local structure. In this domain, the Porod approximation could be used when  $Q \cdot R_g \gg 1 \gg Q \cdot a$  where  $a$  is the persistence length which defines the local stiffness of the backbone (i.e. silica monomer  $\sim 3 \text{ \AA}$ ) [57]. The scattered intensity decays with power law; therefore a Porod plot of  $\log I$  against  $\log Q$  provides information on the "fractal dimension" of the scattering objects. At high- $Q$ , one can approximate:

$$I(Q) = \frac{A}{Q^n} + B \text{ or } \text{Log}[I(Q) - B] = \text{Log}(A) - n\text{Log}(Q) \quad (2.10)$$

where  $A$  is related with the coherent scattering of the sample, and  $B$  is related to the scattering background (contains contributions from the scattering of the sample cell, the cell holder, and incoherent scattering from the sample). Systematic deviations from the Porod law have been interpreted in terms of microstructural features of the system [58]. Positive deviations ( $n < 4$ ) are attributed to thermal density fluctuations or mixing between the phases, while negative deviations ( $n > 4$ ) are caused by diffuse phase boundaries [58]. Integer values of the porod slope  $n$  relate to well-defined geometries such as  $n = -1$  for rigid rods,  $n = -2$  for sheets, and  $n = -3$  for spheres [17].

The mass of a conventional crystalline solid with long range order increases directly proportion to the volume of the sample; i.e. the mass of a spherical sample with radius  $r$  increases with  $r^3$  [17]. Due to random irreversible covalent branching, as in sol-gel silicates, structures can become less dense as they grow. Such systems are called mass fractals, and their mass increases with a smaller power of radius than 3 reflecting in Porod slopes from -1 to -3 [59]. The branching can also produce a structure consisting of crumpled surfaces, i.e. a sheet of paper pressed loosely into a ball [59]. The total surface areas of such structures increase more rapidly with radius than their masses; thus producing Porod slopes varying from  $-3$  to  $-4$ . These structures are known as surface fractals. The dimension of a surface fractal ( $D_s$ ) is given by  $(6 + n)$ .  $n = -3$  relates to a dense structure, while  $n = -4$  ( $D_s = 2$ , Porod's law) corresponds to smooth-surface fractals. Different examples for fractal Porod exponents are given in Figure 2-11. Another interpretation for porod slopes between 3 and 4 for a porous body is polydispersity in pore size. However, the surface fractal scaling and pore polydispersity are geometrically equivalent making the experimental differentiation very difficult [17].





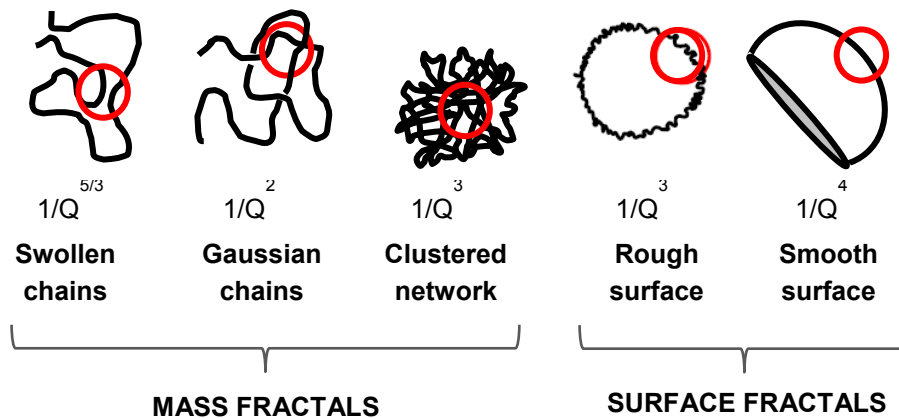


Figure 2-11. Different fractal Porod exponents. Adapted from [17].

SANS measurements for used in this research are carried out at Low-Q Diffractometer (LQD) at LANSCE [60]. LQD uses the time of flight technique, Figure 2-12 and can access a broad range of  $Q$  ( $0.003$  to  $0.5 \text{ \AA}^{-1}$ ) allowing to probe structures with dimensions from  $10$  to  $1000 \text{ \AA}$ .

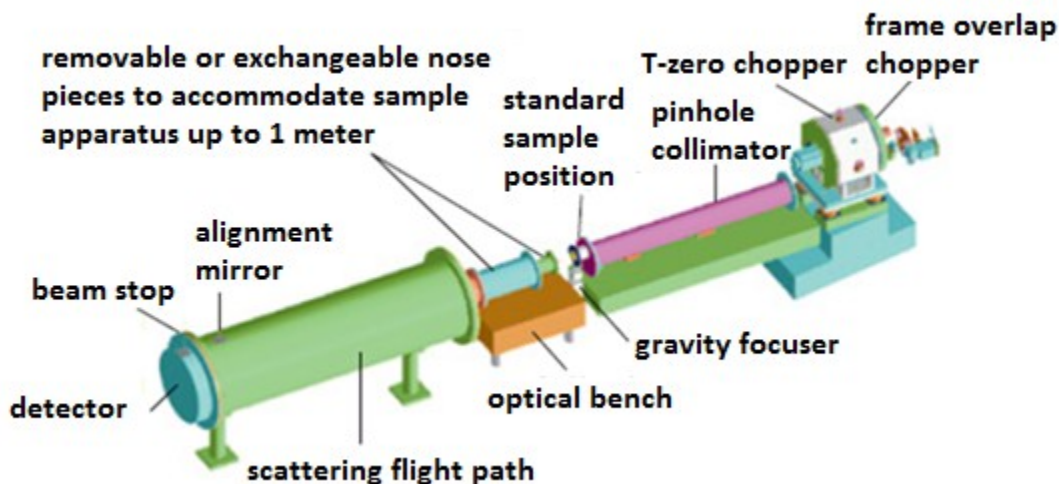


Figure 2-12. The Low-Q Diffractometer (LQD) at LUJAN Center of LANSCE is designed to study large-scale structures with dimensions from  $10$  to  $1000 \text{ \AA}$ .

## 2.3 Scanning X-ray Transmission Microscopy (STXM)

X-rays, like gamma- and alpha-rays, are forms of ionizing radiation. When absorbed by the samples, they might have sufficient energy to excite and promote an absorbing atom's core-electron to higher unoccupied states above the Fermi level or into a free unbound state (the continuum). Each core shell has a distinct binding energy. During a measurement, when the X-ray energy exceeds the ionization threshold values of a core shell electron, a sudden increase in

absorption cross-section. This gives a sudden rise to a so-called absorption edge, with each edge representing a different core-electron binding energy (i.e. Figure 2-13) [61].

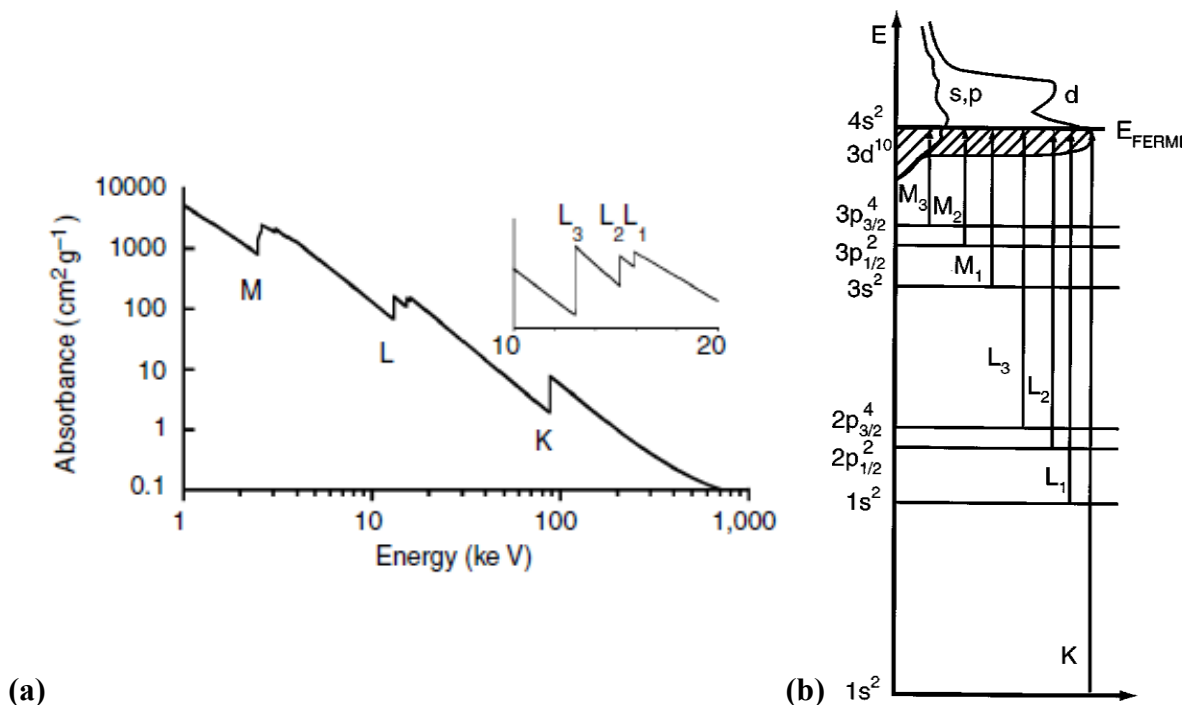


Figure 2-13. (a) Low-resolution X-ray absorption spectrum for *Pb*, adapted from [61]. The overall decrease in the absorption as a function of energy is punctuated by three major sharp transitions are seen (K-, L-, and M-edges), corresponding to excitation of an electron from  $n=1$ , 2, and 3 shells, respectively. At higher resolution both the L- (shown in inset) and the M-edges are split. (b) Nomenclature of absorption edges (or “ionization” edges) of core electrons excited into unoccupied atomic/molecular orbitals above the Fermi level.

The core-electron binding energy increases with increasing atomic number, ranging from 284 eV for the *C* K-edge to 115,606 eV for the *U* K-edge. The L-edges are at significantly lower energies than the corresponding K-edge (e.g., 270eV for the *Cl* L<sub>1</sub>-edge, 20,948eV and 17,166eV for the *U* L<sub>2</sub>- and L<sub>3</sub>-edges) [61]. Electron binding energies for the common elements found in samples investigated in this study are summarized in Table 2-1.

Table 2-1. Electron binding energies for the elements found in samples used in this study, in electron volts (eV), in their natural forms. Values are taken from [62] except as follows \*Values taken from [63], with additional corrections †Values taken from [64].

Element	Z	K 1s	L <sub>1</sub> 2s	L <sub>2</sub> 2p <sub>1/2</sub>	L <sub>3</sub> 2p <sub>3/2</sub>	M <sub>1</sub> 3s	M <sub>2</sub> 3p <sub>1/2</sub>	M <sub>3</sub> 3p <sub>3/2</sub>
H	1	13.6						
C	6	284.2*						
O	8	543.1*	41.6*					
Na	11	1070.8†	63.5†	30.65	30.81			
Al	13	1559.6	117.8	72.95	72.55			

<b>Si</b>	14	1839	149.7*b	99.82	99.42			
<b>K</b>	19	3608.4*	378.6*	297.3*	294.6*	34.8*	18.3*	18.3*
<b>Ca</b>	20	4038.5*	438.4†	349.7†	346.2†	44.3 †	25.4†	25.4†

After penetrating through a sample with mass thickness  $x$  (mass per unit area), and density  $\rho$ , a narrow parallel monochromatic X-ray beam with incident intensity  $I_0$  emerges with intensity  $I$  following the exponential Beer-Lambert attenuation law:

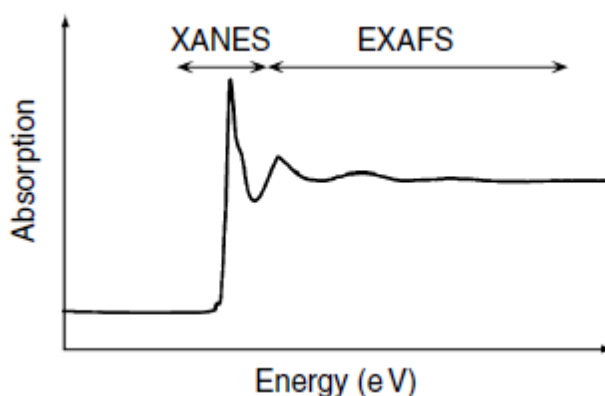
$$I(E) = I_0(E) \cdot e^{-(\mu(E)/\rho)x} \quad (2.11)$$

This equation can be rewritten as:

$$\mu(E)/\rho = x^{-1} \cdot \ln(I_0/I) \quad (2.12)$$

The mass attenuation coefficient  $[\mu/\rho]$  ( $\text{cm}^2/\text{g}$ ) depends on the types of atoms and density  $\rho$  of the sample; and can be calculated through measured values of  $I_0$ ,  $I$  and  $x$ . Mass attenuation coefficient is also called mass absorption coefficient or mass extinction coefficient. The product  $\mu_L = \mu \cdot \rho$  ( $\text{cm}^{-1}$ ) is called the linear absorption coefficient.  $\mu(E)$  is sometimes called the total cross-section for X-ray absorption at energy  $E$ .

X-ray absorption spectroscopy (XAS) focuses on the measurement of X-ray absorption cross-section in the vicinity of one or more absorbing edges by exciting the core-electron into unoccupied atomic/molecular orbitals above the Fermi level [61]. XAS is divided into two regimes (see Figure 2-14): (1) Near Edge X-ray Absorption Fine Structure (NEXAFS) (sometimes called X-ray Absorption Near-Edge Structure (XANES)) for bound states and low energy resonances in the continuum; and (2) Extended X-ray Absorption Fine Structure (EXAFS) for the oscillations above the edge, which can extend for 1000eV or more when the outgoing electron is well above the ionization continuum.



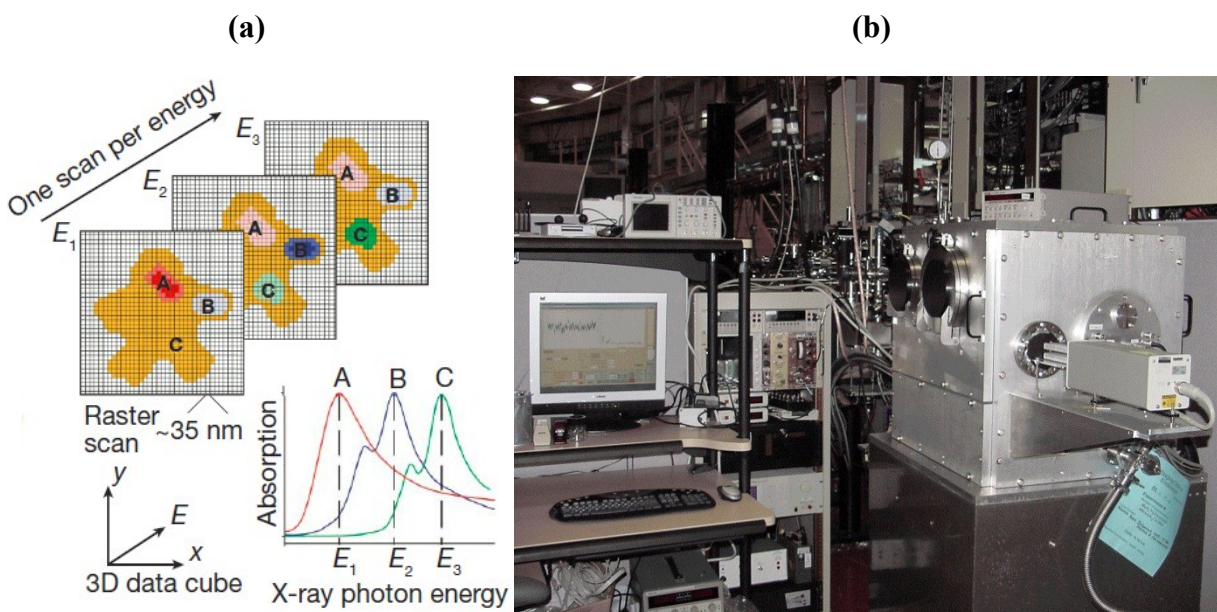
**Figure 2-14. Schematic illustration of an X-ray absorption spectrum, showing the structured absorption that is seen both within ca. 50 eV of the edge (the XANES) and for several hundred to >1,000 eV above the edge (the EXAFS). Taken from [61]**

The distinction between XANES and EXAFS is arbitrary, since the same fundamental physical principles govern photoabsorption over the entire XAS region and there is no

unambiguous definition that distinguishes between “near-edge” and “extended” structure [61]. These transitions are caused by the absorption of an X-ray photon with energy tuned by means of synchrotron radiation to the ionization energy of the electron and lead to a pronounced fine structure in the X-ray absorption spectrum.

The X-ray absorption spectra record the absorption intensity as a function of the incoming photon energy. The total intensity of the spectrum is given by the number of unoccupied states in the initial state, while the spectral shape reflects the density of states for the core hole state. This allows XAS to provide element-specific information about the density of states, local atomic structure, lattice parameters, molecular orientation, the nature, orientation, and length of chemical bonds as well as the chemical state of the sample. As a local probing technique, XAS also allows determining coordination environment of an X-ray absorbing atom of interest within 5Å of distance. This method can be used for species either as precipitates in crystalline phase as well as in amorphous chemical conditions (ex. surface-sorbed species).

Scanning transmission X-ray microscopy (STXM) is a transmission microscopy technique with a monochromatic X-ray beam produced by synchrotron radiation [18,65]. In the STXM beamlines, the energy of the beam can be varied in the beamline over a wide energy range [*i.e.*, 130 to 2100 electron volts (eV)]. The beam is focused on the sample by using a condenser zone plate and a 2-dimensional image is collected by scanning the sample stage at a fixed photon energy. Two types of results can be collected at a STXM beamline. First, image contrast data are obtained from differential absorption of X-rays depending on the chemical composition of the sample. Second, image stacks or line scan data can be obtained by scanning the sample in the x–y direction (image stack) or x direction (line scan) of selected sample areas at energy increments of 0.1 eV over the energy range of interest (e.g., 270 to 330 eV for K and 1060 to 1120 eV for Na), Figure 2-15a.



**Figure 2-15. (a) Diagram of a typical STXM data acquisition method. By acquiring images at different X-ray photon energies (for example  $E_1$ ,  $E_2$  and  $E_3$ ), a three-dimensional data cube with full spectral**

**information at every pixel is obtained. This data can be used to image and distinguish between specific chemical species (for example species A, B and C). [66] (b) Beamline 11.0.2. at ALS.**

Here, x refers to the horizontal direction, y refers to the vertical direction, and x–y refers to the plane perpendicular to the X-ray beam. In addition to two-dimensional images, the stack image produces a near-edge X-ray absorption fine structure (NEXAFS) spectrum for a specific element on each pixel of the image. One pixel can be as small as 30 nm. Counting times for the images are on the order of a few milliseconds or less per pixel. Normalization and background subtraction of the spectra were performed by dividing each spectrum from the sample by the spectrum of the sample-free location. Elemental maps of samples can be obtained by subtracting the image obtained below the absorption energy level from the image obtained above the absorption energy level. Axis 2000 software (Version 2.1) [67] can be used to align image stacks and extract NEXAFS spectra from the image stack or line scan measurements. In this study, the STXM results were collected at ALS Beamline 11.0.2.2 and Beamline 5.3.2.1.

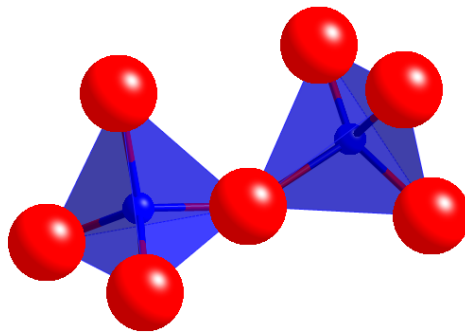
## **2.4 Conclusion**

The aim of this chapter was to introduce major X-ray and neutron characterization techniques used in this study. Total scattering (PDF) provides information on local atomic distances and coordinations. STXM allows 25-nm spatial resolution element-based image contrast and K or L NEXAFS spectra at each 25 nm x 25 nm pixel in a STXM image. Small angle scattering (SAS) experiments provide important information on as particle size, density fluctuations and homogeneity of the sample. Each of these methods is most powerful when interpreted with other methods, experimental or computational.

# 3

## Amorphous Silica

The term silica covers various materials having the stoichiometric composition of  $\text{SiO}_2$ . It is a major component of the earth crust; and it forms the silicate minerals in our rocks and soil when combined with magnesium, aluminum, calcium and iron oxides [68]. Silicas can be natural or synthetic, crystalline or amorphous; yet, the building block of all silica structures at low pressure is the  $\text{SiO}_4$  tetrahedron formed from four oxygen atoms at the corners of a regular tetrahedron with a silicon at the center (Figure 3-1) where the oxygen ion is considerably larger than the  $\text{Si}^{4+}$  ion [68]. The  $\text{Si-O}$  bond is the most stable of the  $\text{Si-X}$  bonds; and all forms of silica contain this bond. The average length of this bond is around 1.62 Å. Due to the partially ionic nature of the  $\text{Si-O}$  bond, the observed bond length is smaller than the sum of the covalent radii of silicon (1.11 Å) and oxygen atoms (0.66 Å) and is responsible for the high stability of siloxane bond [68]. There are over 35 known well-defined crystalline silica phases including quartz, tridymite and cristobalite. Their  $\text{Si-O}$  bond length,  $\text{Si-O-Si}$  bond angle are very well-studied. However, this is not the case for amorphous silicas.



**Figure 3-1.**  $\text{SiO}_4$  tetraheda: oxygen (red), silicon (blue).

Amorphous silicas have been of importance to civil engineers for more than two millennia. Romans utilized an almost pure form of amorphous colloidal silica in their mix designs for high strength – high durability concrete [69]. Today, silica fume and rice husk ash, both almost pure amorphous silicas, are amongst the most well-known supplementary cementitious materials used in modern cement and concrete industry. Opals are hydrated silicas commonly found as impurities in the concrete aggregates; and they are also of importance. They tend to react with alkalis in the pore solution of hydrated cement and form a hygroscopic

material that can imbibe large amounts of water and expand. When confined in a matrix, the volumetric expansion can result in durability problems. In advanced stages, this can even lead severe structural problems. Details of this deleterious reaction are given in chapter 4. The main focus of chapter 3 is broadening our basic scientific knowledge on these three amorphous silicas using advanced X-ray and neutron characterization techniques. This might allow us to look from a different angle to the reactions they are involved with. Chapter 3 also forms a base line for chapter 5 and 6 that are exploring alkali-silica reaction gels, and glassy portion of fly ash F.

## 3.1 Materials

### 3.1.1 Silica fume and rice husk ash

Silica fume, a byproduct from the induction arc furnaces used in the silicon metal and ferrosilicon alloy industries, is a highly pozzolanic material. The  $SiO$  vapors, produced by the reduction of quartz to silicon, oxidize and condense in the low-temperature zone of the furnace to form very pure, small spherical particles consisting of noncrystalline  $SiO_2$ . The material removed by filtering the outgoing gases in bag filters has an average diameter on the order of 0.1  $\mu m$ . When used as a supplementary cementitious material in portland cement based systems; it yields high strength – high durability products [70]. Rice husk ash, another highly pozzolanic material is produced by the controlled combustion of rice husks (shells produced during the dehusking operation of paddy rice) [71,72]. Each metric tonne of paddy rice generates about 200 kg of husk. Upon on combustion of the husk, it is possible to yield approximately 40 kg ash. Folliard and Mehta [73] provided a careful study of the durability of concrete mixtures containing rice husk ash.  $^{29}Si$  MAS NMR measurements [74] on rice husk ash showed that if the husk is burned in a controlled temperature, the resulting ash contains only  $SiO_4$  tetrahedral units. The chemical composition of the silica fume and the rice husk ash used in this study are given in Table 3-1. Typical silica fume and rice husk ash particles are shown in Figure 3-2.

**Table 3-1. Chemical composition (weight %) of the silica fume and the rice husk ash used in this study. The XRF measurements are conducted at McCone Building, Berkeley.**

<b>Oxide Composition (wt. %)</b>		
	<b>Silica Fume</b>	<b>Rice Husk Ash</b>
<b>SiO<sub>2</sub></b>	92.5	89.4
<b>Al<sub>2</sub>O<sub>3</sub></b>	0.2	0.1
<b>Fe<sub>2</sub>O<sub>3</sub></b>	0.1	0.1
<b>K<sub>2</sub>O</b>	1.1	1.6
<b>TiO<sub>2</sub></b>	-	-
<b>CaO</b>	0.6	0.7
<b>Na<sub>2</sub>O</b>	0.1	-
<b>SO<sub>3</sub></b>	-	-
<b>MgO</b>	0.4	0.4
<b>MnO</b>	0	0.2
<b>LOI</b>	4.7	6.7



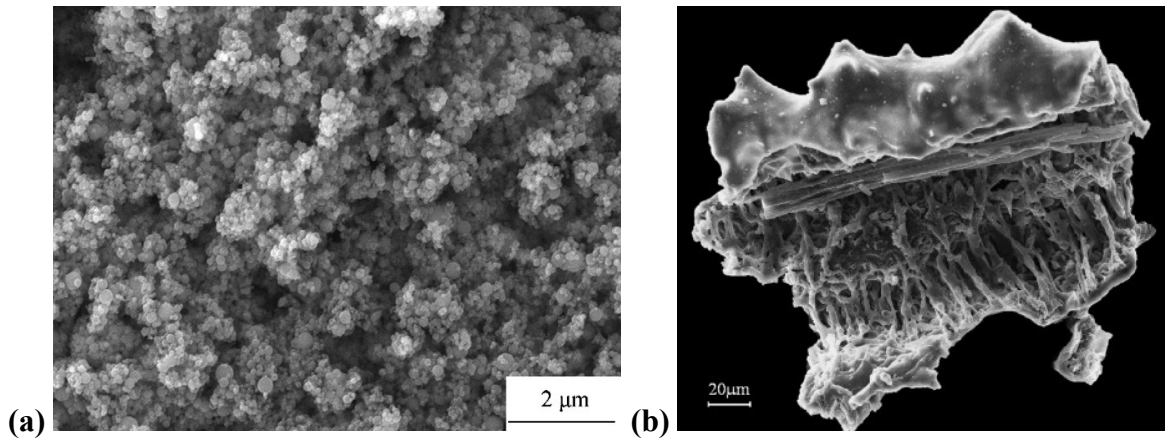


Figure 3-2. SEM image of typical (a) silica fume [75], and (b) a rice husk ash [76] particle.

### 3.1.2 Opal

Opals occur in vesicles and veins, and formed by precipitation from saturated silica solutions due to a decrease in temperature or pH [77–79]. In general, amorphous opal (opal-A) is the first type of opal to form (Figure 3-3). During diagenesis driven by time, temperature or pressure, opal-A might convert into metastable cristobalite/tridymite (opal-CT) and finally to quartz in cherts [80–82]. When the proportion of cristobalite is much greater than that of tridymite opal it is labeled as opal-C. Opal is also infamous as a highly reactive aggregate in concrete, responsible for the decay of concrete structures [83]. Thus, it was of importance to this research.



Figure 3-3. An Opal-A<sub>G</sub> sample formed in sedimentary rocks of Middle to Upper Devonian age at Pedro II, Piauí, northeastern Brazil.

Opal-A has two varieties depending on the long-range silica linkage being either network-like or gel-like referred to as opal-A<sub>N</sub> and opal-A<sub>G</sub>, respectively [84]. Opal-A<sub>N</sub> or hyalite, typically botryoidal and colorless, has a glass like texture, whereas opal-A<sub>G</sub>, consists of mono- or polydisperse spheres of hydrated silica held together by non-crystalline silica cement [85]. Precious Opal, the variety used most often in jewelry, is composed of silica spheres 150 to 300 nm in diameter in a hexagonal or cubic close-packed lattice. Ordered silica spheres produce



the iridescent colors by causing the interference and diffraction of light passing through the microstructure of the opal. The regularity of the sizes and the packing of the spheres determine the quality of precious opal. Small-angle neutron scattering is used to relate the range of sizes of the spherules to opals distinctive play of color [86]. In opal-CT, diagenetic derivative of opal-A, intermediate-range ordering begins by six-membered silica rings mimicking intergrowths of cristobalitic and tridymitic end-members [87]. Opal-CT consists of a wide variety of internal structures such as spherical aggregates of plate-like crystallites called lepispheres (spheres of blades), spherulites or fibrolites [85].

There are more than 500 minerals known to incorporate water in various forms [88]. Water can be present as free, hydrogen-bonded water (e.g. in clays), as a ligand to a cation (e.g. in sheet silicates), or as a surface species (e.g. in zeolites). Frequently, the interaction of water with its surroundings is relatively weak (van der Waals or hydrogen-bonding interactions), and water is then structurally disordered, which makes obtaining structural information using diffraction methods difficult. In hydrous silicate glasses, at low total water contents, hydroxyl groups formed by reaction between water and the silicate network are the dominant hydrous species. When the total water content exceeds a few weight percent (~4%) most of the water is dissolved as molecular water. The hydroxyl group concentration initially increases with total water content, but beyond this limit it becomes stable at a maximum value [89]. Opals contain significant amounts of water (1-10 wt%) [86]. Infrared (IR) studies show that water in opals are present in various forms: as isolated molecules trapped in the SiO<sub>2</sub> matrix with weak hydrogen bonding, as confined water that resides in large voids with extensive hydrogen bonding, or as silanols at structural defects or at silica surfaces [90,91]. The presence of silanol groups was established by nuclear magnetic resonance [91]. However, molecular water adsorbed in intergranular interstices dominates in opal.

In this study, natural opal specimens obtained from various sources (Opal-AG: Honduras, Brazil; Opal-CT: Mexico, Peru, Tanzania, Ethiopia) were investigated.

## 3.2 Results and discussions

### 3.2.1 Scanning Electron Microscopy (SEM) and X-ray Diffraction (XRD)

SEM measurements are conducted on a high resolution, cold field emission Hitachi S-5000 located at Giannini Hall-Berkeley. Two samples, an A<sub>G</sub> and a CT opal from northeastern Brazil, were chosen for the microscopic investigations. Samples were then coated with a thin coating of palladium/gold alloy; and placed into the microscope. The microscope was operated at 5kV to minimize charging problems.

The X-ray powder diffraction (XRD) measurements presented with the following SEM images were performed using a PANalytical X'Pert PRO Materials Research Diffractometer located at McCone Building-Berkeley. Small pieces of the opal samples were very finely ground and loaded into metal sample holders. Data were collected using a cobalt target that produces X-ray with a wavelength of 1.789 Å. The X-ray diffraction pattern of opal-A<sub>G</sub> is characterized by a

single, broad band centered on  $\sim 4.1\text{\AA}$  [92]. A relatively sharper peak compared to opal- $A_G$  at  $\sim 4.11\text{\AA}$ , a secondary reflection around  $4.3\text{\AA}$  (attributed exclusively to low tridymite) and an additional reflection around  $2.5\text{\AA}$  are indicators of opal-CT [93].

Obtained SEM images are given in Figure 3-4 and Figure 3-5. An opal- $A_G$  fracture surface might not always reveal the silica spheres in a SEM image due to the similar compositions of the cement and the spheres, which is the case for the opal- $A_G$  sample we measured (Figure 3-4a). Hence; a brief HF etching was applied to sample resulting in dissolving most of the silica spheres and allowing the connecting silica cement to be observable (Figure 3-4b). The XRD patterns for this sample (Figure 3-4 inset) produces a single diffuse band centered around  $4.1\text{\AA}$ .

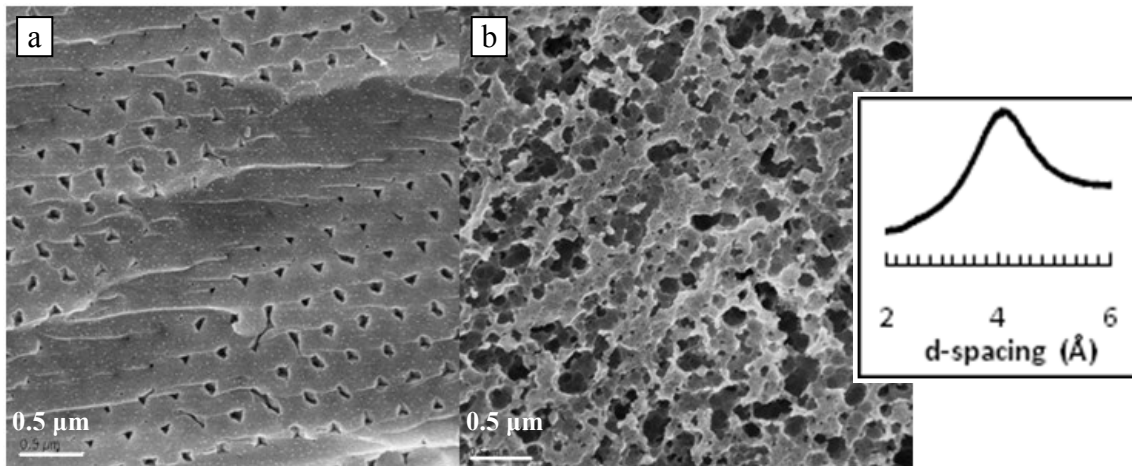


Figure 3-4. SEM images (25 000 $\times$ ). Translucent to milky opal- $A_G$  from Brazil: (a) fracture surface, (b) after HF etching. The silica spheres are dissolved revealing the connecting silica cement. (Inset) XRD pattern.

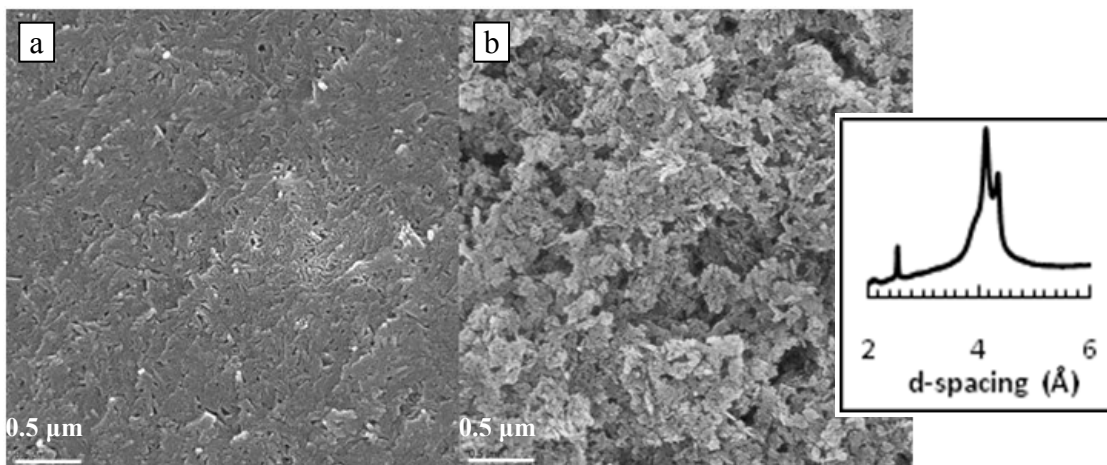


Figure 3-5. SEM images (25 000 $\times$ ). Milky opal-CT from Brazil: (a) fracture surface, (b) after HF etching. Milky opal-CT from Brazil formed from small platelets. (Inset) XRD pattern.

Opal-CT might consist of a wide variety of internal structures such as spherical aggregates of plate-like crystallites called lepispheres, spherulites or fibrolites [85]. Most of the time fracture surfaces for opal-CT appear vaguely granular; as is the case for the measured opal-CT sample (Figure 3-5a). After a brief HF etching the small platelets of the opal-CT sample became visible, Figure 3-5b. The XRD pattern of the opal-CT sample (Figure 3-5 inset) has the main peak  $\sim 4.11 \text{ \AA}$ , a secondary reflection around  $4.3 \text{ \AA}$  and an additional reflection around  $2.5 \text{ \AA}$ .

### 3.2.2 Nuclear Magnetic Resonance (NMR) Spectroscopy

The broad and low intensity Bragg peaks in the XRD patterns of opals make the structural interpretations difficult [87]. Hence, for opals with similar XRD patterns,  $^{29}\text{Si}$  NMR has been used to probe the structure [94]. NMR is a powerful technique to probe the local environment surrounding particular nuclei, i.e., at the scale of nearest-neighbour and next-nearest-neighbour [95]. Interpretation of  $^{29}\text{Si}$  NMR spectra provides information on the local silicate tetrahedral environment, designated as  $Q_n$ , where ‘Q’ represents the silicon tetrahedron bonded to four oxygen atoms and ‘n’ is the connectivity, i.e., the number of other ‘Q’ units attached to the central  $\text{SiO}_4$  tetrahedron under study [96].  $^{29}\text{Si}$  NMR is especially useful in examining  $\text{Si-O}$  bonding. An increase in the number of  $\text{SiO}_4^{4-}$  units bonded to each Si center produces an increase in the average electron density around the central Si atom. This leads to a more negative chemical shift for successively increasing n values in  $Q_n$  as seen in Figure 3-6.

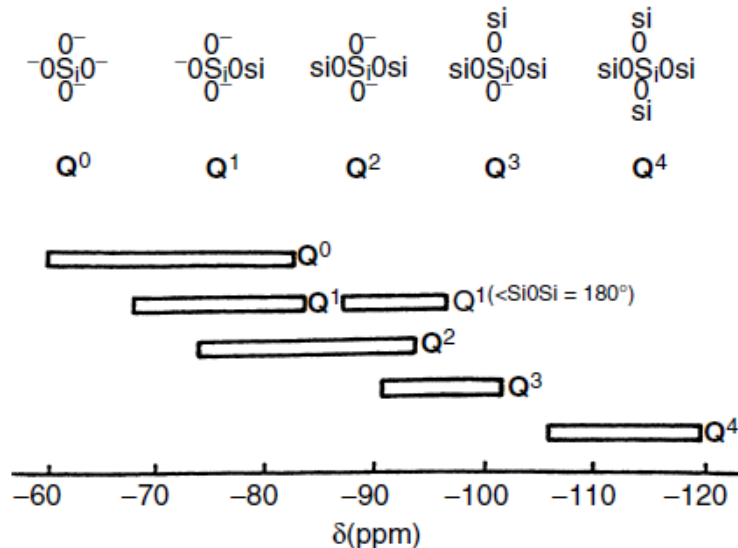


Figure 3-6. Typical ranges of  $^{29}\text{Si}$  chemical shifts of  $Q_n$  units in silicate. Taken from [97].

In this study,  $^{29}\text{Si}$  and  $^{23}\text{Na}$  magic angle spinning (MAS) NMR spectroscopy were used to investigate the opal- $A_G$  and opal-CT samples from Brazil. All NMR spectra were recorded using a Bruker Ultrashield 400WB Plus with a 9.4T magnet, located at Advanced Nanofabrication Imaging and Characterization Lab, KAUST-Saudi Arabia. The finely ground opal samples were packed into 4mm zirconia rotor and sealed at the open end with a Vespel cap. The rotor was the

spun at 14 kHz operating at 105.84MHz for  $^{23}\text{Na}$  and 79.495MHz for  $^{29}\text{Si}$ . The magic angle in all cases was set using KBr to  $54.734^\circ$ . The obtained spectra are shown in Figure 3-7.

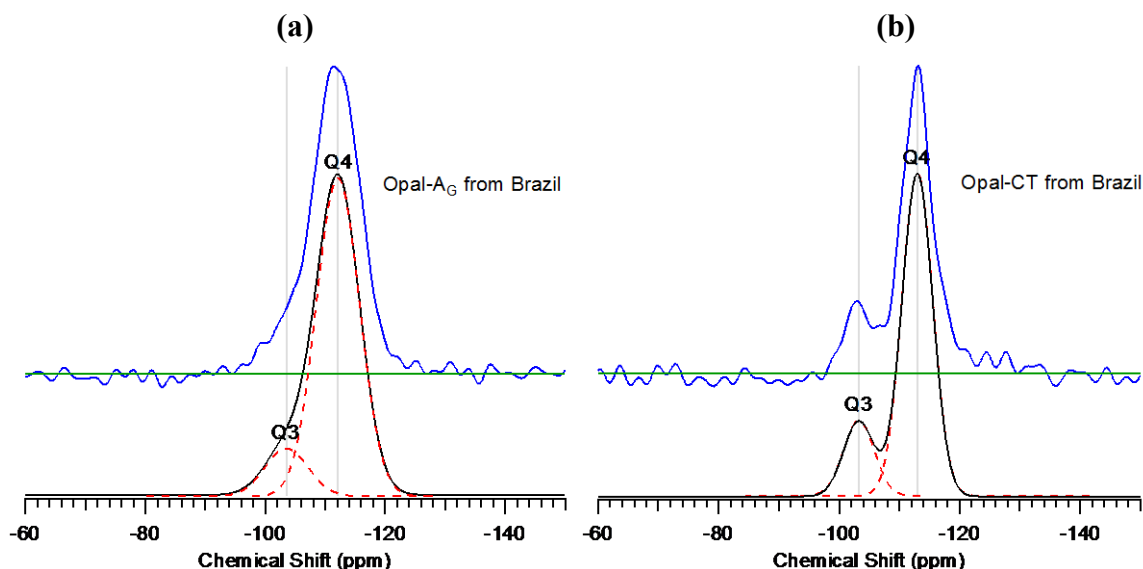


Figure 3-7.  $^{29}\text{Si}$  MAS-NMR spectra of (a) opal- $\text{A}_6$  and (b) opal-CT from Brazil. Q4 sites are dominating both spectra. The spectra are scaled to their tallest peak. The figures include the experimental spectrum (medium -blue), background (medium-green), the fitted peaks (bottom-red), and the fitted spectra (black).

The quantitative information on the observed  $\text{Q}_n$  species is obtained through least-square fitting Gaussian or Lorentzian functions to the peaks. For these samples, employing Gaussian function produces a better fit. The results of the deconvolution are summarized in Table 3-2.

Table 3-2. Isotropic chemical shift  $\delta$ , relative integral intensity  $I$  for Gaussian lines fitted to the  $^{29}\text{Si}$  MAS NMR spectra, full width at half maximum (FWHM) values and mean number of NBO per silicate tetrahedron for Opal- $\text{A}_6$  and Opal-CT samples from Brazil.

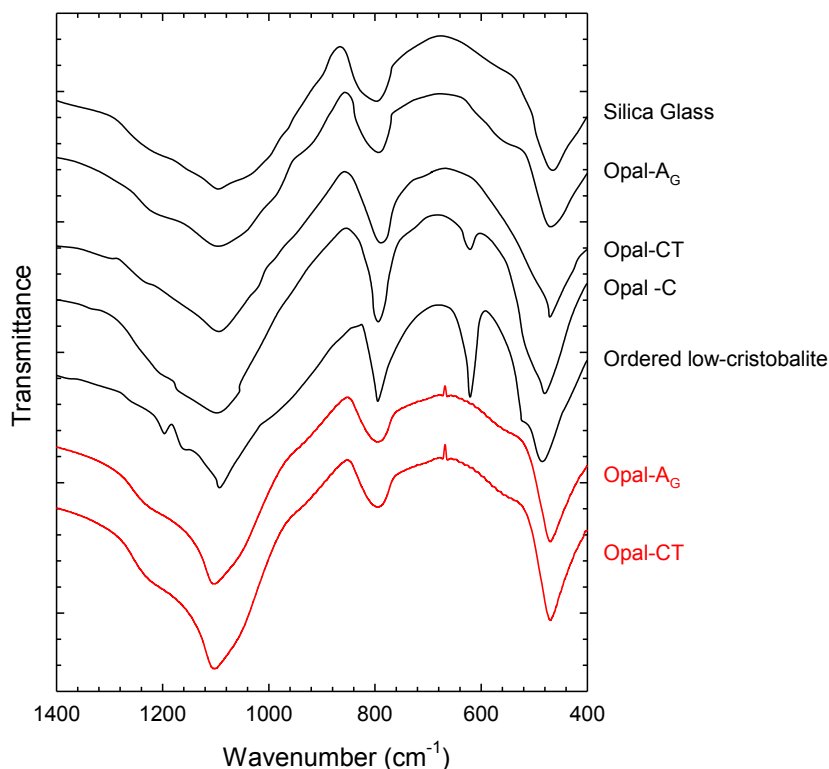
Sample	Q3			Q4			NBO
	$\delta$ (ppm)	$I$ (%)	Width (ppm)	$\delta$ (ppm)	$I$ (%)	Width (ppm)	
Opal- $\text{A}_6$	-103.5	13.0	5.1	-112.1	87.0	5.1	13%
Opal-CT	-103.3	18.9	3.6	-113.0	81.1	3.6	19%

The two main resonances centered around -103 and -112 ppm are attributed to Q3 and Q4 units respectively. The Q3 silicate polymerization represents the structural defects in the framework of tetrahedral which are associated with hydrogen, most likely as terminal silanol groups either on surfaces or at internal defects [98]. The estimated Q3:Q4 ratios are 13:87 and 19:81 for opal- $\text{A}_6$  and Opal CT samples, respectively. The fit width of the fitted peaks is also of importance; as the broadness of the signals indicates variations in the local environments of the silicon atoms. The width for the opal- $\text{A}_6$  sample is higher than the value for the opal-CT sample. These results are in close agreement with those of other reported values [91,94,98]. It is

important to note that the chemical shift for Q4 in cristobalite is  $-108.5$  [99], and for tridymite, there are various chemical shifts for Q4 ranging from  $-109.1$ — $114.3$  [100].

### 3.2.3 Fourier Transform Infrared (FTIR) Spectroscopy

Fourier transform infrared (FTIR) spectra were collected with a Thermo-Nicolet Nexus 6700 FTIR spectrometer equipped with an ATR accessory. Samples were ground and measured by the KBr-technique using ca. 2mg of sample and 100mg of KBr in the pellets. The spectrometer is located at Johannes Gutenberg University Mainz (JGU)-Germany. The obtained infrared spectra for the opals in comparison with measurements from literature are given in Figure 3-8.



**Figure 3-8. Measured Infrared absorption spectra of the opals from Brazil (red) in comparison to micro- and non-crystalline opal, synthetic silica glass, and ordered low-cristobalite measurements (black) by Graetsch *et al.* [101].**

A summary for qualitative deconvolution of the vibrational features is given in Table 3-3. For all silicates with tetrahedrally coordinated silicon including the tested opals, the broad bands near  $480$ ,  $790$  and  $1100$   $\text{cm}^{-1}$  are common [101]. These bands are attributed to asymmetric stretching and bending modes [102]. In amorphous silica, opal- $A_G$  and opal-CT the atomic displacements are no longer correlated and only localized  $Si-O$  stretching and  $O-Si-O$  bending vibrations remain [101]. The spectra of silica glass, opal- $A_G$  and opal-CT samples mainly differ by the increasing broadness of the absorption bands [101]. Broadening of the absorption bands is an indication of the variations of the dipole moments caused by slightly varying surroundings of the  $SiO_4$  tetrahedra [101]. The increasing broadness of the bands from opal-C/-CT to opal-A can

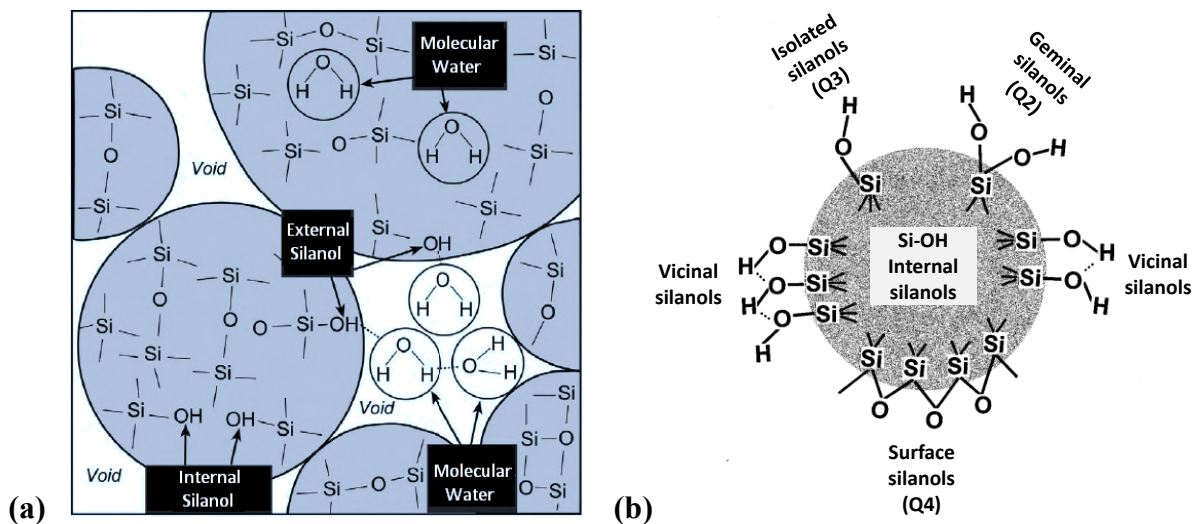
be explained by differences in the variations of the local tetrahedra arrangements. [101]. However, a significant broadening was not observed for the measured Brazilian opals.

**Table 3-3. Summary of experimental frequencies ( $\text{cm}^{-1}$ ) of the tested opals from Brazil shown in Figure 3-8.**

Wavenumber ( $\text{cm}^{-1}$ )			Vibrational Movement	Interpretation	Ref.
Opal-A <sub>G</sub>	Opal-CT	Literature			
477	469	478	Si-O-Si bending (asym.)	Si-O-Si	[103] [102,104]
795	793	817	Si-O-Si bending (asym.)	Si-O-Si	[103]
1100	1102	1091	Si-O stretching (asym.)	Si-O-Si	[103]

### 3.2.4 Thermal Analysis

The water is incorporated into opal's structure in two ways: as molecular water and as silanol groups. Estimates for total water content of opal-A ranges from 2.1–12.1 wt% [105]. However, the total water content may be even higher. 1.2–9.8 (average 6.8) wt% of it is attributed to molecular water; and remaining 0.4–2.4 (average 1.0) wt% is attributed to silanols [105]. Figure 3-9 illustrates different types of water found in natural opals. Molecular water in opal can occur as isolated molecules trapped in the  $\text{SiO}_2$  matrix with weak hydrogen bonding, or as adsorbed water that resides in relatively large voids with extensive hydrogen bonding. The silica surface contains both the siloxane bonds ( $\text{Si-O-Si}$ ) and silanols ( $\text{Si-OH}$ ). Silanols are strong adsorption sites and hydrophilic in nature [106]. Silanols have been divided into external and internal silanols according to their location [91]. Internal silanols are located at structural defects; and the external silanols are located on silica surfaces with strong hydrogen bonds. In addition to isolated hydroxyl groups, geminal and vicinal hydroxyl groups may also occur within natural opals. Twin hydroxyl groups occur most likely at the lattice imperfections caused by incomplete polycondensation of silica tetrahedra, such as at the surfaces of the silica spheres where the continuous silica network is interrupted [84,91].



**Figure 3-9. (a) Schematic diagram showing different forms of water in opal-A<sub>G</sub>. Adopted from [105]. (b) Types of silanol groups and siloxane bridges on the surface of amorphous silica. Adopted from [107].**

In this study, thermogravimetric analysis is used to obtain information on the water content of the tested opals. We used different heating rates during the measurements. It is important that the thermal analysis of opals is conducted at low heating rates; as water diffuses only slowly out of opal, particularly when the pore network is mostly closed. The water loss behavior is strongly dependent on the heating rate. Figure 3-10 shows our TGA measurements on various opal samples. The two measurements marked with red are conducted at Los Alamos National Laboratory-NM. The remaining measurements are conducted at CALERA-CA.

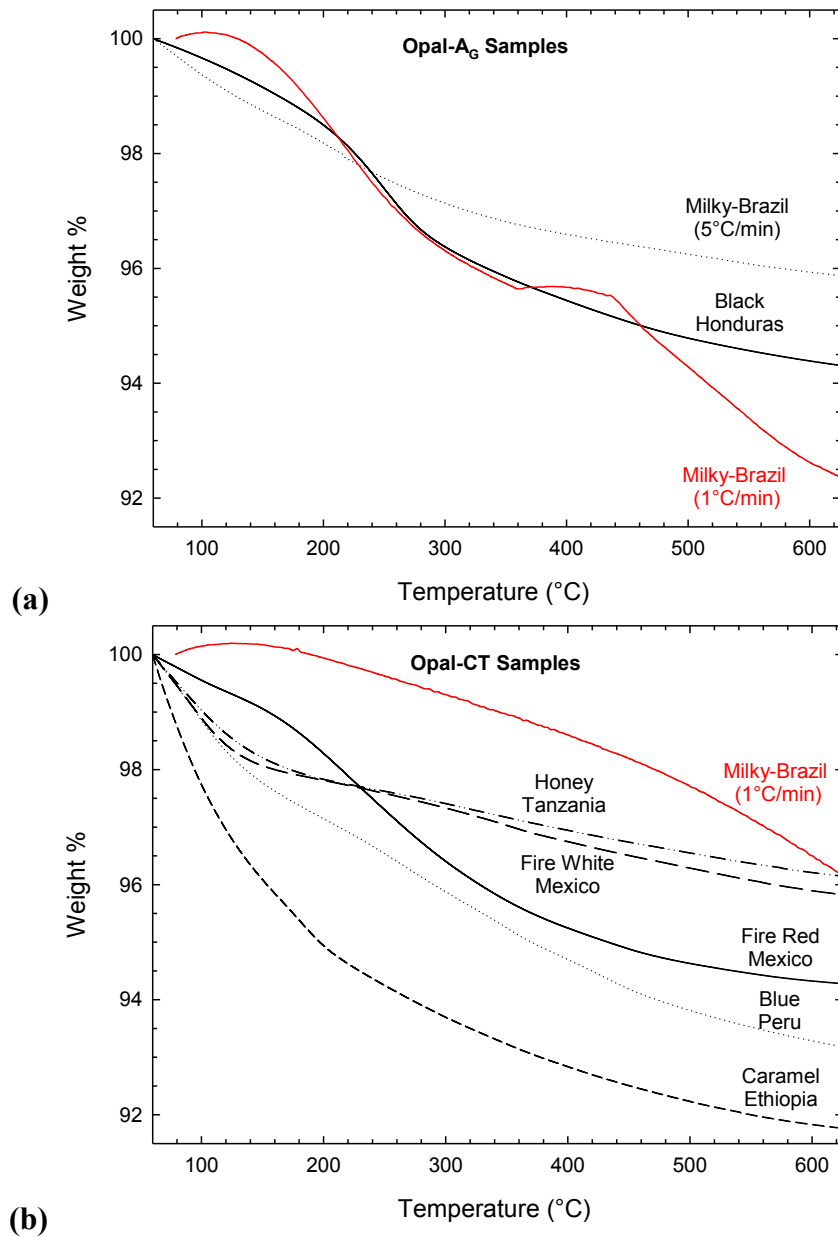


Figure 3-10. Thermogravimetric analyzer (TGA) data obtained for various (a) opal-A<sub>G</sub>, and (b) opal-CT samples. The heating rate is 10°C/min unless otherwise is noted. Measurements marked with red are conducted at Los Alamos National Laboratory-NM; the remaining measurements are conducted at CALERA-CA.

In the TGA of hydrated amorphous silicas, water produces mass losses at two temperature ranges, at below 190°C due to physically absorbed water and at 200 – 600°C associated with structurally bound water. These values are summarized in Table 3-4.

Table 3-4. Weight loss of opal samples upon heating

Origin	Color	Weight loss (%)		
		up to 190°C	up to 600°C	between 190-600°C
<i>Opal-A<sub>G</sub></i>				
Brazil	Milky	1.38	3.76	2.38
Honduras	Black	1.19	5.46	4.27
<i>Opal-CT</i>				
Ethiopia	Caramel	3.64	7.00	3.36
Mexico	Red	1.31	5.46	4.15
Mexico	White	1.61	3.58	1.97
Tanzania	Honey	1.63	3.31	1.68
Brazil	Milky	0.20	3.50	3.30

### 3.2.5 Total Scattering

Silica glass is a continuous network made of corner sharing  $SiO_4$  tetrahedra where each oxygen bridges two tetrahedra (*i.e.* only  $Q^4$  speciation). A schematic 2D Zachariasen [108] model for pure silica glass is given in Figure 3-11a. However, a more complex system might contain 75%  $Q^3$  (tetrahedra with one free non-bridging oxygen), 25%  $Q^2$  (two non-bridging oxygens). Figure 3-11-b illustrates X-ray and neutron scattering measurements on silica glass (data from [43]). The most noticeable difference in the X-ray and neutron measurement is the appearance of the  $Q_2$  peak in the neutron spectrum which arises from  $O-O$  interactions.

For glasses of  $AX_2$  stoichiometry the first sharp diffraction peak (FSDP) of the  $S(Q)$  has been associated with intermediate range ordering with a periodicity of  $2\pi/Q_1$  where  $Q_1$  is the position. For silica glass, this ordering beyond the first few nearest neighbor silica tetrahedra arises from the boundaries between a succession of cages comprising the structure of a 3-D covalent network [14]. Therefore, the position and shape of the first sharp diffraction peak  $Q_1$  can provide information on different sized ring distributions within the material. The measurements on silica glass (Figure 3-11b) suggest an intermediate range ordering with a periodicity of  $2\pi/Q_1 \sim 6 \text{ \AA}$ . The second diffraction peak at position  $Q_2$  has been linked to chemical or extended range ordering with a periodicity of  $2\pi/Q_2 \sim 3 \text{ \AA}$  and the local  $Si-O-Si$  and  $O-Si-O$  bond-angle distributions can persist to distances as large as  $>5 \text{ \AA}$  [31,43]. The similar features in  $S_N(Q)$  and  $S_X(Q)$  at higher  $Q$ -ranges are dominated by the  $SiO_4$  tetrahedra present in the glass.



The total neutron and X-ray pair distribution functions for silica glass are given in Figure 3-11-c. As expected, X-rays and neutrons produce different total pair-distribution functions. Si is the predominantly scattering atom as it is heavier, but there are twice as many oxygen atoms. Therefore, the Si and O partials are weighted similarly for X-rays. However, oxygen dominates the spectra for neutrons, since O has a larger neutron cross section and is more abundant. Consequently, the *Si-Si* interactions, and hence the *Si-O-Si* bond angle, is best obtained from the X-ray data; whereas the *O-O* interactions and the *O-Si-O* bond angle are best studied with neutron data [14].

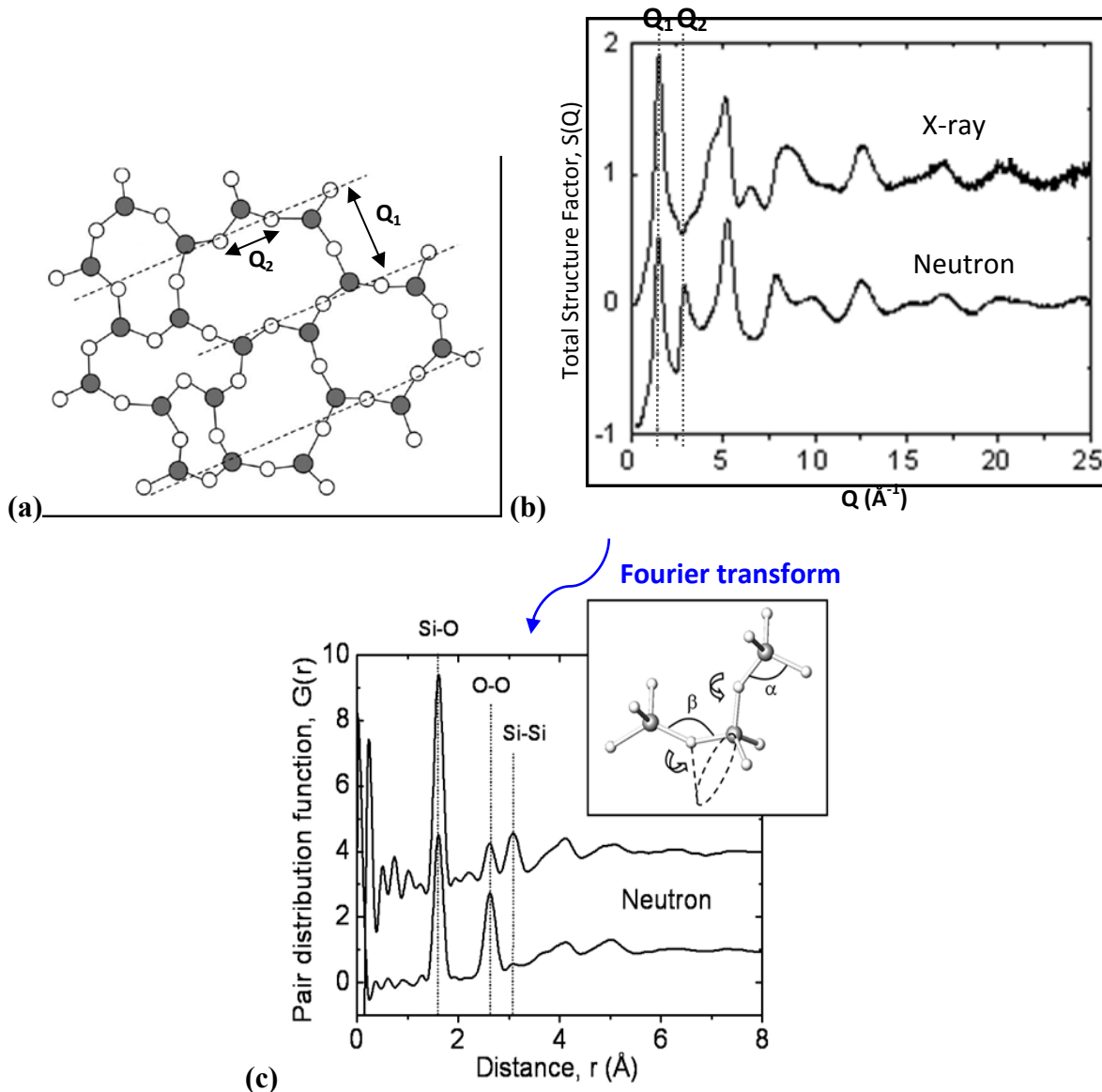
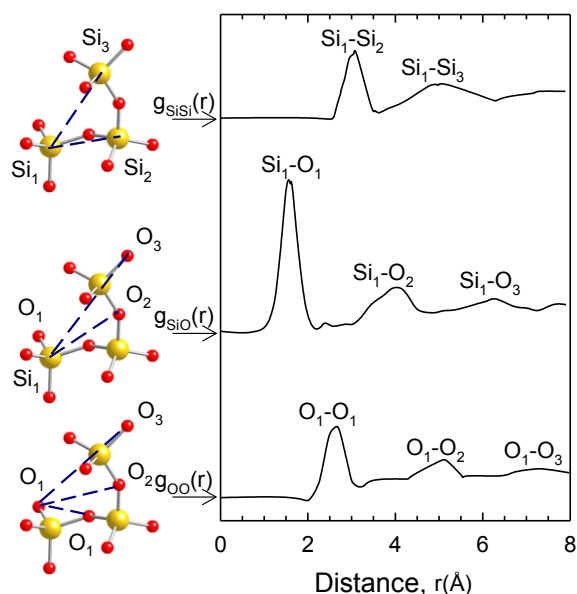


Figure 3-11. (a) 2-D representation of Zachariasen [108]–Wright [14] continuous network model for a glass structure with corner-sharing tetrahedral oxides (i.e. Si atoms, ●, and O atoms, ○) (adapted from [43]). The dashed lines of periodicity ( $Q_1$ ) arise from correlations between cages which comprise the glassy silicate network.  $Q_2$  represents the length scale of the bulk chemical ordering of the network. (b) Measured X-ray and neutron total structure factors for glassy  $\text{SiO}_2$  [31].  $Q_1$  is the first sharp

diffraction peak. (c) The total X-ray and neutron radial pair distribution functions for vitreous SiO<sub>2</sub>. The inset shows the local tetrahedral and packing torsion angles [31].

Figure 3-12 provides the breakdown of the total X-ray pair distribution function,  $G_X(r)$ , for glassy SiO<sub>2</sub> in terms of its partial distribution functions,  $g_{\alpha\beta}(Q)$ . For SiO<sub>2</sub> there are three partial pair distribution functions in terms of element specific contributions, namely *Si-O*, *O-O* and *Si-Si*. The specific atomic correlations between adjacent tetrahedra contribute in each case can be seen. The first few peaks define the *SiO*<sub>4</sub> tetrahedra. The polyhedral connectivity (average orientations of adjacent polyhedral) is defined by typically up to 5 or 6 Å depending on the size of polyhedra. The Si<sub>1</sub>-Si<sub>2</sub> distance is pretty robust and very important for giving an indication of the average ring size.



**Figure 3-12. Faber-Ziman defined partial pair-distribution functions in terms of element specific contributions for SiO<sub>2</sub> glass:  $g_{SiSi}(r)$ ,  $g_{SiO}(r)$  and  $g_{OO}(r)$ . The peaks in the distribution functions are illustrated by the distances indicated in the atomistic plots of three corner shared *SiO*<sub>4</sub> tetrahedra [31].**

In this study, silica fume, rice husk ash and natural opal specimens from various sources (Opal-AG: Honduras, Brazil; Opal-CT: Mexico, Peru, Tanzania, Ethiopia) were investigated by total scattering methods. High-energy X-ray diffraction measurements were conducted on the beamline 11-ID-C at the APS using incident beam energy of ~115keV. The detector was placed at 657.87 mm. Details of the method and the beamline have been discussed in chapter 2. Powdered samples were placed in 2mm diameter kapton tubes with 0.1mm wall thickness. A Perkin-Elmer amorphous silicon detector was placed perpendicular to the incident beam at a distance of 426 mm from the sample (see Figure 3-13). Measurements were conducted at ambient conditions. In the data analysis the intensity function,  $I(Q)$ , was calculated from the raw X-ray data using Fit2D [109]. Then, the intensity function was corrected for the sample and instrument effects such as Laue diffuse scattering, and X-ray polarization after background

subtraction using PDFgetX2 [34]. This software yielded the total structure factors,  $S(Q)$ , that was then Fourier transformed to the pair distribution function,  $G(r)$ .

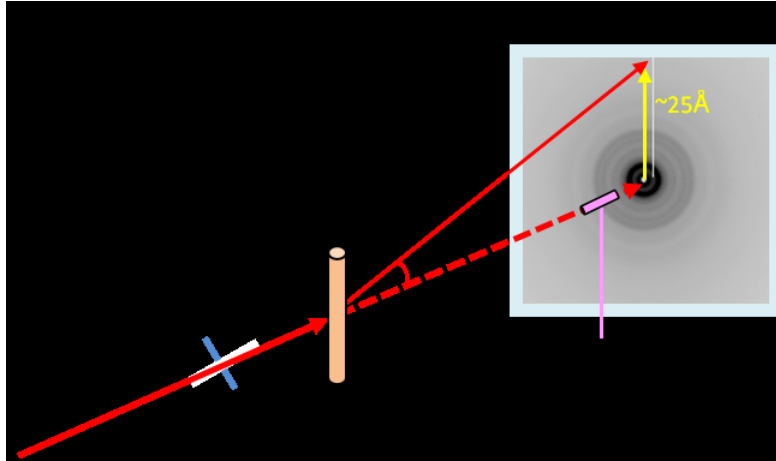


Figure 3-13. Schematic for a scattered beam from a sample (APS Beamline 11-ID-C setup)

### 3.2.5.1 Silica fume and rice husk ash

First sharp diffraction peaks (FSDPs) are seen in a wide range of glasses from framework structures. For glassy  $\text{SiO}_2$ , the FSDP is related to intermediate range ordering (ordering beyond the first few nearest neighbor tetrahedra) with characteristic repeat distance. The decrease in the characteristic repeat distance is an indication of decreased intermediate range order. The measured X-ray total structure factors for silica fume and rice husk ash with silica glass are given in Figure 3-14. The  $Q_1$  positions (and widths relating to coherence) are close for all amorphous silicas, suggesting a similar intermediate range ordering with a periodicity of  $2\pi/Q_1 \sim 4.2 \text{ \AA}$ .

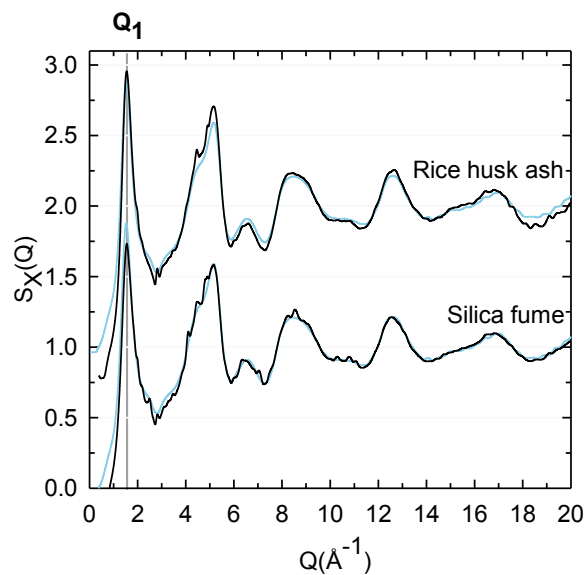


Figure 3-14. The measured X-ray structure factors,  $S_x(Q)$  silica fume and rice husk ash.  $S_x(Q)$  of silica glass (blue) is also shown for comparison.

Measured structure factors for silica fume and rice husk ash are Fourier transformed to obtain their  $D_X(r)$ , Figure 3-15. The near neighbor correlations in Figure 3-15 can be labeled utilizing our knowledge on silica glass.  $Si_1-O_1$  distance is found to be  $\sim 1.62 \text{ \AA}$  which is an indication for  $SiO_4$  tetrahedra. The  $O_1-O_1$  distance of  $2.62 \text{ \AA}$  provides an  $O-Si-O$  angle of  $\sim 109^\circ$ . The measured  $3.08 \text{ \AA}$   $Si_1-Si_2$  distance is robust and provides an indication of the average ring size. For both samples  $Si_1-O_2$ ,  $O_1-O_2$ , bond lengths are observed as  $4.11 \text{ \AA}$ , and  $5.04 \text{ \AA}$ , respectively. These values are very similar to that of a silica glass, suggesting similar topology (related with distribute of n-sized rings) of silica fume and rice husk ash to silica glass network. Silica glass is known to have a wide distribution of ring sizes with  $n=6$  being the most common, but also a significant amount of  $n=4,5,7$  and  $8$  membered rings present [32].

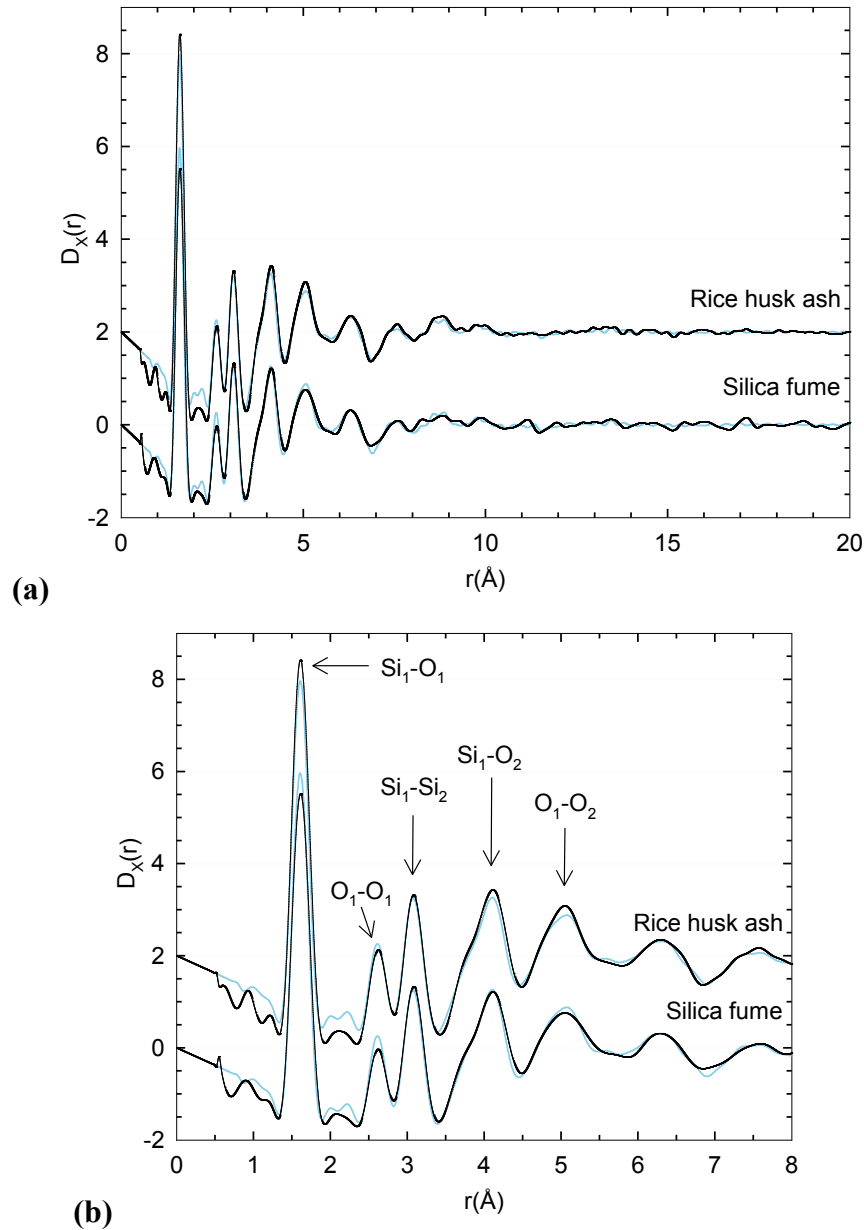
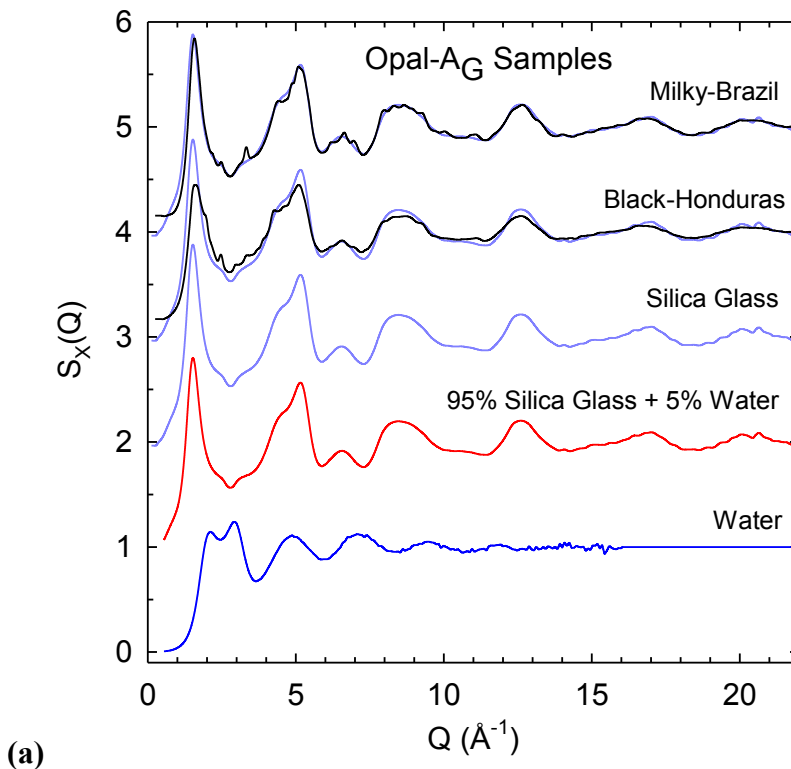


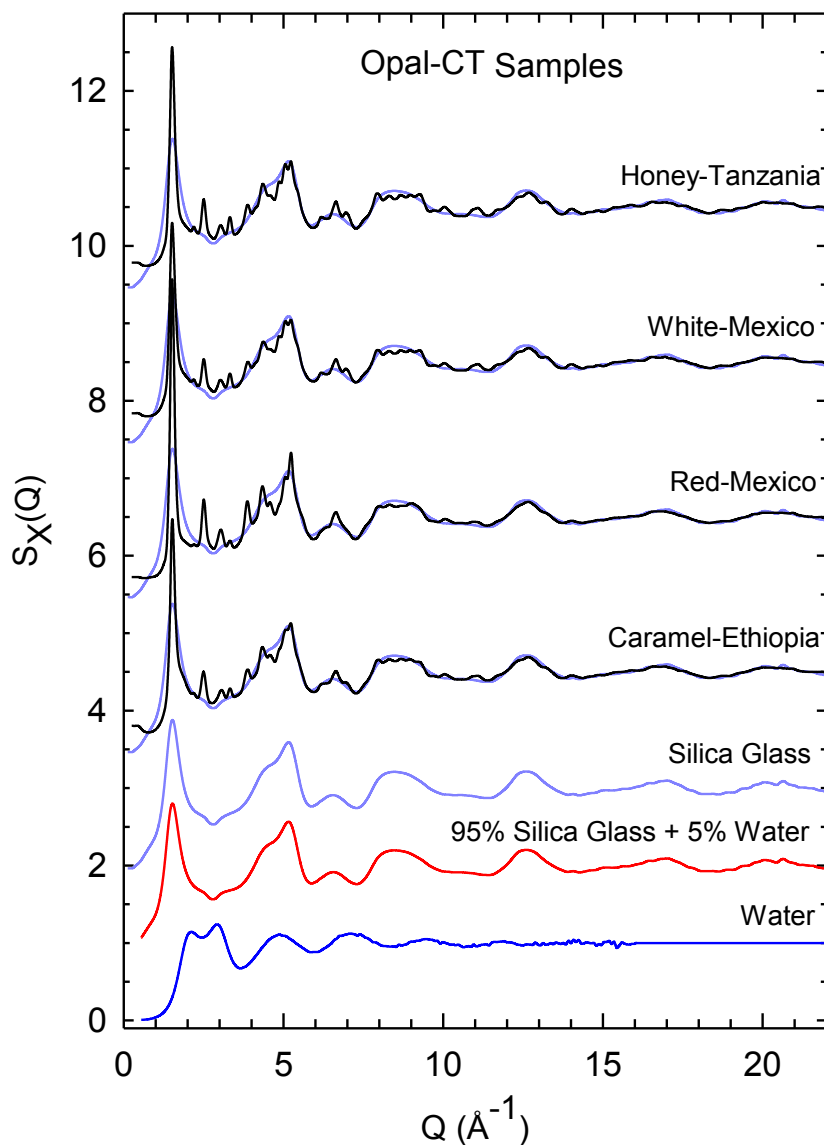
Figure 3-15. The X-ray differential distribution function  $D_x(r)$ , Q-range (a) 0-20  $\text{\AA}^{-1}$  and (b) 0-8  $\text{\AA}^{-1}$ .  $D_x(r)$  of silica glass (blue) is also shown for comparison.

### 3.2.5.2 Opal

The measured total X-ray total structure factors for opal- $A_G$  and opal-CT samples are given in Figure 3-16. For opals, the position of the FSDP ( $Q_1$ ) would be expected to be related to intermediate range ordering like in silicate, or alkali silicate glasses. The full width at half-maximum (FWHM) of the FSDP is also of importance. The sharpness of FSDP is an indication of increased structural order. While obtaining a FSDP of a tested sample, first a cubic polynomial was fitted as a background. Then, a Lorentzian function was fitted to the low-Q region of  $S(Q)$  to minimize the contribution of the following peaks. The Lorentzian function resulted in a better fit than the Gaussian alternative. This allowed precisely determining intensity, position ( $Q_1$ ), and FWHM of the FSDP of the tested sample.

The results of the FSDP analysis are summarized in Table 3-5. The FSDP position around 1.52(5)  $\text{\AA}^{-1}$  for opal samples is consistent with the values reported for silica glass in the literature. The shift to higher Q for FSDP in opal- $A_G$  samples when compared to opal-CT samples indicate a reduced characteristic repeat distance in real space. The intensity of the FSDP of opal- $A_G$  samples is lower than the intensity of opal-CT samples.





(b)

Figure 3-16. The measured X-ray structure factors,  $S_x(Q)$ , of silica glass (blue), water (navy) and (a) amorphous opals (black) and (b) opal-CT samples (black). The silica glass with 5% water content curve is obtained from weighted sum of the  $S(Q)$  curves of silica and water.

Table 3-5. Analysis of first sharp diffraction peaks of opal samples (weight loss below 600°C is attributed to water loss).

Origin	Color	Water (wt%)	Peak position $Q_1(\text{Å}^{-1})$	Peak Height	Peak Area	FWHM ( $\text{Å}^{-1}$ )
Silica glass	Colorless	0.00	$1.52 \pm 0.001$	$1.10 \pm 0.013$	$0.51 \pm 0.011$	$0.44 \pm 0.005$
<i>Opal-A<sub>G</sub></i>						
Brazil	Milky	3.76	$1.56 \pm 0.003$	$1.06 \pm 0.034$	$0.44 \pm 0.023$	$0.39 \pm 0.009$
Honduras	Black	5.46	$1.57 \pm 0.020$	$0.98 \pm 0.073$	$0.50 \pm 0.058$	$0.48 \pm 0.021$

*Opal-CT*

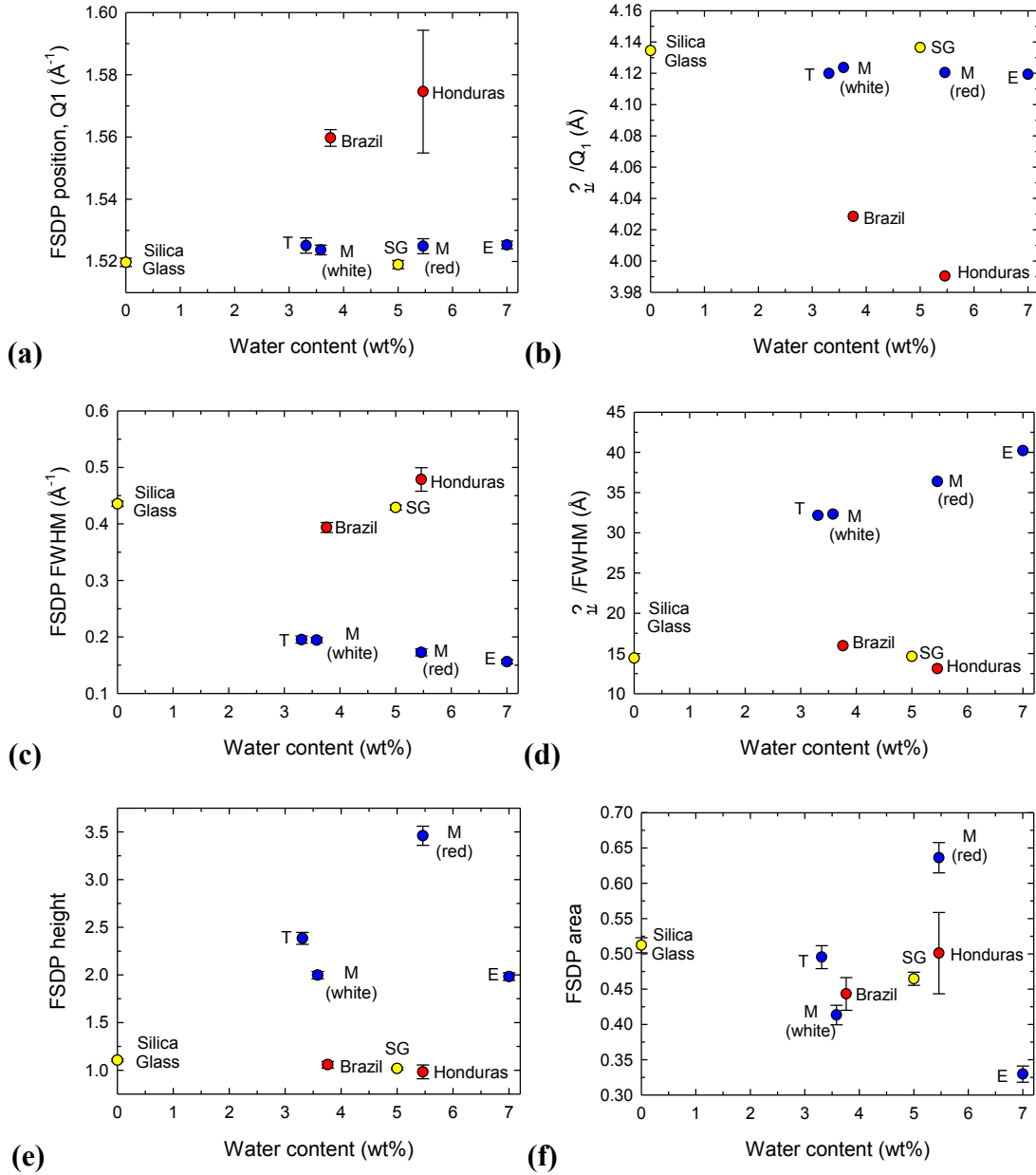
Ethiopia	Caramel	7.00	$1.53 \pm 0.001$	$1.98 \pm 0.040$	$0.33 \pm 0.011$	$0.16 \pm 0.004$
Mexico	Red	5.46	$1.52 \pm 0.002$	$3.46 \pm 0.101$	$0.64 \pm 0.021$	$0.17 \pm 0.006$
Mexico	White	3.58	$1.52 \pm 0.002$	$2.00 \pm 0.039$	$0.41 \pm 0.014$	$0.19 \pm 0.005$
Tanzania	Honey	3.31	$1.53 \pm 0.002$	$2.38 \pm 0.062$	$0.50 \pm 0.016$	$0.20 \pm 0.006$

The peak position of FSDP ( $Q_1$ ) is related to the characteristic repeat distance ( $2\pi/Q_1$ ) in real space atomic arrangements. Results are summarized in Table 3-6. The characteristic repeat distance for opal-  $A_G$  samples is around 4 Å. For opal-CT samples this value rises to roughly 4.1 Å. The correlation length ( $2\pi/\text{FWHM}$ ) for opal-  $A_G$  samples is around 15 Å, whereas it is larger than 30 Å in opal-CT samples. The increase in characteristic repeat distance and the correlation length could be explained by progressing polymerization of silicon-oxygen network structure resulting in relatively more ordered opal-CT samples when compared to opal- $A_G$  samples. It is also important to note that there is no global understanding of the correlation length yet; as it is highly system dependent [110].

**Table 3-6. Characteristic repeat distance,  $2\pi/Q_1$  and coherence length,  $2\pi/\text{FWHM}$ .**

Origin	Water (wt%)	Characteristic Repeat Distance	Correlation length
		$2\pi/Q_1(\text{Å})$	$2\pi/\text{FWHM}(\text{Å})$
Silica glass	0.00	4.13	14.43
<i>Opal-<math>A_G</math></i>			
Brazil	3.76	4.03	15.96
Honduras	5.46	3.99	13.13
<i>Opal-CT</i>			
Ethiopia	7.00	4.12	40.22
Mexico (Red)	5.46	4.12	36.38
Mexico (White)	3.58	4.12	32.32
Tanzania	3.31	4.12	32.18

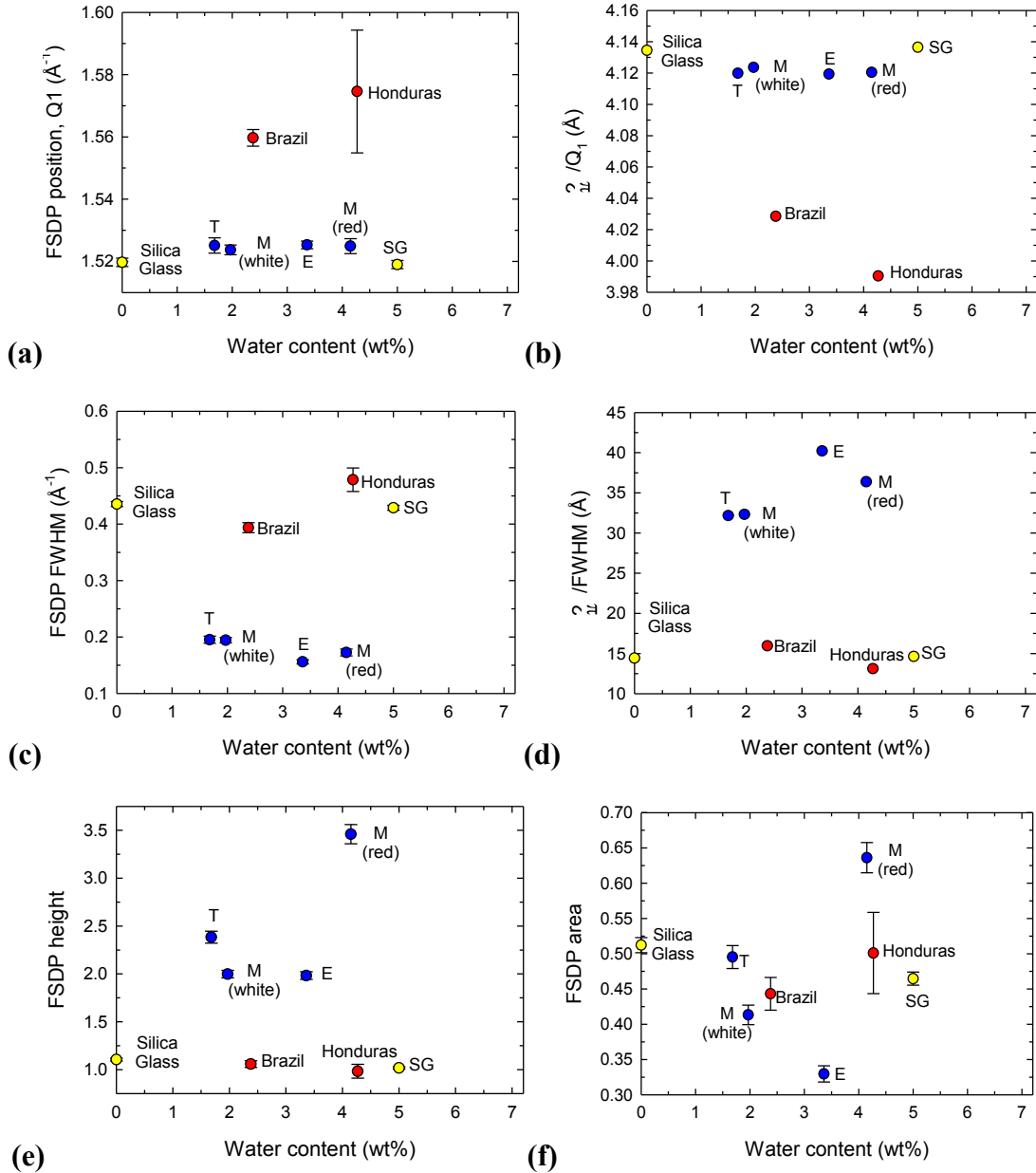
The effect of water on the structure of sodium tetrasilicate glasses has been studied by analyzing the FSDP in the neutron scattering structure factor; and it is found that both the characteristic repeat distance, the correlation length and the FSDP intensity decrease as water concentration increases [111]. This might be explained by depolymerization of the glass network with addition of water. In our study, a pattern related with water content has not been observed. Instead, we observed distinct populations according to the type of the opal as discussed above (Figure 3-17).



**Figure 3-17. FSDP analysis with respect to water content of opals: silica glass (yellow), opal-A<sub>6</sub> (red) and opal-CT (blue). The data points for silica glass with 5% water content are obtained from weighted sum of the S(Q) curves of silica and water.**

An alternative version of Figure 3-17 with respect to water loss between 190-600°C is shown in Figure 3-18. We observe a very similar pattern to that of total water content suggesting that this type of water has more effect on these results.

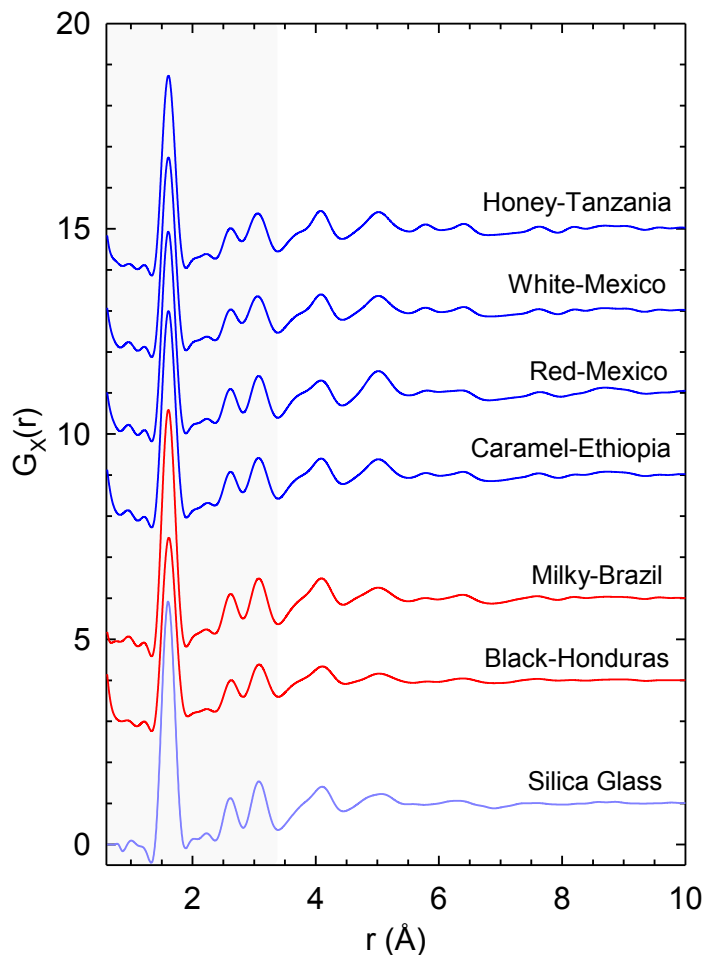




**Figure 3-18. FSDP analysis with respect to water loss between 190-600°C of opals: silica glass (yellow), opal-A<sub>6</sub> (red) and opal-CT (blue). The data points for silica glass with 5% water content are obtained from weighted sum of the S(Q) curves of silica and water.**

As discussed in chapter 2, in this work two normalizations schemes for the PDF's are plotted first is  $G(r)$ , which is normalized to the macroscopic density of the material such that  $G(r) \rightarrow 1$ , at high- $r$ , and  $G(r) = 0$ , means zero probability of finding an atom at that  $r$ -value. Alternatively the function  $D(r) = 4\pi r [G(r) - 1]$ , may be plotted to emphasize higher- $r$  structure, this function oscillates about zero, and the negative slope at low- $r$  values, is related to the macroscopic density of the material. Measured structure factors for opals are Fourier transformed to obtain the  $G_X(r)$  of natural opals. Resulting patterns are summarized in Figure 3-19. All opals

show a similar short range ordering; and their  $G(r)$  patterns are very similar to that of silica glass up to 5 Å. Earlier in the chapter, we have discussed the pair distribution of silica glass in detail (Figure 3-11 and Figure 3-12). This can be used to interpret the opal patterns. The first few peaks of the opal  $G(r)$ s define the  $SiO_4$  tetrahedra.



**Figure 3-19. Measured X-ray (a) pair distribution  $G_X(r)$  functions for natural opals.**

A Gaussian fit with a linear background is applied to the 1.32-3.44 Å range in order to identify the first three peaks of the pattern. A sample fit is given in Figure 3-20. Obtained results for the Gaussian fits of the first three peaks to  $G_X(r)$  are summarized in Table 3-7. For all opals, the first peak ( $Si_1-O_1$  correlations) is at  $\sim 1.61$  Å and the second peak ( $O_1-O_1$  correlation) is at  $\sim 2.62(1)$  Å similar to that of silica glass implying that the structure of opals is very similar over the distance scale of a single  $SiO_4$  tetrahedron. For all opal samples, the position of the  $Si_1-O_1$  and  $O_1-O_1$  correlations are slightly shifted to the higher values when compared to that of silica glass. This can be explained by higher amount of non-bridging oxygen atoms in opals; as the  $Si-BO$  bond length is smaller than  $Si-NBO$  bond length. Besides the slight shifts in the position of the first peak, a general broadening of the first peak (increased FWHM) is observed, suggesting an increased disorder in the network. The broadening is more prominent in the opal- $A_G$  samples. The FWHM of the second peak ( $O_1-O_1$  correlation) slightly decreases. The third peak ( $Si_1-Si_2$

correlations) is at  $\sim 3.06(2)$  Å; and this correlation is positioned slightly lower for opals when compared to that of silica glass. The  $Si_1-Si_2$  distance is pretty robust and very important for giving an indication of the average ring size.

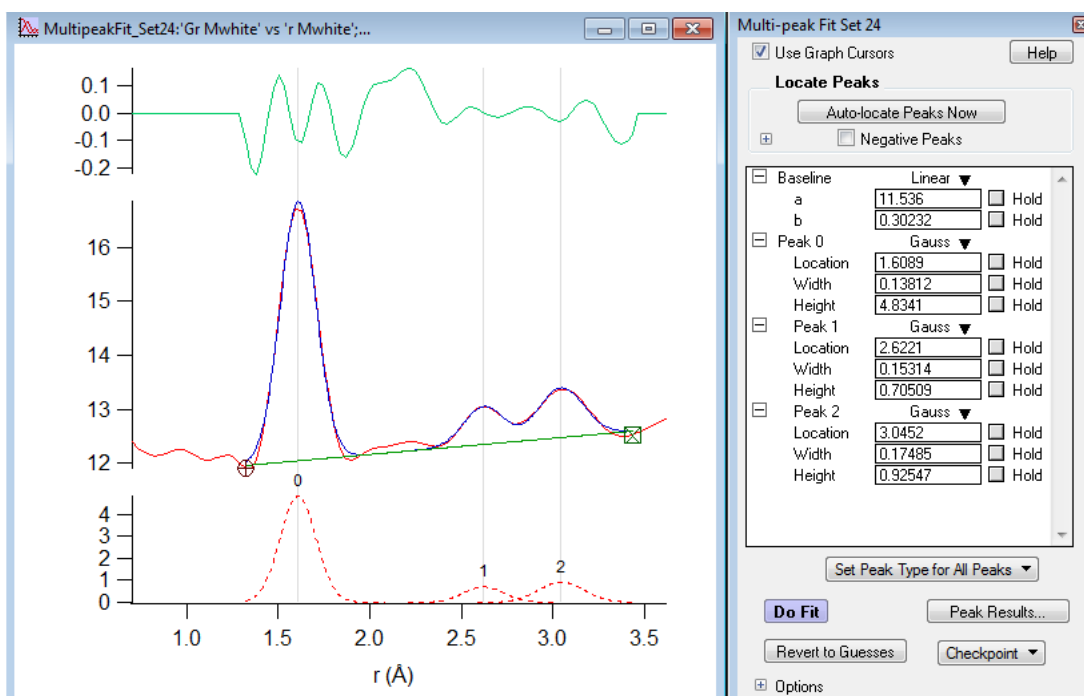


Figure 3-20. Gaussian fit to  $G_x(r)$  for the 1.32-3.44 Å range.

Table 3-7. First three correlations of the X-ray pair distribution function of opals

Origin	Water (wt%)	Peak position (Å)			FWHM (Å)		
		Si <sub>1</sub> -O <sub>1</sub>	O <sub>1</sub> -O <sub>1</sub>	Si <sub>1</sub> -Si <sub>2</sub>	Si <sub>1</sub> -O <sub>1</sub>	O <sub>1</sub> -O <sub>1</sub>	Si <sub>1</sub> -Si <sub>2</sub>
Silica Glass	0.00	1.605	2.611	3.072	0.229	0.221	0.249
<i>Opal-A<sub>G</sub></i>							
Brazilian	3.76	1.608	2.615	3.063	0.233	0.225	0.238
Honduras	5.46	1.617	2.624	3.071	0.241	0.223	0.269
<i>Opal-CT</i>							
Ethiopian	7.00	1.610	2.614	3.062	0.232	0.256	0.271
Mexico (Red)	5.46	1.607	2.613	3.068	0.228	0.239	0.256
Mexico (White)	3.58	1.609	2.622	3.045	0.230	0.255	0.291
Tanzania	3.31	1.609	2.622	3.045	0.229	0.252	0.292

Figure 3-21 shows the position of first three peaks of  $G_x(r)$  with respect to water content of the measured opals. There is not an observable trend with respect to total water content. However, there is a light trend with respect to the water loss between 190-600 °C. Within opals, the Si<sub>1</sub>-Si<sub>2</sub> correlation length tends to increase with respect to increasing water loss. The O<sub>1</sub>-O<sub>1</sub> correlation length for opal-CT samples tends to decrease with increasing water loss; while for

opal-AG samples it increases. Existence of a correlation between the FWHM of the peaks and the water content was investigated in Figure 3-22; but, a correlation was not observed.

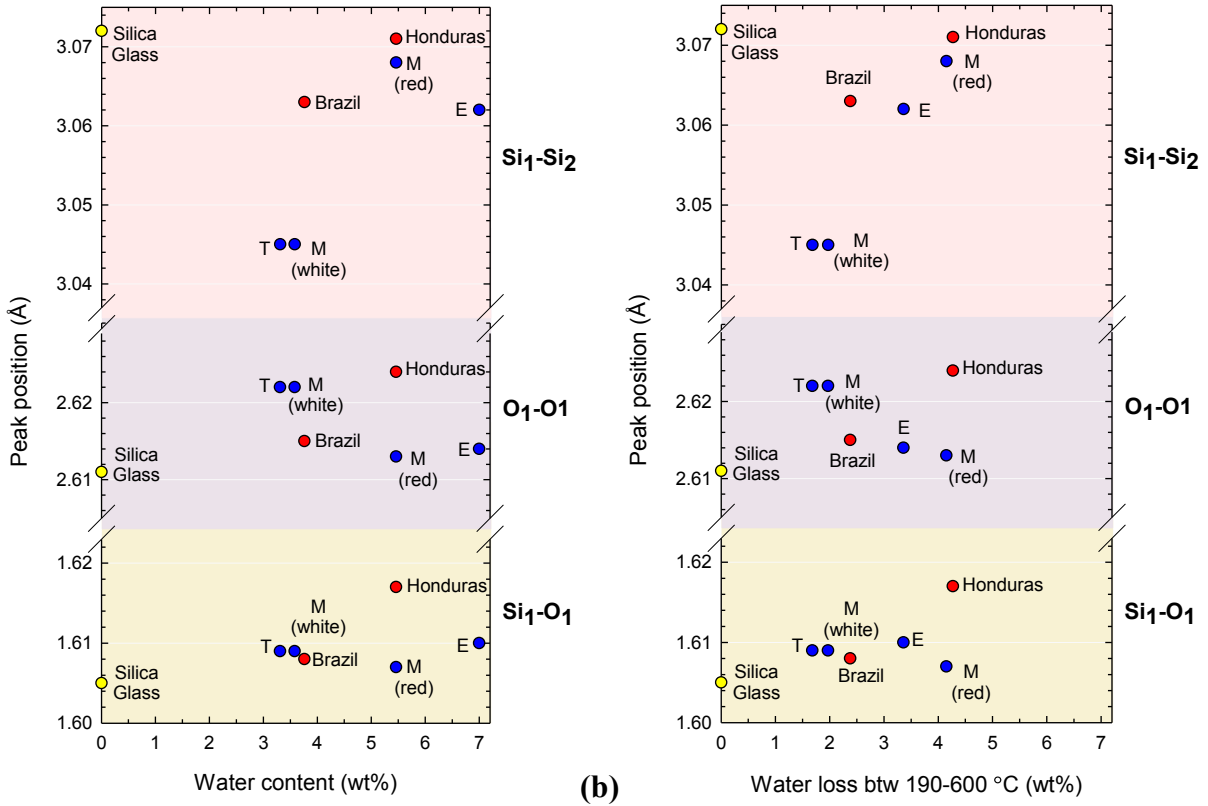
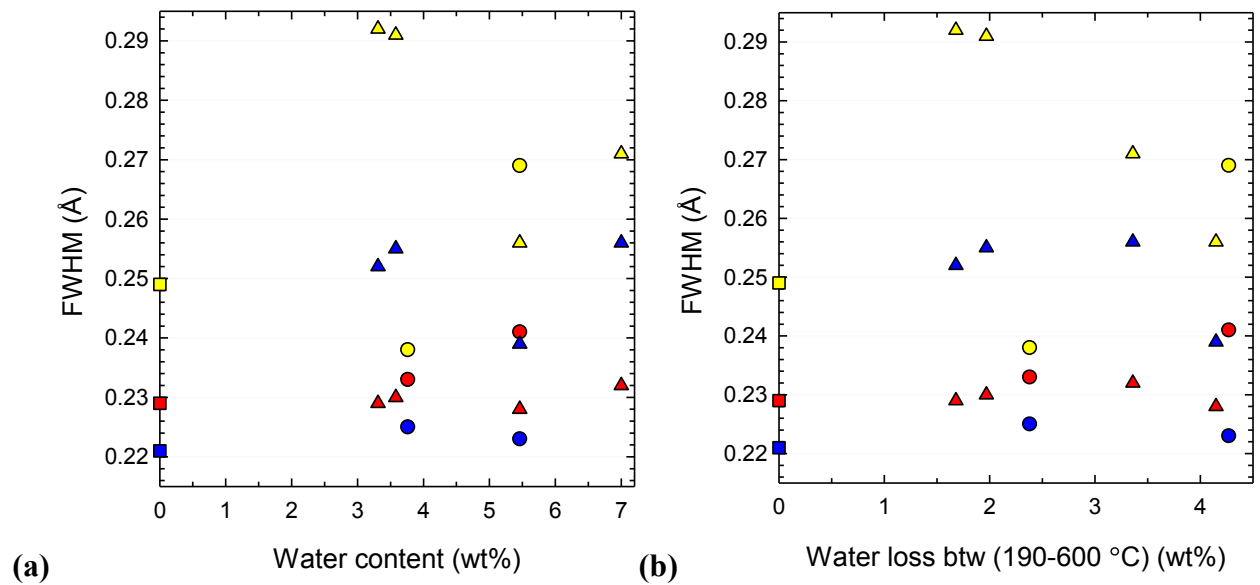


Figure 3-21. The position of first three peaks of  $G_x(r)$  of opal-AG (red), opal-CT (blue) and silica glass (yellow) samples with respect to their (a) total water content and (b) water loss between 190-600°C.



**Figure 3-22.** The FWHM for the first three peaks of  $G_X(r)$  of opal- $A_G$  (circle), opal-CT (triangle) and silica glass (square) samples with respect to their (a) total water content and (b) water loss between 190-600°C. Red:  $Si_1-O_1$ , blue:  $O_1-O_1$  and yellow  $Si_1-Si_2$ .

For an ideal tetrahedron the ratio of  $r_{OO}/r_{SiO}$  is 1.633 giving a tetrahedral angle  $\Phi$  ( $\equiv O-Si-O \equiv$ ) of  $109.5^\circ$ . Table 3-8 lists the ratios calculated from the values in Table 3-7. The tilt of the  $Si-O$  bond  $\theta$  is calculated from  $\sin \theta/2 = r_{SiSi}/2r_{SiO}$ .

**Table 3-8.** Tetrahedral angle and the tilt of the  $Si-O$  bond  $\theta$  for opals

Origin	Water (wt%)	$r_{OO}/r_{SiO}$	$\Phi$ ( $\equiv O-Si-O \equiv$ )	$r_{SiSi}/r_{SiO}$	$\theta$ ( $\equiv Si-O-Si \equiv$ )
Silica Glass	0.00	1.627	$108.9^\circ$	1.913	$146.2^\circ$
<i>Opal-<math>A_G</math></i>					
Brazilian	3.76	1.626	$108.8^\circ$	1.905	$144.5^\circ$
Honduras	5.46	1.623	$108.5^\circ$	1.900	$143.6^\circ$
<i>Opal-CT</i>					
Ethiopian	7.00	1.624	$108.5^\circ$	1.902	$143.9^\circ$
Mexico (Red)	5.46	1.626	$108.8^\circ$	1.909	$145.2^\circ$
Mexico (White)	3.58	1.630	$109.2^\circ$	1.893	$142.3^\circ$
Tanzania	3.31	1.630	$109.2^\circ$	1.893	$142.4^\circ$

The obtained values for  $r_{OO}/r_{SiO}$  and tetrahedral angle  $\Phi$  are very close to that of an ideal tetrahedron. Up to fourfold rings, the  $O-Si-O$  bond angle are distorted. For rings with 5 or more tetrahedral, the  $O-Si-O$  bond angle distributions peaks very close to  $109^\circ$  [112]. This suggests that opals have mostly larger rings.

The tilt of  $Si-O$  bond angle  $\theta$  is also of importance, and allows understanding the glass structure beyond basic tetrahedron. The correlation between the ring size and  $\theta$  has been well studied. Larger ring sizes are expected to have larger  $\equiv Si-O-Si \equiv$  bond angle  $\theta$ . Whenever an n-fold ring is formed in a glass, it tends to reduce its energy (hence, the energy of the glass) by relaxing  $\theta$  towards the lowest energy possible [113]. For opals the calculated  $\theta$  values are  $\sim 144^\circ$  indicating corner shared connectivity of the tetrahedra. This also correlates with rather open network in amorphous  $SiO_2$  associated primarily with 5, 6 and 7-membered rings [31]. It is also important to note that in silicates  $\theta$  becomes narrower as the  $Si-O$  bond lengthens [114,115].

In order to emphasize higher-r structure, we have utilized  $D_X(r)$  as discussed previously. Figure 3-23 shows simulated  $D_X(r)$  patterns, and atom specific weighted partial  $D_X(r)$ s for cristobalite and tridymite. The patterns are calculated from the structural parameters given by Downs et al. [116] and Konnert et al. [117] using PDFFIT[118] with  $S_{ratio}$  of 0.8,  $r_{cut}$  of 2.0 and  $spdiameter$  of 30. When compared to amorphous silica, these two silica polymorphs are very different in intermediate/long range due to strong ordering.

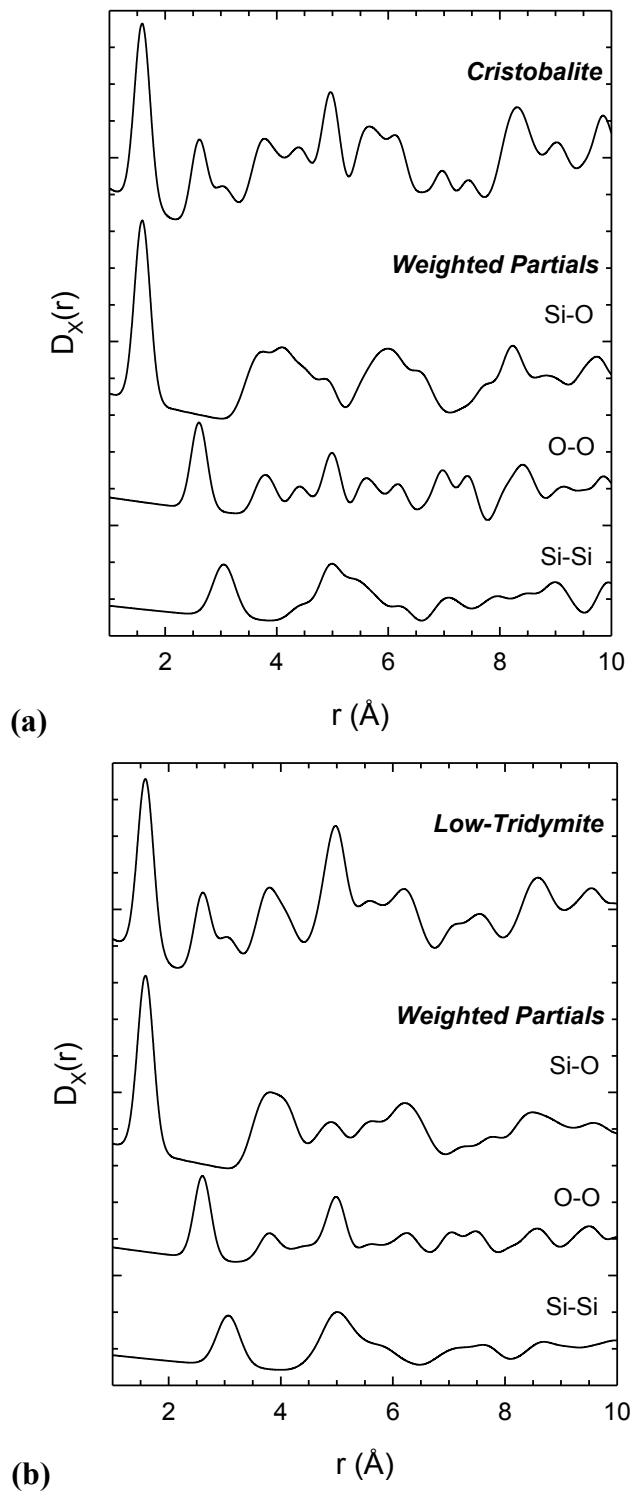


Figure 3-23. The simulated atom specific weighted partial  $D_x(r)$ s for (a) cristobalite and (b) low-tridymite. The patterns are calculated from the structural parameters given by Downs et al. [116] and Konnert et al. [117] using PDFFIT [118] with  $s_{\text{ratio}}$  of 0.8,  $r_{\text{cut}}$  of 2.0 and  $\text{spdiameter}$  of 30.

Figure 3-24 shows the  $D_X(r)$  of the opal samples allowing us to extract more information. In general,  $D_X(r)$  of silica looks more similar to the opals when compared to that of cristobalite and low-tridymite. The polyhedral connectivity, average orientations of adjacent polyhedra, is defined by typically up to 5 or 6 Å depending on the size of polyhedra. A Gaussian fit with a linear background is applied to the 3.44~7.60 Å range in order to identify the correlations beyond the first three peaks. Obtained results are summarized in Table 3-9. The Si<sub>1</sub>-O<sub>2</sub> correlations for all opals are located around 4 Å. The ~5 Å peak has contributions from both O<sub>1</sub>-O<sub>2</sub> and Si<sub>1</sub>-Si<sub>3</sub>. The other mixed correlations up to 7.60 Å are very similar for all the samples.

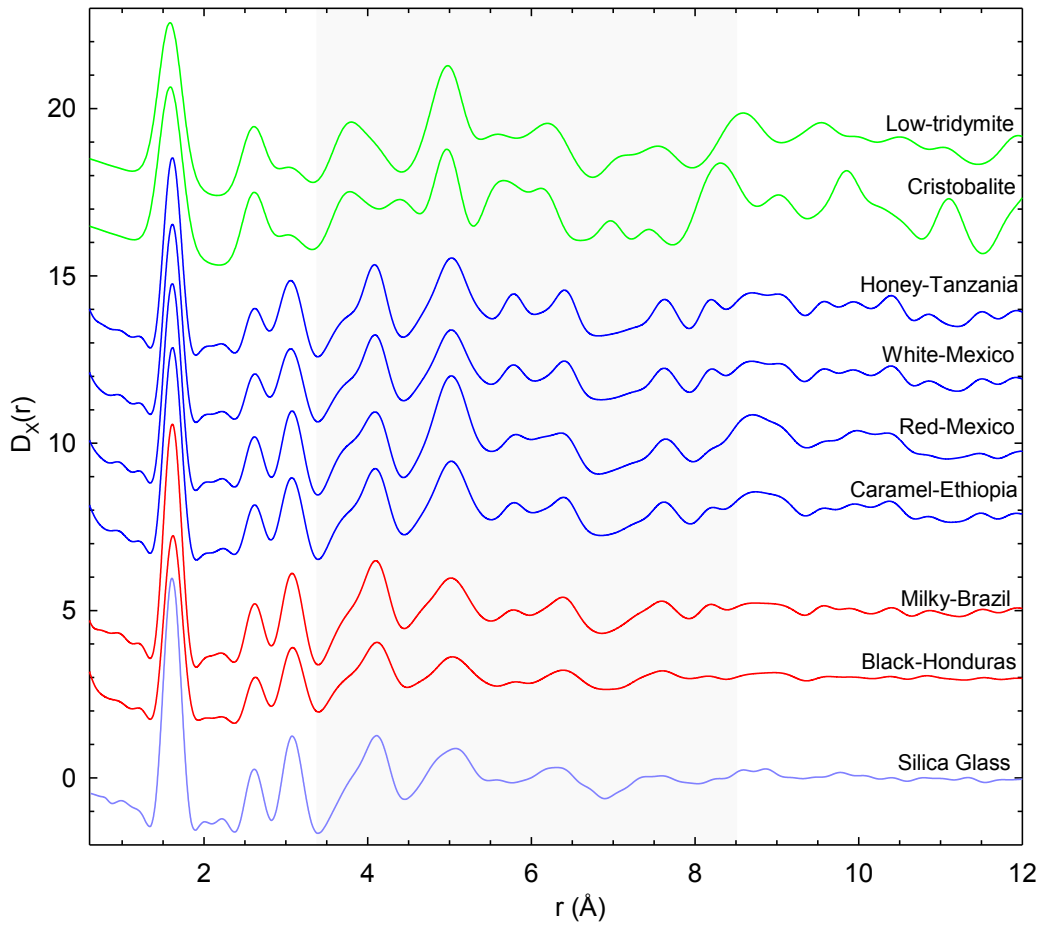


Figure 3-24. Measured  $D_X(r)$ s for natural opals. Simulated  $D_X(r)$ s for low tridymite and cristobalite are calculated from the structural parameters given by Downs et al. [52] and Konnert et al. [53] using PDFFIT [54] with  $s_{\text{ratio}}$  of 0.8,  $r_{\text{cut}}$  of 2.0 and  $sp_{\text{diameter}}$  of 30.

Table 3-9. The correlations of the X-ray differential distribution function  $D_X(r)$  of opals within 3.44~7.60 Å range.

Origin	Water (wt%)	Peak position (Å)			
		Si <sub>1</sub> -O <sub>2</sub>	O <sub>1</sub> -O <sub>2</sub> Si <sub>1</sub> -Si <sub>3</sub>	Mixed correlations	
Silica Glass	0.00	4.041	5.024	6.164	7.555

<i>Opal-A<sub>G</sub></i>						
Brazilian	3.76	4.047	4.994	5.790	6.364	7.529
Honduras	5.46	4.061	5.026	5.800	6.378	7.554
<i>Opal-CT</i>						
Ethiopian	7.00	4.037	5.013	5.809	6.375	7.593
Mexico (Red)	5.46	4.007	5.013	5.840	6.381	7.600
Mexico (White)	3.58	4.046	5.016	5.793	6.380	7.601
Tanzania	3.31	4.047	5.020	5.800	6.381	7.615

Figure 3-25 shows  $D_X(r)$  for the opal up to 40 Å. We do not observe correlations beyond 12 Å for amorphous opals. We do see some weak correlations up to 40 Å for opal-CT samples.

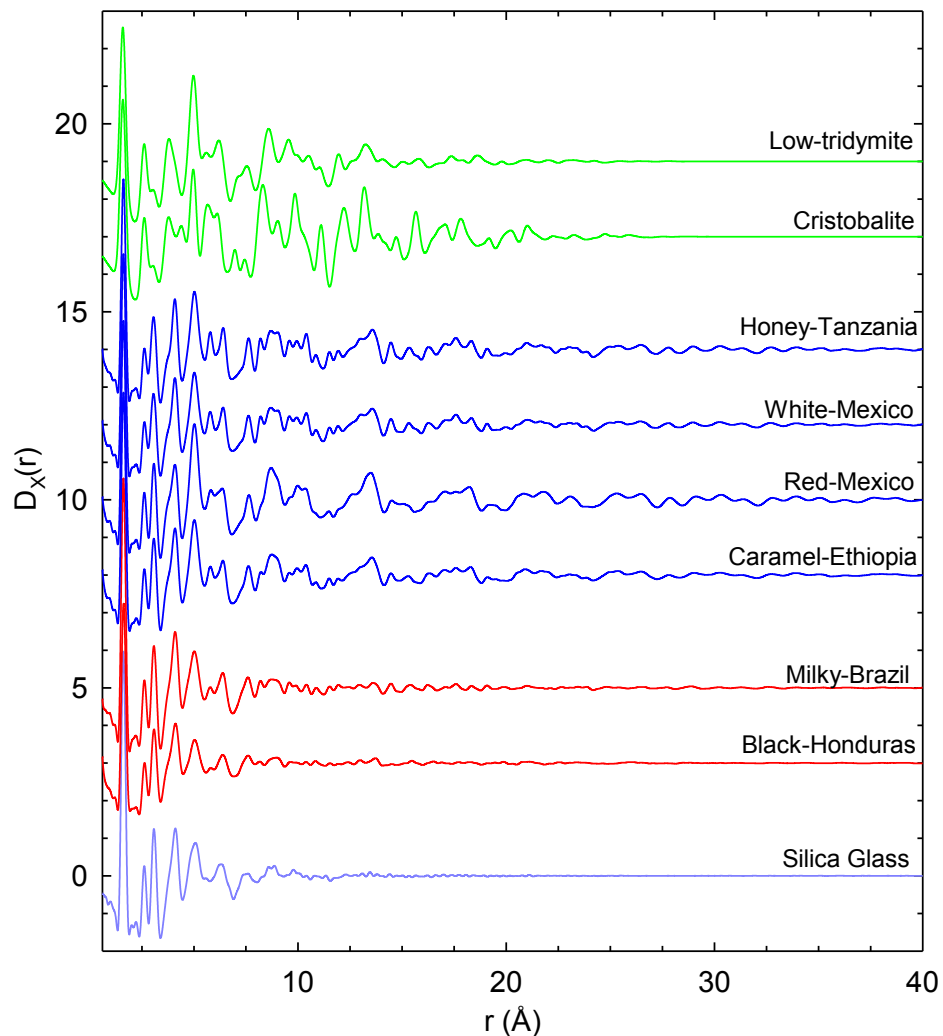


Figure 3-25. Measured  $D_X(r)$ s for natural opals. Simulated  $D_X(r)$ s for low tridymite and cristobalite are calculated from the structural parameters given by Downs et al. [116] and Konnert et al. [117] using PDFFIT [118] with  $s_{\text{ratio}}$  of 0.8,  $r_{\text{cut}}$  of 2.0 and  $s_{\text{diameter}}$  of 30.



The Brazilian opal- $A_G$  sample was also measured with neutrons at NPDF beamline located at LANSCE. Details of the beamline are described in Chapter 2. The experimental procedure is similar to that of X-rays. First the powdered opal sample was sealed inside a standard extruded cylindrical vanadium container. Then, the container was placed with in the experiment chamber of NPDF. The data was collected at room temperature for approximately 6 hours. The raw data was normalized with respect to a vanadium rod data using PDFGetN. However, In order to analyze the collected data, we need to remove the incoherent scattering primarily due to the presence of hydrogen within the tested opal from  $S_N(Q)$ . A scaled water pattern combined with a polynomial is used to provide background to obtain the  $S_N(Q)$  used in the transforms, Figure 3-26.

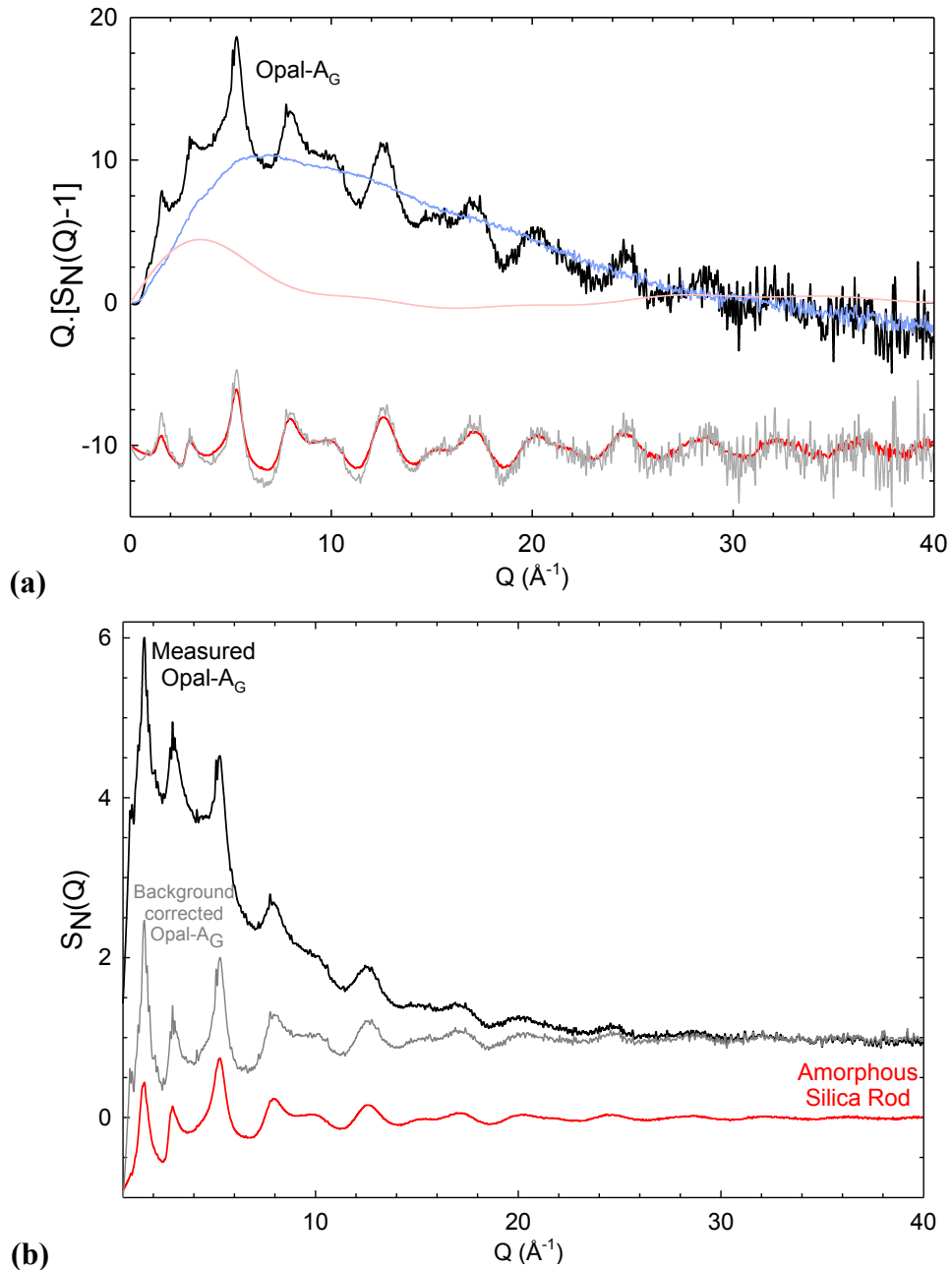


Figure 3-26. The measured (a)  $Q \cdot [S_N(Q)-1]$  and (b)  $S_N(Q)$  patterns for opal- $A_G$  from Brazil (black) and amorphous silica rod (red). The background corrected patterns for opal- $A_G$  (gray) are obtained through subtracting a scaled water pattern (blue) and an additional polynomial (pink) from the opal- $A_G$   $Q \cdot [S_N(Q)-1]$  pattern.

The Figure 3-27 illustrates the obtained X-ray and neutron structure factors on silica glass. It is important to note that the silica glasses measured are coming from different sources, and the information on their production procedure is not known. The analysis of  $S(Q)$  is summarized in Table 3-10. We confirm our finding with X-rays with using neutron. One extra information we obtained is the identifying the  $Q_2$  peak in the neutron pattern arising from O-O interactions.

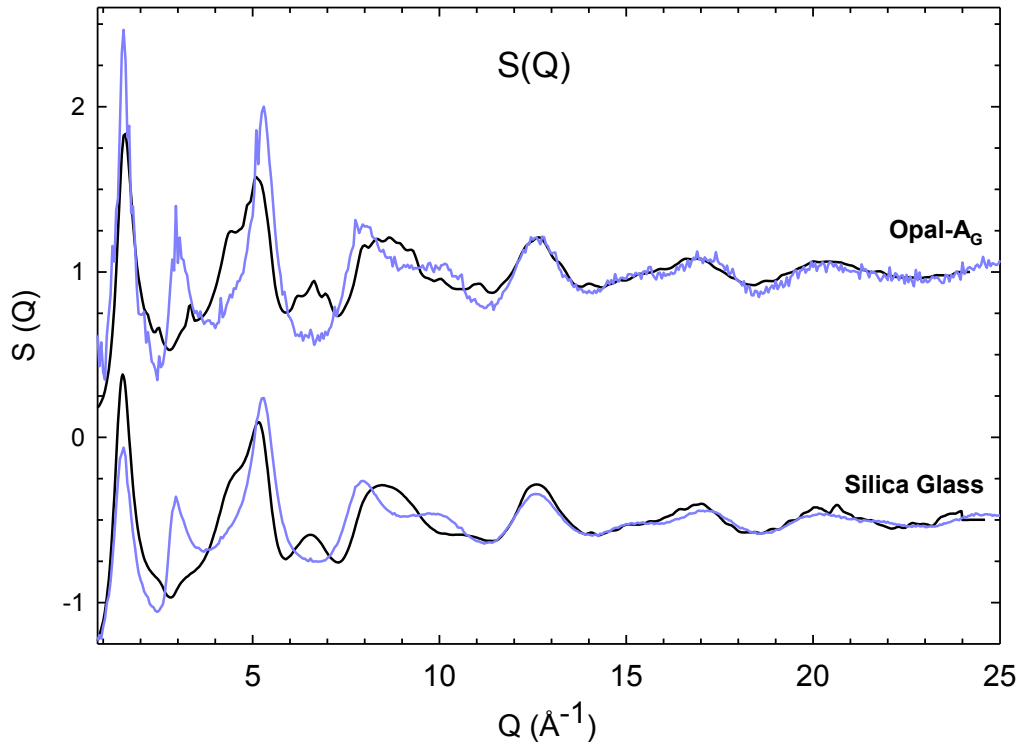


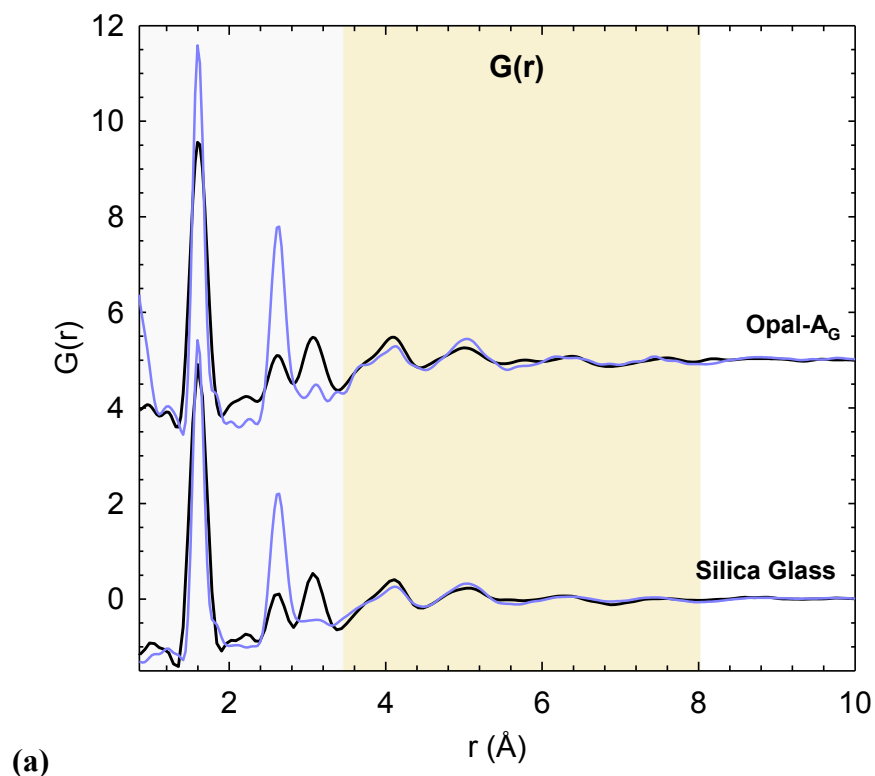
Figure 3-27. The measured X-ray (black) and neutron (blue) structure factors,  $S(Q)$ , of silica glass and amorphous opal from Brazil.

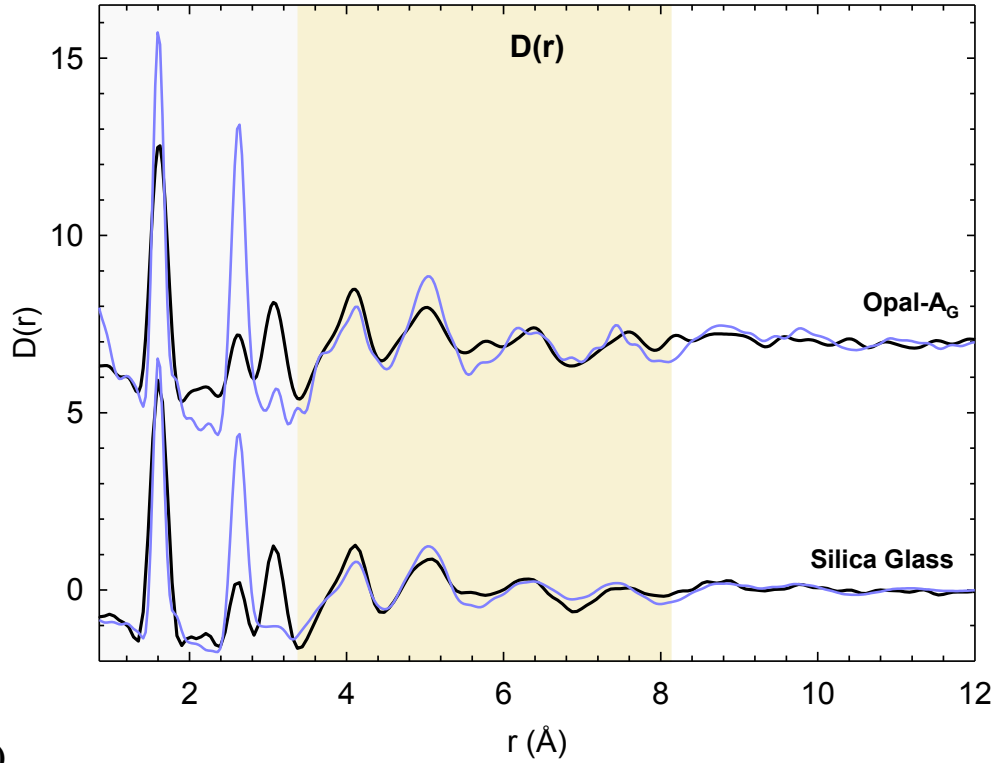
Table 3-10. Analysis of first sharp diffraction peaks of  $S_N(Q)$  and  $S_X(Q)$  for silica glass and amorphous opal from Brazil.

Water (wt%) Beam	Silica glass		Opal- $A_G$ from Brazil	
	<i>X-ray</i>	<i>Neutron</i>	<i>X-ray</i>	<i>Neutron</i>
$Q_1$				
Peak position ( $\text{\AA}^{-1}$ )	$1.520 \pm 0.001$	$1.529 \pm 0.006$	$1.560 \pm 0.003$	$1.559 \pm 0.008$
Peak Height	$1.105 \pm 0.013$	$1.049 \pm 0.028$	$1.058 \pm 0.034$	$1.767 \pm 0.071$
Peak Area	$0.512 \pm 0.011$	$0.634 \pm 0.031$	$0.443 \pm 0.023$	$0.918 \pm 0.067$

FWHM ( $\text{\AA}^{-1}$ )	$0.436 \pm 0.005$	$0.568 \pm 0.022$	$0.394 \pm 0.009$	$0.488 \pm 0.027$
$2\pi/Q_1(\text{\AA})$	4.134	4.109	4.028	4.030
$2\pi/\text{FWHM}(\text{\AA})$	14.426	11.057	15.961	12.872
<b>Q<sub>2</sub></b>				
Peak position ( $\text{\AA}^{-1}$ )	-	$3.003 \pm 0.022$	-	$3.032 \pm 0.012$

The obtained neutron structure factors for silica glass and opal-A<sub>G</sub> from Brazil are Fourier transformed to obtain their  $G_N(r)$  and  $D_N(r)$ s. Resulting patterns are summarized in Figure 3-28. A Gaussian fit with a linear background is applied to the 1.32-3.44  $\text{\AA}$  range to  $G(r)$ s, and 3.44~8.00  $\text{\AA}$  range to  $D(r)$ s in order to identify the correlations. The results are summarized in Table 3-11. Si is the predominantly scattering atom for X-rays since Si is heavier than O. However, O is the main scatterer for neutrons since O has a larger neutron cross section. The information concerning the Si-Si correlations, and hence the *Si-O-Si* bond angle, is best obtained from X-ray measurements whereas the *O-O* interactions and the *O-Si-O* bond angle are best studied with neutrons [14]. A small discrepancy between neutron and X-ray results exists outside the experimental uncertainties. Wright attributed this to variations in Si and O electron distributions using the X-ray data reduction procedure to describe the covalently bonded network [14]. Our neutron results on Brazilian opal-A<sub>G</sub> sample are very similar to our X-ray results. This further confirms our analysis. The neutron and X-ray results on the measured silica glasses show some discrepancy in the  $\text{Si}_1\text{-Si}_2$  correlation. This might be explained by possible differences in their production procedures.





(b) Figure 3-28. Measured neutron (blue) and X-ray (black)  $G(r)$  and  $D(r)$ s for silica glass and amorphous opal from Brazil.

Table 3-11. The correlation analysis of the X-ray and neutron pair distribution functions for silica glass and amorphous opal from Brazil up to 8 Å.

Water (wt%)	Silica glass		Opal-A <sub>G</sub>	
	0.00		3.76	
Beam	<i>X-ray</i>	<i>Neutron</i>	<i>X-ray</i>	<i>Neutron</i>
<b>Peak position (Å)</b>				
Si <sub>1</sub> -O <sub>1</sub>	1.605	1.606	1.608	1.605
O <sub>1</sub> -O <sub>1</sub>	2.611	2.625	2.615	2.623
Si <sub>1</sub> -Si <sub>2</sub>	3.072	3.059	3.063	3.057
Si <sub>1</sub> -O <sub>2</sub>	4.041	4.052	4.047	4.030
O <sub>1</sub> -O <sub>2</sub> , Si <sub>1</sub> -Si <sub>3</sub>	5.024	5.029	4.994	5.026
Mixed correlations	6.164	6.298	5.790	6.257
	7.555	7.433	6.364	7.447
			7.529	7.447
<b>FWHM (Å)</b>				
Si <sub>1</sub> -O <sub>1</sub>	0.229	0.160	0.233	0.162
O <sub>1</sub> -O <sub>1</sub>	0.221	0.214	0.225	0.209
Si <sub>1</sub> -Si <sub>2</sub>	0.249	0.596	0.238	0.517
$r_{OO}/r_{SiO}$	1.627	1.634	1.626	1.634
$\Phi$ ( $\equiv$ O-Si-O $\equiv$ )	108.9	109.6	108.8	109.6

$r_{\text{SiSi}}/r_{\text{SiO}}$	1.913	1.904	1.905	1.905
$\theta (\equiv\text{Si-O-Si}\equiv)$	146.2	144.4	144.5	144.5

### 3.3 Conclusions

This chapter focused on characterizing a variety of amorphous silicas that are often discussed in the cement and concrete literature. The comparison of silica fume and rice husk ash with silica glass showed that even though they have very different microstructures, they are indeed very similar in short range. This allows us to better interpret and model their usage.

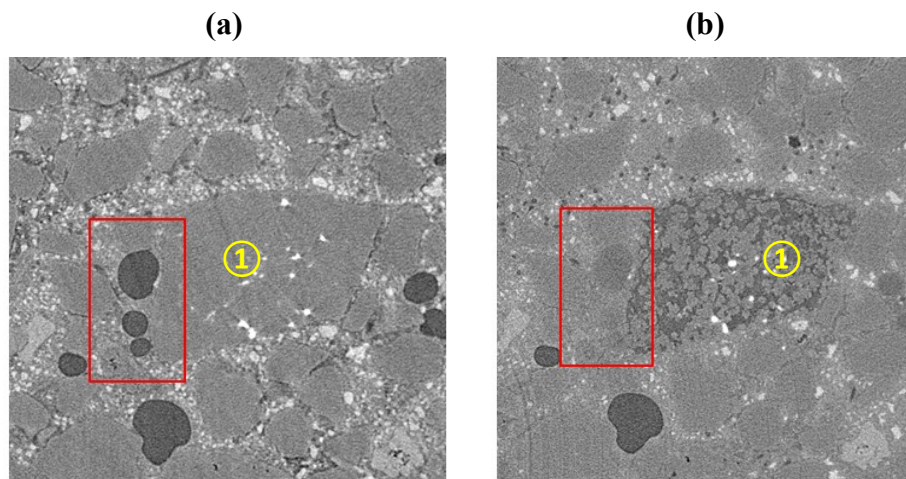
Opals can be problematic for engineering applications when used as a concrete aggregate due to opal's higher alkali-silica reactivity. Before investigating hydrated alkali silicate reaction gel and fly ash, studying opal provides some expertise to go forward. Characterization of amorphous and microcrystalline opals through SEM provided us to see how different their microstructures are. NMR study showed that opals are mainly composed of Q3 and Q4 species. The total scattering investigations on opal focused on understanding the effect of water. In all opal samples, we observed a shift in FSDP towards higher Q indicating an increased characteristic repeat distance when compared to silica glass, silica fume and rice husk ash. The shift was more prominent in opal-A<sub>G</sub> samples.

The analysis of the distribution functions of opals provided us a deeper insight on these complex hydrated-silicas. For all opals, the  $Si_1-O_1$  correlations were located at  $\sim 1.61(1)$  Å and the  $O_1-O_1$  correlations were located at  $\sim 2.62(1)$  Å. These positions were slightly shifted to the higher values when compared to that of silica glass, silica fume and rice husk ash. This could be explained by higher amount of non-bridging oxygen atoms in opals. Besides the slight shifts in the position, a general broadening of the first peak (increased FWHM) was also observed, suggesting an increased disorder in the network. The  $Si_1-Si_2$  correlations were centered slightly lower for opals when compared to that of silica glass at around  $\sim 3.06(2)$  Å giving an  $\equiv\text{Si-O-Si}\equiv$  bond angle  $\theta \sim 144^\circ$  indicating corner shared connectivity of the tetrahedral, possibly a rather open network in amorphous  $SiO_2$  associated primarily with 5, 6 and 7-membered rings. The positions of the higher correlations for opals continued to coincide up to 8 Å. The correlations of opal-AG samples got consistently broader and diminished around 12 Å. The correlations for opal-CT samples got weaker; however, continued up to 40 Å consistent with their more ordered structure.

# 4

## Alkali Silica Reaction

Modern portland cement concrete is a composite consisting of aggregate and hydrated cement matrix with highly alkaline pore solution. This is an ideal environment for embedded steel reinforcement. A passive layer, formed between the steel and the cement matrix, protects the reinforcement from corrosion. On the other hand, the highly alkaline environment is not a friendly environment for certain reactive aggregates with amorphous or poorly-crystalline silica phases, causing them to corrode. The reaction results in an amorphous, hydrophilic gel mainly composed of silica derived from the aggregates, and alkalis ( $K^+$  and  $Na^+$ ) and water from the pore solution of the hydrated cement matrix. The gel can also contain smaller amounts of other ions present in the pore solution, such as calcium, aluminum, and iron. The ASR gel is hygroscopic and can irreversibly expand by imbibing large amounts of water. However, this can become problematic if the gel is confined in a matrix such as hardened cement paste: The volumetric expansion of the gel can result in localized internal stresses that cannot be dissipated by migration of the gel into the voids and this might lead to extensive micro-cracking in the concrete. In advanced stages, ASR can lead to loss of stiffness, strength, and impermeability of concrete. As an example of the damage caused on the aggregates, Figure 4.1 shows micro-tomographic scans conducted at ALS Beamline 8.3.2 on mortars. The aggregate is severely dissolved, and adjacent voids were filled with the reaction gel:



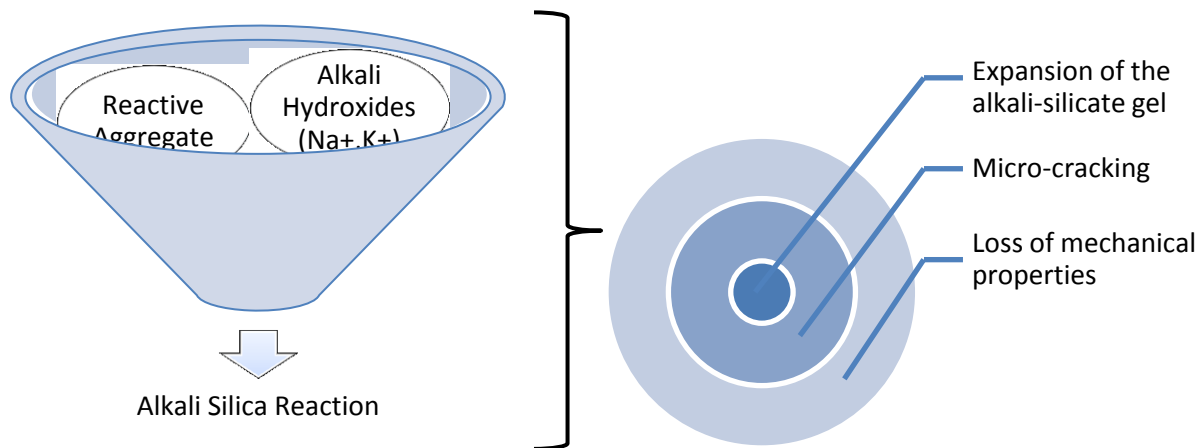
**Figure 4-1. Reconstructed slice of a mortar with polymer fiber (a) 1 week old; (b) after alkali-silica reaction (ASR). Aggregate ① is severely dissolved after the ASR attack. The adjacent voids (red box) are filled with gel.**

Episodes of ASR have been reported in various types of concrete structures all around the world [1]; yet, the ASR occurrence is not very common considering the vast number of unaffected structures [119]. The reaction is mainly limited to geological regions where ASR susceptible type rocks are abundant [1]. In most of the cases, the ASR damage of concrete is identified after an incubation time that can be as long as a few decades. The incubation times may differ depending on the size of the reactive aggregate, and the silica species and grains sizes in those aggregates. Accessibility of the concrete pore solution to the reactive site also plays a role [1]. Unlike corrosion of reinforcement, sulfate attack, and other surface-controlled deterioration mechanisms of the concrete; ASR is an intrinsic and bulk deterioration mechanism that is not just limited to the exposed concrete surface. Instead, ASR takes place due to a specific combination of the aggregate and the cement used; and once the specific combination is satisfied the repair of ASR damaged structures extremely complicated. Even though ASR is not that common, when it does occur the damage to the structure can be extensive, leading to a considerably reduced service life, especially in unreinforced structures that do not possess the tensile strength to resist the expansion and cracking produced by the reaction [120]. Specifically in dams, the proximity to water exacerbates the effect of the reaction [3]. In mega dam projects costing multiple billion dollars, the planning and construction of the dam might easily take 2 to 3 decades. ASR can significantly shorten the service life of these structures that are designed to last 200-300 years. Affording the time and money for an untimely replacement of these structures is very difficult. However; once ASR damage is observed, it creates significant risks of a potential malfunctioning or even failing of the structure [3]. The amount of ASR related expansion often varies throughout the concrete. Therefore, uneven or differential concrete swelling in structures may occur resulting in misalignments, deflections and separation of adjacent members. In some cases, closure of joints can be observed resulting in extrusion of jointing material, and spalling of concrete at the joints. ASR damaged concretes have reduced load bearing capacity and the fatigue life of concrete; also lose significant portion of their elastic modulus as their coarse aggregate is compromised.

Map-cracking is a common symptom of ASR in unreinforced concrete structures. These macro-cracks are generally located within 25 to 50 mm of the exposed concrete surface, and their width at the exposed concrete surface can range from 0.1 mm to over 10 mm [121]. It is difficult to distinguish map-cracking due to ASR from map-cracking due to freeze-thaw attack. In reinforced concrete structures, the ASR related cracks follow the embedded reinforcement. In ASR damaged structures, a transparent glaze covering the cracked walls and pop-outs of extruding gel can also be observed. In those cases, moisture movement through pores and cracks in concrete transports the gel to the surface where it extrudes.

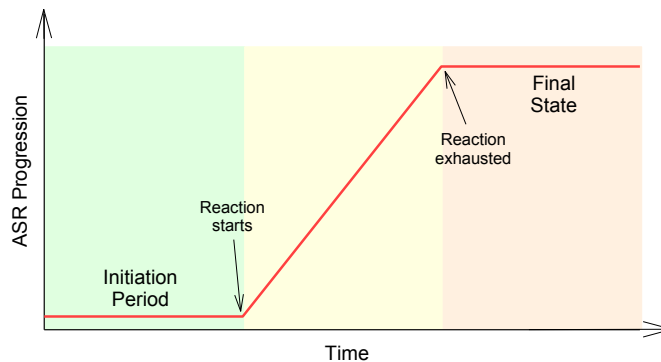
There are three necessary conditions to initiate and sustain ASR in concrete (Figure 4-2): (1) a reactive aggregate must be present; (2) the concentration of alkali hydroxides ( $Na^+$ ,  $K^+$  —  $OH^-$ ) in the concrete pore solution must be high enough; and (3) sufficient moisture must be present [122]. These conditions also determine the rate and extent of the ASR related damage to the concrete structure. Hence, the classical ASR prevention methods focus on eliminating these

conditions. Such methods include using supplementary cementitious materials (such as fly ash, silica fume, slag, and natural pozzolans) to reduce the amount of alkali ions in pore solution while also making the concrete less permeable; carefully selecting the aggregates to limit the amount of reactive silica present and limiting the equivalent sodium oxide content ( $Na_2O_e = wt\% Na_2O + 0.658 \times wt\% K_2O$ ) of the cement to less than 0.6% by mass as suggested by ASTM C 150. Following these preventive measures allows avoiding ASR in newly built structures in most cases. However, enforcing a full implementation of these measures may not always be possible (*i.e.* in a location where non-reactive aggregates and low-alkali cement is not available at a reasonable cost [123]).



**Figure 4-2. (Left) Necessary conditions to initiate and sustain ASR in concrete. The classical ASR prevention methods focus on eliminating at least one the three necessary conditions required. (Right) Stages of the ASR damage in concrete.**

As ASR in concrete is a time-dependent, multistage deterioration process, the related damage may occur after years or even decades of good performance. Therefore, there is a potential for ASR to affect apparently stable structures over time. A schematic for progression of ASR over time is shown in Figure 4-3. In the field, the reaction initiation and development is very slow. Therefore, the research on ASR is generally conducted on accelerated samples in laboratory. However, in many cases the correlation between the laboratory samples and the concrete in the field is not simple.





**Figure 4-3. Schematic for progression of ASR over time.**

The common ASR mitigation techniques focus on treating the three conditions listed above. Some of the common mitigation and rehabilitating practices are listed below; even though these methods show a broad diversity, none of them provides an effective long-term solution:

- local application of repair mortar by hand to cover up the cracks is a cosmetic measure with negligible enhancement of service life;
- applying lithium based compounds [124] through topical and vacuum applications (*i.e.* Figure 4-4a) to immobilize incipient alkali-silica gel is not very effective, as compounds cannot penetrate into the concrete via its pore system more than 1 mm unless the concrete is cracked – at which point it gets rather useless to prevent ASR;
- reducing the internal relative humidity below 80% through improvement of the drainage of the structure, application of exterior cladding, or applying a coating or a penetrating sealer. Sealers (such as siloxanes and silanes) prevent external water from penetrating into the concrete, but also allow water vapor within the concrete to exit, (Figure 4-4b). Surface abrasion and UV radiation is a problem for longevity of this application;
- injecting the fracture pattern with epoxy or polyurethane resin;
- installing additional reinforcement by gluing metal strips or carbon fiber mats on the surface introduces additional shear against non-reinforced parts;
- driving hundreds of rock bolts through an already heavily cracked concrete produces holes through interlocking pieces of concrete rubble held together by a cage of rebar;
- slot cutting with a wire saw to release stress and accommodate further expansion accepts that the structure will continue to expand;
- peeling the concrete cover behind the rebar (if exists) and restore to original profile with new concrete: the remaining original concrete can still expand and experience cracking.



**Figure 4-4. (a1) Topical and (a2) vacuum application of lithium nitrate solution on ASR-affected highway barriers [124]. Folliard *et al.* [124] found the topical and vacuum applications of lithium nitrate was ineffective in reducing the reactions due to lack of penetration of the solution. (b) Topical application of 40 percent-Silane Solution (solvent-based) to ASR-affected highway barrier in Massachusetts [125]. Penetration depths of silane solutions are typically measured to be less than 5 or 6 mm. Generally, this depth is adequate for preventing water from entering the concrete while**

allowing internal water vapor to escape, resulting in a lowered internal relative humidity of concrete [125]. However, surface abrasion and UV radiation reduces the longevity of this treatment. Also, if the moisture is available from an untreatable surface, this treatment would not be very effective.

In 1940, Stanton [83] linked the extensive concrete cracking in a number of bridges and pavements along the California coast to a reaction occurring between the opaline and cherty aggregate and the alkaline pore fluid in concrete. Today, 70 years after the “expansion of concrete through reaction between cement and aggregate” was first reported, the deleterious alkali-silica interaction continues to be one of the primary deterioration mechanisms of modern concrete. This chapter starts with discussing the reaction mechanisms in detail. Then, selected micrographs of damaged concrete structures are presented. This will provide an introduction to the field gels discussed in chapter 5.

## 4.1 Reaction mechanisms

ASR is a process with multiple steps. Details of the reaction mechanism has been widely discussed in literature [126–130]. The reaction initiates with the dissolution of silica on the surface of the aggregate particles [127], followed by the formation of the gel near the aggregate surface [31]. Over time the formed gel can also migrate through the porous hydrated cement matrix. The hydrolysis of precursor molecules and condensation of silanol (*Si-OH*) groups are the two main chemical reactions that take place during this process.

### 4.1.1 Dissolution of silica

The bulk of any silica is composed mainly of (*Si-O-Si*) linkages, and the flexibility of the (*Si-O-Si*) linkage allows  $SiO_4$  tetrahedra to polymerize in various number of silica polymorphs. The most common form of silica is quartz; cristobalite is the second [131]. Quartz is a major constituent in a number of rocks, such as granite and sandstone [131]. It can also occur by itself either in highly crystalline or cryptocrystalline form [131]. Other crystalline silica polymorphs include tridymite, and diatomite. There are also a number of non-crystalline glasses or sol-gel phases, and micro/mesoporous materials. [132]. In all silica polymorphs (except stishovite), silica tetrahedral share corners forming a three-dimensional network of (*Si-O-Si*) bonds which have mainly a covalent character [131]. At the surface, the silica structures terminate in either siloxane groups ( $\equiv Si-O-Si \equiv$ ) with the oxygen on the surface, or one of the several forms of silanol groups ( $\equiv Si-OH$ ) [133]. Furthermore, the silica tetrahedra on quartz surfaces have distinct bonding coordinations at terraces and steps [134,135], Figure 4-5. At a step edge on the (100) quartz surface, the Q2 groups are bonded to two bridging oxygens. In contrast, the Q3 groups of a terrace have a higher connectivity to the solid via binding to three bridging oxygens [136].

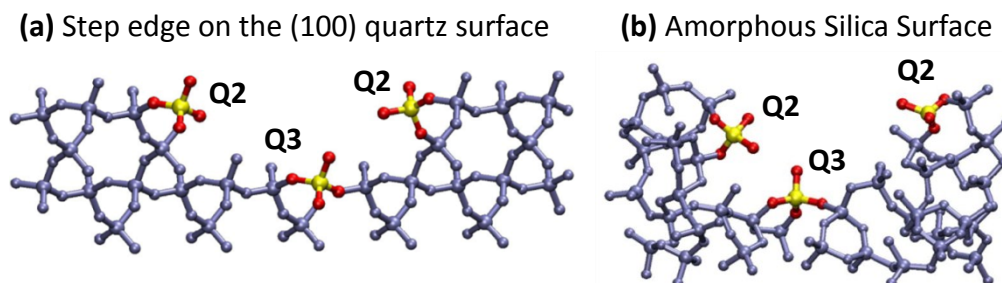


Figure 4-5. Illustration of (a) quartz and (b) amorphous silica showing Q2 and Q3 species as tetrahedra with two and three coordinations to the surface, taken from Dove *et al.* [136]. The Q3 groups have higher connectivity to the solid through three binding oxygens. The physical model holds that amorphous surfaces are repeatedly, atomically roughened at a length scale that is the average distance over which Q2 groups must be removed to return to a Q3-enriched SiO<sub>2</sub> surface [136].

The ‘corrosion’ behavior of silicas has long been a topic of interest for the materials scientists and medical researchers. The *Si–O* bond character in quartz is predominantly covalent, with only ~25% ionicity [1] explaining the generally poor solubility of quartz in aqueous solutions. Compared to quartz, the solubility of amorphous silica is much higher. A typical amorphous silica solubility diagram at 25°C is given at Figure 4-6 [137–139].

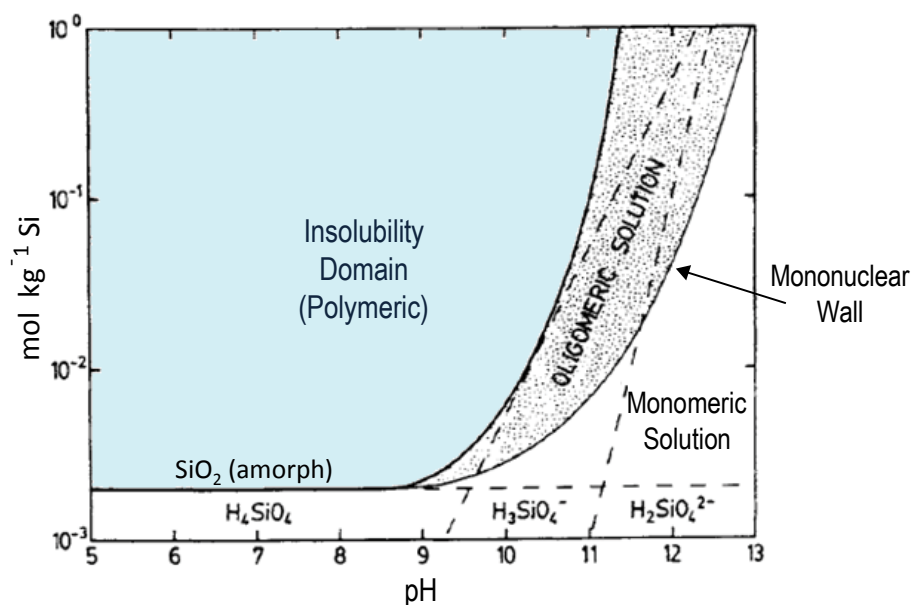


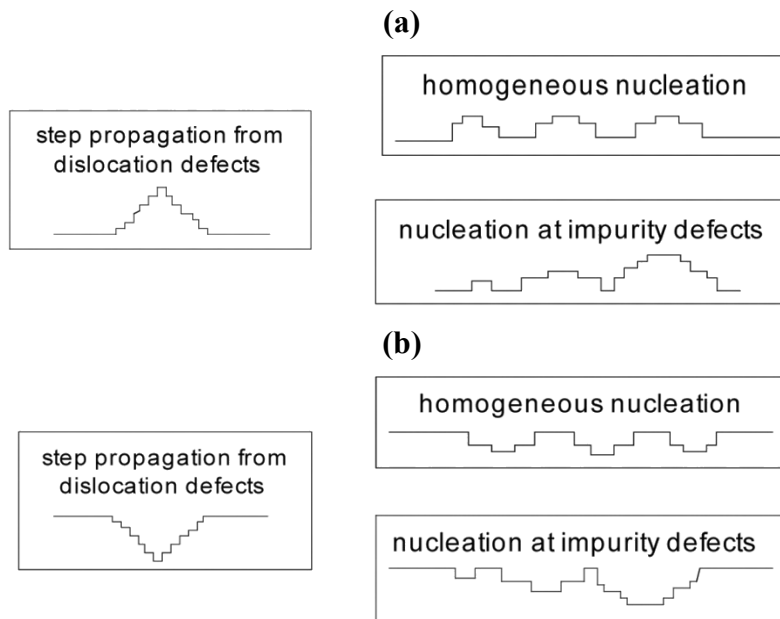
Figure 4-6. Amorphous silica solubility diagram at 25 °C. The mononuclear wall represents the lower limit for stability of multinuclear silica species. Adapted from [137,140,141].

The figure provides a semi-quantitative description of the nature of aqueous silica at a given pH. Over time, there have been some modifications on the figure. The location of the insolubility line and the mononuclear wall has been slightly altered as the amount of available data and calculations increase [142]. Still, it is generally accepted below the mononuclear wall; the silicate species are in true solution [139]. If the SiO<sub>2</sub> concentration is high enough, the

monomeric species based on  $H_4SiO_4$  (such as  $SiO(OH)^{-3}$ ,  $SiO_2(OH)^{-2}$  ions whose proportions will increase with pH) are in equilibrium with polymeric ones [143]. At this conditions, the polymeric species (including cyclic trimeric ( $H_8Si_3O_{10}$ ) units and cage-like structures) are mostly ionized [143]. Above the curve, within the insolubility region, metastable colloidal systems exist containing roughly spherical particles with a negative charge [143].

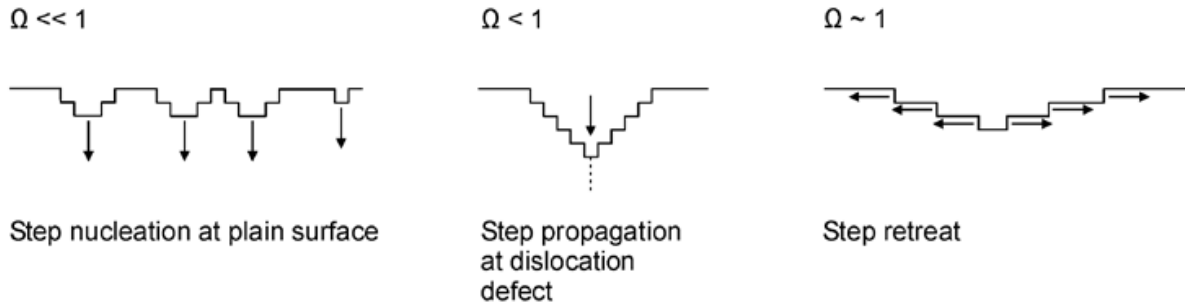
The basic thermodynamic principles predict that dissolution rates should increase with increasing driving force or chemical potential; however, experimental studies on major silicate minerals show that this is much more complex [136]. The dissolution rates of both quartz and amorphous silicas are increased 50–100 times in the presence of major alkaline or alkaline earth cations (such as  $K^+$  and  $Na^+$ ) are introduced to otherwise pure solutions [136,144]. The behavior is unique to pure  $SiO_2$  phases. In contrast, silicate minerals have only a weak sensitivity to the introduction of electrolytes [145]. Explanations of these behaviors based on widely used rate models had shortcomings; thus, scientists tried a different approach, and used mechanistic models developed to illuminate crystallization in order to understand mineral dissolution [136].

A mechanistic model of nucleation-driven crystal growth was introduced in 1980's. The model described growth kinetics in terms of four primary parameters: temperature, supersaturation, step edge energy, and step kinetic coefficient [146]. The theory looked at the probability of growth at dislocation defects vs. growth by nucleation of 2-D adatom islands either at impurity defects or homogeneously across the surface through examining energy barriers to growth, as illustrated in Figure 4-7a. The theory also provided a mechanistic and quantitative description of dissolution rates by analogous, reversed processes that assumes rates were controlled through the same four parameters [147]. In analogy to growth mechanisms, release of solutes to solution occurs at a rate that is controlled by overcoming energy barriers to 'corrosion' either at dislocation defects or by nucleating 2-D vacancy islands at impurities or homogeneous sites. Figure 4-7b illustrates dissolution as the 'reversed' nucleation-driven processes [147].



**Figure 4-7. Illustrations of mechanistic model for (a) nucleation-driven crystal growth; and (b) dissolution as a reversed nucleation-driven process. Taken from [147].**

Figure 4-8 shows three different regimes of mineral dissolution depending on the dominant mechanism of dissolution [148] where  $\Omega$  identifies with the saturation degree. At very high undersaturation ( $\Omega \ll 1$ ), 2-D pits or vacancy islands can nucleate at perfect surfaces even when a dislocation is not present [148]. The activation energy barrier for this mechanism is high [149]. Closer to equilibrium ( $\Omega < 1$ ), 2-D pitting on plain surfaces will cease; yet, step nucleation can proceed at dislocation defects due to the associated strain field [148].



**Figure 4-8. Illustrations of physical model for classical crystal dissolution by opening etch pits and step retreat. The dominant dissolution mechanism depends on the level of undersaturation. At very high undersaturations 2-D pits or vacancy islands can nucleate perfect surfaces. At lower levels, step nucleation can still proceed at dislocation defects. Near equilibrium step nucleation ends, and step retreat becomes the dominant dissolution mechanism.  $\Omega$  identifies with the saturation degree. Taken from [148]**

As the saturation degree reaches near-equilibrium ( $\Omega \sim 1$ ), only step retreat is possible, and no more steps can form at the surface or near dislocation defects. Step nucleation only occurs at crystal edges and the crystal becomes progressively smoother and edges more rounded [150]. This model relates the dissolution rate to the density of steps present or nucleated at the surface and the velocity of step retreat at the surface [148]. Both parameters are a function of the degree of solution undersaturation; thus the dissolution rate will decrease sharply when the undersaturation degree approaches equilibrium.

Nucleation-driven dissolution of crystalline materials involves creating a vacancy island followed by retreat of the newly created step edges [147]. At the silica surface, Gratz and Bird [135] defined Q2 and Q3 sites as the two predominant types of sites available for reaction with water. Quartz shows different reactivities for Q3- and Q2-coordinated groups and corresponding differences in surface energies [147]. In the absence of electrolytes, rates are dominated by removing Q2 groups at preexisting step edges and dislocation defects. Q3 sites, however, are kinetically inaccessible because of the high activation barrier for removing this more highly coordinated surface species from a terrace [136]. The excess free-energy barrier to creating nuclei by removing Q3 groups from a quartz surface at homogeneous regions is higher than for Q3 groups coordinated with compositional defects. With electrolytes in solution, the energy barrier to detaching the less reactive Q3 groups is reduced. This results in a transition from dissolution at preexisting step edges and dislocation defects (detachment of Q2 groups) to

the homogeneous nucleation of vacancy islands across the entire surface (plucking of Q3 groups) [136]. This is a nucleated process because each vacancy island creates the equivalent of a new step edge on the surface and expands the perimeter of more reactive Q2 sites that increase surface energy [136]. For example, surface complexation models for quartz in  $Na^+$  solutions provide a fairly accurate picture of surface speciation. Only the silanol sites, where hydroxyl groups are bound to a silica atom, are thought to participate in adsorption/desorption reactions.  $Na^+$  should adsorb as a simple outer-sphere complex, Figure 4-9 [138]. The presence of  $Na^+$  thus enhances tendency of silica surfaces to develop a negative charge [151].

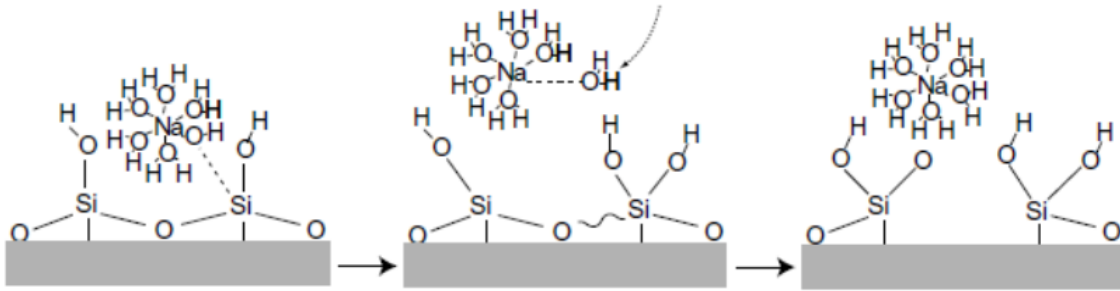


Figure 4-9. The  $-OH-$  ligand in a  $NaOH^0$  complex hydrolyzes the Si center [152].

Amorphous silica lacks the crystalline order that can be studied with classical terrace, ledge, and kink-based models of crystal growth and dissolution. Despite variations in  $Si-O-Si$  bond lengths and angles, all of these materials share the same fundamental chemical unit, silica tetrahedron. The surface groups of amorphous silica have Q2 and Q3 sites as in quartz. A similar picture to the quartz dissolution can be drawn for dissolution for amorphous silica assuming that Q3 and Q2 species are the reacting units [136]. The variability of  $Si-O-Si$  bond lengths and angles is apparent, Figure 4-5b. However, when the differently arranged groups (Figure 4-5b), of the Q2 and Q3 surface species in amorphous silica are compared to that of quartz (Figure 4-5a), the amorphous silica surface can be thought in a similar manner. Therefore, the disordered surface of amorphous silica can be visualized as a “rumpled” structure of differently coordinated  $Si$  surface groups without discrete terrace, ledge, or kink (Figure 4-10a) [136].

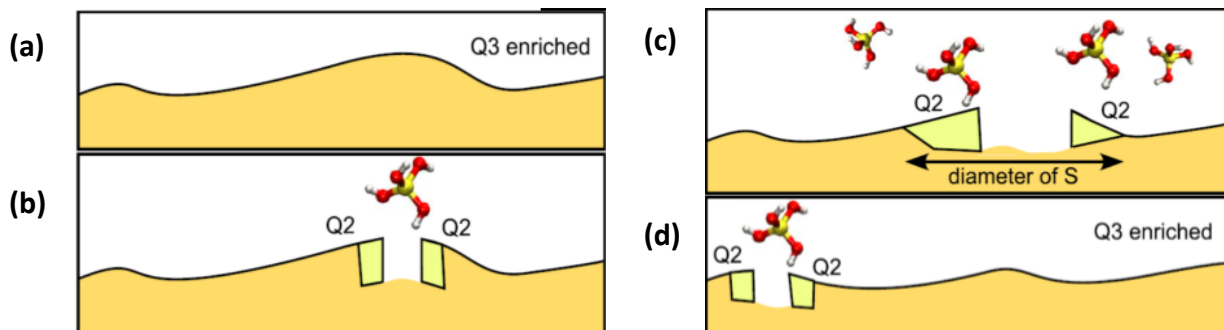


Figure 4-10. Illustration of amorphous silica dissolution by a simple rumpled structure concept. (a) After initial rapid dissolution of highly coordinated groups, a steady-state surface develops. (b) With each nucleated detachment of a highly coordinated Q3 species from the surface, a perimeter of higher-energy Q2 species is formed (Figure 4-5B). (c) Reactive Q2 groups retreat over area,  $S$ , until (d)

**the affected surface returns to the lower-energy Q3-rich surface and the process regenerates new reactive vacancies. Taken from Dove et al. [136].**

In a crystalline silica polymorph, strong bonds of the framework show a complete 3-D polymerization. This can be observed through  $^{29}\text{Si}$  magic angle spinning (MAS) NMR spectra with dominant Q4 peaks. The dissolution rate of aggregates in concrete containing such silicate minerals with very high concentration of Q4 groups is relatively low; and the dissolution occurs at time spans much longer than the engineered concrete's lifetime even in the presence of electrolytes [128]. This is not the case for concretes with aggregates containing disordered silica polymorphs such as opal. These have a less complete polymerization, with considerable amount of Q3 sites as shown in chapter 3. In this loose structure, reactions can move at a much faster pace making ASR a significant risk and engineering challenge.

### **4.1.2 Polymerization of silica and gelling**

Dissolved silica polymerize and form complexes depending on solution chemistry and age [1,138]. The soluble form of silica is a monomer orthosilicic acid with the formula  $\text{Si}(\text{OH})_4$ . It is a weak acid. In  $25^\circ\text{C}$  water, it is stable for long periods of time at levels below ca. 100ppm [153]. Once the concentration exceeds the solubility of the amorphous solid phase, at about 100-200 ppm, it undergoes auto-polycondensation reactions [153]. This oligomerization-polymerization-precipitation process of silicic acid has been extensively studied [68,154]. At ambient temperatures, the process begins with the condensation of monosilicic acid to form disilicic acid and continues with monomer addition to form trisilicic acid and tetrasilicic acid [138]. The oligomerization proceeds to minimize the abundance of uncondensed  $\text{Si}-\text{OH}$  bonds in favor of the more condensed  $\text{Si}-\text{O}-\text{Si}$  bonds [138]. After forming trimers, the molecules start to adopt ring structures (cyclize). Ring structures enable a more condensed oligomer than is afforded by a chain-like configuration [154,155]. Silica monomers and dimers ( $\text{H}_6\text{Si}_2\text{O}_7$ ) preferentially bond to these cyclic oligomers rather than forming higher-order linear oligomers [153]; and the condensed oligomers continue to grow through monomer or dimer addition.

In solutions between pH 2 to 7, the oligomer stabilizes when the diameter of the colloids reaches 2 to 3 nm, and these colloids may persist for long periods [138] until condensation reactions cause coalescence and precipitation from solution [154]. At higher pHs, the polymer growth (formation of silicate oligomeric silicate anions) proceeds via cyclic trimeric silicate polyanions which are more stable than linear silicate anions at this pH [156]. Also, at high pHs the silica surface has a high concentration of  $\equiv\text{Si}-\text{O}^-$  that the Coulomb repulsion between the aggregating clusters hinders the aggregation. As a result, the gelation time increases. Due to higher Coulomb repulsion inside the clusters, more open structures with lower fractal dimension are formed. The colloids grown in basic media can reach over 200nm.

When a sol system with precursor molecules in a solvent is gelled, it first becomes viscous, and then it develops rigidity. Thus, it fills the volume originally occupied by the sol. On the other hand, when a sol is coagulated or flocculated, a precipitate is formed. In a dilute system, the precipitate will settle out, but in a concentrated system the precipitate may be too voluminous to separate and will remain as a thixotropic mass. The difference between a sol, gel, and precipitate is illustrated in Figure 4-11 [68].

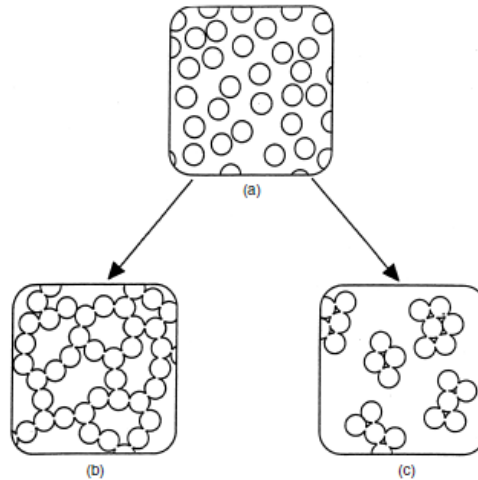


Figure 4-11. Silica gel versus precipitate: (a) sol, (b) gel, and (c) flocculation and precipitation. Taken from [138].

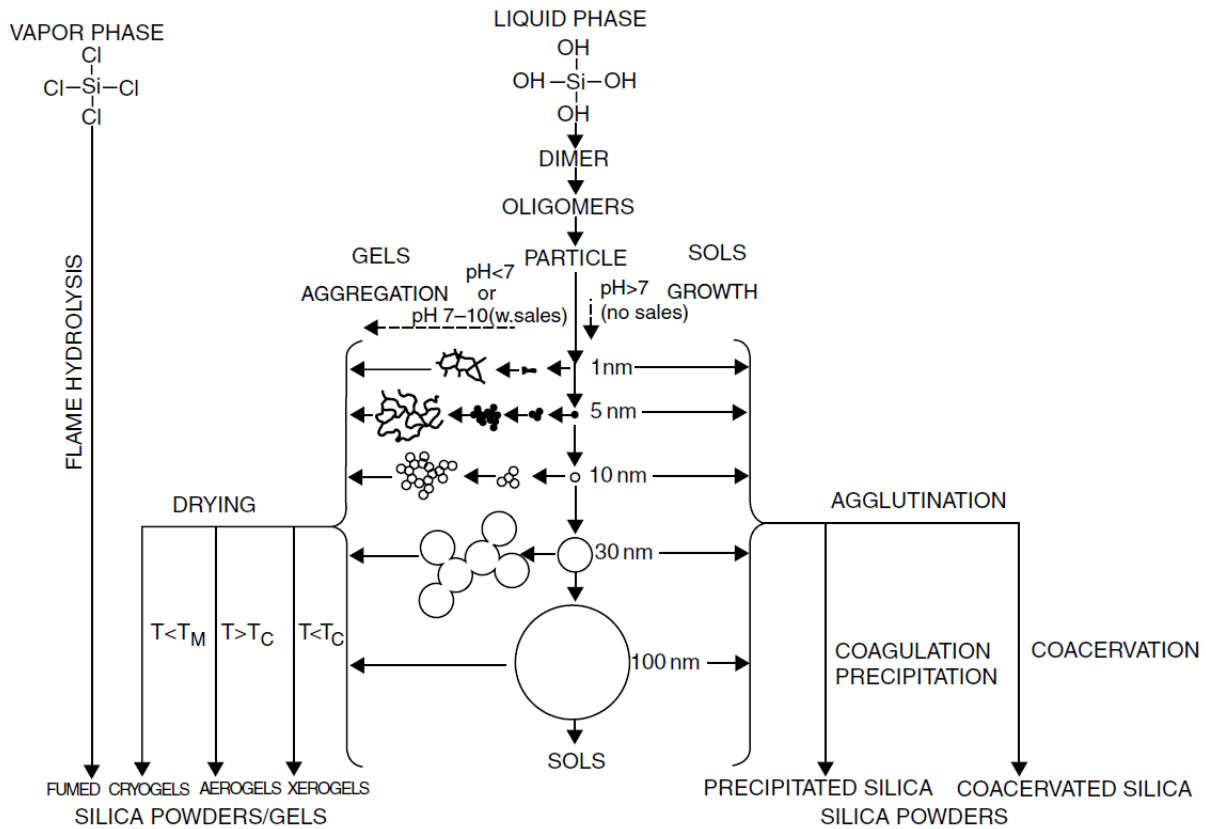


Figure 4-12. Formation of silica sols, gels, and powders by silica monomer condensation-polymerization followed by aggregation or agglutination and drying. Growth of nascent colloidal particles with a decrease in numbers occurs in basic solutions in the absence of salts (i.e., opal-A precipitation) [82]. In acid solutions or in basic solution with low salt concentration the colloidal silica

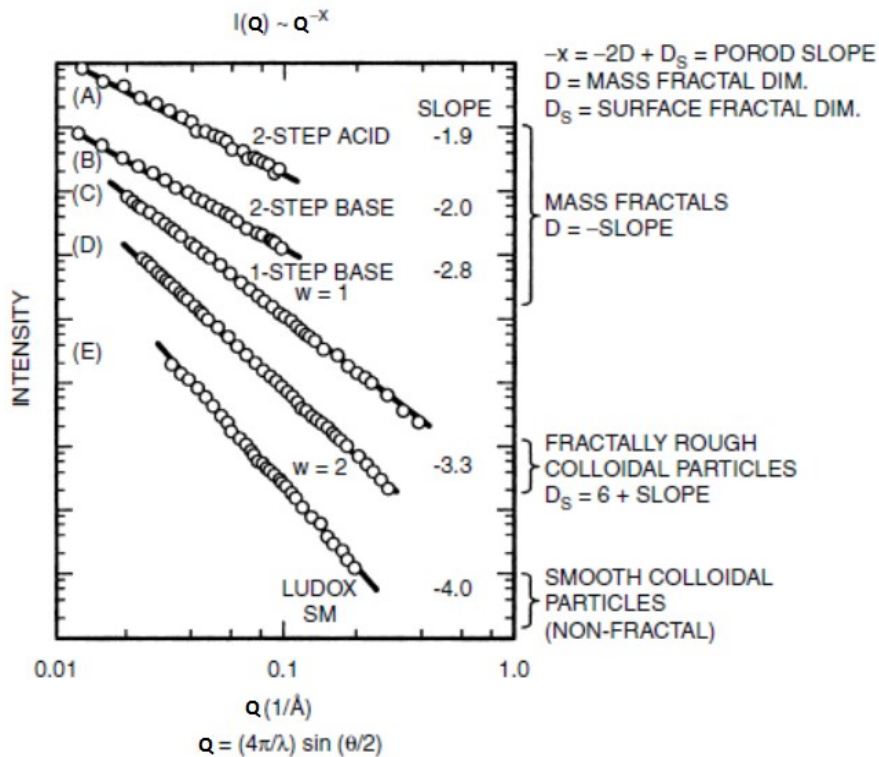


particles form gels by aggregation into three- dimensional networks (i.e. opal-CT precipitation). Taken from [68].

According to Iler [138], the way in which colloidal silica particles aggregate or link together can be described in the following manner [68]:

1. *Gelling*: The particles are linked together in branched chains that fill the whole volume of sol so that there is no increase in the concentration of silica in any macroscopic region in the medium. Instead, the overall medium becomes viscous and is then solidified by a coherent network of particles that, by capillary action, retains the liquid [68]. The synthesis variables that determine the texture of the gels are generally those affecting the balance between hydrolysis and condensation of the precursors, such as pH, water content, and dilution [157].
2. *Coagulation*: The particles come together into relatively close-packed clumps in which the silica is more concentrated than in the original sol so the coagulum settles as a relatively dense precipitate. A simple way to differentiate between a precipitate and a gel is that a precipitate encloses only part of the liquid from which it is formed [68].
3. *Flocculation*: The particles are linked together by bridges of the flocculating agent that are sufficiently long so that the aggregated structure remains open and voluminous. It is apparent that these differences will be observed mainly in dilute sols containing only a few percent of silica. In concentrated mixtures one can distinguish a gel, which is rigid, but not between a coagulate and a flocculate [68].
4. *Coacervation*: The silica particles are surrounded by an adsorbed layer of material that makes the particles less hydrophilic, but does not form bridges between particles. The particles aggregate as a concentrated liquid phase that is immiscible with the aqueous phase [68].

The distinction between particulate and polymeric silicate sols is also evident from small-angle scattering [57,158]. Figure 4-13 summarizes scattering data obtained from a commercial aqueous silicate to that obtained from a variety of silicate sols prepared from alkoxides [159]. This data can be effectively studied through the fractal approach. Fractals are disordered systems for which disorder can be described in terms of non-integral dimension. As described in chapter 2, the fractal dimension of an object of mass  $M$  and radius  $r$  is defined by the relation  $M \sim r^{D_f}$  where  $D_f$  is the mass fractal dimension of the object [68].  $D_f$  has many of the properties of a dimension, but is often fractional; hence, it is called fractal dimension [160]. For Euclidian (uniform, non-fractal) objects  $D_f$  equals to the dimension of space  $D$ . In 3-D, the mass  $M$  of a sphere scales as  $r^3$ ; thus  $D \propto r^3$ . For fractal objects,  $D_f$  is less than the dimension of space:  $D_f < 3$ .



**Figure 4-13. Log of scattered intensity vs. log of Q obtained by small-angle x-ray scattering (SAXS) for alkoxide-derived gels prepared under different hydrolysis conditions and a commercial aqueous silicate. Adopted from [159].**

Fractal geometry also describes surface fractals. The surface area  $S$  is related to the radius  $r$  by a fractional power  $S \propto r^{D_s}$  where  $D_s$  is called the surface fractal dimension.  $D_s$  is smaller than  $D$ , but larger than  $D - 1$  [68].  $D_s$  relates an object's area to its size. In 3-D,  $D_s$  varies from 2 for a smooth (non-fractal) surface to 3 for a fractal surface. So, it can also be used as a measure of roughness [160]. The power-law relationships implied by the data in Figure 4-13 can be interpreted on the basis of fractal geometry by  $I \sim Q^P$  where  $P = -2D + D_s$  where  $I$  is the intensity and  $P$  is the Porod slope [159]. Smooth, colloidal, uniform, non-fractal particles in the aqueous silicate sols have  $D = 3$  and  $D_s = 2$ ; hence give  $P = -4$ . The various alkoxide derived gels shown are either mass or surface fractals. Kinetic growth models illustrated in Figure 4-14 can be used to visualize these results.

Reaction-limited conditions imply that the condensation rate is sufficiently low with respect to the transport (diffusion) rate that the monomer or cluster can sample many potential growth sites before reacting at the most favorable one. Reaction-limited conditions are obtained for most silicate synthesis schemes [159]. In monomer-cluster aggregation (MCA), growth occurs by the addition of monomers to higher molecular weight species (clusters) rather than themselves; thus, MCA requires a continual source of monomers. Because growth occurs monomer-by-monomer under reaction-limited conditions, all potential growth sites are accessible; the result is compact, uniform (non-fractal) objects characterized by  $P=-4$ . The base-catalyzed condensation mechanism favors the reaction of low- and high-molecular weight

species; so the growth is biased toward MCA [159]. In cluster-cluster aggregation (CCA), monomers are depleted at an early stage of the growth process; hence further growth occurs by the addition of clusters to both monomers and other clusters. Strong mutual screening of cluster interiors leads to branched objects characterized by a mass fractal dimension  $D \approx 2$  ( $P \approx -2$ ) [155]. MCA and CCA are just two of many plausible growth models, and the predictions of  $P = -4$  and  $P = -2$  for these two aggregation processes are not unique [159].




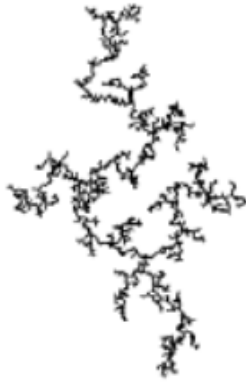
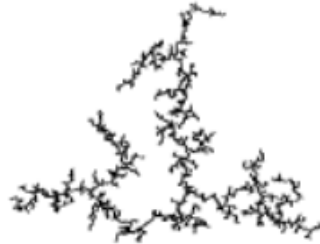
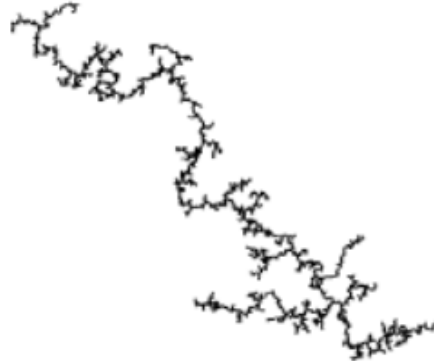
	Reaction-Limited	Ballistic	Diffusion-limited
Monomer-cluster	Eden	Vold	Witten-Sander
			
	D=3.00	D=3.00	D=2.50
Cluster-cluster	RLCA	Sutherland	DLCA
			
	D=2.09	D=1.95	D=1.80

Figure 4-14. Kinetic growth models in a 2-D embedding space. Common names for the models as well as the mass fractal dimension  $D$  of their 3-D analogs are given. Adopted from [158].

The physical and chemical changes that occur after gelation but before complete drying are referred to as aging [159]. During this process polymerization continues while syneresis (shrinkage of gel, and resulting expulsion of liquid from the pores) and coarsening might occur. The kinetics of syneresis depends on the driving force (polymerization), the mobility of the gel network, and the rate of fluid flow through the contracting network. Iler's view of aging is represented schematically in Figure 4-15a [138]. The higher solubility of surfaces with positive curvatures causes dissolution there and reprecipitation on interparticle contacts that have negative curvatures and lower solubilities. This coarsening process, driven by a reduction in the solid-liquid interfacial energy, builds necks between particles that significantly strengthen the

gel network [159]. As an example, an alkoxide-derived gel is aged under basic conditions, where coarsening is enhanced, causes reorganization of a mass fractal ( $D = 1.8$ ) into a surface fractal ( $D_s = 3$ ) accompanied by an increase in the solid–liquid interfacial area from about 900 to 1500  $\text{m}^2/\text{g}$  [159]. Although coarsening occurs under these conditions, apparently the dissolution–reprecipitation process creates a microporous “skin” at the solid–liquid interface that accounts for the unexpected increase in surface area [159].

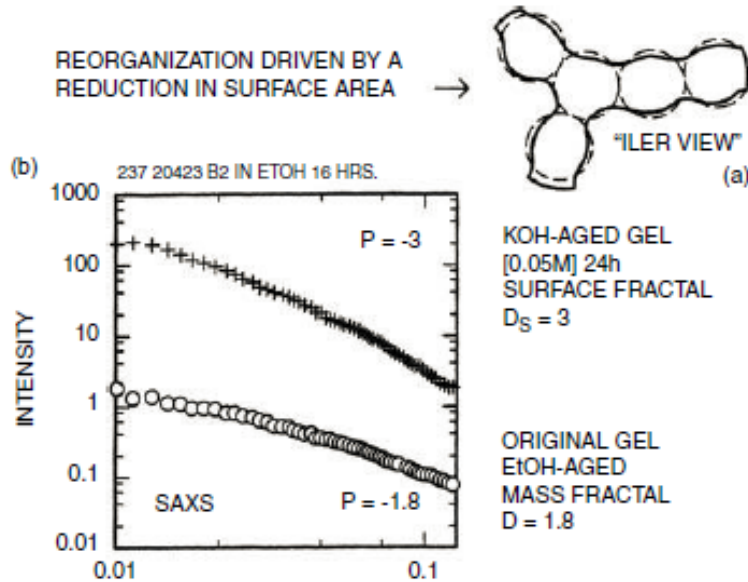
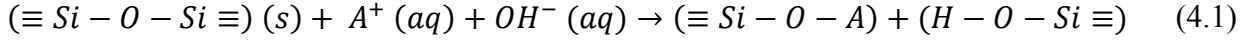


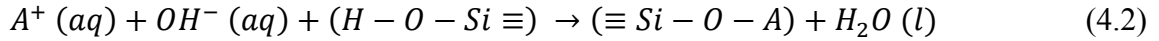
Figure 4-15. (a) Coarsened structure that results from aging a network of particles under conditions in which there is partial solubility of the condensed phase. Material is removed from surfaces with positive curvatures and deposited at interparticle contacts that have negative curvatures; “neck” formation results [138]. (b) Porod plots obtained by SAXS for an alkoxide-derived gel prepared at neutral pH in a 90% ethanol–10% water solvent (original gel EtOH-aged) and a similar gel aged for 24 h in 0.05 M KOH in ethanol (KOH-aged gel) [159].

### 4.1.3 Alkali silica reaction

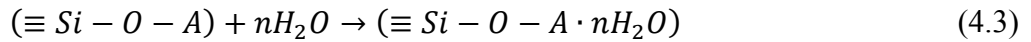
An ordinary portland cement has four main components tricalcium silicate ( $\text{C}_3\text{S}$ ), dicalcium silicate ( $\text{C}_2\text{S}$ ), tricalcium aluminate ( $\text{C}_3\text{A}$ ), and tetracalcium aluminoferrite ( $\text{C}_4\text{AF}$ ). When mixed with water, the portland cement hydrates and forms several hydration products; calcium silicate hydrate (C-S-H), calcium hydroxide (CH), and mono- and tri-sulfate hydrates. The portland cement hydration reactions in any ordinary concrete increase the alkali concentration and pH of the pore solution significantly. In this hyperalkaline environment (above ca. pH 12), ASR initiates topochemically at the interface of the reactive aggregate and the alkaline solution. The silica surface becomes negatively charged by  $\text{OH}^-$  attack. The cations are attracted to the sites of negative charge. The surface siloxane bridging bonds are ruptured via nucleophilic attack of  $\text{OH}^-$  to generate alkali silicates and silicic acids [126]. A simplified stoichiometrical representation of rupture of a siloxane bond into alkali silicate and silicic acid can be written as:



where  $A^+$  is the alkali cations  $Na^+$  and  $K^+$  dissolved in the concrete pore fluid. Even though “Na=K” is an oversimplification; and given equations still provide insight. The newly formed or existing surface silanols can also react with alkalis to form alkali silicates. A simplified stoichiometrical representation of a surface silanol reacting immediately with  $OH^-$  to form alkali-silicate is given below:



The exchange reaction replacing protons  $H^+$  in the silanol with  $A^+$  dissolved in the concrete pore solution is an acid-base reaction lowering the alkalinity of the system. The reaction products are water and an amorphous alkaline silica gel. The alkali cations, unlike the  $H^+$  proton, cannot enter into the electronic structure of the oxygen ion; thus they are more easily hydrated. The resultant oligomeric alkali silicate gel is highly hygroscopic - its volume is expanded by the hydration [161]. It immediately reacts with nearby water to generate hydrated alkali silicate gel [161]. Simplified stoichiometrical representation of this reaction can be written as:



where  $n$  denotes the hydration number of the silicate anion. The excess  $OH^-$  present in the pore fluid gradually breaks down the siloxane bridges in the formed alkali silica gel, reducing its integrity and opening up the structure for further imbibition of water and uptake of additional solute constituents [1]. The increase of alkali oxide concentration leads to continuous decrease of the intensity of the peak at six-membered rings and an increase of larger rings. These depolymerization and repolymerization reactions do not occur randomly. Silanol groups are hydrophilic and attract water, while siloxane bridging bonds are hydrophobic and repel water [162].

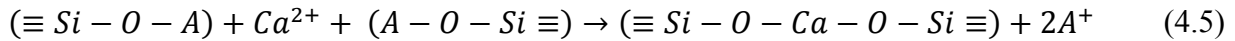
Concrete is a porous material, and the hygroscopic alkali silicate is rheologically a fluid material. As the formed alkali-silicate gel hydrates and expands, it slowly diffuses into the interfacial transition zone between the aggregate and the cement paste, nearby pores and preexisting cracks surrounding the aggregate to reduce its expansive pressure [161]. One of the most important properties governing the gel mobility is its viscosity. ASR gel shows a wide range of viscosities. At the initial stages of the gel formation, it is very viscous. Then, depending on alkali and water content its viscosity changes. In general, gels with higher alkali content are more fluid and more hydrated [163]; thus, a portion of the highly-hydrated, relatively fluid gel is extruded, and dissolved into the pore solution [164], whereas the less-hydrated, more solid alkali-silicate remains beneath [161].

Dissolved constituents ( $Ca^{2+}$ ,  $Al^{3+}$ , etc.) present in the concrete pore water may interact with the gel. In portland cement systems, calcium always plays an important role. A highly reactive silica gel in saturated calcium hydroxide solution (without alkalis) will form two products: silica gel with  $Ca:Si$  ratio ranging between 0.15 to 0.20, and  $C-S-H$  of  $Ca:Si$  ratio within 1.2 to 1.4 [165]. In dilute solutions containing both calcium and alkali hydroxide, the highly tractive silica gel dissolves, but it promptly precipitates as Ca-alkali-silicate hydrate [166].

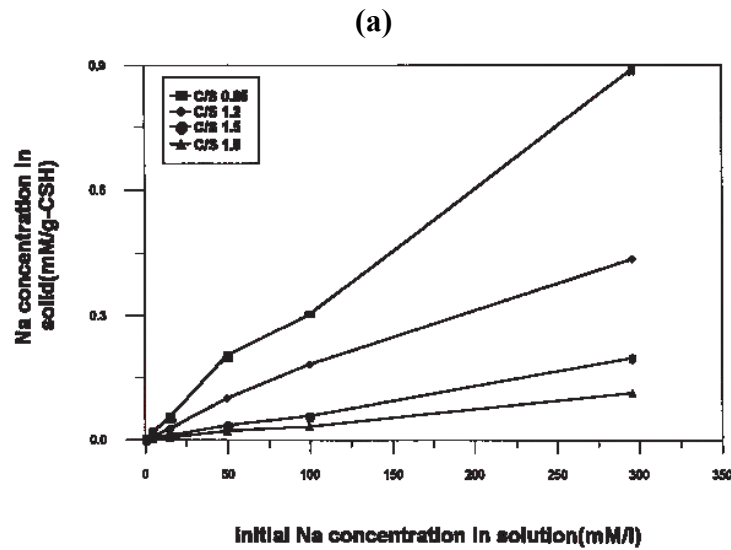
The concentration of  $Ca^{2+}$  ions is inversely proportional to the square of  $OH^-$  concentration:



Therefore, the decrease  $OH^-$  concentration through the consumption of  $OH^-$  ions due to disintegration of the reactive aggregate induce gradual dissolution of  $Ca^{2+}$  ions from  $Ca(OH)_2$  into the pore solution [161]. The highly-hydrated alkali-silicates at the surface of the particle or in the pore solution react with the available  $Ca^{2+}$  ions, and form a Ca-rich/alkali-poor  $C-A-S-H$  gel through a cross-linking reaction which converts two independent bonds to one bond [161,167]:



where the released alkali cations can further react with aggregate [164].  $C-A-S-H$  can be considered as  $C-S-H$  containing some alkali. The  $C-A-S-H$  gel contains certain amount of alkali ions; yet it has little swelling capacity, and it does not generate any expansive pressure if  $CaO$  constitutes 53% or more [167]. This can be explained by the shrinkage of the silicate by the release of alkali ions and hydration water during the  $Ca$ -rich gel formation [161,164], and by the much lower hygroscopicity of  $C-A-S-H$  gel compared to that of an alkali-silica gel. The highly-hydrated alkali-silica gel also may possibly interact with existing  $C-S-H$  to make a more polymerized (more  $Si$ -rich)  $C-S-H$ . As the  $Ca:Si$  ratio of the  $C-S-H$  decreases; its alkali binding capacity increases (Figure 4-16). The alkalis can be bound into  $C-S-H$  at acidic silanol sites [168].



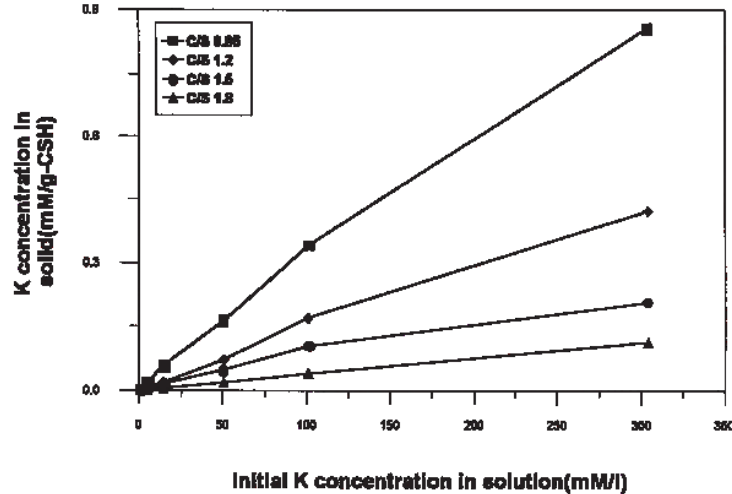


Figure 4-16. (a) Sodium and (b) potassium steady-state concentrations in solid *C-S-H* of varying *Ca:Si* ratios as a function of aqueous alkali concentration at 20°C [168].

The effect of aluminum is not of interest in this study; thus, it will not be discussed.

Up until this stage, the reaction sequence is very similar to the pozzolanic reaction of silica dominant mineral admixtures in terms of forming highly polymerized *C-S-H* by consuming reactive silica and  $Ca^{2+}$  [167]. However, in the same conditions, the pozzolanic reaction not only reduces the expansion of concrete due to ASR, but also improves the quality of concrete in the long term [19,169]. The main difference between a pozzolan and a reactive aggregate is their particle size. A pozzolan can be thought of as a finely ground reactive aggregate. High fineness, at least that of portland cement, is necessary for efficient pozzolanic reactions [169].

The *Ca*-rich alkali-silica gel formed is hard; yet allows penetration of the alkaline solution into the aggregate leading into continuation of alkali-silica gel formation on the reacted site [161]. Eventually, the  $Ca(OH)_2$  is depleted locally, and the available  $Ca^{2+}$  will be limited as it would be bound up in stable solid phases; thus, the rate of calcium availability is insufficient to convert all of the newly formed alkali-silicate gel into *Ca*-rich gel. Beneath the *Ca*-rich gel, closer to aggregate surface *Ca*-poor ASR gel will continue to form. However, even though the outer *Ca*-rich gel is semi-permeable, it does not allow diffusion of the newly formed inner *Ca*-poor ASR gel [170]. Hence, the *Ca*-poor gel is confined generating expansive pressure that can lead to cracking of the outer *Ca*-rich gel and the surrounding cement paste [171].

## 4.2 Scanning Electron Microscopy (SEM) Investigations

There are several studies on composition of the alkali-silica reaction gel [163,172,173]. These studies conclude that the ASR gel does not have a unique composition even throughout the same concrete sample. This section aims to provide the reader microscopic visualization of a damage sample. For that reason, we have chosen to study two ASR damaged concrete samples



from Brazilian dams using a Zeiss EVO SEM equipped with an EDAX EDS detector located at McCone Hall, Berkeley. The EDS capability of the microscope allowed us to get compositional information.

#### 4.2.1 ASR damaged concrete samples

We have received ASR damaged concrete samples (by courtesy of Professor Haroldo de Mayo Bernardes) from water intake of the Jaguari Hydroelectric Power Plant; and also from Paulo Afonso IV.

The Jaguari Hydroelectric Power Plant (Figure 4-17a), located on the Jaguari River between the cities of Jacareí and São José dos Campos (at São Paulo state, Brazil) has been operating since 1972 and has installed capacity of 27.6 MW in two generating units. The power plant reservoir has an area of 56 km<sup>2</sup> and its main purpose is to control the flow of Rio Paraíba do Sul. Companhia Energetica de Sao Paulo (CESP) is responsible for managing the Jaguari Dam and its hydroelectric power plant. According to data provided by technicians who worked at the time of construction of the plant, the distribution of the aggregates was 60% for coarse aggregate and 40% for the fine aggregate; the cement content was 320kg/m<sup>3</sup>; and the cement:aggregate ratio was 1:6-7 [174]. More detailed information on the macroscopic scale damage on concrete samples from Jaguari Dam can be found in [174]. The Paulo Afonso Hydroelectric Complex (Complexo Hidrelétrico de Paulo Afonso), also known as the Paulo Afonso Complex, is a system of three dams and five hydroelectric power plants on the São Francisco River near the city of Paulo Afonso in Bahia, Brazil. The complex exploits an 80 m natural gap on the river, known as the Paulo Afonso Falls. Constructed in succession between 1948 and 1979, the dams support the Paulo Afonso I, II, III, IV and Apollonius Sales (Moxotó) power plants which contain a total of 23 generators with an installed capacity of 4279.6 MW. The Paulo Afonso Dam IV (Figure 4-17b) located 2 km southwest of the falls is 35 m high and 7430 m long. The dam is an earth and rock-fill type but contains 1053 m in length of concrete structures which include the power plant's intake and the spillway. The concrete structures are undergoing a process of expansive reaction. The first effects were noted in 1985, when cracks appeared in thin structures such as walls and slabs. Some related mechanical problems were also observed, including inclination of the turbine generator axle, tilting of the turbine top, variations in the tolerance space between the paddles and deformation of the turbine case.





**Figure 4-17. General views of (a) Jaguari Hydroelectric Power Plant, (b) Paulo Afonso Hydroelectric Power Plant.**

The sample preparation is straightforward. First, polished thin sections of the ASR damaged concrete samples were prepared. Then, thin sections were coated with a 20 nm-thick carbon coat by using a vacuum evaporator at pressures less than  $10^{-4}$  torr. The carbon coat was necessary to prevent charging during measurements. The thickness of the coat was determined by using brass pieces as indicators. Brass changes color from orange (15 nm) to indigo red (20 nm) to blue (25 nm) and then to bluish green (30 nm) with increasing coating thickness. Due to carbon's low atomic number, it has a minimal effect on the X-ray spectrum, either in terms of producing X-ray lines or absorbing X-rays; thus, it is a good coating choice for this study as we are also interested in the elemental composition. However, some charging still occurred during the measurements; and the fuzzy white sections within the aggregates are artifacts of the measurement.

### **4.2.2 Results and discussions**

Backscattered electron (BSE) images of the polished thin sections allow different phases to be identified. Phases with greater average atomic number appear brighter. Phases with lower average atomic number appear darker. Concrete is an isotropic material. Thus, we can estimate that the 2-D images represent the bulk material. Cracks through the aggregate particles, some of which filled with the reaction gel, are a typical symptom of ASR.

The first sample is a test sample from Jaguari Dam. Figure 4-18 shows BSE micrograph of area with ASR damaged aggregates showing the extent of the reaction. There is significant amount of ASR gel formation, and the cracks going through the fine aggregates ① and ② are completely filled with the ASR gel.

Table 4-1 summarizes the elemental compositions obtained by EDS of the selected areas in Figure 4-18. The aggregate is almost pure  $SiO_2$  with very small amount of  $Na$  and  $Al$ . The ASR gel is also rich in  $Si$  and  $O$ , but it also has a higher  $K$  and  $Ca$  content when compared to the aggregate. The gels exposed to the cement matrix (G6-G8) have higher  $Ca$  content, when compared to the gels filling up the cracks within the aggregate (G1-G5).

The elemental maps in Figure 4-19 show the progression of the deleterious ASR more clearly. There are four identifiable phases: the aggregate, the ASR gel, the cement matrix, and the ettringite. The  $Si$  and  $O$  rich aggregates that are very poor in other elements are easily identifiable. The formed ASR gel is also rich in  $Si$ , but also rich in alkalis, specifically  $K$ ; therefore, the gel formations can be clearly identified from the  $K$  map. The cement matrix is much richer in  $Ca$  when compared to other phases. The Sulphur  $S$  rich areas indicate the voids filled with ettringite.

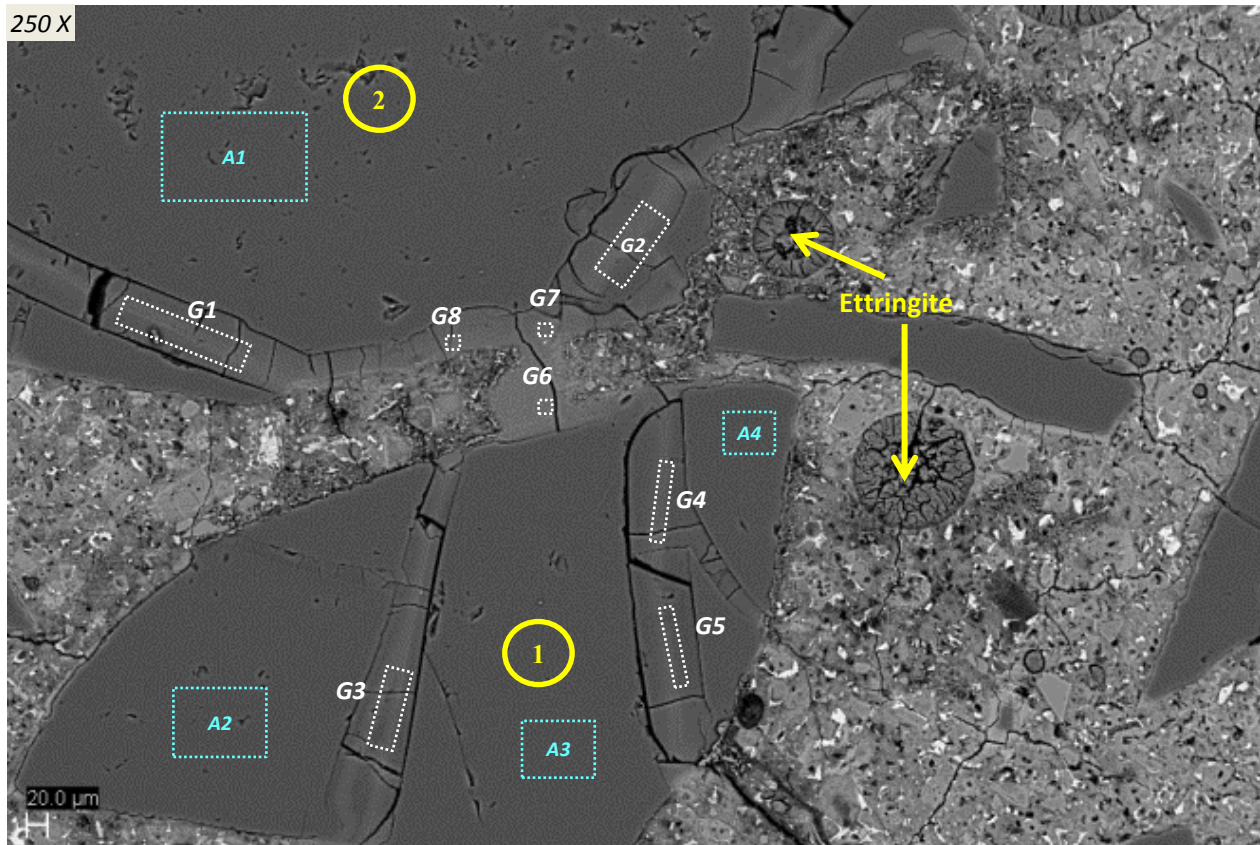


Figure 4-18. BSE micrograph of the polished thin section of the concrete test sample from water intake of Jaguari Power Plant. The fine aggregates ① and ② are significantly damaged due to ASR. The ASR gel formations can be visually identified. There are shrinkage cracks on the gel from pre-preparation exsiccation. A1-A4 (blue) and G1-G8 (white) indicate the areas where elemental compositions are collected for the fine aggregate and ASR gel respectively.

Table 4-1. Elemental compositions of selected areas on Figure 4-18a, mol %.

Aggregate	A1	A2	A3	A4	Average
<b>O</b>	59.8	59.4	59.6	58.2	59.3
<b>Na</b>	2.7	2.9	2.7	3.0	2.8
<b>Al</b>	1.5	1.6	1.4	1.6	1.5
<b>Si</b>	35.9	36.1	36.3	37.2	36.4
<b>Sum</b>	100.0	100.0	100.0	100	100.0

Gel	G1	G2	G3	G4	G5	G6	G7	G8	Average
<b>O</b>	49.8	54.3	51.6	56.0	57.3	53.1	55.2	49.8	53.8
<b>Na</b>	2.2	4.2	4.7	2.1	2.2	2.9	1.1	2.2	2.4
<b>Mg</b>	0.0	0.0	0.8	0.8	0.0	0.0	1.2	0.0	0.5
<b>Al</b>	3.0	3.0	2.7	2.7	2.3	2.3	8.2	3.0	4.5
<b>Si</b>	30.1	21.7	23.6	24.6	24.6	22.5	24.2	30.1	24.2

<b>K</b>	3.9	4.0	5.1	4.1	4.2	4.5	3.6	3.9	4.3
<b>Ca</b>	10.3	12.0	10.2	8.8	8.3	13.5	4.3	10.3	8.9
<b>Fe</b>	0.6	0.8	1.2	0.8	1.0	1.3	2.0	0.6	1.3
<b>Sum</b>	100.0	100.0	100.0	100.0	100.0	100.0	100.0	100.0	100.0
<b>(Na+K):Si</b>	0.35	0.36	0.33	0.38	0.36	0.20	0.25	0.23	0.31
<b>Ca:Si</b>	0.07	0.12	0.09	0.08	0.08	0.42	0.17	0.27	0.16
<b>(Na+K):(Si+Al)</b>	0.33	0.33	0.31	0.35	0.34	0.19	0.24	0.22	0.29
<b>Ca:(Si+Al)</b>	0.07	0.11	0.09	0.08	0.07	0.41	0.16	0.26	0.16

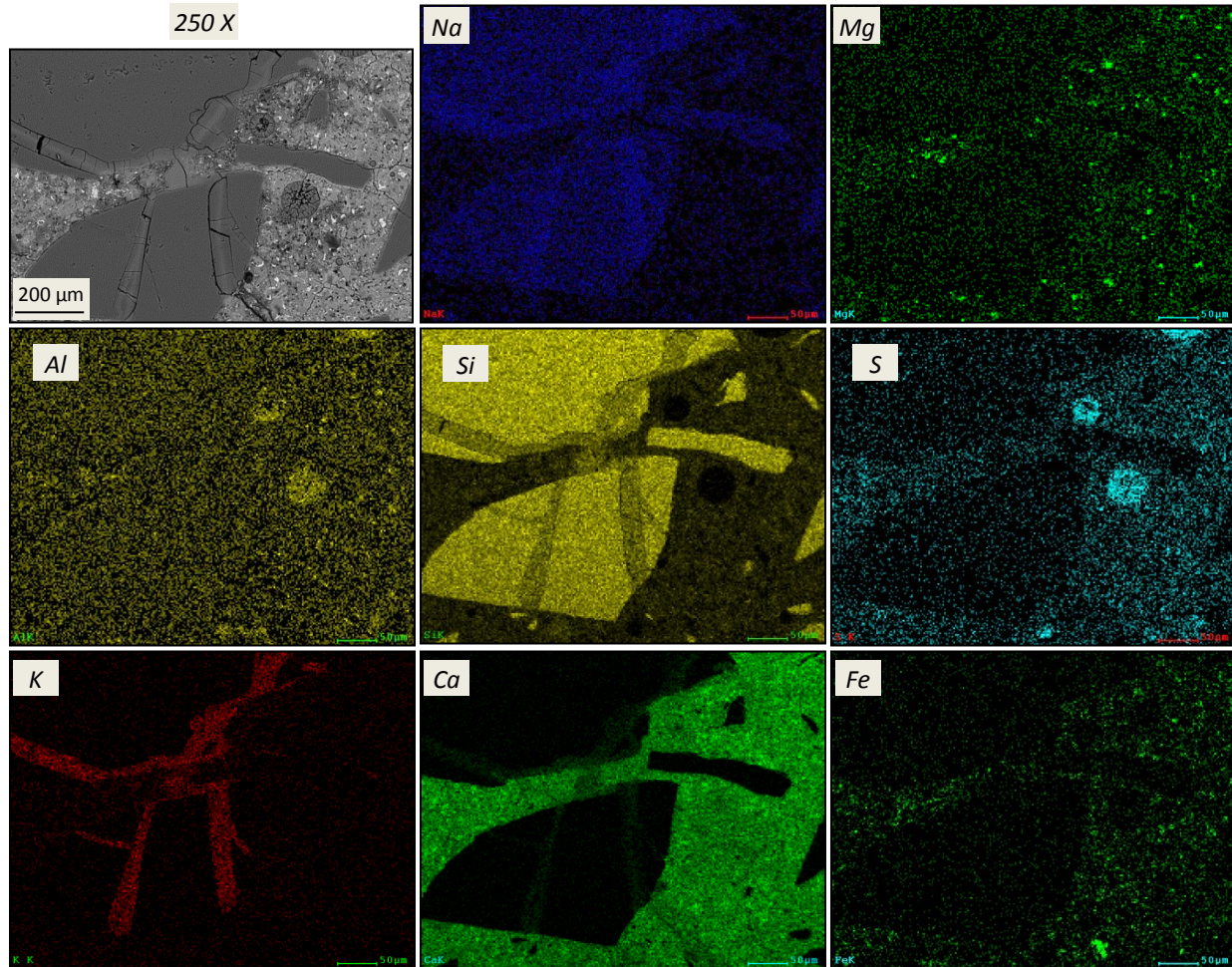


Figure 4-19. The Na, Mg, Al, Si, S, K, Ca and Fe elemental maps the Jaguari Dam sample corresponding to areas shown in Figure 4-18 (250 X). Significant ASR gel formation can be observed. The inner gel is incorporates less alkalis when compared to the gel extruded into the cement paste.

ASR often coexists with delayed (due to higher temperatures during initial hydration) or additional (due to internal sulfate sources) ettringite formation. ASR promotes delayed ettringite formation (DEF) by decreasing the pH of the system. The primary ettringite formation during the initial stages of portland cement hydration is necessary for the stiffening of the system. However, in a hardened concrete, DEF can be deleterious. DEF related damage was first observed in heat



treated, precast concretes to weathering with frequent wetting. Yet, this is not a must and DEF can also be observed in concrete structures with no heat treatment. There is an on-going discussion on the primary cause of the damage: the expansion due to ettringite formation; or high heat treatment temperatures and shrinkage. Ettringite filling the air voids, and partially surrounding the aggregate can be an indication of DEF. BSE micrograph on a second area on the Jaguari thin section shows high possibility of DEF, Figure 4-20.

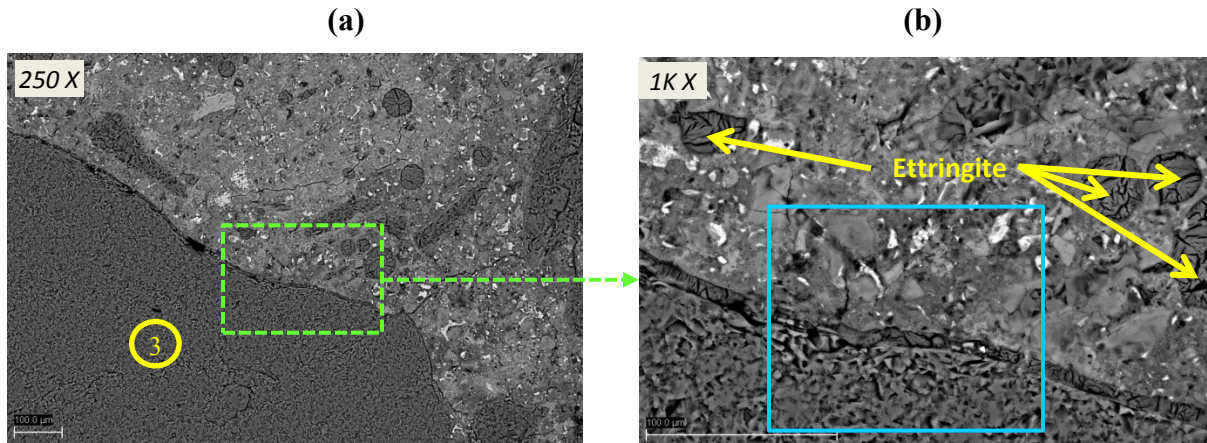
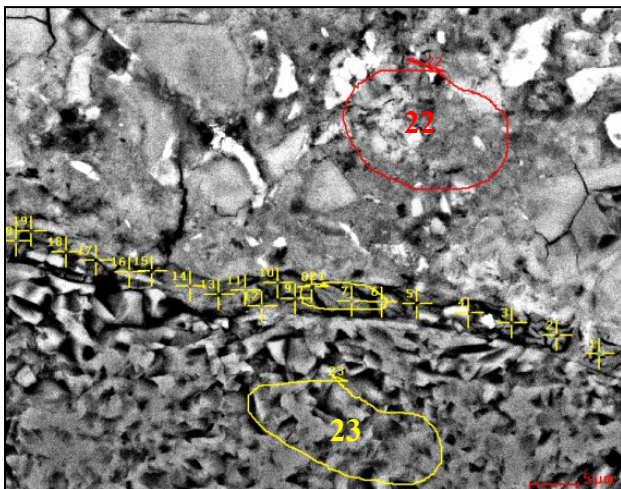


Figure 4-20. BSE micrographs of the polished thin section of the concrete test sample from water intake of Jaguari Power Plant focusing on an area affected by DEF at various magnifications (a) 250 X, (b) 1000 X. Significant amount of ettringite in the air voids and in the cracks along the cement matrix - coarse aggregate ③ contact can be observed. The blue box shows the area where EDS measurements shown in Table 4-2 are collected.

Table 4-2 summarizes the average elemental compositions collected on the yellow marked area shown in Figure 4-20. The aggregate is pure  $\text{SiO}_2$  (area 23). The ettringite formation surrounding (spots 1-21) the aggregate is rich in Ca, S, and Al.

Table 4-2. Average elemental compositions of the DEF, aggregate and the cement matrix of the selected areas, mol %.



	1-21	22	23
		<i>Cement</i>	
	<i>Ettringite</i>	<i>Matrix</i>	<i>SiO<sub>2</sub></i>
<b>O</b>	56.2	60.4	60
<b>Al</b>	5.7	1.66	0.4
<b>Si</b>	7.11	9.9	40
<b>S</b>	3.53	0.71	0.2
<b>Ca</b>	27.5	27.3	0.1
<b>Sum</b>	100.0	100.0	100.0

The elemental maps in Figure 4-21 show the progression of DEF clearly. There are three main phases: the aggregate, the cement matrix and the ettringite. The aggregate is rich in Si and O, but poor in other elements. The matrix is rich in Ca. The ettringite surrounding the aggregates and filling the voids is identifiable by richer S and Al content.

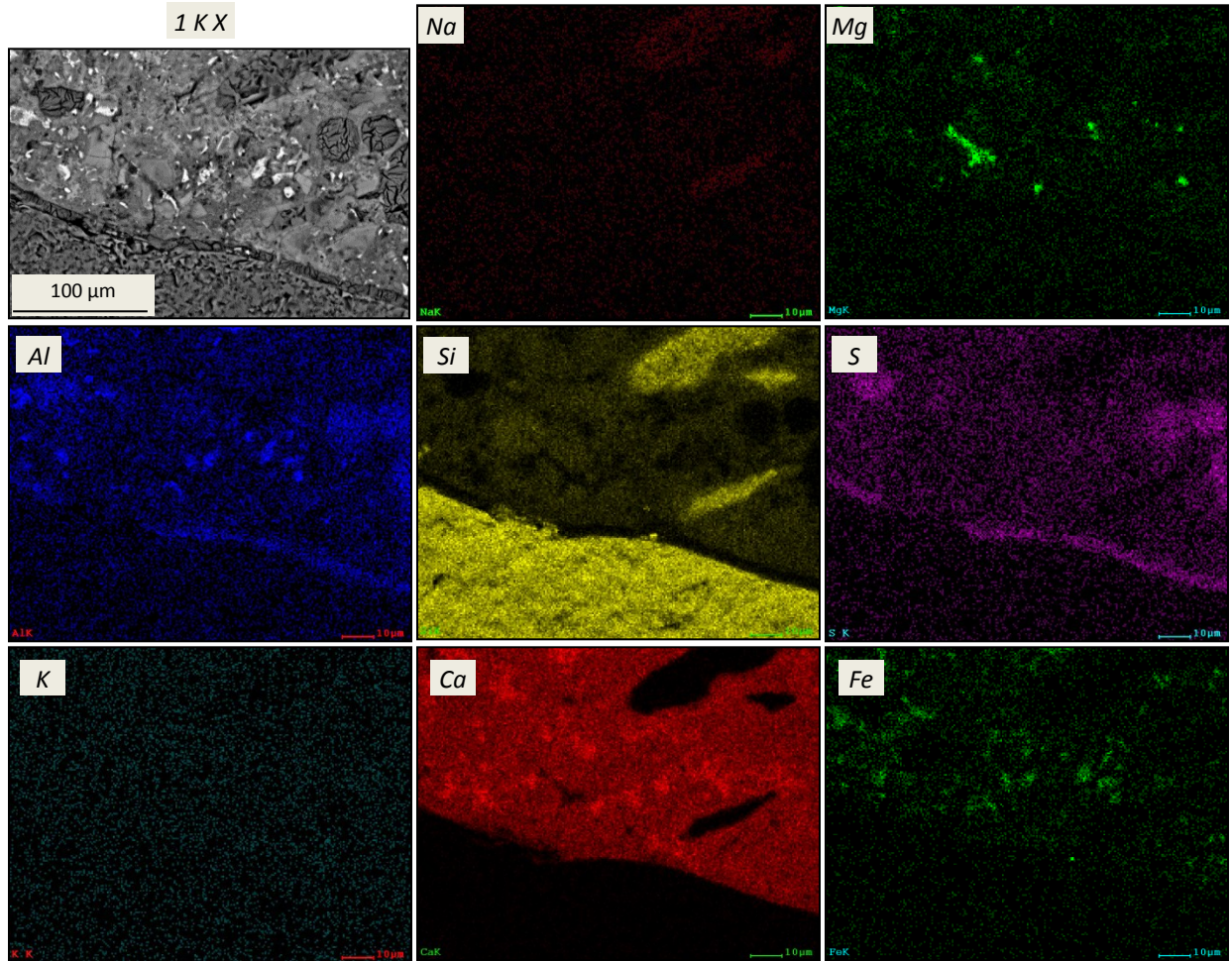


Figure 4-21. The Na, Mg, Al, Si, S, K, Ca and Fe elemental maps the Jaguari Dam sample corresponding to areas shown in Figure 4-20 (1K X): Ettringite in the air voids and in the cracks along the contact between cement matrix and the coarse aggregate identified by S.

The second concrete sample is from Paulo Afonso IV. It contains feldspars as coarse aggregates. Figure 4-22 shows BSE micrographs of the sample at various magnifications. The ASR gel formation going through the coarse aggregate forms cracks going through the aggregate.

(a)

(b)



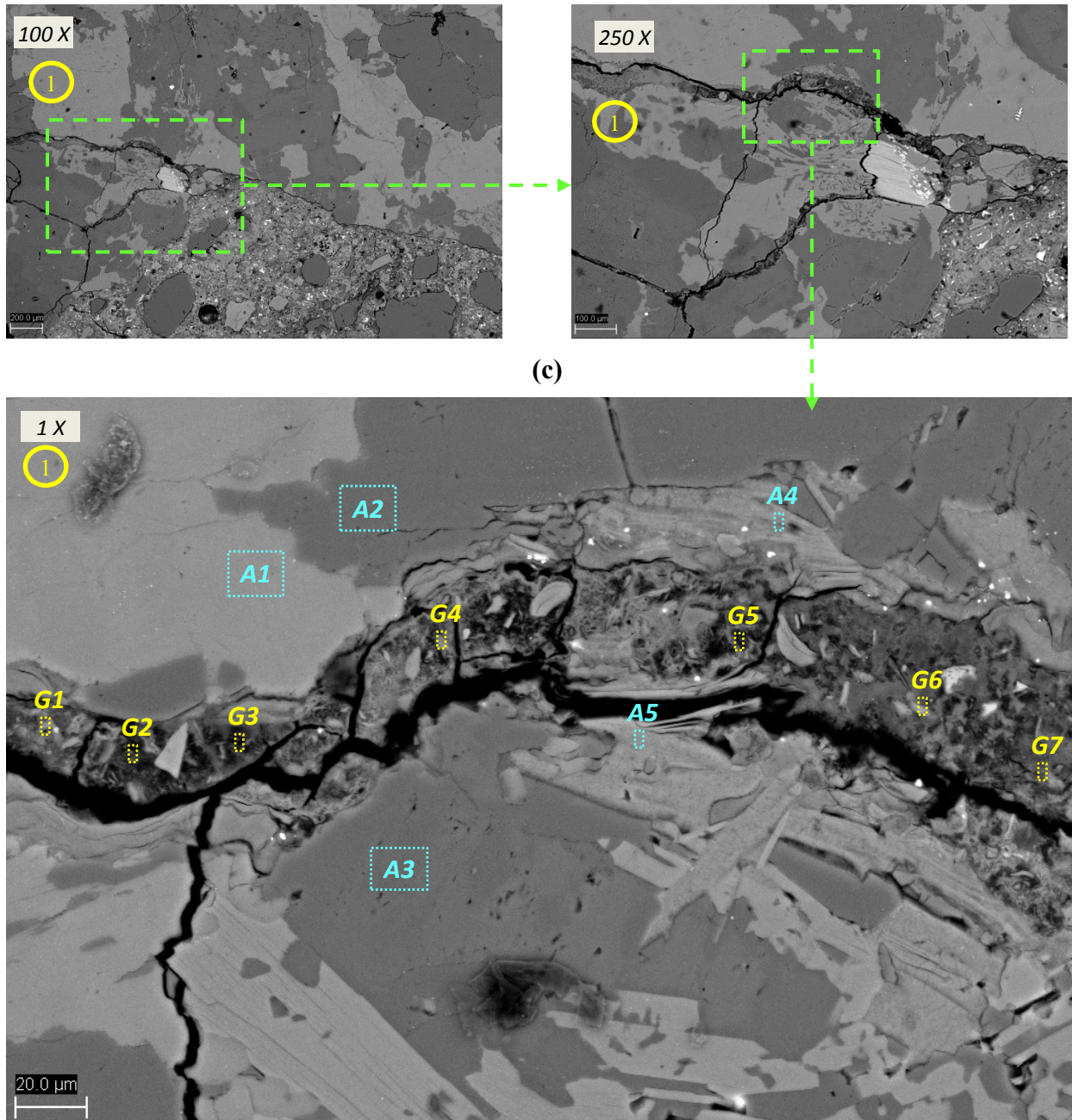


Figure 4-22. BSE micrographs at various magnifications from Paulo Afonso IV sample, possible ASR gel formation through the coarse feldspar ①: (a) at 100 X, (b) at 250X, and (c) 1000 X. A1-A5 (blue) and G1-G7 (yellow) indicate the areas where elemental compositions are collected for the fine aggregate and ASR gel respectively.

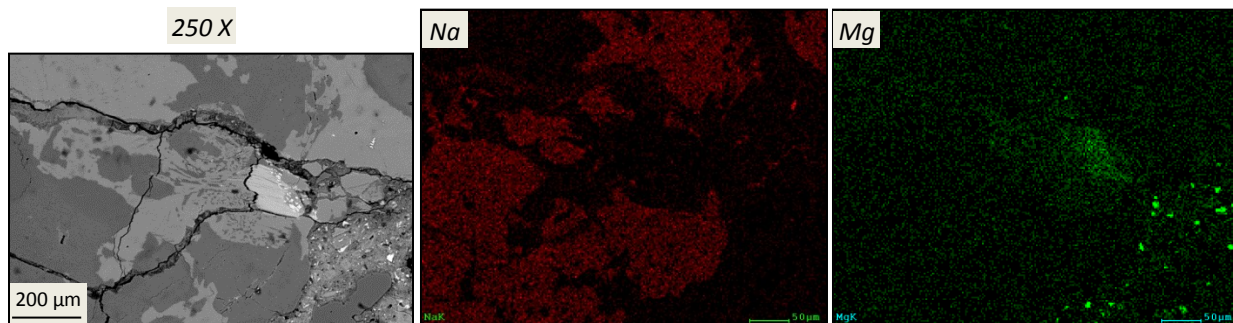
Table 4-3 summarizes the elemental compositions of the selected areas in Figure 4-22. The aggregates are mainly composed of Al, Si and either K or Na. The gel is rich in Si and alkalis; but also incorporates some Ca.

Table 4-3. Elemental compositions of selected areas on Figure 4-22, mol %.

<b>Aggregate</b>	<i>A1</i>	<i>A2</i>	<i>A3</i>	<i>A4</i>	<i>A5</i>
<b>O</b>	49.4	53.2	53.4	52.6	53.1
<b>Na</b>	0.0	7.5	7.6	0.0	0.0
<b>Mg</b>	0.0	0.0	0.0	1.3	1.3
<b>Al</b>	9.9	10.2	10.0	13.7	11.8
<b>Si</b>	30.5	28.5	28.2	23.1	22.3
<b>K</b>	10.2	0.0	0.0	6.3	4.9
<b>Ca</b>	0.0	0.6	0.8	0.9	3.6
<b>Fe</b>	0.0	0.0	0.0	2.1	3.0
<b>Sum</b>	100.0	100.0	100.0	100.0	100.0
<b>Na:Al</b>	-	0.73	0.76	-	-
<b>K:Al</b>	1.02	-	-	0.46	0.41
<b>Si:Al</b>	3.07	2.79	2.81	1.69	1.90
<b>Ca:Al</b>	-	0.06	0.08	0.07	0.31

<b>Gel</b>	<i>G1</i>	<i>G2</i>	<i>G3</i>	<i>G4</i>	<i>G5</i>	<i>G6</i>	<i>G7</i>	<b>Average</b>
<b>O</b>	49.8	54.3	51.6	56.0	57.3	53.1	55.2	52.1
<b>Na</b>	2.2	4.2	4.7	2.1	2.2	2.9	1.1	3.8
<b>Mg</b>	0.0	0.0	0.8	0.8	0.0	0.0	1.2	0.3
<b>Al</b>	3.0	3.0	2.7	2.7	2.3	2.3	8.2	11.0
<b>Si</b>	30.1	21.7	23.6	24.6	24.6	22.5	24.2	27.6
<b>K</b>	3.9	4.0	5.1	4.1	4.2	4.5	3.6	4.1
<b>Ca</b>	10.3	12.0	10.2	8.8	8.3	13.5	4.3	0.6
<b>Fe</b>	0.6	0.8	1.2	0.8	1.0	1.3	2.0	0.5
<b>Sum</b>	100.0	100.0	100.0	100	100.0	100.0	100.0	100.0
<b>(Na+K):Si</b>	0.20	0.38	0.41	0.25	0.26	0.33	0.20	0.29
<b>Ca:Si</b>	0.34	0.55	0.43	0.36	0.34	0.60	0.18	0.02
<b>(Na+K):(Si+Al)</b>	0.19	0.33	0.37	0.23	0.24	0.30	0.15	0.20
<b>Ca:(Si+Al)</b>	0.31	0.49	0.39	0.32	0.31	0.54	0.13	0.01

The elemental maps in Figure 4-23 show the ASR damage on the feldspar more clearly. The coarse aggregate can be identified by high Al, and low S content. The crack going through the aggregate filled with gel is easily identifiable from the Al map, due to gels low Al content. The Ca map also is interesting. The aggregate is poor in Ca, whereas the cement matrix is rich in Ca; and the gel has some Ca.



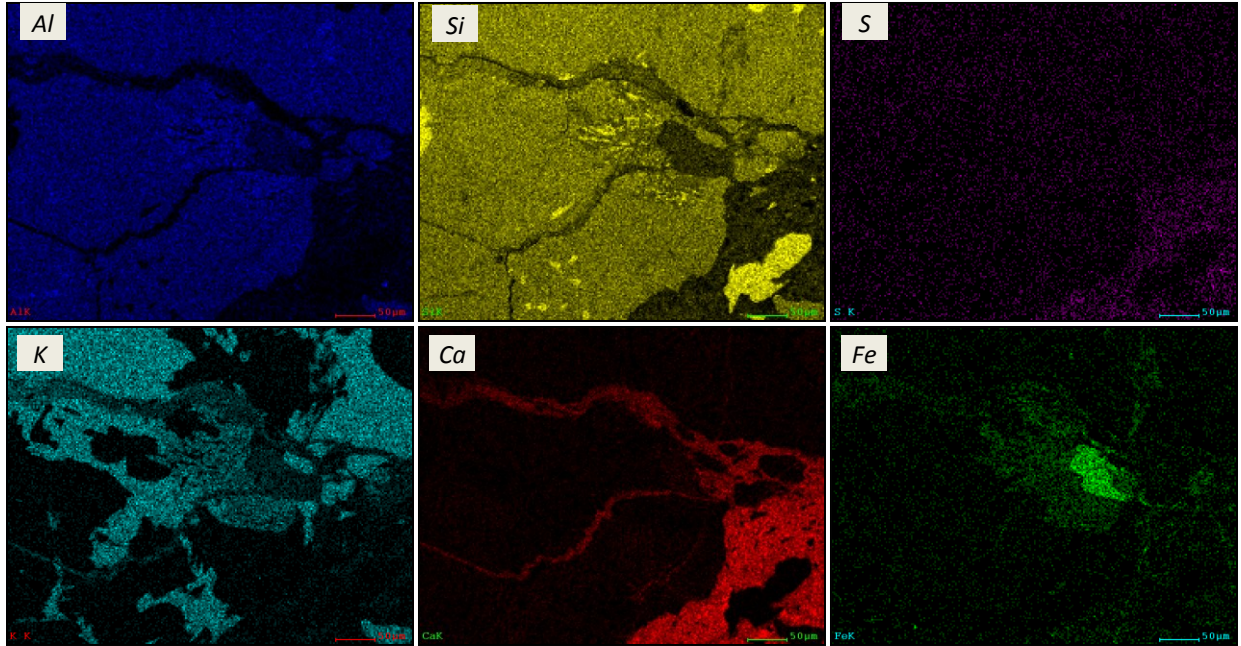


Figure 4-23. The Na, Mg, Al, Si, S, K, Ca and Fe elemental maps the Paulo Afonso Dam sample corresponding to area shown in Figure 4-22 (250 X).

Collected gel compositions are summarized in Figure 4-24.

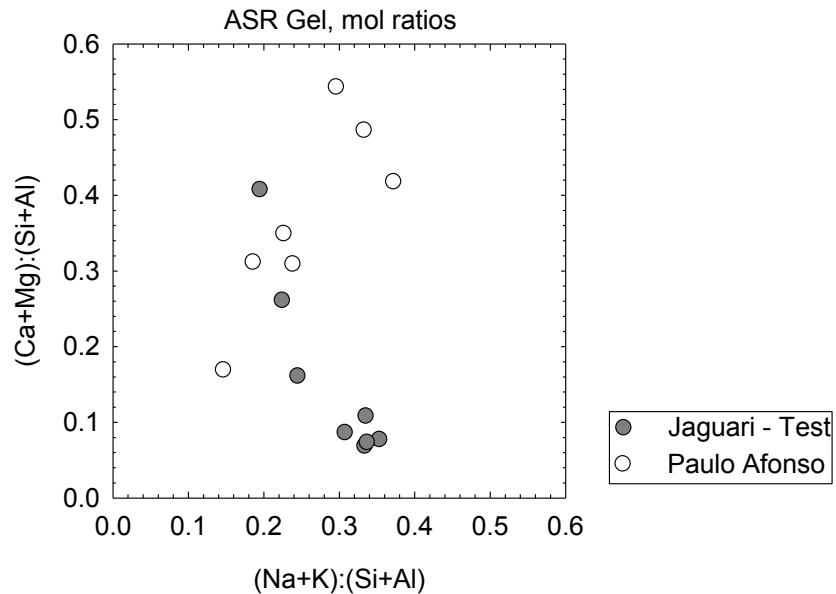


Figure 4-24. Summary of ASR gel compositions collected from the damaged samples, molar ratios of (Ca+Mg):(Si+Al) versus (Na+K):(Si+Al).

As seen, there is a wide range of compositions. The (Na+K):(Si+Al) molar ratios of the gels range between 0.15 to 0.37; while the (Ca+Mg):(Si+Al) ratios vary between 0.07 to 0.54. The used cement and aggregate compositions are of the major factors affecting the gel



composition. The age of the gel and the location of it within a sample also effect the gel composition. Considering the samples are more than 40 years old, the formed gels are possibly highly aged.

## **4.3 Conclusions**

Alkali silica reaction (ASR) is a deleterious interaction within concrete resulting in dissolution of the reactive silica portion of aggregates, and formation of a very hygroscopic amorphous gel. When confined in a matrix, this gel can generate high mechanical stresses, eventually leading to cracking. At advanced stages, it may cause loss of structural integrity. This chapter has two major goals. The first goal is to provide an understanding of the reaction mechanisms. This has been done by going step by step: the dissolution of silica, polymerization of silica, and the alkali-silica reaction. The second goal of this chapter is to provide examples of ASR damaged concrete samples to allow the reader to visualize the damage.

# 5

## Alkali Silica Reaction Gel

Alkali-silica reaction (ASR), as discussed in chapter 4, is one of the significant deterioration mechanisms in modern concrete. Even though known for decades, there is a lack of a firm understanding at molecular and nanometer scales of the reaction product (a highly hygroscopic gel) and of its expansion when exposed to moisture. This hinders development of novel mitigation techniques that are cheap and effective. A deeper understanding at those scales will give scientists and engineers a significant advantage in their battle. This chapter starts with reviewing the existing experimental results on gels synthesized in the laboratory and field gels collected from Furnas Dam (ASR<sub>F</sub>), Brazil at the molecular- and nanometer-scale. After that, the experimental findings of this study on the field ASR gels from Furnas Dam, and Moxoto Dam are summarized in section 5.2. The Moxoto Dam gel (ASR<sub>M</sub>) has not been studied prior to this research. The experimental findings confirmed some of the previous findings (NMR and IR) on ASR<sub>F</sub>; while providing new information on ASR<sub>M</sub>. The gels were also studied by total scattering and small angle scattering.

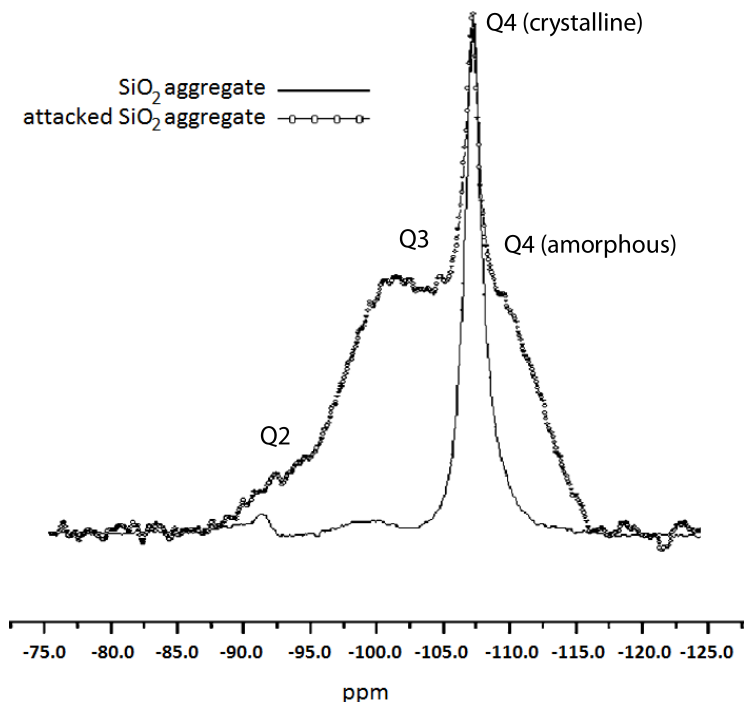
### 5.1 Previous experimental literature on alkali-silica reaction at molecular and nanometer scale

This section provides a state-of-the-art review on the experimental findings on alkali-silica reaction gel at molecular and nanometer scale. As discussed in chapter 4, a long initiation period is required for the field ASR gels to form. Therefore, many researchers worked on samples with accelerated ASR in the laboratory.

#### 5.1.1.1 Nuclear Magnetic Resonance (NMR) Spectroscopy

NMR has been used to follow ASR of a reactive aggregate, and also to characterize the final product. A study on flint, a hard, sedimentary cryptocrystalline form of the mineral quartz, provides changes on the <sup>29</sup>Si NMR spectrum before and after ASR attack (Figure 5-1 [130,175]) Before ASR, three tetrahedral environments can be distinguished in the flint spectrum: (1) the main, sharp peak located at -107 ppm is related to crystalline Q4 sites; (2-3) the other (much smaller) peaks are attributed to Q3 and Q2 sites. Flint is a very reactive aggregate when ASR is considered. After ASR, a significant increase on the intensity of Q3 peak is observed. In addition

to this, a new peak located at -110 ppm is formed attributed to amorphous Q4 sites; and might be explained by deformation/relaxation of the direct neighborhoods of Q4 sites [130].



**Figure 5-1.**  $^{29}\text{Si}$  MAS NMR spectra of a flint before and after ASR attack. After the attack a dramatic increase in Q3 sites and a new formation of amorphous Q4 sites is observed. Taken from [175]. But references above point to 1

Another study using time resolved  $^{29}\text{Si}$  MAS NMR [176] interprets ASR on amorphous silica. Figure 5-2 shows spectra of the amorphous silica after 6, 30 and 168 hrs of reaction. The dashed lines are attributed to Q4 (-110 ppm), Q3 (-101 ppm) and Q2 species (-91 ppm). As the reaction proceeds, a decrease in the Q4 species is observed consequently with formation of new Q3 and Q2 species. Evolution of the species is summarized in Table 5-1. The sample before ASR had 95.6% Q4 and 4.4% Q3 sites. After 168 hours of reaction, sample had 54.6% Q4 (41% consumed), 36.8% Q3 (32.3% created) and 8.6% Q2 sites. This suggests that Q3 species formation dominates the process [176].

To complement the  $^{29}\text{Si}$  MAS NMR results, time resolved  $^{29}\text{Si}$  CP/MAS experiment was also conducted. The cross polarization (CP) process uses magnetization transfer from protons to silicon nuclei to give qualitative information about the Qn species bound to proton, (*i.e.* those bearing hydroxyl groups). Therefore, the resonance of nuclei close to protons increases in intensity. This allows identification of germinal hydroxyl groups (Q2), free hydroxyl groups (Q3) and siloxane groups (Q4) from the obtained CP MAS spectra [177]. A  $^{29}\text{Si}$  CP/MAS NMR spectrum of an amorphous porous silica is given in Figure 5-3. There are three main signals observed at -91, -100 and -109 ppm that are assigned to germinal hydroxyl groups (Q2), free hydroxyl groups (Q3), and siloxane groups (Q4).

Figure 5-2b shows selected spectra from the time resolved  $^{29}\text{Si}$  CP/MAS experiment on amorphous silica subjected to ASR [176]. In the unreacted amorphous silica, no peak is observed indicating the absence of *Si-OH* species. This is expected, as there is no water in the reference sample. As the ASR proceeds, several resonances appear at -91, -101 and -110 ppm. These newly formed resonances are attributed to Q<sub>2</sub>, Q<sub>3</sub> and Q<sub>4</sub> sites respectively [176] suggesting a strong increase in the bound water.

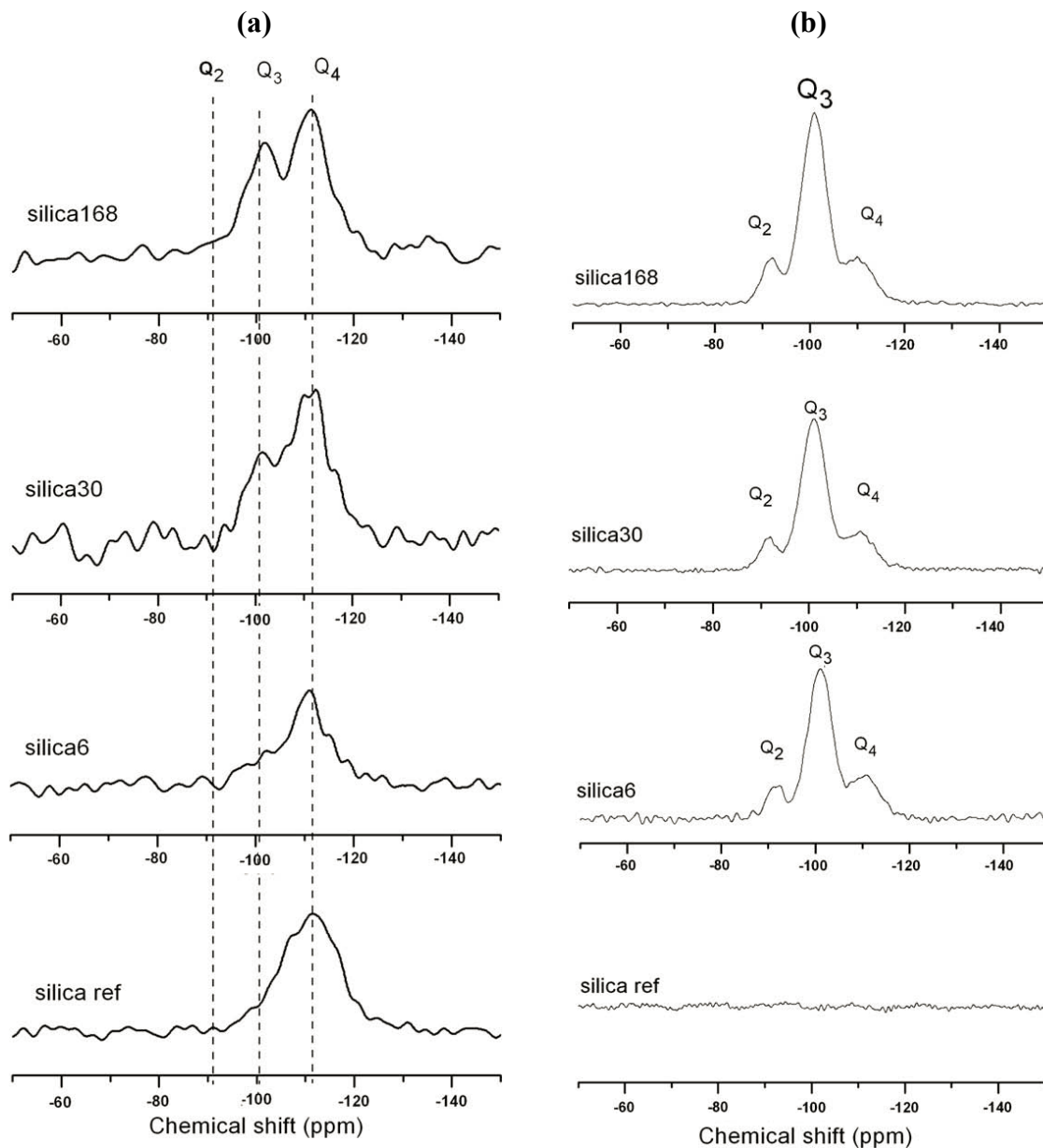


Figure 5-2. Time resolved NMR spectra for amorphous silica samples subjected to ASR up to 168 hrs: (a)  $^{29}\text{Si}$  MAS, and (b) CP/MAS [176].  $^{29}\text{Si}$  MAS spectra show that Q<sub>3</sub> formation dominates the ASR.

Table 5-1. Summary for time resolved NMR spectra for amorphous silica samples subjected to ASR up to 168 hrs. Adapted from [176].

	Time of reaction (hrs)	TG loss (%)	NMR					
			Q4		Q3		Q2	
			$\delta$ (ppm)	(%)	$\delta$ (ppm)	(%)	$\delta$ (ppm)	(%)
SilicaRef	0	-0.24	-111.2	95.6	-100.2	4.4	-	-
Silica6	6	-4.66	-110.6	86.1	-101.0	13.9	-91.5	n.q.
Silica30	30	-	-110.6	77.6	-100.9	22.4	-91.6	n.q.
Silica168	168	-9.96	-110.4	54.6	-100.9	36.8	-91.8	8.6

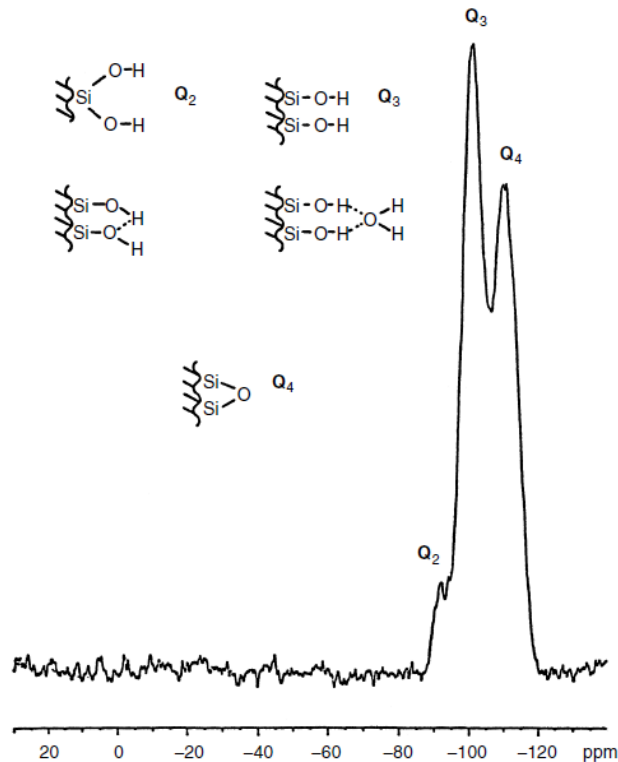


Figure 5-3.  $^{29}\text{Si}$  CP/MAS NMR spectrum of amorphous porous silica [97].

Even though there are detailed studies on ASR in laboratory conditions, the studies on the field gel has been limited to gels from one source, Furnas Dam [178–180]. The detailed NMR studies on Furnas Dam gel revealed that its local structure has mainly disordered lamellar  $\text{Q}^3$ -like silicate connectivity, Table 5-2 [179]. The mean number of non-bridging oxygens for the field gel was found to be  $\sim 1$ . This is a value that is substantially larger than the value for potassium silicate glasses with similar  $\text{K}_2\text{O}$  content, 0.51. This difference (1 to 0.51) indicates a larger amount of hydroxyl groups in the field gel compared to a potassium-silicate glass.

Table 5-2. Oxide Composition and  $^{29}\text{Si}$  MAS NMR results for 4 ASR gel samples collected from different locations a Furnas Dam [178].

Oxide Composition (mol%)				$^{29}\text{Si}$ NMR				
SiO <sub>2</sub>	K <sub>2</sub> O	Na <sub>2</sub> O	CaO	Q1	Q2	Q3	Q4	NBO/Si tetrahedron

80.8	14.3	3.2	1	2	19	56	23	1
80.1	14.4	3.2	1.5	2	21	48	29	0.96
76.3	17.1	5.1	1.3	4	30	45	21	1.17
80.1	13.1	6.1	0.4	-	17	50	32	0.84

### 5.1.1.2 X-ray absorption near edge structure (XANES) and extended x-ray absorption fine structure (EXAFS) spectroscopy

X-ray absorption spectroscopy (XAS) has also been used to investigate ASR. As discussed in chapter 2, there are different experimental setups utilizing XAS. XANES studies [130,175,181] provide information on short-range order of silicon atoms in ASR damaged samples. Figure 5-4 shows the XANES spectra of a  $\text{SiO}_2$  aggregate before and after ASR attack. In Figure 5-4a, we see two spectra: the  $\text{SiO}_2$  aggregate before ASR attack, and a crystalline  $\text{SiO}_2$  as a reference. The fine structure peaks A, B and C are characteristic for crystalline  $\text{SiO}_2$  [182]. The peak A is due to transition from electrons 1s of Si towards the 3p-like state [182,183]. For the reference  $\text{SiO}_2$ , the peak A is located at 1847 eV. This value can be used as a proof of tetrahedrally coordinated Si. A similar peak A is observed for the unreacted aggregate indicating in the aggregate Si is also in a tetrahedral environment of oxygen. After ASR attack (Figure 5-4b), the position of peak A remains constant. This suggests that the tetrahedral Si environment is preserved. However, the peak A gets broadened suggesting amorphisation of the aggregate at some level. The B and C peaks are attributed to multiple scattering in crystalline silica [182,183]. Their intensity depends on the evolution of crystal structures. In an amorphous silica sample these peaks would not exist. Therefore, tracking the changes in peaks B and C provide a good indication of amorphisation of an aggregate. After ASR, even though the peak C position stays the same, its amplitude decreases significantly [175]. This further confirms an increased amorphous behavior around silicon atom after ASR.

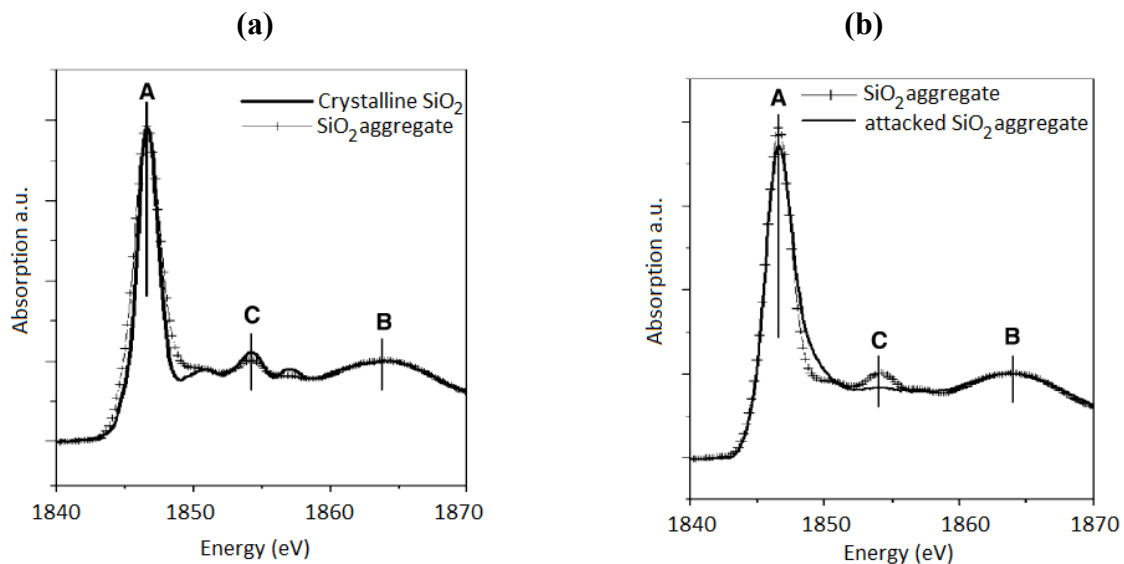


Figure 5-4. Si-K XANES spectra of (a) crystalline  $\text{SiO}_2$  used as a reference and the aggregate before attack, (b) the aggregate before and after ASR. Taken from [175].

The EXAFS experiments have also been conducted to obtain information on short-range order around silicon atoms [130,175]. The Fourier transforms of the EXAFS signal gives radial distributions, Figure 5-5. In the reference  $\text{SiO}_2$ , each atom is tetrahedrally coordinated by oxygen with a  $\text{Si-O}$  distance of  $1.60 \pm 0.02 \text{ \AA}$ . This peak includes contributions from  $\text{Si-NBO}$  and  $\text{Si-BO}$  distances. The  $\text{Si-O}$  peak in the unreacted aggregate spectrum is at the same position (Figure 5-5a); but, it has a lower amplitude suggesting an increased disorder which is in agreement with the XANES results. After ASR attack (Figure 5-5b), the amplitude of this peak starts to increase due to the equivalence of the  $\text{Si-O}$  distances in the  $\text{SiO}_2$  tetrahedra after amorphization [130], but still tetrahedrally coordinated by  $\text{O}$  as shown by XANES results. The second peak represents the second nearest neighbor,  $\text{Si-Si}$ . During the ASR, the amplitude of the second peak remains almost unchanged.

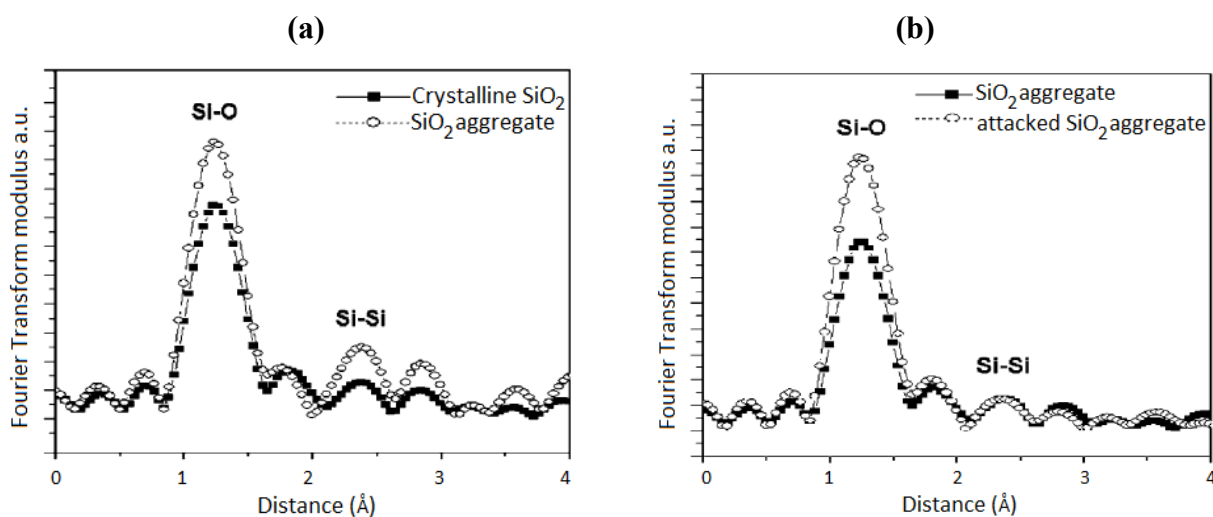
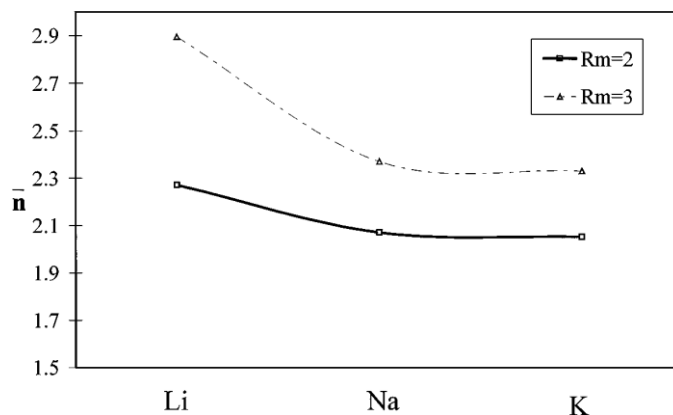


Figure 5-5. EXAFS Fourier transforms modulus at Si-K edge from (c) reference crystalline  $\text{SiO}_2$  and the aggregate before attack, and (d) the aggregate before/after ASR attack. Taken from [175].

### 5.1.1.3 Small Angle Scattering

Silica gels produced in strongly basic ( $\text{pH} > 10$ ) silico-(calco)-alkaline sols have been studied through small angle scattering in detail [184–189].

In the precursor silico-alkaline solutions, a variety of polysilicates ions (dimer, trimer, cyclic hexamer, cubic octamer, *etc.*) are present. Structural description of these species (whose structural unit is the monomeric orthosilicate anion  $\text{SiO}_4^{4-}$ ) can be found at [190]. It has been shown that the fraction of the silicate species in the precursor sols is controlled by hydroxide concentration and by the nature of the counterion (*i.e.*, the alkaline ion) [184,185], Figure 5-6. Studies also present that for a constant hydroxide concentration, the larger species are strongly stabilized by larger counterions ( $\text{Li}^+$ ,  $\text{Rb}^+$ , and  $\text{Cs}^+$ ); whereas the linear species are stabilized by relatively small counterions ( $\text{Na}^+$  and  $\text{K}^+$ ) [189].



**Figure 5-6.** Evolution of mean degree of connectivity ( $\bar{n}$ ) of silico-alkaline solutions ( $[\text{SiO}_2] = 1.5 \text{ mol}\cdot\text{L}^{-1}$ ) as a function of alkali ion and molar ratio where  $\bar{n} = \frac{\sum_n n \times Q^n}{\sum_n Q^n}$ , and  $R_m = [\text{SiO}_2/\text{A}_2\text{O}]$  where A= Li, Na or K. Taken from [184].

At low molar ratios ( $R_m = [\text{SiO}_2/\text{A}_2\text{O}]$ ; A = Na or K), the silico-alkaline solution contains weakly polymerized silicate species [138]. Degree of polymerization of the solution can be strongly enhanced by increasing  $R_m$ . At higher molar ratios ( $R_m > 2$ ), the solutions can be considered colloidal [184]. Higher molar ratios allow the formation and growth of the aggregates through hydrolysis and condensation reactions; and the initial precursor sol turns into a final gel state. The resulting gel can be described as an infinite aggregate with a continuous skeleton enclosing a continuous liquid phase [159].

Calcium, an important element for portland cement based systems, plays an important role in the gelation of silico-alkaline solutions [184]. For a given solution, gelation time decreases as the Ca concentration increases. In silico-alkaline solutions with a constant calcium concentration, the gelation time increases in the following order of alkaline ions: sodium, potassium, lithium, rubidium, and cesium [189]. Calcium also strongly affects the structure of the alkali-silica. The incorporation of the Ca ions into the precursor solutions results in an irreversible aggregation of the colloidal silicate species. Ca ion can be considered as a “catalyst” bringing two silicate entities together and then being replaced by a siloxane bond [184]. This Ca related aggregation process can be in two groups according to the Ca concentration of the solution. In low calcium systems, the aggregates grow by reaction limited cluster aggregation (RLCA). In high calcium systems, diffusion- limited cluster aggregation (DLCA) governs. The schematic of the aggregation processes can be found in chapter 4.

A study on precursor silico-alkaline solutions with low-Ca content ( $[\text{Ca}(\text{OH})_2] = \sim 0.08 \text{ mol L}^{-1}$ ) lead to gels composed of aggregates exhibiting a fractal structure within a wide scale range extending from less than 10 to more than 1000 Å with the same fractal dimension over the whole scale range, Figure 5-7a. The solutions with a high-Ca concentration ( $[\text{Ca}(\text{OH})_2] = \sim 0.5 \text{ mol L}^{-1}$ ) yielded gels composed of a large number of rather small fractal aggregates and much larger particles, Figure 5-7b. The mechanism of particle growth and the structure of the final gels were not noticeably modified, neither by the nature of the alkaline ions nor by their molar ratio [189].



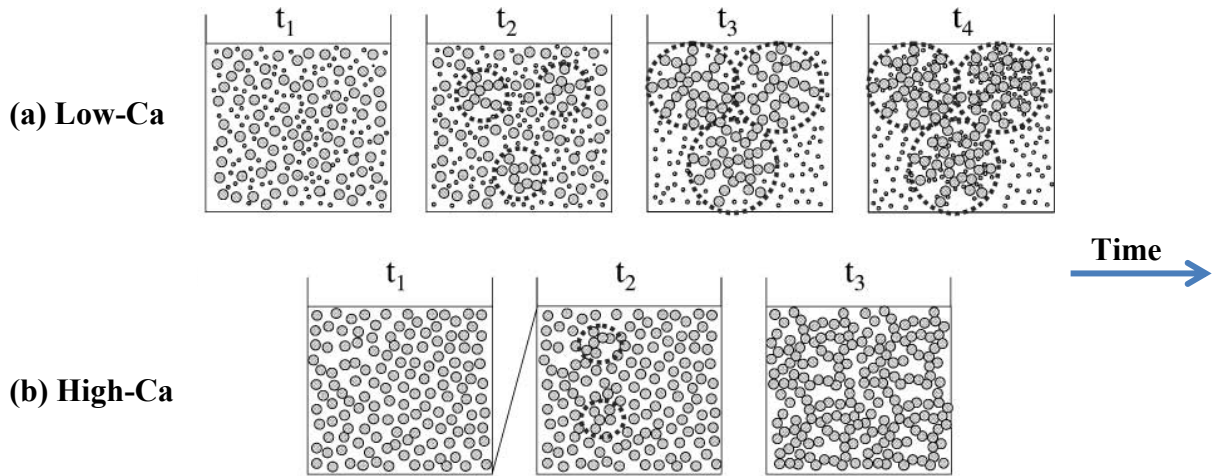
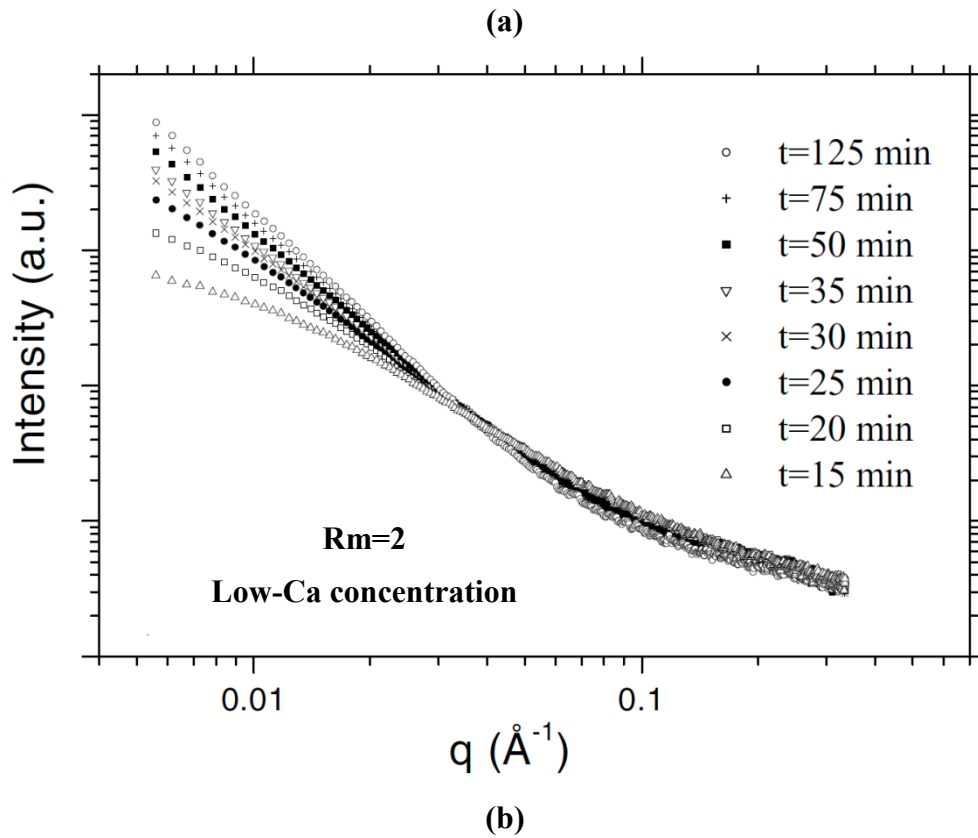
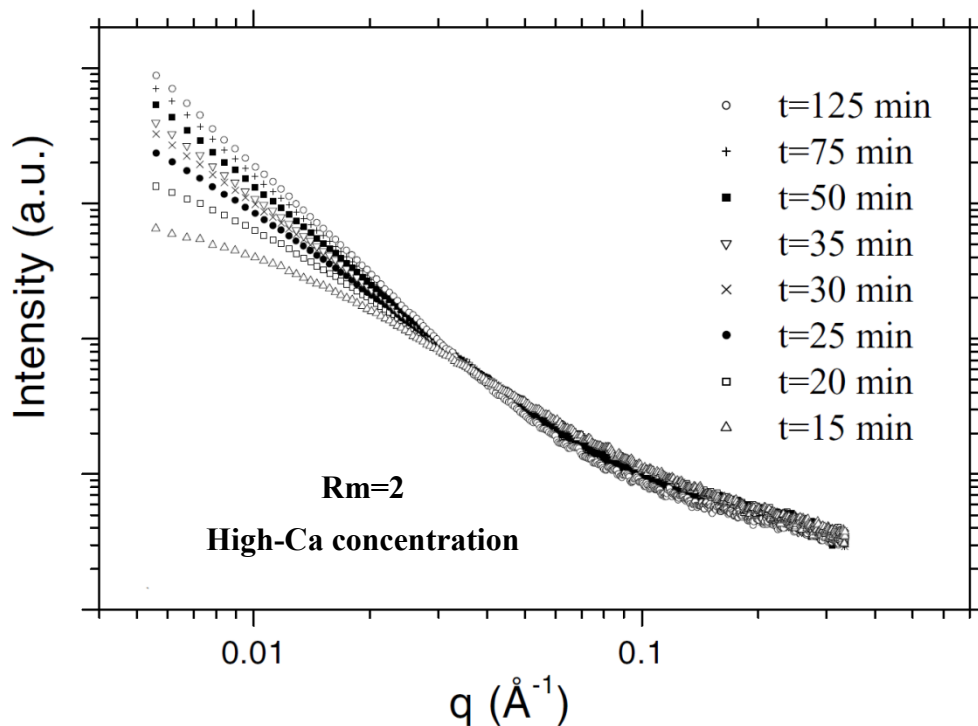


Figure 5-7. Schematic views of aggregation process involved in gel formation in sols with (a) low and (b) high calcium content [187].

The evolution of the gelation can be followed through small angle scattering experiments. Figure 5-8 shows time-resolved SAXS curves for a sodium silicate solution ( $[SiO_2] = 1.5 \text{ mol}\cdot\text{L}^{-1}$ ,  $[NaOH] = 1 \text{ mol}\cdot\text{L}^{-1}$ ,  $R_m=2$ ) destabilized by  $Ca$  at low concentration ( $[Ca(OH)_2] = \sim 0.08 \text{ mol}\cdot\text{L}^{-1}$ ) and high concentration ( $[Ca(OH)_2] = \sim 0.05 \text{ mol}\cdot\text{L}^{-1}$ ) [187,188].





**Figure 5-8. Sequence of experimental SAXS curves corresponding to the studied sodium silicate system with  $R_m=2$  and (a) low-Ca concentration, (b) high-Ca concentration. Taken from [187,188]**

Structural variations associated to the aggregation process can be followed through the evolution of the shape of the SAXS curves with time [188]. Obtained fractal dimensions  $D$  and correlation lengths  $\zeta$  for different aggregation times are plotted in Figure 5-9 for the low-Ca case. Over time, the fractal dimension  $D$  of the fractal aggregates increase. The  $\zeta$  values could only be determined from the three first curves (15, 20 and 25 min). At longer times, the aggregates were too large to be probed within the Q-range covered within this experiment. At the beginning of the experiment  $\Delta t_1$ , the precursor sol was composed of a mixture of 30% monomers and 70% oligomers with equivalent radius of sphere closed to 3 and 6 Å, respectively [185]. The addition of Ca ions in the solution induced the aggregation of most of these particles. After 15 min, aggregates had a fractal dimension  $D$  of 1.9 and correlation length  $\zeta$  of 120 Å [185]. A  $D$  of 1.9 suggests that the formation of the initial aggregates was governed by DLCA mechanism. During the  $\Delta t_2$  interval, the correlation length of the fractal aggregates grew from 120 to 332 Å, and  $D$  increased from 1.9 to 2.2 indicating a transition from a predominantly DLCA mechanism to a RLCA. The  $\Delta t_3$  interval  $D$  reached 2.5 due to possible densification or aging process promoted by the additional aggregation of isolated monomers from the sol. Complementary rheological study of the gel suggests the percolation of the aggregates had already occurred at the end of this interval. During  $\Delta t_4$  interval  $D$  of the percolated gel network increases up to 2.75, but increase happened at a lower rate. The densification of the gel network slowly goes on as up to total consumption of the remaining monomers in the solution.

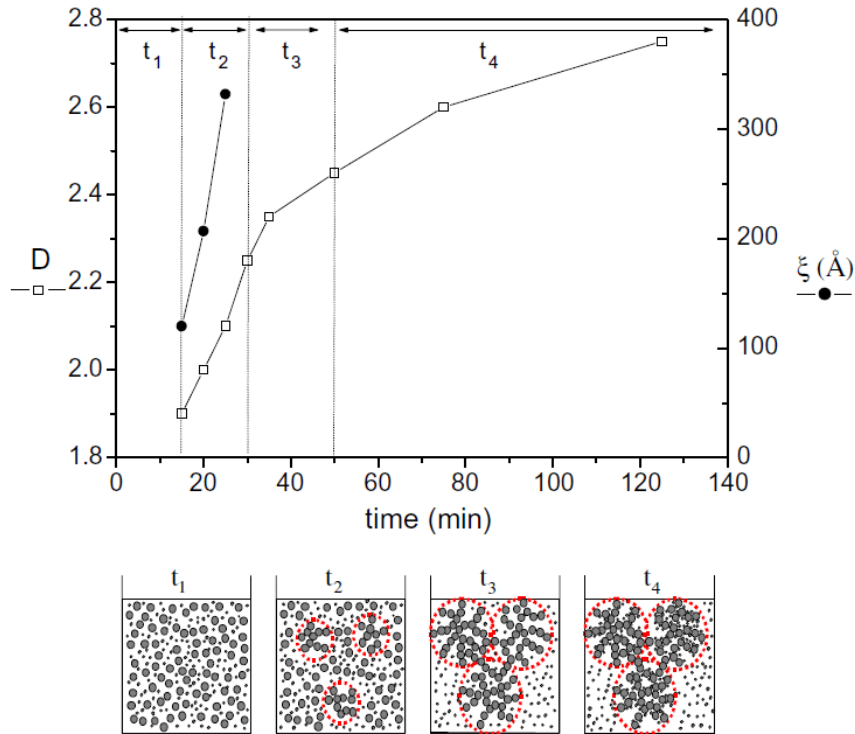


Figure 5-9. (Top) Correlation length  $\xi$  and fractal dimension  $D$  as functions of the aggregation time. (Bottom) Schematic for the aggregation process. Taken from [188]

## 5.2 Experimental program

The studies discussed in section 5.1 mainly focus on understanding the reaction mechanisms of ASR. The accelerated ASR experiments in laboratory conditions do not reflect fully the field conditions in which initiation of ASR takes commonly a couple decades. The experiments on field gels are limited focusing only to Furnas Dam gel. A deeper understanding of the gel structure at molecular- and nanometer-scale is just as important as understanding the reaction mechanisms. This section focuses on extending the characterization experiments on the Furnas Dam gel; and also testing a secondary gel from Moxoto Dam. Synthesized kanemite, a hydrated layered sodium silicate, is used as reference material in some of the experiments. Figure 5-10 summarizes experimental methods used in this research in characterization of the gels.

### 5.2.1 Materials

In this study, two types of samples are used: (1) field ASR gels collected from Furnas Dam (ASR<sub>F</sub>) and Moxoto Dam (ASR<sub>M</sub>) (Figure 4-17); and (2) synthesized Na-kanemite as a reference material.

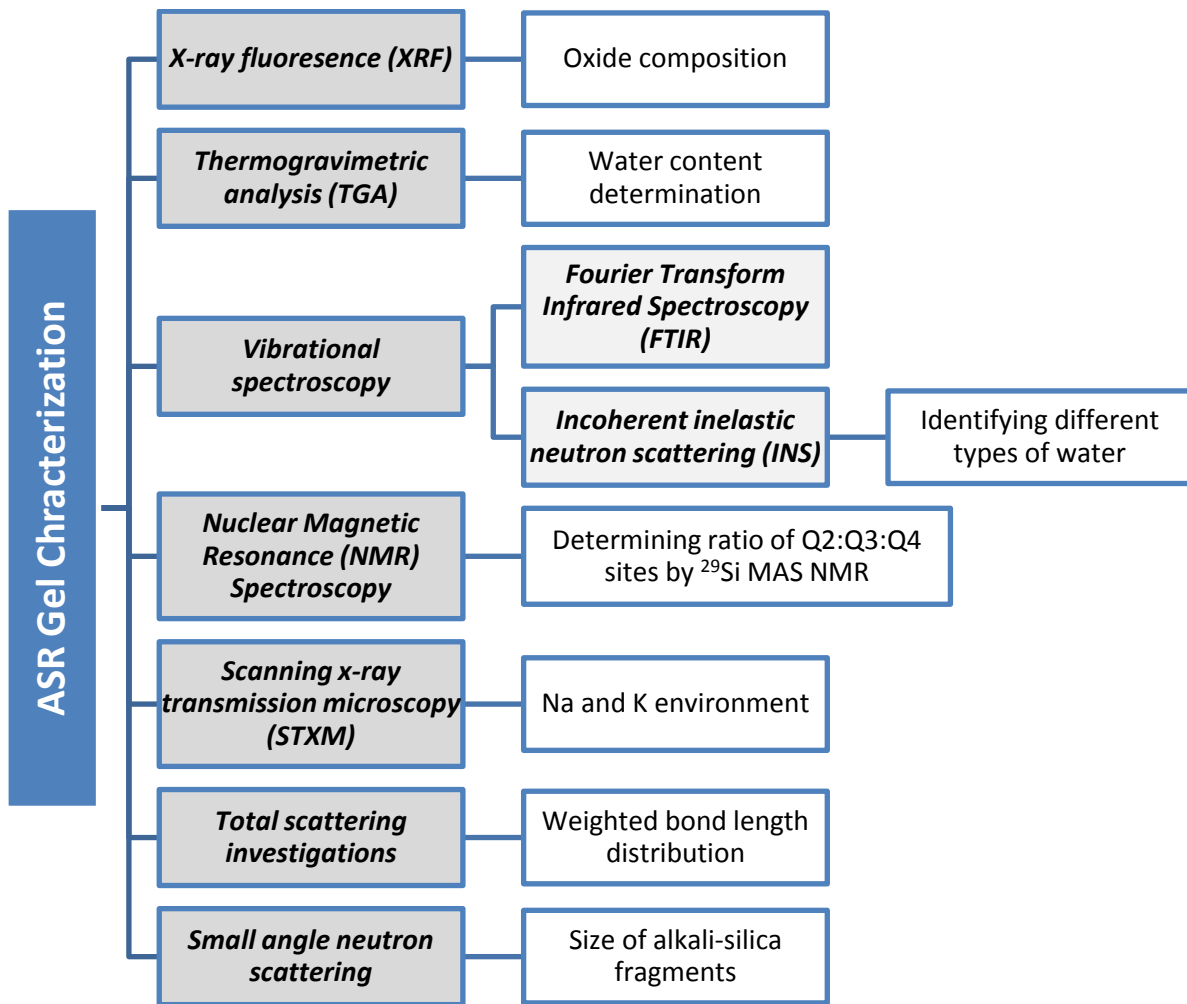


Figure 5-10. Experimental methods with their major goals used in ASR gel characterization.



Figure 5-11. General views of (a) Furnas Hydroelectric Dam located on the Rio Grande in Minas Gerais, Brazil [191] and (b) Moxoto Hydroelectric Plant [192].

### 5.2.1.1 Alkali silica reaction gel

The conducted experiments discussed in this chapter focus on alkali-silica gel obtained from two different dams located in Brazil: Furnas Dam and Moxoto Dam.

The Furnas Dam (Figure 4-17a), is located on the Rio Grande River in Minas Gerais. The earth and rockfill dam was built in 1963 and raises the water surface 30 m (Figure 5-12a). The concrete mix design used for the dam contained 170 kg/m<sup>3</sup> of cement, 550 kg/m<sup>3</sup> of natural and artificial sand, 1590 kg/m<sup>3</sup> of crushed rock with maximum size of 152 mm. The water-cement ratio was 0.70 [191]. The portland cement used had a total equivalent alkali content of 0.60% manufactured nearby Furnas dam were used [191]. Even though the equivalent alkali content of the cement was not high, the quartzite from the excavations started slowly reacting under the moist environmental conditions of the dam. Over the years, the ASR gel formed near the aggregates migrated through the porous hydrated cement matrix creating large macroscopic clusters oozing out of the cracks on the damaged concrete structure's surface as seen in Figure 5-12d,e. In 1995, the symptoms of ASR, including map cracking and staining, were first observed [120]; and the consequent cracking required structural repairs on the dam (see Figure 5-12b,c). Localized repairs, including patching of the concrete and epoxy injection to cracks, were successfully performed [120], while the dam has been generating energy without interruption. The gel fragments used in this study (Figure 5-12e) were hand-picked from the gallery walls in the dam.

The second structure, the Apolonio Sales (after the late founder of the Hydroelectric Company of San Francisco, CHESF) or commonly known as Moxoto Hydroelectric Plant is a part of Paulo Afonso Hydroelectric Complex. Structure is located in the municipality of Delmiro Gouveia, Brazil utilizing the San Francisco River. The hydroelectric plant was built in 1971, and became operational in 1977. Figure 4-17d shows an aerial view of the plant. In 1981, just after 4 years of operation, rubbing problems started to occur in the rotor of the turbine generator. After a thorough investigation run by CHESF), alkali-silica reaction was determined as the primary cause of the malfunctioning of the hydroelectric plant [192]. The reactive quartzite aggregate was singled out as the problematic component of the concrete. Some of the large macroscopic clusters (typical volumes > 1 cm<sup>3</sup>) oozing out of the cracks were used in this study.

The major oxide compositions of the tested gels were found using a Philips PW2400 wavelength-dispersive x-ray fluorescence spectrometer located at McCone Hall, UC Berkeley. 0.5 g of sample finely ground, and mixed with 3.5 g of lithium tetraborate as flux. The mixture was then fused at high temperatures (>1000°C) in a platinum crucible. During this procedure, the crucible was continuously agitated to ensure complete dissolution and mixing. The obtained melt was poured into a circular mold; and cooled to form a glass disc. The elements in the flux (Li, B, and O) are normally not detected by XRF. The water contents were determined by TGA (discussed in 5.2.2.1). The results are summarized in Table 5-3. The  $(K+Na):Si$  molar ratio for ASR<sub>F</sub> is 0.43. ASR<sub>M</sub> has a slightly higher Na content; but the  $(K+Na):Si$  ratio is similar to that of ASR<sub>F</sub> at 0.42. These values are within the compositional ranges we reported on ASR damaged samples in chapter 4, and are very close to the compositions reported for field gels from Furnas Dam [178].



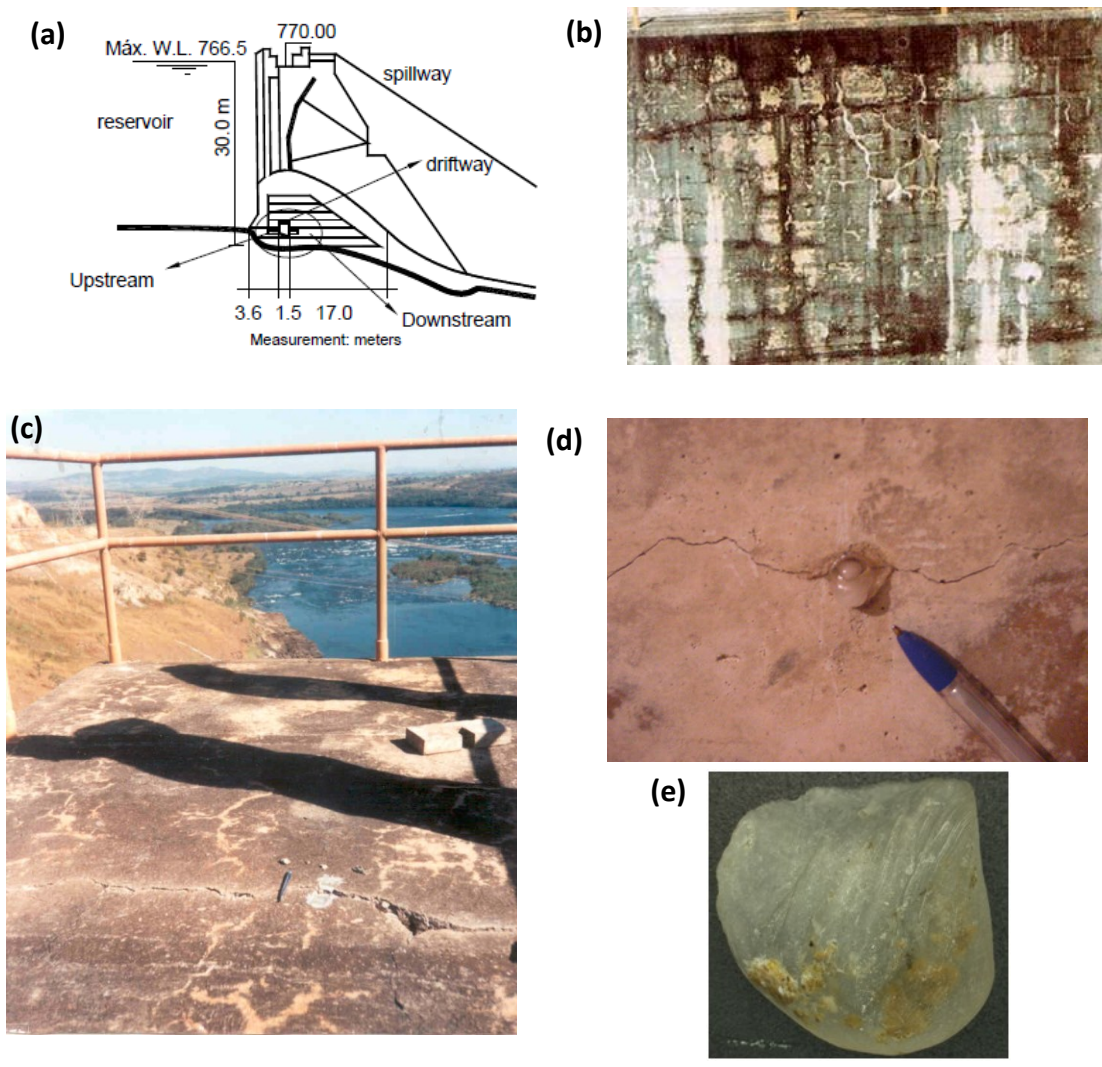


Figure 5-12. (a) Sketch showing a cross section of the spillway [191]. (b) Cracking caused by ASR in the spillway pillar [193]. (c) ASR gel extruding from cracks in the concrete surface of the spillway driftway [191]. (d) Crack along transversal section of a spillway column [191]. (e) ASR gel collected from the dam.

Table 5-3. Major oxides in the tested ASR gels, weight %.

	SiO <sub>2</sub>	K <sub>2</sub> O	Na <sub>2</sub> O	CaO	H <sub>2</sub> O
ASR <sub>F</sub>	68.5	12.1	2.7	0.84	15.7
ASR <sub>M</sub>	65.5	10.3	3.6	1.3	13.8

### 5.2.1.2 Na-Kanemite

Kanemite, a naturally occurring mineral, was first found at Lake Chad, and described by Johan and Maglione in 1972 [194]. It belongs to  $Na_2O \cdot (4-22)SiO_2 \cdot (5-19)H_2O$  series along with other layered sodium silicate hydrates such as makatite, octosilicate, magadiite and kenyaite,

Table 5-4 [195,196]. The series has several common physical properties, including a high capacity for ion exchange, whereby sodium ions can be replaced by protons, and other cations such as Al or large quaternary ammonium ions. With the availability of several different synthetic routes, they are potentially valuable as catalysts or in detergent systems [196]. Except octosilicate (also referred as ilerite), members of these series can occur naturally.

**Table 5-4. Layered sodium silicate hydrate series,  $Na_2O \cdot (4-22)SiO_2 \cdot (5-19)H_2O$  [196].**

Silicate	Space group	Lattice constants (Å)			Angle $\beta$ (°)	Basal spacing (Å)	Connectivity Ratio (Q3:Q4)
		a	b	c			
<i>Makatite</i> [195] $Na_2O \cdot 4SiO_2 \cdot 5H_2O$	monoclinic P2 <sub>1</sub> /c	7.3881(5)	18.094(3)	9.5234(5)	90.64(1)	9.03	1:0
<i>Kanemite</i> [197] $Na_2O \cdot 4SiO_2 \cdot 7H_2O$	orthorhombic Pbcn	4.946(3)	20.502(15)	7.275(3)	-	10.3	1:0
<i>Octosilicate</i> [198] $Na_2O \cdot 8SiO_2 \cdot 9H_2O$		7.345	12.74	11.25	99.3	11.0	1:1
<i>Magadiite</i> [199] $Na_2O \cdot 14SiO_2 \cdot 10H_2O$	monoclinic	7.25	7.25	15.69	96.8(2)	15.6	1:3
<i>Kenyaite</i> $Na_2O \cdot 22SiO_2 \cdot 10H_2O$	monoclinic	7.79	19.72	7.3	95.9	20.0	unknown

Kanemite has an orthorhombic-type structure, having a space group Pbcn [197]. It consists of corrugated silicate sheets  $[Si_2O_4OH]_n$  alternating with hydrated Na sheets coordinated to six water molecules [200], Figure 5-13. This results in a layered structure with a basal spacing of 10.3 Å. The silicate sheets contain puckered six-membered rings of  $HOSiO_3-SiO_4$  units (Q<sup>3</sup>). These sheets can be described as a built up of unbranched vierer single chains  $(Si_4O_{12})_n$  where the chains condense to form sheets perpendicular to z-axis. The Na sheet is composed of hydrated Na in distorted octohedral coordination. The <sup>29</sup>Si MAS NMR on synthesized kanemite shows a sharp Q3 peak located at -101ppm.

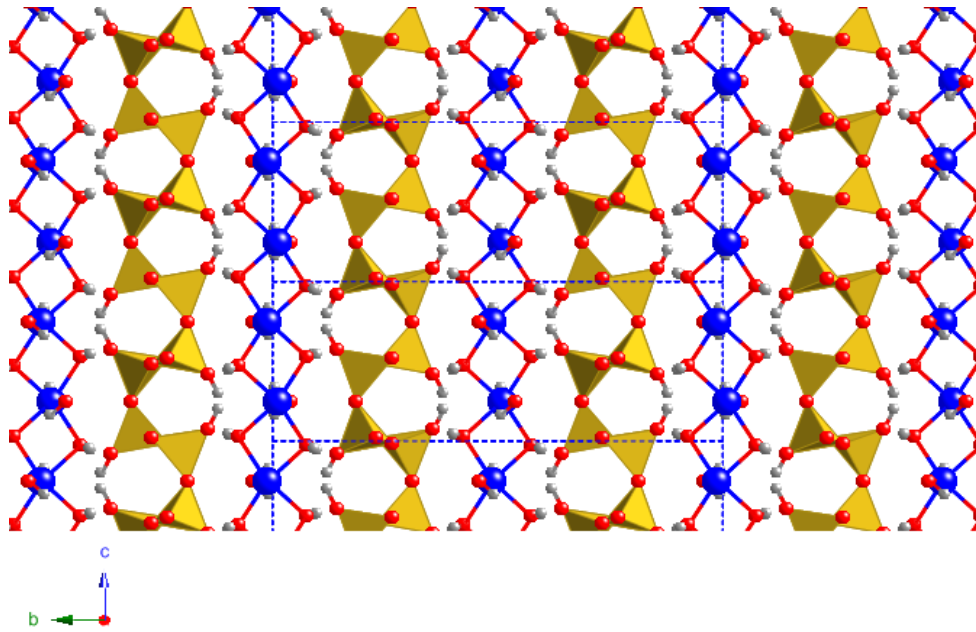
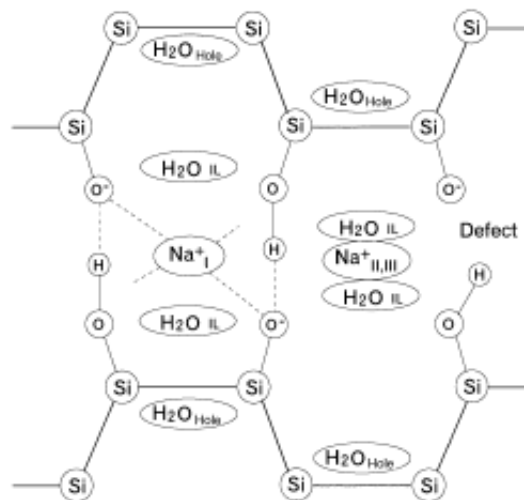


Figure 5-13. Atomic model of kanemite based on [196,197]: O, red; H, gray; Si, yellow; and Na, blue. Water molecules are octahedrally coordinated to sodium ions. The structure does not show missing water molecules that are expected in the puckered regions of the silicate sheets. The interlayer spacing between the silicate sheets is 10.3 Å. Dashed lines define the unit cell.

Hayashi [201] proposes that there are three types of water in kanemite: external surface water, interlayer water, and hole water within the puckered regions of the silicate sheet, Figure 5-14. The external surface water is very mobile. Upon heating, it will desorb. The interlamellar water will also desorb. However, with decreasing water content, the interlayer spacing will also decrease limiting the mobility of the water. The hole water is the least mobile, as it is trapped within the holes of the folded  $SiO_3OH$  hexagonal rings [201]. Kanemite shows structural and physical similarities to the clay minerals, such as reversible hydration and dehydration and exchange by inorganic and organic cations.





**Figure 5-14. Schematic structure of kanemite, including a defect region. Taken from [201].**

The Na-Kanemite used in this study was synthesized at Los Alamos National Laboratory through the sol-gel method (with the help of Dr. Luke Daemen):

1. In a 400 mL teflon beaker, disperse 60.08 g (1 mol) of fine (325 mesh) of silica,  $SiO_2$  (60.08 g/mol) powder in 100 mL of methanol.

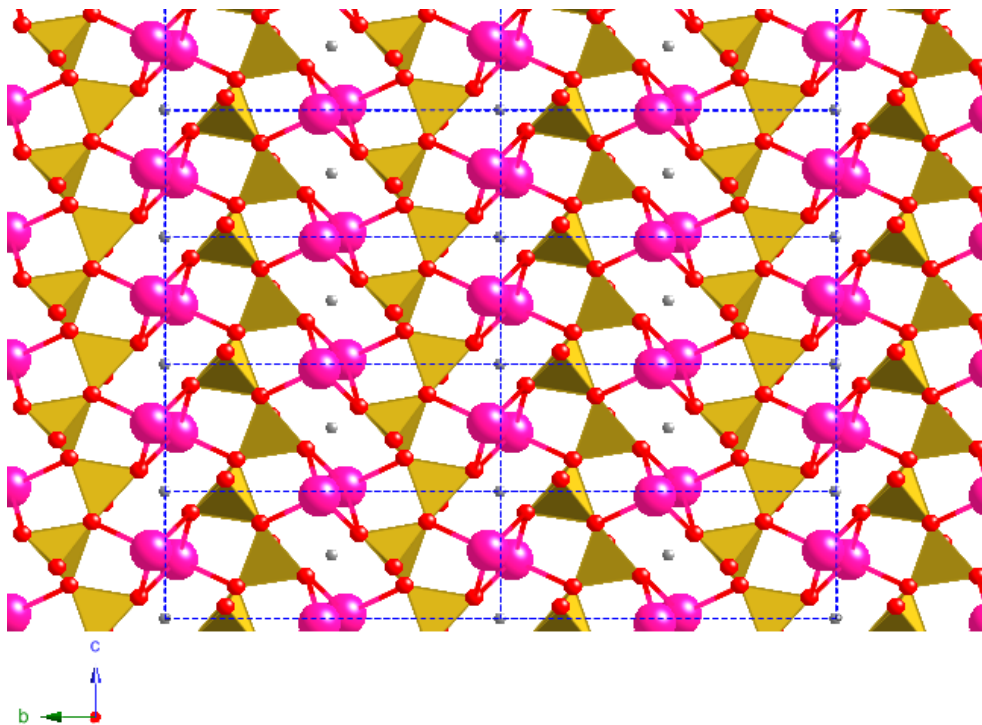
2. In a 150 mL glass Erlenmeyer, carefully dissolve 40 g (1 mol) of  $NaOH$  (40 g.mol) in 40 mL  $H_2O$ . Chill this solution. (Note: 2x excess of  $NaOH$ )

3. With stirring, slowly add the  $NaOH$  solution to the  $SiO_2$  suspension in methanol. Place the resulting gel in an oven heated to 100 °C. After 2-3 hours, cool to room temperature. A very hard, solid mass forms.

4. Grind the resulting gel with a mortar and pestle and place the coarse powder in a large porcelain or alumina cup. The gel volume expands upon calcination. The volume of the cup should be larger than the volume of gel placed in it or spillage may occur. Calcine in air at 700 °C in a box furnace for 5 to 6 hours.

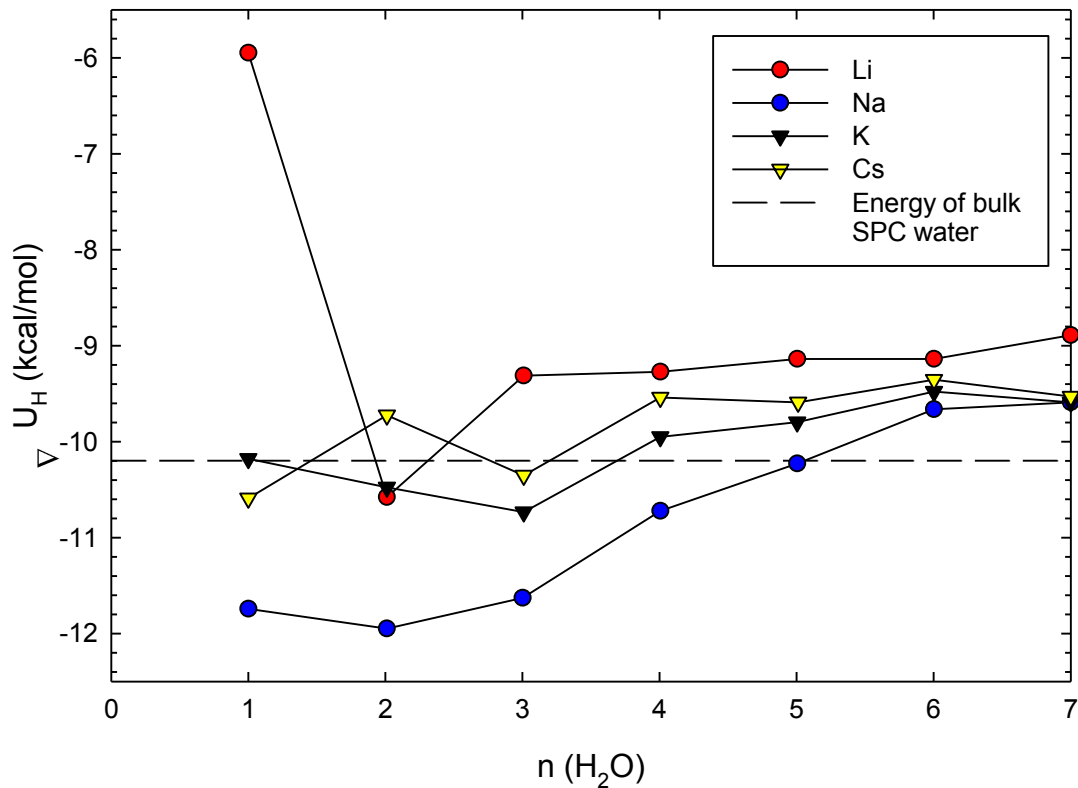
5. Pulverize the solid foam that formed in the cup after cooling to room temperature and grind with a mortar and pestle. Disperse the resulting fine powder in 500 mL of  $H_2O$  in a large beaker. Stir for 10-15 minutes. Filter and wash with another 500 mL of  $H_2O$ . Dry in air.

A so called ‘K-Kanemite’ also exists ( $KHSi_2O_5$ ), Figure 5-15. The layered potassium silicate is first described at [202]. The computed basal spacing for it is 6.27 Å.



**Figure 5-15. Atomic model of K-kanemite ( $KHSi_2O_5$ ) based on [202]: O, red; H, gray; Si, yellow; and K, pink. The interlayer spacing between the silicate sheets is 6.27 Å. Dashed lines define the unit cell.**

ASR gels show a broad range of morphologies and chemical compositions depending on gel aging and reactions with the surrounding cement matrix. As a result, there is a considerable variation in gel structure. However, Wieker *et al.*'s [203,204] proposal that the ASR gel has a structure similar to disordered kanemite ( $Na,K$ )  $HSi_2O_5 \cdot 3H_2O$  has been gaining acceptance. Considering that ASR gel has a similar structure to kanemite, Kirkpatrick *et al.* [200] conducted MD calculations on hydration energies of *Na*- and *K*-kanemite. Their goal was to determine if there is a significant thermodynamic driving force of incorporation of water into the interlayer galleries of any kanemite-like nano-sized fragments, or not. If the hydration energy is significantly less than the energy of bulk water (using simple point charge potential model), then a thermodynamic driving force exists water will be incorporated into kanemite interlayers. This would suggest that much of the water in the ASR gel might be incorporated in the interlayers. However, if there is a small (or positive) driving force, then the bulk of the water in the ASR gel is likely to be held in other ways. The resulting hydration energies in comparison with bulk water SPC water are given in Figure 5-16. The *Na*-kanemite results in a hydration energy considerably less than that of bulk SPC water for 1-, 2, and 3- $H_2O$ ; beyond 3, it is comparable or greater. This result suggests that up to 3- $H_2O$ , there is a significant thermodynamic driving force for water incorporation. For *K*-kanemite, the computed hydration energy is comparable to or greater than the energy of SPC water for all water contents. This indicates that there is no substantial thermodynamic driving force for any amount of interlayer water. The computed hydration energies for *Li*- and *Cs*-kanemite also do not support incorporation of interlayer water.



**Figure 5-16. MD computed hydration energies for Li-, Na-, K- and Cs-kanemites versus water content [200].**

MD modeling of kanemites by Kirkpatrick *et al.* [200] show that incorporation of large amounts of water in kanemite-like layers is not energetically favorable. Na-kanemite accommodates at most 3 H<sub>2</sub>O per formula unit. This equates into 33.7 wt% of the water free formula. K-kanemite does not incorporate any water at all. However, tested field gels, which are richer in K than Na, can exhibit up to 100-150 wt% gain when exposed to humidity. Therefore, water incorporation into interlayers cannot be the main mechanism of gel expansion. Instead, a kanemite based model for the gel can be used to explain silicate nano-particle surfaces containing both anionic non-bridging oxygens (*Si-O<sup>-</sup>*) and *Si-OH* groups which provide a structure on which the alkali cations and water molecular are organized to build an effective *H*-bonding network [200]. This network can stabilize large amounts of water in the gel. These results are in line with Prezzi *et al.*'s [205,206] proposal that ASR gel expansion is analogous to the swelling behavior of colloid suspensions.

## **5.2.2 Characterization Experiments on the Field Gels**

### **5.2.2.1 Thermogravimetric analysis**

Standard calorimetric measurements (DSC) were performed by means of a Q2000 (TA Instrument) located at Centro de Fisica de Materiales (CSIC, UPV/EHU) in Spain by Dr. Silvina Cerveny using heating rates of 10 K/min. Hermetic aluminum pans were used for all the samples. The sample weight was about 10 mg. Thermogravimetric analysis was done by using a TGA-Q500 (TA Instruments). All the measurements were conducted under high-purity nitrogen flow over a temperature range 30–1000 °C with a ramp rate of 5 K/min.

The TGA response of *Na*-Kanemite shows a first rapid initial drop of the mass (from room temperature up to ~100°C), see Figure 5-17. The total moisture content ( $c_w$ , expressed as grams of water/grams of dry particles) for of the tested kanemite was calculated as the loss of mass at 160°C divided by the sample weight at the same temperature and found as 32.1 wt%. After 15 minutes in vacuum,  $c_w$  went down to 12.7%. After 45 minutes,  $c_w$  was 5.7%. Then, the sample was rehydrated. The  $c_w$  rose to 16.7%. The changes in  $c_w$  are summarized in Table 5-5

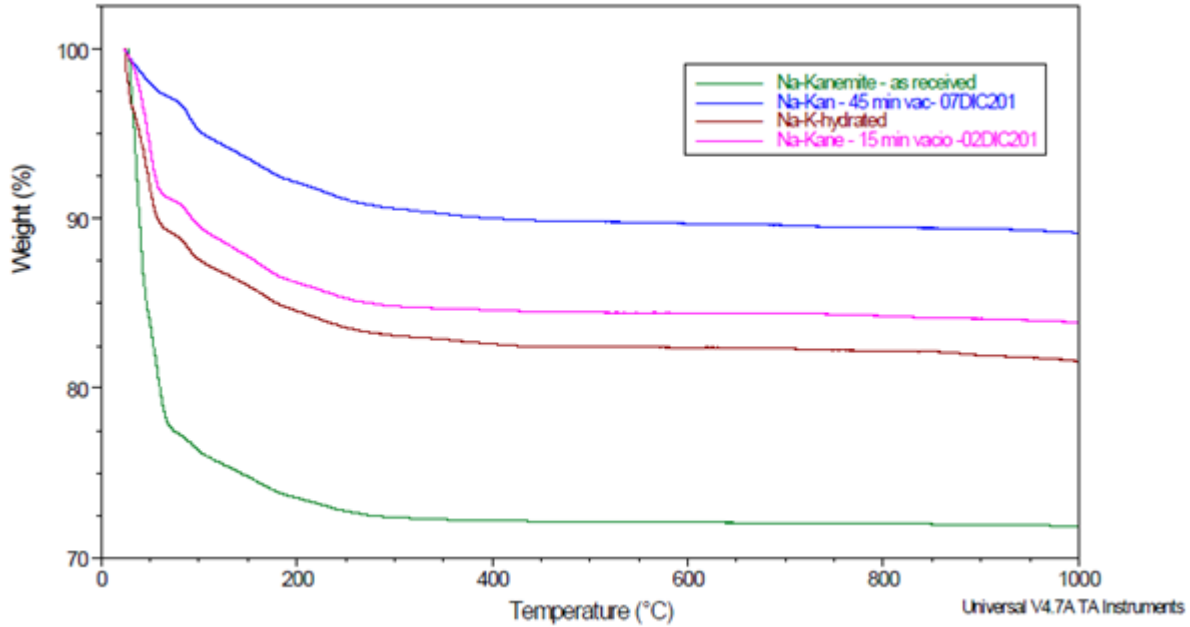


Figure 5-17. TGA response of Na-Kanemite. 92% of water is lost by 300°C. Above 700°C kanemite transforms into tridymite, which retains some water in its structure.

Table 5-5. Progression of water content  $c_w$  of Na-Kanemite

Treatment	$c_w$ [wt%]
As received	32.10
15 min vacuum	12.74
45 min vacuum	5.70
Rehydrated	16.70

According to Hayashi [201], water in kanemite is lost at four steps. We also observed a stepped water loss. At step 1 ( $< 47^\circ\text{C}$ ), the surface water was released. Interlamellar water might be released at two steps; step 1 and step 2 ( $47\text{--}85^\circ\text{C}$ ). Water within hexagonal rings was lost at step 3 ( $85\text{--}136^\circ\text{C}$ ) and step 4 ( $> 135^\circ\text{C}$ ). Also at step 4, some of hydroxyl groups were lost.

The TGA response of the field gels are shown in Figure 5-18. A stepped, but a more gradual water loss was observed for the gels. The measured  $c_w$  for  $\text{ASR}_F$  was 15% and for  $\text{ASR}_M$  was 20%. It is important to mention that the field gels can dehydrate/rehydrate considerably. Therefore, the TGA response of the gels might differ at different measurements conducted at different times.

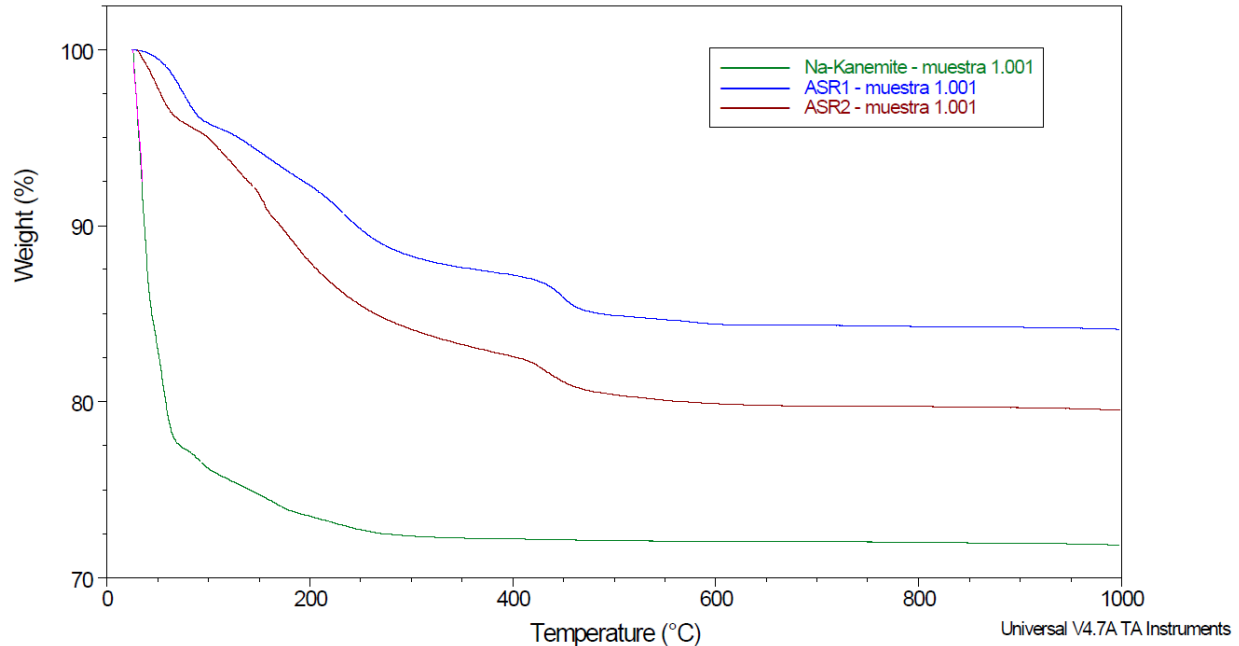


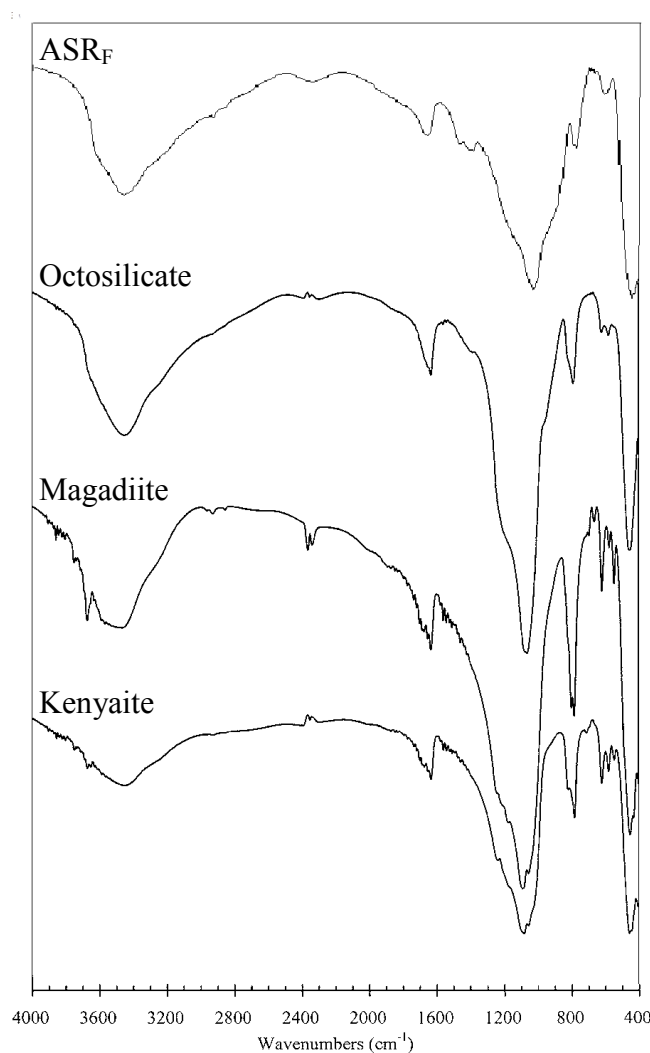
Figure 5-18. TGA response of field gels. ASR1: Furnas Dam, ASR2: Moxoto Dam.

### 5.2.2.2 Vibrational spectroscopy

#### 5.2.2.2.1 Fourier Transform Infrared Spectroscopy

It is widely accepted that the vibrations due to silicate layer and associated cations follow the frequency order [207,208]:  $Si-O-Si$  stretching (asymmetric) >  $Si-O$  stretching >  $Si-O-Si$  stretching (symmetric) >  $Si-O-Si$  bending >  $O-Si-O$  bending >  $Na,K-O$  stretching. In general,  $Si-O-Si$  stretching (asym.) modes appear within  $1200 - 1000\text{ cm}^{-1}$ . The  $Si-O-Si$  stretching (sym.) is expected to appear in the region  $700 - 400\text{ cm}^{-1}$  [207,209]. The layered (silicates with NMR Q3 populations) silicates also contain  $Si-O$ . The corresponding  $Si-O$  stretching is located in the  $1100-1050\text{ cm}^{-1}$  region. Within the light of this knowledge, let's first examine the kenyaite spectrum [210]. The sharp peak at  $3670\text{ cm}^{-1}$  may be assigned to free hydroxyl groups. The broad band at  $3645\text{ cm}^{-1}$  may be due to hydrogen bonded hydroxyls. The shoulder at  $1250\text{ cm}^{-1}$  can be assigned to asymmetric stretching mode of  $Si-O-Si$ . This is a characteristic of five-membered rings of  $SiO_4$  tetrahedra [207]. The bands at  $1900$  and  $1055\text{ cm}^{-1}$  may be attributed to the  $Si-O$  stretching vibration [211]. The strong band at  $452\text{ cm}^{-1}$  is an indication of existence of some six-membered rings. The magnadiite ( $Na_2O \cdot 14SiO_2 \cdot 10H_2O$ ) spectrum is also similar [210]. The sharp peak at  $3670\text{ cm}^{-1}$  can be attributed to isolated hydroxyl groups [212]. The broad band at  $3445\text{ cm}^{-1}$  may be attributed to strong  $H$ -bonded  $OH$  groups. The shoulder at  $1238\text{ cm}^{-1}$  is related to the asymmetric stretching mode of  $Si-O-Si$ , a sign of five-membered rings [207]. The bands at  $1081$  and  $1057\text{ cm}^{-1}$  may be attributed to the  $Si-O$  stretching (asym.) [211]. The band at  $452\text{ cm}^{-1}$  indicates presence of six-membered rings. Other bands at  $781$ ,  $709$ ,  $618$ ,  $578$ ,  $545\text{ cm}^{-1}$  can be assigned to double rings, and at  $457\text{ cm}^{-1}$  to  $Si-O-Si$  bending (asym.) [213]. In the octosilicate ( $Na_2O \cdot 8SiO_2 \cdot 9H_2O$ ) spectrum [210] the hydroxyl-stretching mode appears around  $3660\text{ cm}^{-1}$ ; however, it is a shoulder band instead a sharp one. The shoulder at  $1224\text{ cm}^{-1}$  is attributed to asymmetric stretching mode of  $Si-O-Si$ , and is an indication of five-membered rings [207]. The

band at  $1092\text{ cm}^{-1}$  can be assigned to stretching vibration of *Si-O*. The bands at 787, 619, and 578 are attributed to symmetric stretching



**Figure 5-19. FT-IR spectra of ASR<sub>F</sub> (courtesy of Paulo Monteiro) and of synthesized kenyaite, magadiite, and octosilicate [210].**

The spectrum of ASR<sub>F</sub> was collected at Brazil. The discussions on the layered silica spectra are based on [207,210]. The peaks at  $1154$  and  $1037\text{ cm}^{-1}$  can be assigned to asymmetric and symmetric stretching vibration of *Si-O* respectively. The peak located at  $953\text{ cm}^{-1}$  is related to the stretching of *Si-O-Na,K*. The peak at  $457\text{ cm}^{-1}$  suggests some six-membered rings exists in the gel. The shoulder at  $1250\text{ cm}^{-1}$  can be attributes to five-membered rings. The broad band extending from  $3700$  to  $2300\text{ cm}^{-1}$  is associated with *X-OH*, where *X = H or Si* [179]. This also indicates that there is a considerable amount of *OH* groups in the silica matrix. The band between  $1660$  to  $1642\text{ cm}^{-1}$  (*H-O-H*) supports that there is molecular water [88].

#### 5.2.2.2.2 Incoherent inelastic neutron scattering

When water and ice is concerned, the neutron vibrational spectroscopy has some advantages over traditional optical spectroscopies based on interaction of light with electrons, such as infrared absorption and Raman scattering. First, because of the rather simple nature of the neutron-nucleus interaction, there are no selection rules in INS; all modes are potentially observed in the neutron vibrational spectrum. This is not the case for IR and Raman spectroscopy. In water and ice, the normal selection rules governing the interaction of light radiation with matter are broken due to the local structural disorder making the spectral analysis complex [214]. In addition to this, even though IR and Raman spectroscopy are very sensitive to the intra-molecular modes involving *O-H* stretching and bending, they are less sensitive to intermolecular modes involving the vibrations of  $H_2O$  molecules against each other [214]. Second, the total neutron scattering cross section of hydrogen is very large (82 barns versus 4.2 barns for oxygen) making observing hydrogen (and, therefore, water) dynamics with INS easier. Third, large amplitude motion translates into large scattering intensities. Hence, water librational, bending, and translational modes show up strongly in the neutron vibrational spectrum, thanks to the relatively large amplitude of motion of hydrogen atoms in these modes. Similarly, the dynamics of silanol groups can be detected in neutron vibrational spectroscopy ( $3650\text{ cm}^{-1}$ ). Furthermore, neutrons penetrate through matter easily, allowing the resulting vibrational spectrum to be an average over the sample volume of several  $\text{cm}^3$ . This is in contrast to optical techniques with infrared or visible light that probe only the sample surface, a potential problem because of water concentration gradients and possible partial surface dehydration in the ASR gel. Thus, INS has been a preferred method to investigate molecular structures in water at a variety of conditions (e.g. [214–216]). In optical spectroscopy measurements based on light scattering, there is nearly zero momentum transfer. Unlike those, in INS there is a significant momentum transfer accompanying the energy transfer. The recoil effects on the unbound molecules during scattering broaden the INS bands significantly. Therefore, by INS, mainly the information on molecular vibrations of bound molecules is obtained making INS an ideal technique to obtain information on bound water in the ASR gel.

Incoherent inelastic neutron scattering (IINS) spectra were collected on the Filter Difference Spectrometer (FDS) at the Manuel Lujan, Jr. Neutron Scattering Center at Los Alamos National Laboratory. This instrument is designed for high count rates using a large  $3\text{ sr}$  ( $9848.4\text{ deg}^2$ ) solid-angle detector [14]. The gels were placed in a sealed cylindrical aluminum sample holder under a helium atmosphere (for heat transfer). The samples were cooled from room temperature to 10 K in a closed-cycle refrigerator on FDS in approximately 3 hours. Initially IINS spectra were collected at 10 K for both gels. Roughly a year later, IINS spectra were collected once more at 10 K and 300 K for  $\text{ASR}_M$ . Then, the  $\text{ASR}_M$  sample was dehydrated in the oven at  $80^\circ\text{C}$ , and the measurements were repeated at 10 K and 300 K. Measured data were a convolution of the scattering law of interest with a resolution function [217]. The FDS spectra were obtained by numerical deconvolution of the instrumental function from the collected raw data. An approximate background correction is obtained through subtraction of the scattering from a vanadium rod placed in the same aluminum sample holder as used in all measurements. Vanadium is a completely incoherent and nearly isotropic scatterer, which serves to illuminate the immediate environment of the sample with the incident neutron energy spectrum. The corresponding vibrational spectrum contains the contribution from this

environment (heat shield, vacuum shroud, sample holder and various aluminum windows).

Figure 5-20a shows deconvoluted neutron vibrational spectra of the gels from 100 to 1300  $\text{cm}^{-1}$  at 10K. The IINS spectrum of ice Ih and Kanemite are also added for comparison. The units are in wavenumber ( $\text{cm}^{-1}$ ) where  $1 \text{ cm}^{-1} = 8.065^{-1} \text{ meV}$ . The intensity could not be normalized to the mass of the sample; as the mass of the samples were unknown. In this range; two types of water motion can be probed; the librational modes and the alkali–water or water–water stretch modes [218]. For a water molecule in a general force field there will be three librations (rock, twist and wag), one for each axis of rotation, but these will only be seen if there is a restoring force present for each libration [218]. For a water molecule attached to one cation there will be one water-cation stretch mode and for two cations there will be two: one for the symmetric stretch and one for the antisymmetric stretch of the two water-cation bonds [218]. There will also be a third normal mode present which changes the angle subtended by the water molecule (Na–W–Na bend), but this involves no motion of the water and thus will not be visible. The two spectra collected a year apart for ASR<sub>M</sub> looks considerably different. This can be due to drying of the sample over time.

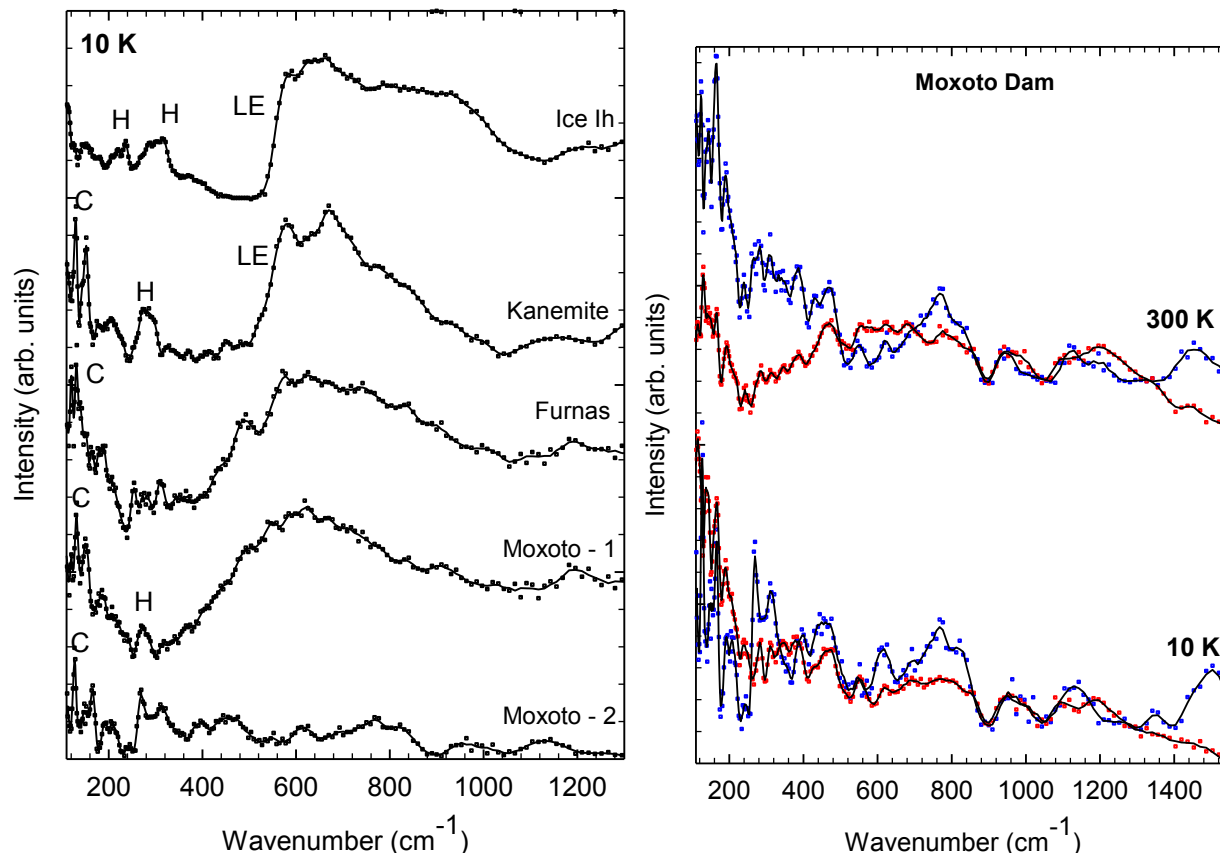
A comparison of ASR<sub>M</sub> to dehydrated ASR<sub>M</sub> spectra at 10 K allows us to differentiate different types of water present in the gel, Figure 5-20b. The vibration around 1000  $\text{cm}^{-1}$  could be assigned to asymmetrical stretch of *Si-O*. This peak is used to normalize the spectra, as this peak is not strongly affected from dehydration. The sharp peak at 140  $\text{cm}^{-1}$  is related with ( $K^+$  or  $Na^+$ ) - water stretch, this peak completely disappears when the gel is dehydrated suggesting that this water is easily lost. The strongest feature of the gel spectra is the broad band from 500 to 850  $\text{cm}^{-1}$ . This band is associated with the librational modes of water. After dehydration, this band disappears suggesting free water loss. The secondary broad bands at 1350 and 1500  $\text{cm}^{-1}$  are very likely to be *OH*-bending. Those bands also disappear after dehydration.

10K spectra can be used to interpret 300K spectra, as for engineering practices the 300 K spectra are more critical. The 300 K spectra for the gel and dehydrated gel are also normalized according to 1000  $\text{cm}^{-1}$  peak. 300 K spectra show a similar behavior to that of 10 K. The peak at 140  $\text{cm}^{-1}$  related with ( $Na^+$  or  $K^+$ ) - water stretch completely disappears after dehydration. The librational band between 500-850  $\text{cm}^{-1}$  is completely lost, suggesting that the free water is lost. The 1500  $\text{cm}^{-1}$  peak related to *OH*-bending also disappears. The 1350  $\text{cm}^{-1}$  peak at 10 K does not exist at 300 K. On a silica surface with silanols there will be several layers of hydrogen bonded water. Probably at 300 K, this ordering is much weaker, thus we don't observe the 1350  $\text{cm}^{-1}$  peak. It is important to note that IINS values are shifted to higher values compared to IR and Raman due to recoil effects.

(a)

(b)





**Figure 5-20. Inelastic neutron vibrational spectra of (a) Ice Ih [219], Kanemite, and ASR gels at 10K, C represents the water-cation (alkali) stretch. H represents hydrogen-bond stretch; (b) Moxoto Dam ASR gel: (blue) initial measurement, (red) measurement after dehydration at 80°C.**

### 5.2.2.3 Nuclear Magnetic Resonance (NMR) Spectroscopy

NMR spectroscopy has been one of the most valuable techniques for probing local geometries of NMR-active nuclei in solids and solutions [190,220]. Currently, the NMR studies on natural ASR gels are limited to synthetic gels or field gels from one source, Furnas Dam [178–180]. In this section, our first goal was using <sup>29</sup>Si and <sup>23</sup>Na magic angle spinning (MAS) NMR spectroscopy to confirm previous findings on the Furnas Dam gel ASR<sub>F</sub>, and to validate the results with a secondary field gel from Moxoto Dam ASR<sub>M</sub>. This allows us to see similarities in local environment in the first few coordination spheres of ASR gels from different sources with different aging histories. In the ASR gel measurements, the same NMR spectrometer used in the opal measurements discussed in chapter 3 was used. For these experiments, only transparent portions of the gels were selected; and finely ground. Then, ground gels were packed into 4mm zirconia rotor and sealed at the open end with a Vespel cap. The samples were spun at 14 kHz on a Bruker Ultrashield 400WB Plus with a 9.4T magnet, operating at 105.84MHz for <sup>23</sup>Na and 79.495MHz for <sup>29</sup>Si. The magic angle in all case was set using KBr to 54.734°. The measured <sup>29</sup>Si MAS-NMR spectra of the two gels are shown in Figure 5-21. The fits to the measured spectra are given in Figure 5-22.

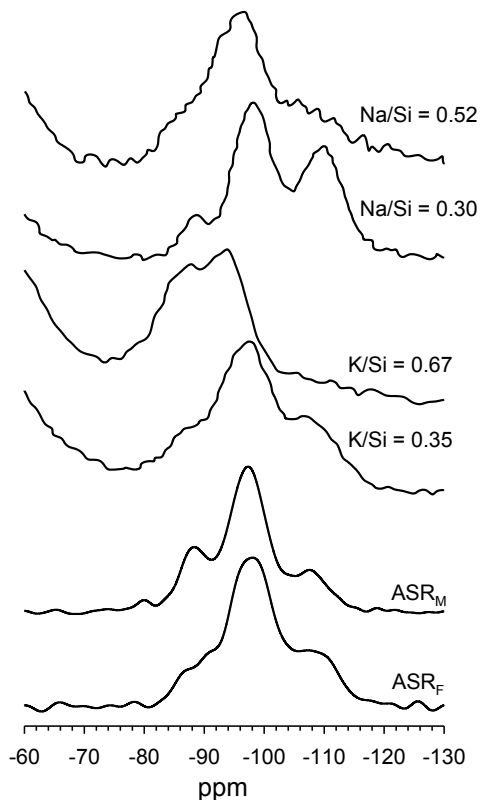


Figure 5-21. Measured  $^{29}\text{Si}$  MAS-NMR spectra for  $\text{ASR}_F$  ( $\text{K/Si} = 0.35$ ,  $\text{Na/Si} = 0.08$ ) and  $\text{ASR}_M$  ( $\text{K/Si} = 0.31$ ,  $\text{Na/Si} = 0.11$ ) compared to synthetic alkali-silica gels from literature [178]. The spectra are scaled to their tallest peak.

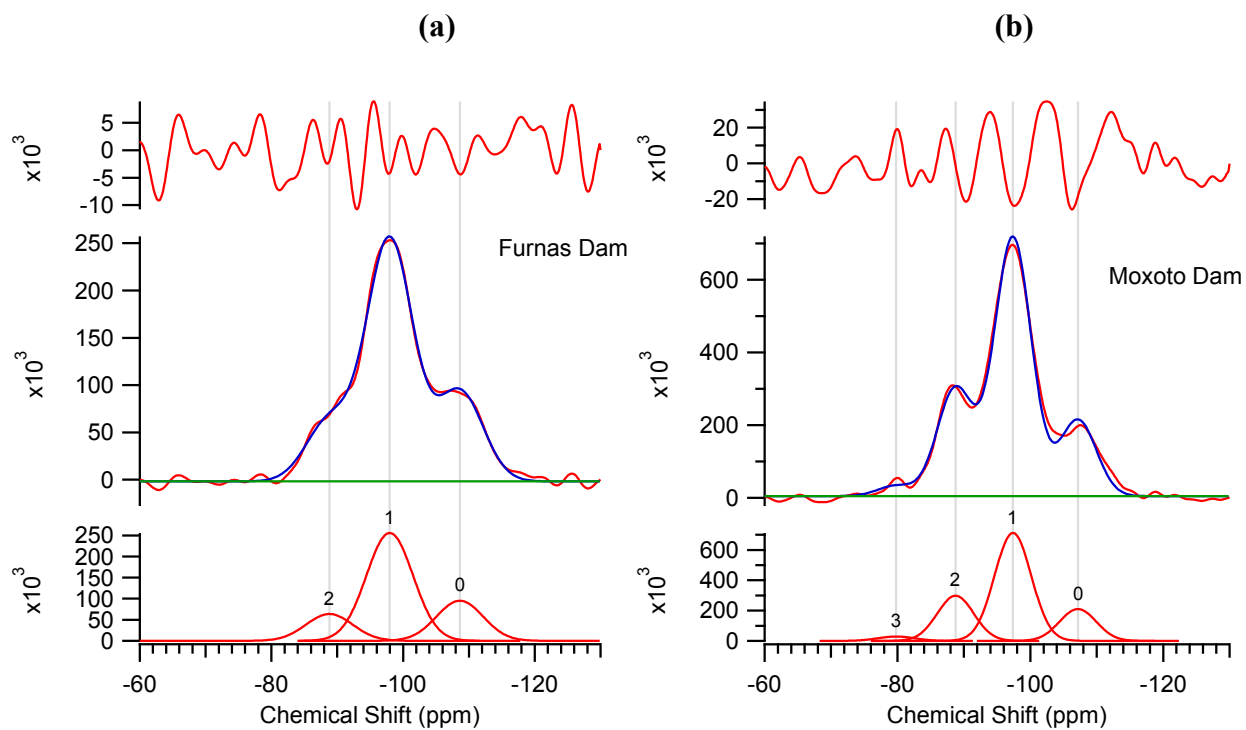


Figure 5-22. Fits to  $^{29}\text{Si}$  MAS-NMR spectra of (a) Furnas and (b) Moxoto Dam gels. The figures include the experimental and fitted spectra (medium: red experimental data, blue: the fitted spectra, green: background), the fitted peaks (bottom), and the residual spectra (top). Q3 sites are dominating both spectra.

For both gels, the  $^{29}\text{Si}$  MAS-NMR spectrum reveals a disordered silicate framework, encompassing  $\text{SiO}_4$  tetrahedra with different degrees of connectivity and structural distortions. The several broad peaks observed in the spectra are typical for a distribution of isotropic chemical shift values caused by structural disorder; and are identified using existing literature on different tetrahedral Qn environments in alkali-silica gel [96,178,179,200].

The quantitative information on the observed Qn species is obtained through least-square fitting of Gaussian functions to the peaks; the results of the deconvolution are summarized in Table 3-2. The Gaussian distributions centered around -80 ppm, -88 ppm, -97 ppm, and -107 ppm are attributed to Q1, Q2, Q3 and Q4 units respectively. The most shielded resonance centered at an isotropic shift of -107 ppm can be attributed unambiguously to Q4 units. The others show a remarkably close agreement with the progressive 10 ppm deshielding expected from each additional non-bridging oxygen [190]. These assignments are in good agreements with previous studies on ASR gel [96,178,179,200] as seen in Table 3-2.

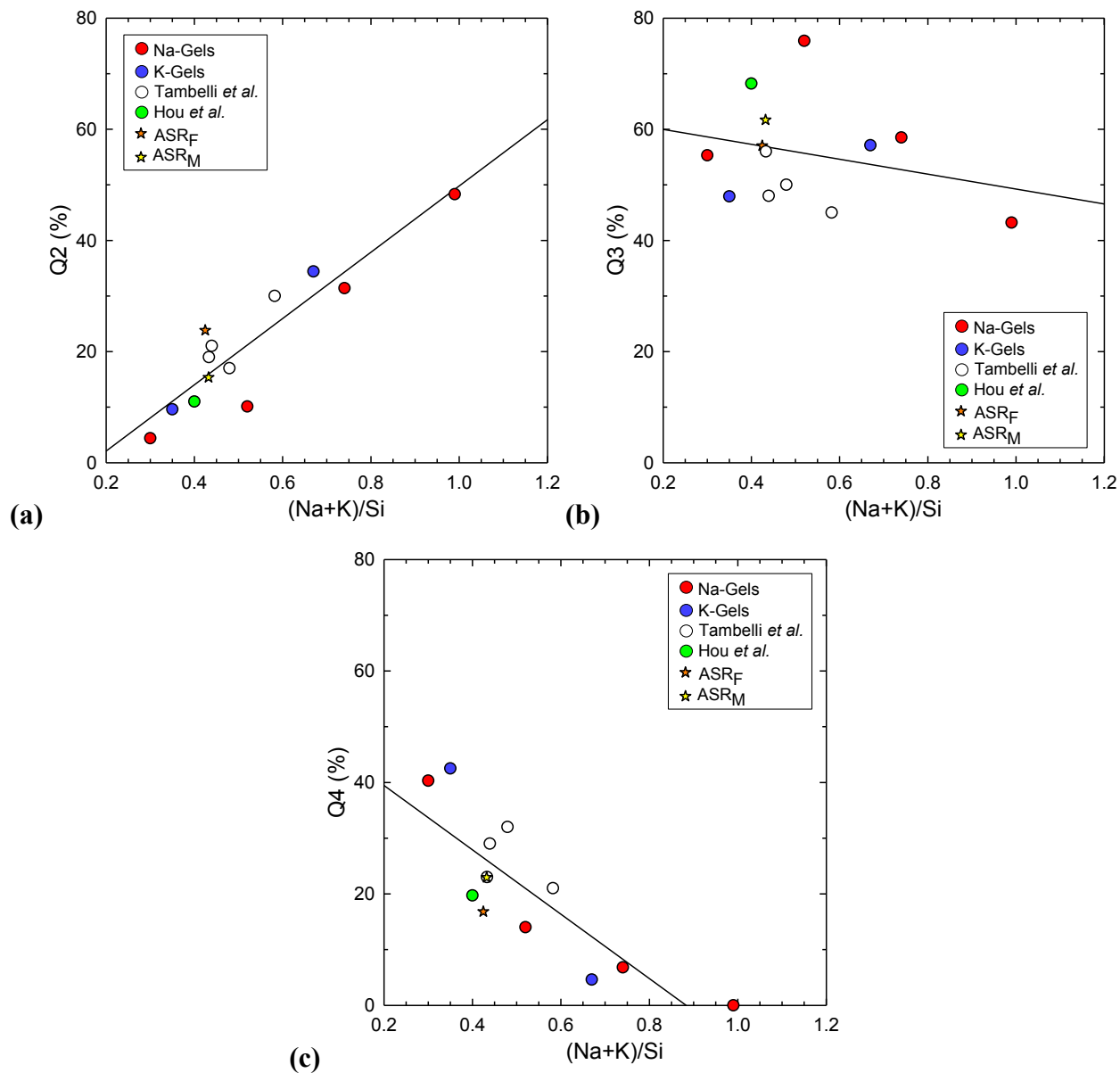
**Table 5-6. Isotropic chemical shift  $\delta$ , relative integral intensity I for Gaussian lines fitted to the  $^{29}\text{Si}$  MAS NMR spectra, and mean number of NBO per silicate tetrahedron for ASR gels collected from Furnas Dam and Moxoto Dam compared to valued obtained from literature for Furnas Dam gel [179].**

Source	(Na+K)/Si	Q1		Q2		Q3		Q4		NBO
		$\delta$ (ppm)	I (%)	$\delta$ (ppm)	I (%)	$\delta$ (ppm)	I (%)	$\delta$ (ppm)	I (%)	
Furnas-A*	0.43	-79.8	2	-88.4	19	-96.9	56	-106.3	23	1.00
Furnas-B*	0.44	-81.1	2	-88.8	21	-97.3	48	-107.3	29	0.96
Furnas-C*	0.58	-78.8	4	-88.0	30	-96.5	45	-105.5	21	1.17
Furnas-D*	0.48	-	-	-88.8	17	-97.8	50	-108.5	32	0.84
ASR <sub>F</sub>	0.43	-	-	-88.8	15	-98.0	62	-108.6	23	0.92
ASR <sub>M</sub>	0.42	-79.8	2	-88.7	23	-97.4	57	-107.2	17	1.12

\* From reference [179]

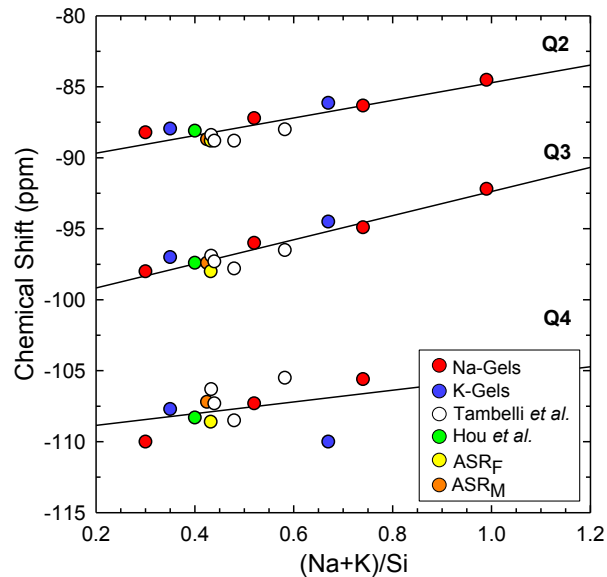
The estimated Q2:Q3:Q4 ratios from ASR<sub>F</sub> and ASR<sub>M</sub> spectra are 15:62:23 and 23:57:17 respectively. Both spectra are dominated by Q3 silicate polymerization, consistent with a locally layered silicate structure [167]. ASR<sub>F</sub> has higher Q4, lower Q2 population when compared to ASR<sub>M</sub> suggesting a more connected gel. Figure 5-23 compares our field gel results with that from literature. It can be seen that as the alkali content increases the Q2 population increases, while the Q4 population decreases. There are detailed studies available in literature on the silicate speciation of alkali-silicate glasses. Consider alkali-silica glasses ( $xM_2O \cdot (1-x)SiO_2$  where  $M$  is the alkali) of similar composition to our gels ( $x = 0.2$ ) [221]. For a K-Si glass, the measured populations are found to be Q3 = 51% and Q4 = 49%; and for a Na-Si glass, those are found to be Q2 = 3%, Q3 = 48% and Q4 = 50%. These values are quite different when compared to our gels. Glasses have much higher Q4, much less Q2 suggesting a much higher Si connectivity. The  $^{29}\text{Si}$  MAS NMR studies on Na-kanemite show only the Q3 signal, meaning

there is only one Si site present in Na-kanemite [201]. This is quite different from the populations obtained for the field gels.



**Figure 5-23. (a) Q2, (b) Q3 and (c) Q4 intensity ratios as a function of (Na+K)/Si for synthetic Na and K gels, and field gel from Hou *et al.* [178] and Furnas Dam field gels from Tambelli *et al.* [179] compared with ASR<sub>F</sub> and ASR<sub>M</sub>.**

Figure 5-24 compares our field gel results with that from literature. It can be seen that with increasing alkali content the <sup>29</sup>Si chemical shift of the Q2 and Q3 sites become progressively less negative (less shielded). The trend for Na and K samples seem to be similar. The field gels also follow this trend, suggesting similarities at the molecular-scale. The slopes of the fitted lines are 6.2, 8.4 and 4.1 ppm per unit (Na+K)/Si for Q2, Q3 and Q4 respectively.



**Figure 5-24. Chemical shifts of  $^{29}\text{Si}$  on Q2 and Q3 sites as a function of  $(\text{Na}+\text{K})/\text{Si}$  for synthetic Na and K gels, and field gel from Hou *et al.* [178] and Furnas Dam field gels from Tambelli *et al.* [179] compared with  $\text{ASR}_F$  and  $\text{ASR}_M$ .**

The mean numbers of non-bridging oxygens per Si tetrahedron (NBO/Si) can be used as a quantitative measure to describe the overall depolymerization of the silicate network [179]. This value is calculated as 0.92 and 1.12 for  $\text{ASR}_F$  and  $\text{ASR}_M$  respectively. For a K-Si glass ( $x = 0.2$ ), the mean NBO per Si tetrahedron is 0.51; and for a Na-Si glass ( $x = 0.2$ ), it is 0.54 [221]. These measured values are close to the theoretical value of an alkali glass ( $x = 0.2$ ) ( $\text{NBO}/\text{Si}_{\text{ASGlass}} \approx 0.55$ ). However, when compared our gels ( $\text{NBO}/\text{Si}_{\text{ASRGel}} \approx 1$ ), a considerable difference is observed. This difference can be explained by the presence of the substantial amount of hydroxyl groups contributing to the depolymerization and disproportion of the silicate network in gels. For Na-Kanemite ( $\text{NBO}/\text{Si}_{\text{Kanemite}} \approx 1.0$ ), this value is very close that of the field gels. Figure 5-25 compares the field gel results with that from literature.

Each NBO requires a net charge of +1 for charge balance. If there are no other charge balancing cations, this imbalance is satisfied with  $\text{H}^+$  coordinated to the NBO [178,222]. Therefore, the mean number of Si-OH groups per Si atom can be calculated from  $(\text{Si-OH}/\text{Si}) = (\text{NBO}/\text{Si}) - (\text{Na}+\text{K})/\text{Si}$ . Figure 5-26 compares our field gel results with that from literature.  $(\text{Si-OH}/\text{Si})$  ratio is 0.49 for  $\text{ASR}_F$ , and 0.69 for  $\text{ASR}_M$ . The kanemite structure, as discussed in section 5.2.1.2, consists of buckled viererkerete (four repeat) silicate sheets with all Si tetrahedral having Q3 polymerization ( $\text{NBO}/\text{Si}_{\text{Kanemite}} \approx 1.0$ ) and half of them having Si-OH NBO ( $\text{Si-OH}/\text{Si}_{\text{Kanemite}} \approx 0.5$ ) [178]. These values are very similar to that of the field gels, suggesting similarities at nanoscale. If the gel had solely kanemite like structure, a dominant Q3 population would be observed due to layered structure, some Q2 population due to sheet edges, and limited Q1 population due to sheet corners. However, the gels have a considerable amount of Q4 population, Therefore, gels cannot be consisting of solely kanemite like fragments possibly due to partial crosslinking.

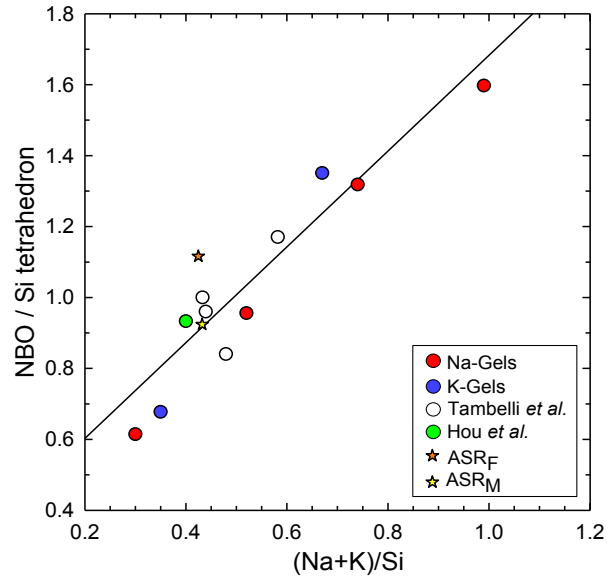


Figure 5-25. Mean number of non-bridging oxygen per Si tetrahedron as a function of  $(Na+K)/Si$  for synthetic  $Na$  and  $K$  gels, and field gel from Hou *et al.* [178] and Furnas Dam field gels from Tambelli *et al.* [179] compared with  $ASR_F$  and  $ASR_M$ .

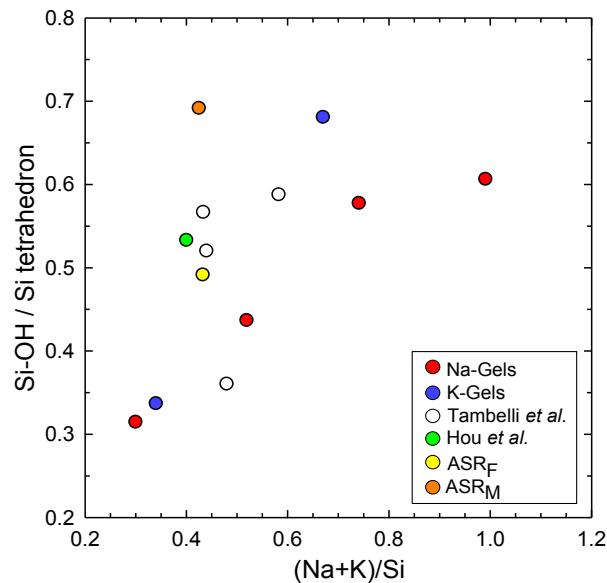
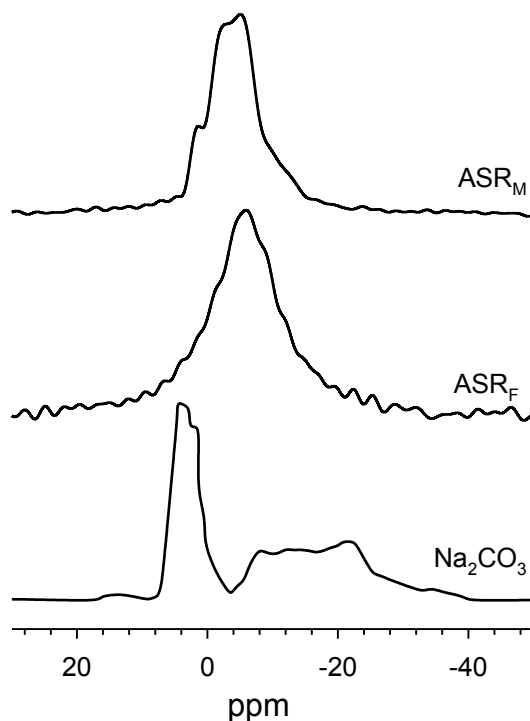


Figure 5-26. Mean number of  $Si-OH$  groups per  $Si$  tetrahedron as a function of  $(Na+K)/Si$  for synthetic  $Na$  and  $K$  gels, and field gel from Hou *et al.* [178] and Furnas Dam field gels from Tambelli *et al.* [179] compared with  $ASR_F$  and  $ASR_M$ .

Minerals and aluminosilicate glasses have been extensively studied by NMR; but the focus has generally been on the network forming cations, Al and Si [223]. Sodium plays a significant role in the ASR gel by balancing some of the negative charges. The  $Na-O$  bonds are more ionic and weaker than  $Si-O$  bonds [224]. The strongly ionic nature of  $Na^+$ , and its inability to form bonds with significant covalent character results in a small overall chemical shift range

with poorly defined  $^{23}\text{Na}$  shift ranges describing Na speciation [225]. Even though there has been very systematic studies to map these ranges [224,226], the  $^{23}\text{Na}$  isotropic  $\delta$  (average  $\delta$ ) chemical shift does not provide an accurate identification of the local Na environment. In general, it can be said that the  $^{23}\text{Na}$   $\delta_{\text{iso}}$  depends on the number and proximity of the oxygen atoms that coordinate Na [227]. It is also observed that  $^{23}\text{Na}$   $\delta_{\text{iso}}$  decreases with increasing Na coordination number and mean Na-O bond length; whereas it decreases with NBO per tetrahedrally coordinated cation. The measured  $^{23}\text{Na}$  NMR spectra are shown in Figure 5-27. The data from literature on the gels report that no differential spin-spin relaxation is occurring across the part of the spectrum used in this study, and therefore the spectra are free from distortions [179].



**Figure 5-27.**  $^{23}\text{Na}$  MAS-NMR spectra of Furnas Dam Gel, Moxoto Dam gels.  $\text{Na}_2\text{CO}_3$  spectrum is also added for comparison as in carbonated samples it might occur [225]. The spectra are normalized to their tallest peaks.

The fits to the measured spectra are given in Figure 5-28. The fit parameters are summarized in Table 5-7. In this study, the center of gravity of the peaks rather than the peak maximum is used. Our results are similar to that of Tambelli *et al.* [179]'s. The broad resonance observed in gels might be due to hydrated  $\text{Na}^+$  ions in the pore water and void spaces within the gel.

The  $^1\text{H}$  MAS NMR spectra of the gels at anhydrous state were also measured, Figure 5-29. The proton NMR experiments were conducted using a WB AVANCE III 600 MHz NMR spectrometer using a Broadband BB/1H 3.2 mm Bruker CP/MAS probe. A temperature of 298K and a spin speed of 20kHz was maintained for all experiments. Each spectrum was induced by a nonselective one pulse using standard (zg) program from Bruker pulse library. The gel was collected from selected areas that had been finally ground, packed in a 3.2mm rotor and sealed at

the open end with a Vespel cap. The rotor was weighed before and after sample packing, in order to attain the weight of the samples. The  $^1\text{H}$  spectrum of a hydrated silica gel spans a broad range of chemical shifts [228], showing a peak maximum near +4 ppm and a tail toward more positive chemical shifts that overlaps the 7-8 ppm range, which corresponds to moderate hydrogen bonding interactions [229].

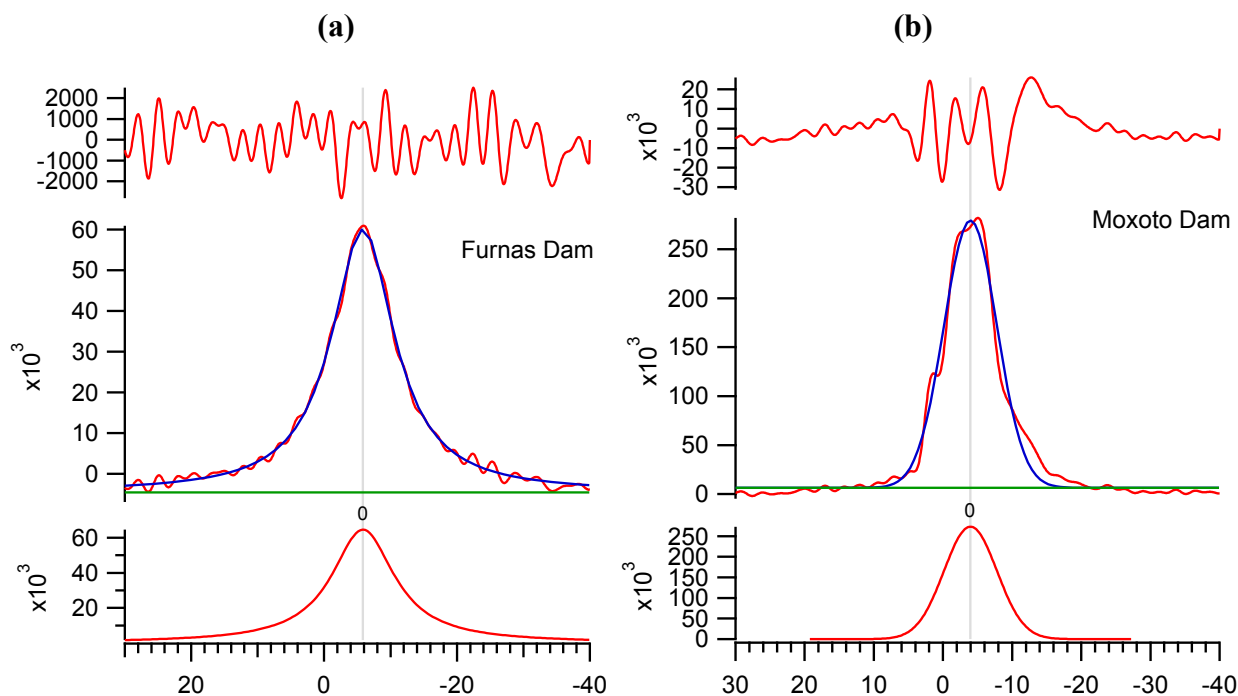


Figure 5-28. Fits to  $^{23}\text{Na}$  MAS-NMR spectra of (a) Furnas, and (b) Moxoto Dam gels. The figures include the experimental and fitted spectra (medium: red experimental data, blue: the fitted spectra, green: background), the fitted peaks (bottom), and the residual spectra (top).

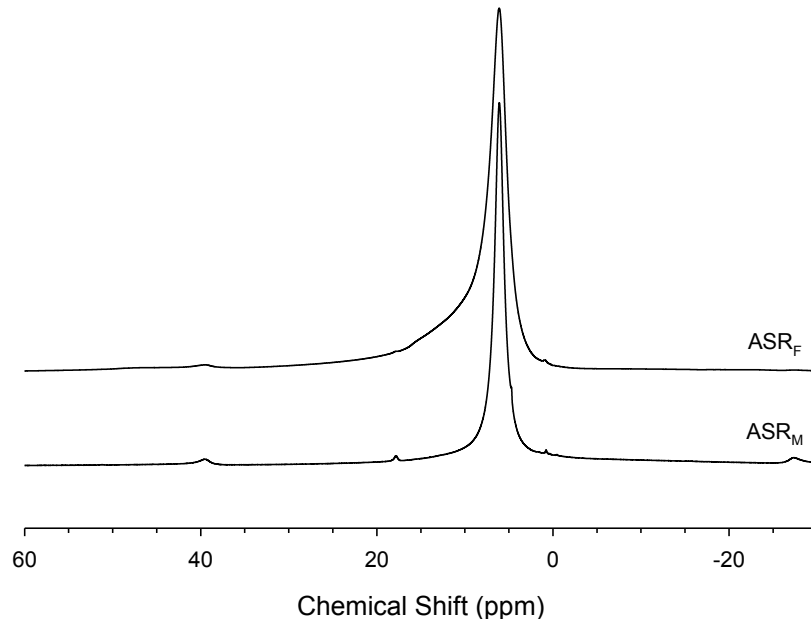
Table 5-7. Parameters of  $^{23}\text{Na}$  MAS spectra fit

Source	Peak	$\delta_{CG}$ (ppm)	FWHM (ppm)
Furnas-A*	Gauss	-5.2	8.1
Furnas-B*	Gauss	-5.3	8.4
Furnas-C*	Gauss	-5.6	8.7
Furnas-D*	Gauss	-6.5	9.2
ASR <sub>F</sub>	Lorentzian	-5.8	11.5
ASR <sub>M</sub>	Gauss	-4.0	9.0

\* Measured with spin-echo technique [179]

These results not only confirm previous NMR findings on Furnas Dam gel, but also present a similar pattern for the Moxoto Dam gel proving that the ASR gel formed under different conditions has a similar structure.





**Figure 5-29.**  $^1\text{H}$  MAS-NMR spectra of Furnas Dam Gel, Moxoto Dam gels. The spectra are normalized to their tallest peaks.

#### 5.2.2.4 Scanning x-ray transmission microscopy (STXM)

In this study, the STXM results were collected at advanced light source (ALS) Beam Line 11.0.2.2. At the beam line, Fresnel zone plates are used for focusing the beam. The resolution of the beam line depends on the spot size; with the current zone plates a resolution of 30 nm is obtained. This beam line is designated for environmental and chemical studies. Details of the method can be found in chapter 2.

The sample preparation was kept simple.  $\text{ASR}_F$  was very finely powdered and placed on a silicon nitride membrane window. The experimental chambers were quickly vacuumed and prepared for the measurements. Sample was focused each time the energy of interest was changed. After focusing, image contrast measurements were performed to identify the elemental locations and line scans were performed on the location of interest to obtain the NEXAFS spectrum. Once it was confirmed that the specific sample area contained interesting spectral information, an image stack was done.

Analysis of the collected data shows that two elements, Na and K, are spatially inversely correlated, *i.e.*, locations with high concentration of Na have low concentration of K, and vice versa resulting in a spatially heterogeneous sample, Figure 5-30.

The potassium map and NEXAFS spectra are shown in Figure 5-31. The spectra look the same regardless of the location. For K, there is not different species or coordination environment as expected, suggesting compositionally homogeneous sample with regard to K.

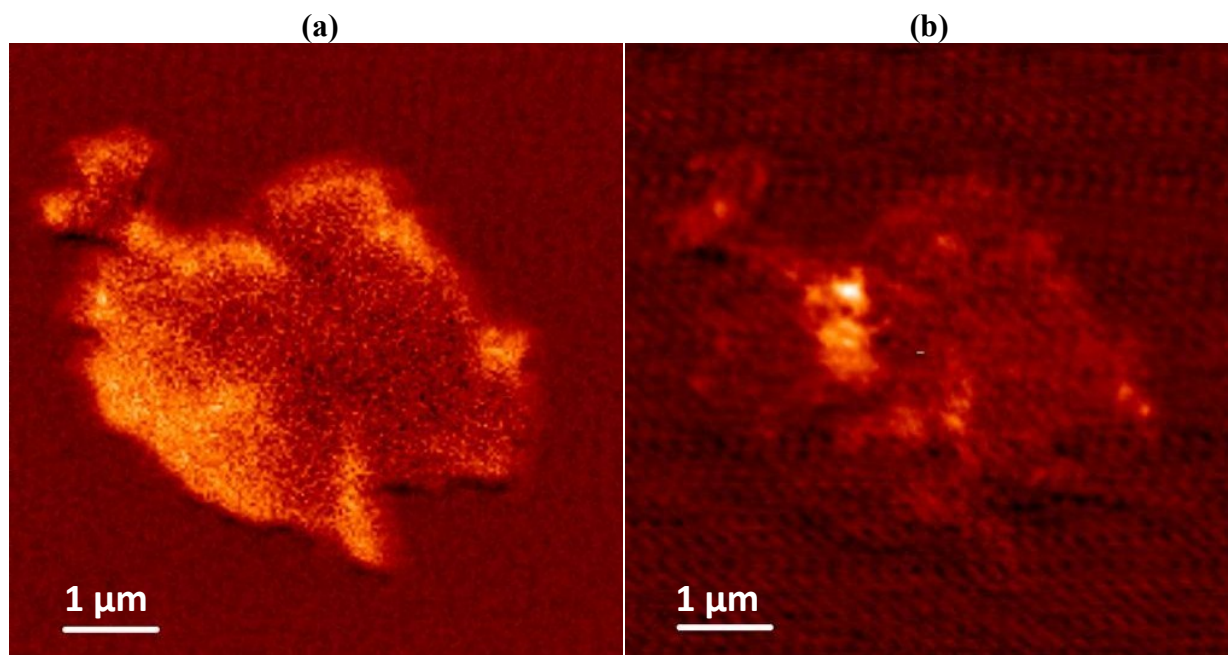


Figure 5-30. (a) STXM image map of sample at potassium  $L_{2,3}$  edge, and (b) STXM image map of sample at sodium K-edge.

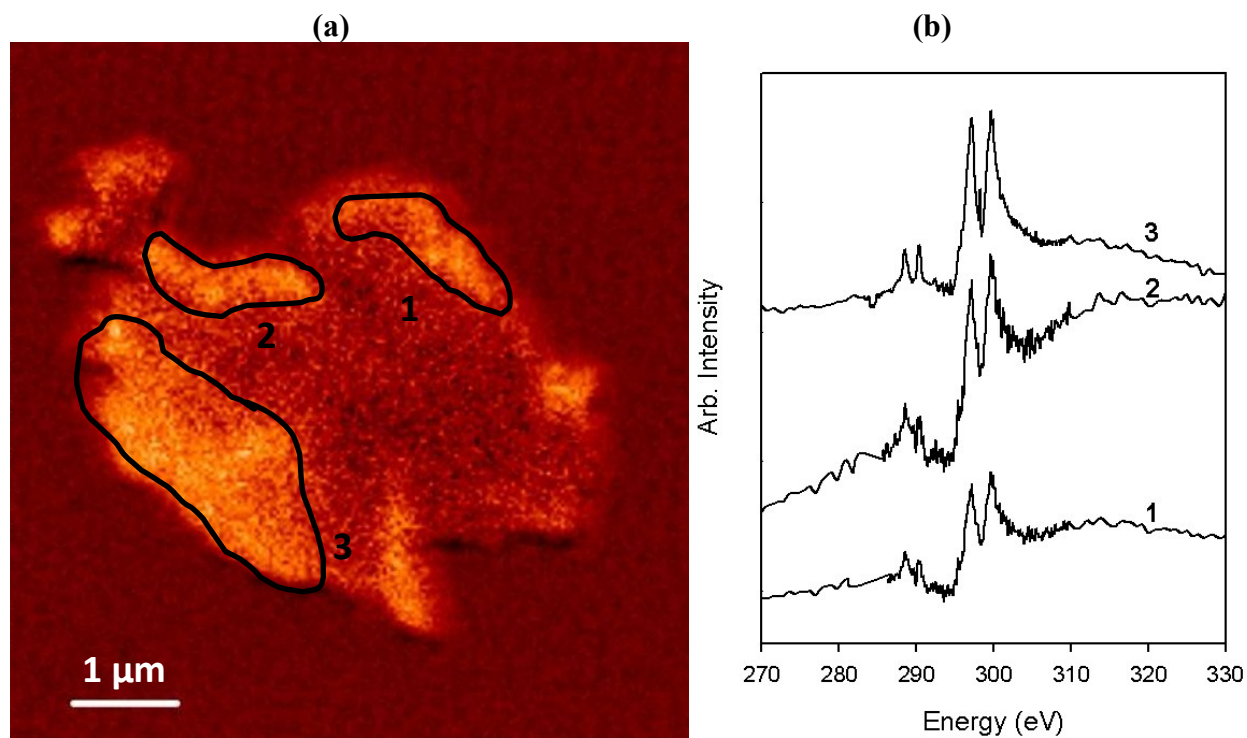
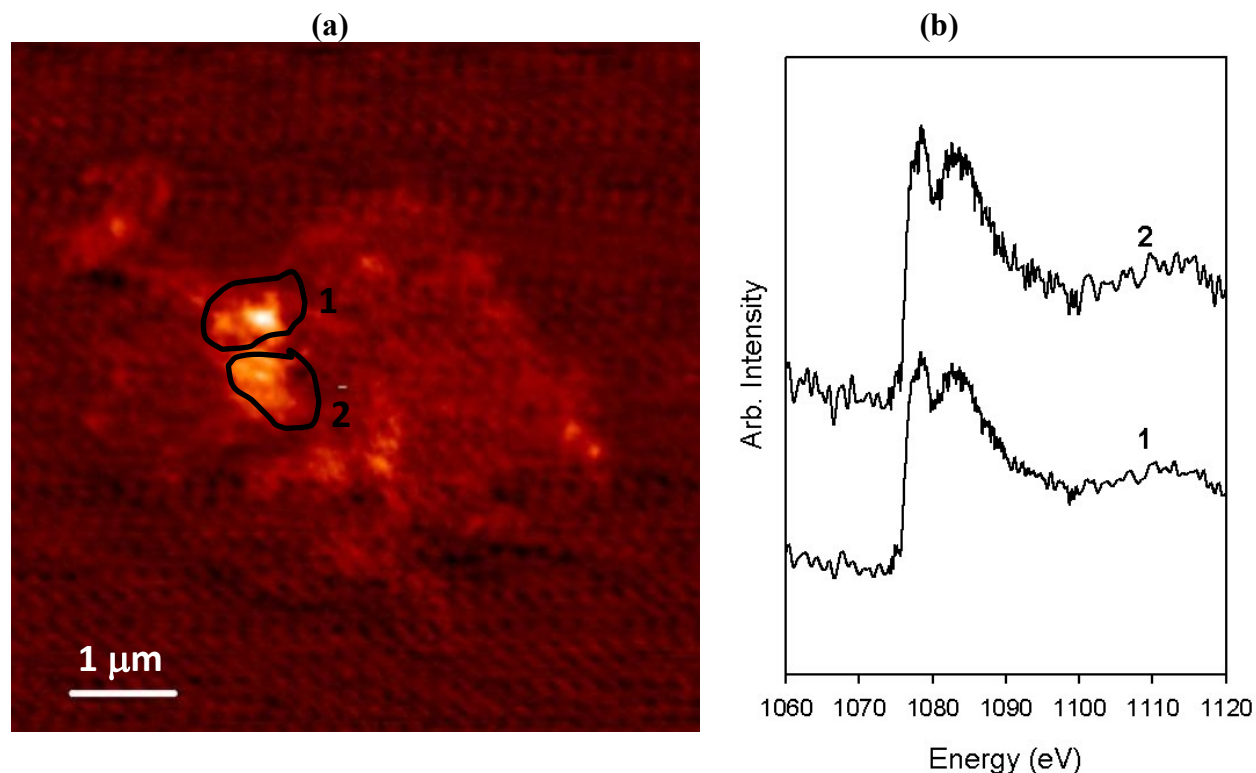


Figure 5-31. (a) STXM image map of sample at potassium  $L_{2,3}$ -edge, and (b) potassium  $L_{2,3}$ -edge NEXAFS spectra of the hot spots shown in (a). Numbers indicate from which the spectrum is taken.

The sodium map and NEXAFS spectra are shown in Figure 5-32. The spectra look the same regardless of the location. For Na, there is not different species or coordination environment, suggesting compositionally homogeneous sample with regard to Na.



**Figure 5-32. (a) STXM image map of sample at sodium K-edge, and (b) sodium K-edge NEXAFS spectra of the two hot spots shown in (a). Numbers indicate from which the spectrum is taken.**

The initial results of our *Si* K-edge measurements on BL 5.3.2 are shown in Figure 5-33. Li *et al.* [230] have shown that *Si* K-edge generally shift to higher energy in its absorption edge with increased polymerization of silicates. Our *Si* K-edge spectra from different locations on the sample show no absorption edge shift. This suggests that there is not a very large difference in the silicate polymerization. The *Si* K-edge can also be used as a fingerprint of the local structural variations in the silicate. A four-oxygen coordinated *Si*, such as in quartz, has a *Si* K-edge absorption edge at around 1846.8 eV whereas six-oxygen coordinated *Si*, such as in stishovite, has its absorption edge at around 1858.3 eV [231]. We observed an edge around 1852 eV. However, we do not have *Si* reference spectra collected at this particular beamline. Therefore, we cannot comment on the *Si* coordination.

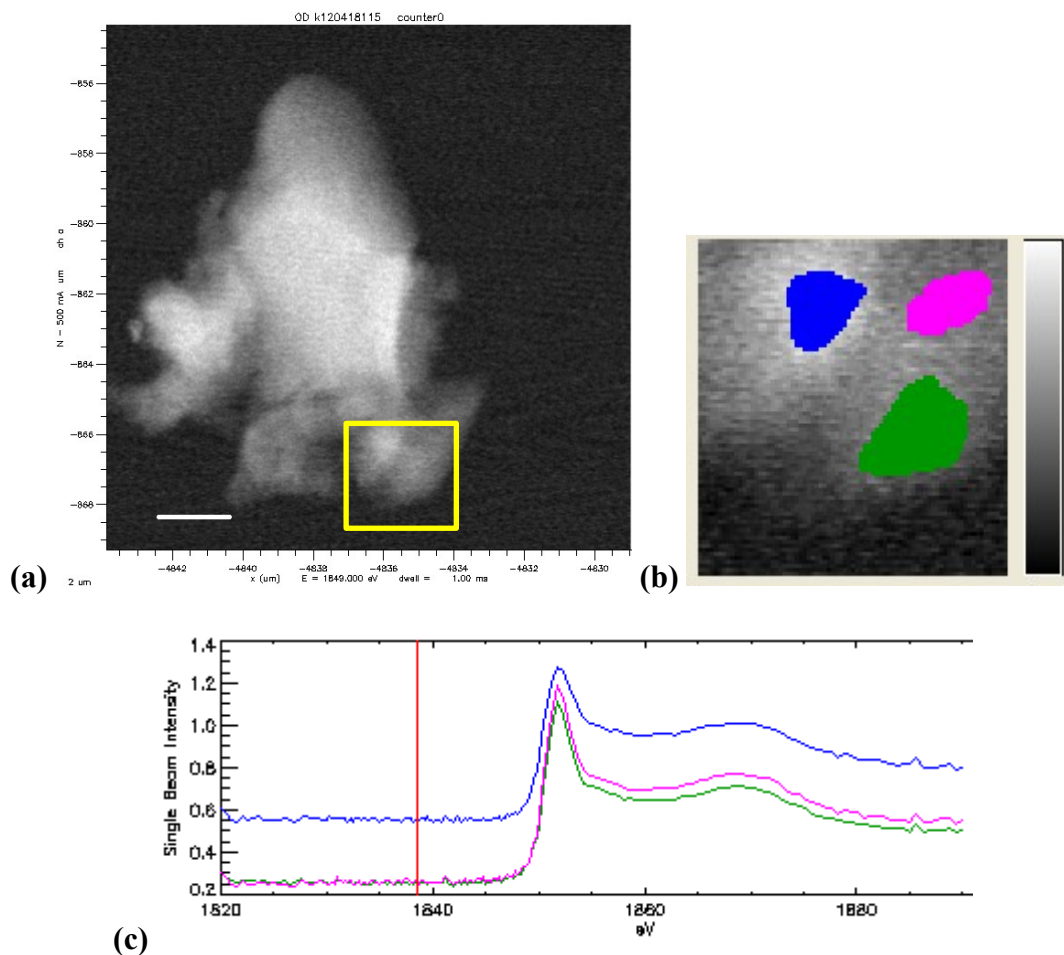


Figure 5-33. (a) STXM image map of sample at sodium Si-edge, (b) close up to the yellow box indicating the locations of the collected, and (c) collected Si K-edge NEXAFS spectra of the chosen areas.

### 5.2.2.5 Total scattering investigations

Benmore and Monteiro [31] recently compared the experimental x-ray PDF of the natural alkali silicate gel from Furnas Dam, Brazil with that obtained from the molecular dynamics (MD) simulation for amorphous Na-kanemite, Figure 5-34. The x-ray PDF results were dominated by scattering from the Si and O atoms (due to their abundance and number of electrons) and showed some evidence of a layering with a periodicity of 9.7 Å. The local silicate structure was similar to the MD Kanemite model, but the experimental O-O peak was considerably broader such that the ordering only persisted over the length-scale of a few polyhedra. This suggests some revisions to the model are required.

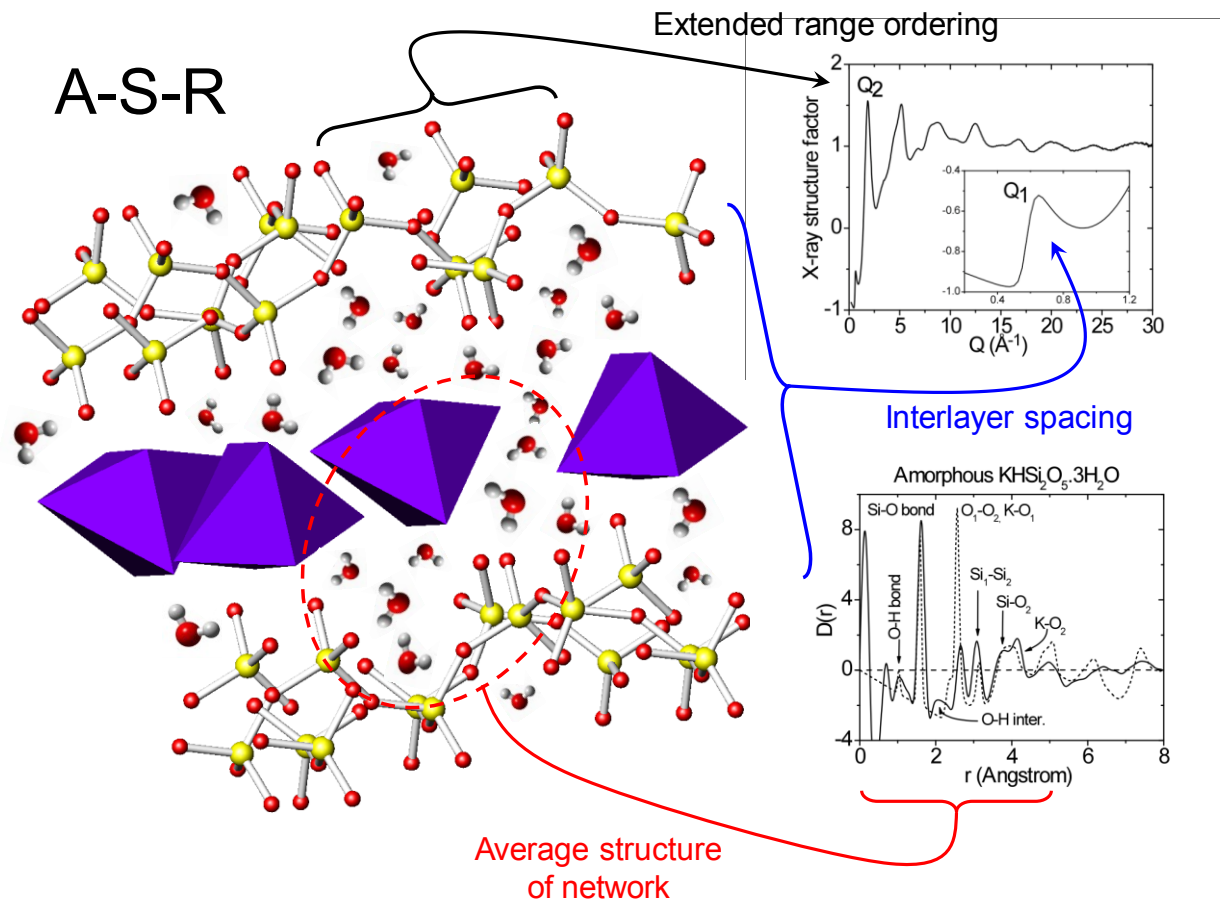


Figure 5-34. (Left) A local structural model of the amorphous K-kanemite ( $\text{KHSi}_2\text{O}_5 \cdot 3\text{H}_2\text{O}$ ) gel consistent with the diffraction data by comparison to the ideal K-kanemite crystal structure [31]. (Right-top) The measured total x-ray structure factor for the amorphous K-kanemite gel from Furnas Dam [31]. (Right-bottom) The x-ray differential distribution function  $\text{DX}(r)$  for the Furnas Dam gel (solid line) compared to the MD Na-Kanemite model [200] (dashed line). Taken from Meral *et al.* [20].

$\text{ASR}_M$  was measured at the high energy x-ray beamline at 11-ID-C at APS, USA operates at 115 keV. Details on the beamline and the total scattering technique can be found in chapter 2. The measured structure factor shows a low peak at  $Q_1=0.65\text{\AA}^{-1}$  similar to  $\text{ASR}_F$  measurements. This small peak, corresponding to a periodicity of  $9.7\text{\AA}$ , does not exist in a  $\text{SiO}_2$  glass [43], or in a K-Si glass [232]. The relatively low intensity of this first peak at  $Q_1=0.65\text{\AA}^{-1}$  implies that the ordering of sheets does not persist much beyond a few layers in real space, see Figure 5-35-a. A broad peak, much stronger than the  $Q_1$  peak, can be found at  $Q_2=1.85\text{\AA}^{-1}$  associated with a periodicity of  $2\pi/Q_2 \sim 3.4\text{\AA}$  due to the chemical ordering of the bulk gel network [233,234]. The similarity of the structure factors of silica glass and  $\text{ASR}_M$  at high- $Q$  is due to the  $\text{SiO}_4$  tetrahedra dominating this region. The  $S_X(Q)$  is Fourier transformed to obtain differential distribution function,  $D_X(r)$  (see Figure 5-35-b) with a Lorch modification function [37] to suppress for artifacts due to the finite measured  $Q$ -range. The obtained  $D_X(r)$  shows a remarkable similarity to  $\text{ASR}_F$  [31].



**Figure 5-35. (a) The measured total x-ray structure factor for Moxoto Dam. (inset) Low-Q measurement focusing on  $Q_1$ . (b) Comparison of the experimental x-ray differential distribution functions  $D_x(r)$  for ASR gels from Moxoto Dam (solid line) and Furnas Dam (dashed line) to amorphous Na-Kanemite simulation by Kirkpatrick *et al.* [31] (blue). Plots are offset for visibility. (blue and dashed lines are scaled down with 0.5) (c) The atom specific weighted partial differential distribution factors for the amorphous Na-kanemite simulation [31]. Taken from Meral *et al.* [20].**

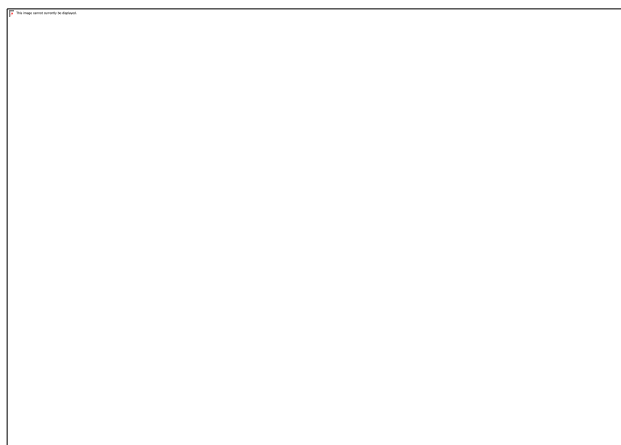
The local structural correlations for  $ASR_M$  are labeled in the light of the information obtained from with Furnas Dam gel and comparison with amorphous Na-Kanemite. Based on the detailed information on varying size polyhedra [235], and prior chemical knowledge of the gel, the peaks at  $1.62 \text{ \AA}$  ( $Si_1-O_1$ ) and  $2.66 \text{ \AA}$  ( $O_1-O_2$ ) in the measured spectra can be confidently assigned to the existence of  $SiO_4$  tetrahedra. A  $K-O$  distance of  $\sim 2.78 \text{ \AA}$  is an indication of  $KO_6$  octahedra. The  $KO_6$  peak for our system is most likely hidden under the  $O-O$  peak as is in the Na-Kanemite MD simulation, Figure 5-35-c. The difference in the first nearest neighbor oxygen-oxygen ( $O_1-O_2$ ) peaks of the simulation and the  $ASR_M$  measurement is substantial. The measured peak is much smaller and broader indicating that the silica tetrahedra are considerably more distorted than the MD model predicts. This suggests a more disordered network structure beyond the distance of a few interconnected polyhedra supporting previously found results of Benmore and Monteiro [31]. The following peaks  $3.08 \text{ \AA}$  ( $Si_1-Si_2$ ), a low-r shoulder at  $3.8 \text{ \AA}$  ( $Si_1-O_2$ ) and a larger peak at  $4.13 \text{ \AA}$  ( $K-O$ ) is identified as other dominant correlations in Figure 5-35-b.



When compared with the simulation results, the measured higher-r peaks are notably smaller and broader with multiple contributions. No distinct structural correlations can be observed beyond  $\sim 10$  Å. These findings support that ordering persists within only a length scale of four or five polyhedra as is the case for the gel from Furnas Dam. The 4.97 Å peak is carefully compared with MD simulation. In the simulation, the 5 Å peak has two contributions; the Si<sub>1</sub>–Si<sub>3</sub> at 4.8 Å and the O<sub>1</sub>–O<sub>2</sub> at 5.08 Å. This implies that the average orientations of the second and third nearest neighbour SiO<sub>4</sub> tetrahedra are much more disordered than those in the regularly aligned corrugated crystalline sheets, and this may allow some water molecules to penetrate the silicate layers. [31]

The PDF analysis results on ASR<sub>M</sub> are consistent with MD simulation findings [178] suggesting that the water penetration to the interlayer volume in significant quantity is not energetically favorable, and that for the large expansions observed in the gel, a continuous polymerized silicate layer is unlikely. The distorted alkali silica structure seems to be a good starting structure; however the PDF data also indicates a need to refine this model. Benmore and Monteiro [31] provided a revised structural model for KHSi<sub>2</sub>O<sub>5</sub>:3H<sub>2</sub>O gel which involves distorted silicate layers (Figure 5-34) showing no distinct preferred orientational correlations beyond  $\sim 10$  Å. The lack of long range ordering in both Furnas and Moxoto Dam ASR gels support that the water molecules are probably located in pores surrounding these alkali silica fragments, as well as within the layers themselves.

Total scattering measurements are also conducted on gel exposed to 100% relative humidity, as understanding how the gel expands is very critical. For both ASR gels, in dry condition, x-ray diffraction patterns exhibit a broad principal peak at  $Q_2 \sim 1.9 \text{Å}^{-1}$  and a sharp smaller low-Q peak at  $Q_1 = 0.66 \text{Å}^{-1}$  which is associated with distorted alkali silica fragments containing pores of water ( $2\pi/Q_1$ )  $\sim 9.5$  Å in size. The  $Q_1$  peak broadens and moves to slightly lower Q-values when hydrated, indicating a larger distribution of the water containing pores (see Figure 5-36). The pores have a periodicity of around 10.5 Å when the gel is mixed with water, but exposing the gel to 100% relative humidity over the course of just 18 hours allows the gel to soak up even more water, creating pore sizes with a periodicity of at least  $\sim 16$  Å.



**Figure 5-36. The measured total x-ray structure factors for the alkali silicate gel (formula  $\sim$  KHSi<sub>2</sub>O<sub>5</sub>:3H<sub>2</sub>O) with various amounts of water. For comparison purposes all spectra were normalized**

at high  $Q$  ( $>10 \text{ \AA}^{-1}$ , see insert) to that of pure ASR gel. The changes in low- $Q$  structure indicate the changing pore size as the gel swells. Curves: ASR +30% water (black), ASR with 70% water (red), ASR gel in 100% relative humidity for 18 hours (blue) and dry ASR gel (green).

The similarity in shape of the real space differential distribution functions for dry and saturated ASR gels between 2-10 $\text{\AA}$  (shown in Figure 5-37) demonstrate that fragments of the distorted silicate layers remain intact, although the systematic inward shift by  $\sim 0.2 \text{ \AA}$  of all the peaks to lower  $r$ -values indicates that the layers become compressed as water is absorbed. This also suggests that no matter how much water is absorbed by the gel the water molecules mostly reside in pores surrounding alkali-silica fragments, as previously predicted by molecular dynamics simulations. The sharp O-H peak at  $\sim 1 \text{ \AA}$  and the large  $1.6 \text{ \AA}$  peak intensity in the differential distribution functions of the water saturated gels is much larger than that observed for bulk water or the dry ASR gel, suggesting a strong interfacial water-kanemite interaction.

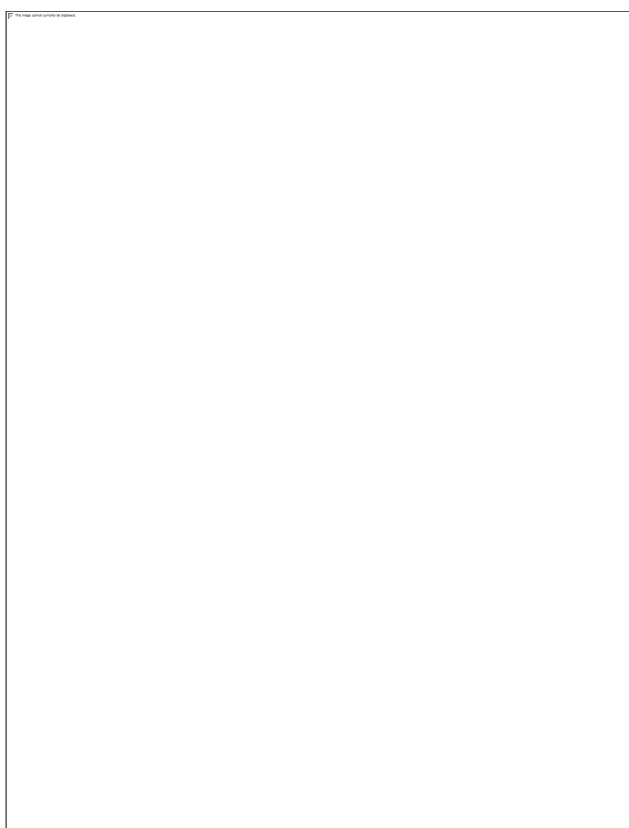


Figure 5-37. The differential distribution functions  $D(r)=4\pi r^2[G(r)-1]$ , where  $G(r)$  is the radial distribution function, show very similar high- $r$  features confirming that fragments of the kanemite structure remain intact in the swollen gel. The increase of intensity of the  $\sim 1 \text{ \AA}$  and  $1.6 \text{ \AA}$  peaks indicate strong interfacial-water correlations exist in the saturated gels. Curves from the top down: ASR gel in 100% relative humidity for 18 hours (solid blue line) versus the sum of the ASR gel plus bulk water curves (black dotted line). ASR gel plus water 30% (solid black line) and 70% (solid red line). ASR gel (solid green line). The bottom magenta curve is that of bulk water.



### 5.2.2.6 Small angle neutron scattering

The small angle scattering studies [184–189] conducted on silico-(calco)-alkaline gels are limited to freshly formed gels from precursor sols at a relatively short amount of times. However, in concrete the ASR gel is formed within the cement matrix at a much slower pace; and commonly, the formed gel is considerably aged possibly for several years, even decades. Hence, our SANS investigation on ASR gels has two main goals: first, to see if the gels from different sources have similar structures at the experimental range; second, to observe the changes in the gel structure after introduction of moisture.

$R_m$  ( $[SiO_2/A_2O]$ ;  $A = Na \text{ or } K$ ) for  $ASR_F$  and  $ASR_M$  are 4.63 and 4.71 respectively. The higher molar ratios of the ASR gel ( $R_m > 2$ ) supports an initial formation and growth of the pre-gel through hydrolysis and condensation reactions leading into a final gel state as discussed in section 5.1.1.3. The resulting ASR gel can be considered as an infinite product with a continuous skeleton enclosing a continuous liquid phase. Even though the concrete pore solution is high in Ca, when the ASR takes place the local Ca-concentration is relatively low. In this low-Ca environment, possibly reaction limited cluster aggregation (RLCA) takes place. In RLCA, the the sticking probability is low, and the clusters need to be in contact many times before they stick (in DLCA clusters stick every time they meet). Details of RLCA are described in chapter 4.

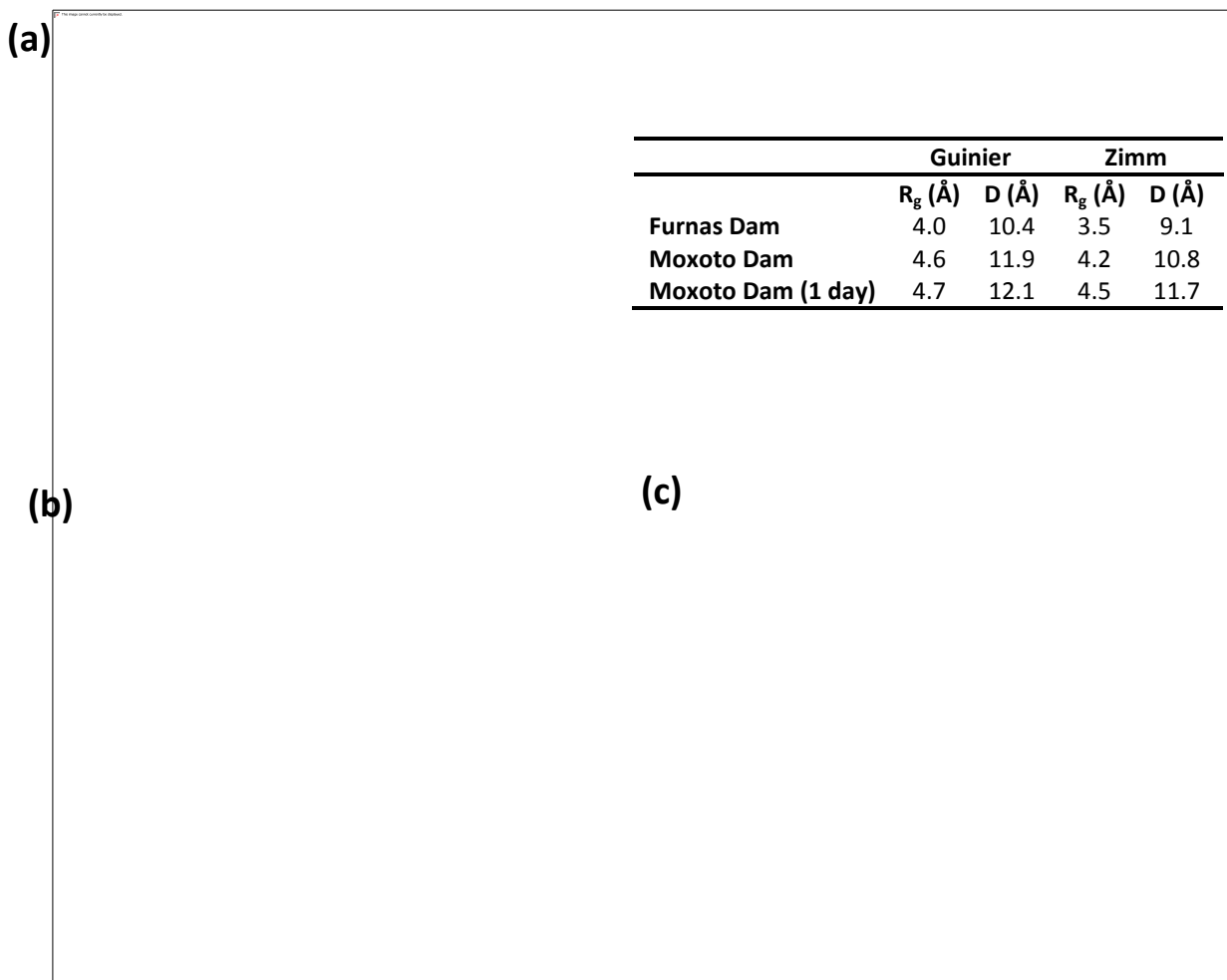
Reaction-limited conditions (most common condition for most silicate synthesis schemes) imply that the condensation rate is sufficiently low with respect to the transport (diffusion) rate that the monomer or cluster can sample many potential growth sites before reacting at the most favorable one [159]. In monomer-cluster aggregation (MCA), growth occurs by the addition of monomers to higher molecular weight species (clusters) rather than themselves; thus, MCA requires a continual source of monomers. Because growth occurs monomer-by-monomer under reaction-limited conditions, all potential growth sites are accessible; the result is compact, uniform (non-fractal) objects characterized by  $P = -4$ . The base-catalyzed condensation mechanism favors the reaction of low- and high-molecular weight species; so the growth is biased toward MCA [159]. In cluster-cluster aggregation (CCA), monomers are depleted at an early stage of the growth process; hence further growth occurs by the addition of clusters to both monomers and other clusters. Strong mutual screening of cluster interiors leads to branched objects characterized by a mass fractal dimension  $D \approx 2$  ( $P \approx -2$ ) [155]. MCA and CCA are just two of many plausible growth models, and the predictions of  $P = -4$  and  $P = -2$  for these two aggregation processes are not unique [159].

The SANS measurements in this study are carried out at Low-Q Diffractometer (LQD) at LUJAN Neutron Scattering Center [60]. LQD uses the time of flight technique and can access a broad range of  $Q$  ( $0.003$  to  $0.5 \text{ \AA}^{-1}$ ) allowing to probe structures with dimensions from 10 to 1000  $\text{\AA}$ . Details of the instrument, and the SANS method can be found in chapter 2.

For the measurements, field ASR samples were sliced into thin sections of thickness  $\approx 1$  mm. Then, the samples were placed into the sample holders; and measured for approximately 6 hours. The  $ASR_M$  was then deuterated by storing at 100%  $D_2O$  relative humidity for a day. A secondary SANS measurement was conducted on the deuterated gel.

Collected SANS data were reduced using standard data reduction methods for time-of-flight low-Q data [60] and corrected for empty cell, and background effects. Absolute scattered intensities,  $I(Q)$ , were obtained by comparison to a known standard and normalization to sample thickness. The experimental scattering curves for the ASR gels are given in Figure 5-38a. Two length scales are evident just by visual inspection of the data.

The data is systematically analyzed through Guinier, Zimm and Porod plots. Details of these analysis methods are given in chapter 2.



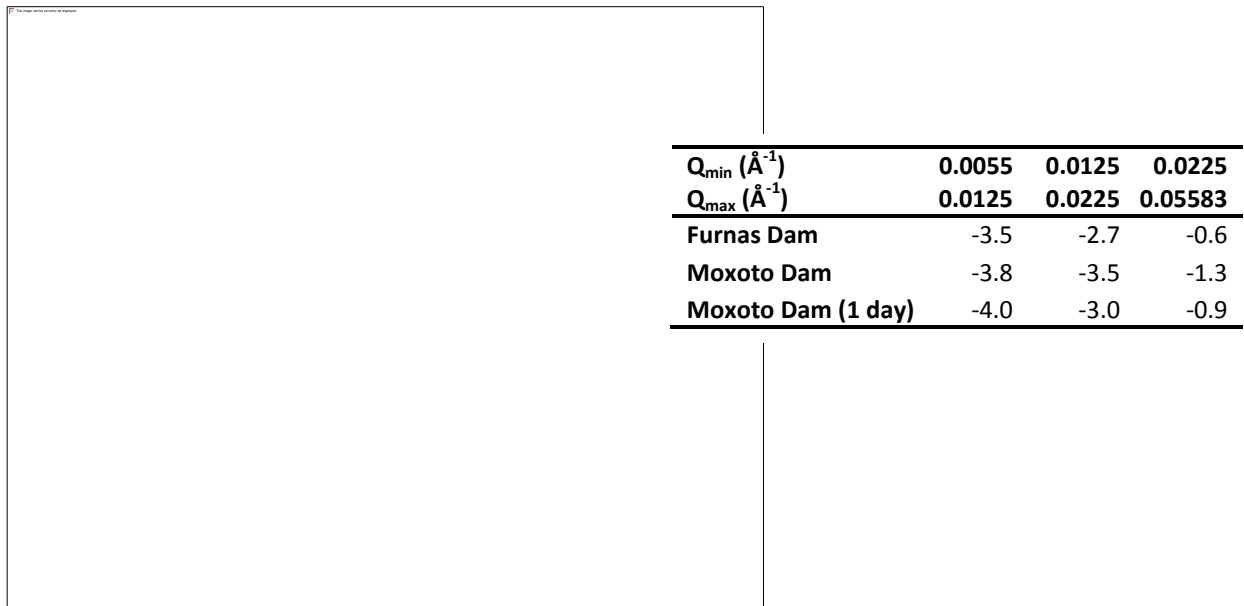
**Figure 5-38. (a) Experimental small angle neutron scattering curves ASR gels, and corresponding (b) Guinier and (c) Zimm plots. (Inset) Summary of the Guinier and Zimm analysis for  $0.06 < Q < 0.27 \text{ \AA}^{-1}$ .**

The Guinier plot for the ASR gels is given in Figure 5-38b. For each ASR gel, the Guinier plot exhibit linearity for  $0.06 < Q < 0.27 \text{ \AA}^{-1}$  region; and in this range, the requirement for Guinier approximation ( $Q \cdot R_g < \sqrt{5/3}$ ) is satisfied. Obtained  $R_g$  from the Guinier analysis are 4.0 and 4.7 Å for  $ASR_F$  and  $ASR_M$  respectively. Accordingly, assuming a spherical morphology, diameters of the scattering objects calculate as 10.4 Å and 11.7 Å suggesting a similar structure for gels from both dams at this length scale. In this region, the  $R_g$  obtained for

the deuterated  $ASR_M$  is  $4.7 \text{ \AA}$  giving a spherical diameter of  $12.1 \text{ \AA}$ . The increase from  $11.7$  to  $12.1 \text{ \AA}$  of the spherical diameter of  $ASR_M$  after deuteration is an indication of possible expansion at this length scale. The Guinier requirement is not satisfied for other length scales; probably due to aggregation or interparticle interference effects; thus, the Guinier analysis would not produce accurate results.

For  $0.06 < Q < 0.27 \text{ \AA}^{-1}$  region, Zimm analysis is also conducted, Figure 5-38c. As mentioned in chapter 2, Zimm plot provides a shape independent radius like the Guinier approximation; and is valid in  $Q \cdot R_g < \sqrt{3}$  region. Through the linear regression fits,  $R_g$  for  $ASR_F$  and  $ASR_M$  are obtained as  $3.5$  and  $4.2 \text{ \AA}$  giving  $9.1$  and  $10.8 \text{ \AA}$  as spherical radii, respectively. The fits to the deuterated  $ASR_M$  Zimm plot results in a  $R_g$  of  $4.5 \text{ \AA}$  with a corresponding spherical diameter of  $11.7 \text{ \AA}$ . The proximity of the Zimm and Guinier analysis results strengthen the results for  $0.06 < Q < 0.27 \text{ \AA}^{-1}$  region.

As previously discussed in chapter 2, the fractal dimension  $D$  quantifies how the mass  $M$  of an object is increases with length  $r$ :  $M \sim r^D$ , whereas the magnitude of the fractal dimension is related with the openness of a structure. As the structure gets more open the fractal dimension gets smaller. The fractal dimension is measured from the power-law decay of the static structure factor in the Porod region determined by small-angle scattering. For the field  $ASR$  gels, Porod slopes are obtained for three different regions; (1)  $0.0055 < Q < 0.0125 \text{ \AA}^{-1}$ , (2)  $0.0125 < Q < 0.0225 \text{ \AA}^{-1}$ , (3)  $0.0225 < Q < 0.0558 \text{ \AA}^{-1}$ , see Figure 5-39. The figure looks considerably different.



**Figure 5-39. Log-Log plot of  $I(Q)$  against  $Q$  for the gels. (Inset) Porod slopes for the selected regions.**

In region 1, the Porod slopes are  $-3.5$  for  $ASR_F$  and  $-3.8$  for  $ASR_M$  giving surface fractal  $D_s$  dimensions of  $2.5$ , and  $2.2$  respectively. This suggests that  $ASR$  gels have rough surfaces. The porod slope of deuterated  $ASR_M$  is  $-4.0$ , suggesting a smooth surface with  $D_s = 2$ . The wetting of

the gel might have resulted in a smoother gel surface. The Porod approximation is not accurate for the regions 2 and 3. The high porod slopes supports that we have cluster-cluster aggregation.

Calculation of the scattering length densities for natural and deuterated samples is also of importance. The scattering length density for the gel ( $\rho_{ASR}$ ) is calculated from the average chemical composition (*Si21.K5.Na2.O56.H17*) and density value ( $2 \text{ g/cm}^3$ ) as  $2.58\text{E-}6 \text{ \AA}^{-2}$ . For a dry sample, the surface area is between the gel and the pores. Neutron scattering contrast  $\Delta\rho$  would be equal to  $\rho_{ASR}$ . For a deuterated ASR sample, the surface area is the area between the ASR gel and water in the pores. The neutron scattering contrast could be calculated from  $(\Delta\rho)^2 = (\rho_{ASR} - \rho_{D_2O})^2$ . If it is assumed no hydrogen/deuterium exchange takes place in the gel,  $(\Delta\rho)^2 = (2.58\text{E-}6 - 6.33\text{E-}6 \text{ \AA}^{-2})^2 = (-3.75\text{E-}6 \text{ \AA}^{-2})^2$ . However, the exchange is inevitable. In the case of full exchange,  $(\Delta\rho)^2 = (3.77\text{E-}6 - 6.33\text{E-}6 \text{ \AA}^{-2})^2 = (-2.56\text{E-}6 \text{ \AA}^{-2})^2$ .

## 5.3 Conclusions

Alkali silica reaction is not well understood at the molecular and nanometer level [167]. To develop effective repair methods requires a better understanding of not only the reaction, but also the reaction product – the ASR gel. The  $^{29}\text{Si}$  NMR analysis showed that ASR gels coming from different sources have similar disordered silicate network structures with different degrees of connectivity, specifically sheet-like (Q3), some fully polymerized (Q4), and chain-like (Q2) silicate units. When compared to alkali-silicate glasses of similar composition, the depolymerization degree of the gels is much higher ( $\text{NBO}_{ASGlass} \approx 0.5 < \text{NBO}_{ASRGel} \approx 1$ ). This difference is due to the presence of a substantial amount of hydroxyl groups contributing to the depolymerization and disproportion of the silicate network in gels.

Analysis of the STXM data shows that two elements, *Na* and *K*, are spatially inversely correlated throughout the gel. For the *Na* and *K*, there is not different species or coordination environment as expected, suggesting compositionally homogeneous sample with regard to *Na* or *K* respectively.

Pair distribution function analysis agreed with previous literature on the persistence of a local amorphous poorly layered alkali-silicate structure. [31] The analysis also confirmed that in the ASR gel, the water molecules mostly reside in pores surrounding alkali-silica fragments. The alkali silica fragments have a periodicity of around  $10.5 \text{ \AA}$  when the gel is mixed with water, but exposing the gel to 100% relative humidity allows the gel to soak up even more water, creating sizes with a periodicity of  $\sim 15 \text{ \AA}$ .

The SANS analyses show two evident length scales. When the high-Q data is considered, the Guinier and Zimm approximations agree on the small length scale which is presumably due to voids in the gel, estimating a spherical radius of  $11 \text{ \AA}$  for gels at natural state, and  $12 \text{ \AA}$  for gels deuterated for 1 day. This result agrees with pair distribution analysis findings.

The INS measurements showed some of the different types of water: free water, *Na* or *K* bound water, and hydrogen bound water. It is important to note that the structurally disordered

ASR gel might have a locally poorly layered structure with some interlayer space for water incorporation. However, the silicate particle surfaces containing both anionic non-bridging oxygens (Si-O-) and Si-OH groups provide a structure on which the alkali cations and water molecules are organized to build an effective hydrogen bonding network that stabilizes large amounts of water in the gel.

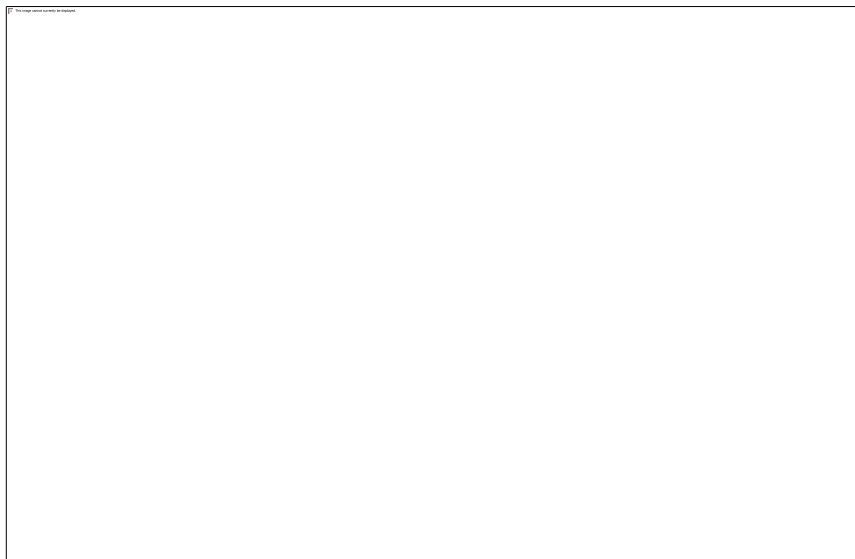
The results are consistent for gels from both sources suggesting that ASR gels formed at different locations have similar structures.

# 6

## Fly Ash

Coal fly ash is an aluminosilicate rich byproduct of combustion of pulverized coal in thermal power plants. It is recovered by filtering operations of the gases emitted during combustion. The fly ash particles are generally finer than cement and mainly consist of spherical glass particles with a basalt-like composition [236] (> 60wt%) with residual hematite ( $\text{Fe}_2\text{O}_3$ ) and magnetite ( $\text{Fe}_3\text{O}_4$ ), char, and some crystalline phases formed during cooling such as mullite ( $3\text{Al}_2\text{O}_3 \cdot \text{SiO}_2$ ), quartz ( $\text{SiO}_2$ ) and sillimanite ( $\text{Al}_2\text{O}_3 \cdot \text{SiO}_2$ ). With global production of approximately 650 million tonnes annually, it is one of the most available, highly amorphous aluminosilicate waste materials [237,238]. The US 2010 fly ash production is around 68 million tons, Figure 6-1a. 62% of the produced fly ash is being dumped into landfill sites and the sea; and only the remaining 38% is utilized in a variety of applications, Figure 6-1b [22]. Some of it is being effectively utilized in pozzolanic cement and concrete production. A limited amount is consumed in manufacturing of sintered materials such as tiles. Using alkali activated fly ash (AAFA) in production of environmentally friendly concretes with favorable mechanical and engineering properties [23] is slowly gaining traction.

(a)



(b)

### US Fly Ash Usage Categories (2010)

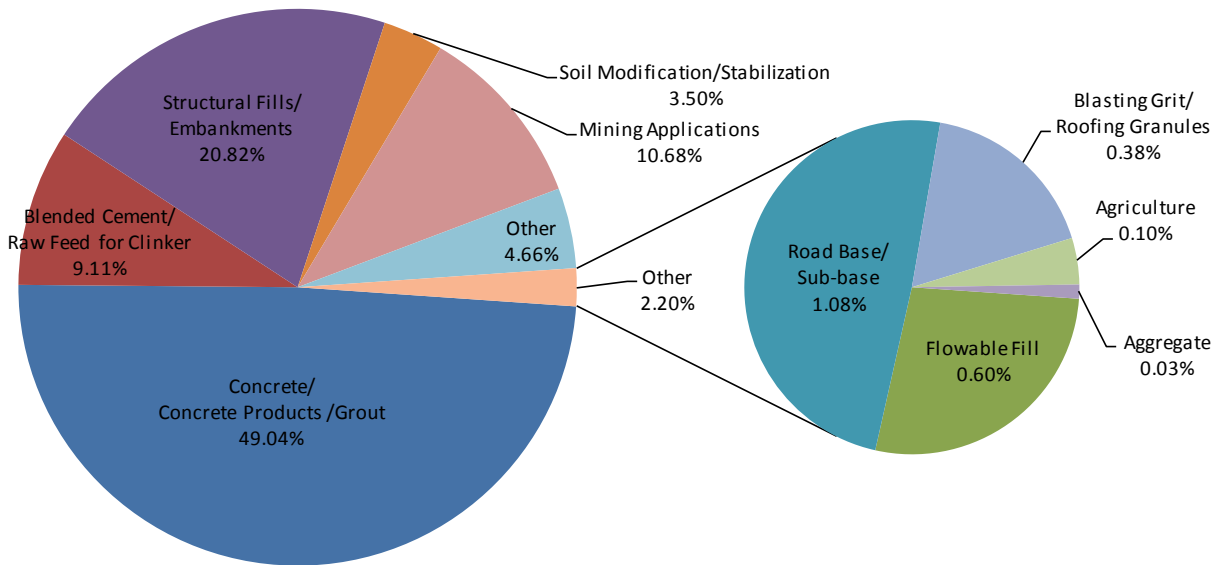


Figure 6-1. (a) US fly ash production and consumption, 1966-2010 [21]; (b) US Fly ash usage categories for 2010 [22].

This chapter starts with briefly introducing two major applications of fly ash in concrete sector: (1) as a pozzolanic material for portland cement replacement; and (2) as an aluminosilicate source for alkali activation. After that, the chapter focuses on the characterization of glassy portion of fly ash glass at an atomic level. This basalt-like glassy portion is of importance as it is the most reactive component of fly ash for construction related applications. First, NMR investigations on the glass are presented. Then, an MD model of the fly ash F glass is provided. High energy X-ray beamline at 11-ID-C at the APS operating at 115 keV was utilized for total scattering investigations to obtain information on the bond length distribution within the glass and to validate the MD model. Beamline 5.3.2 of ALS for STXM measurements was used to prove the local environment of Al and Si.

## 6.1 Using fly ash in cement and concrete industry

Fly ash containing concretes have been utilized successfully in many projects with technical and environmental advantages as a low-cost green alternative to conventional portland cement concrete. One approach is using fly ash as a pozzolanic replacement for portland cement in concrete. The other approach is using fly ash as an aluminosilicate in alkali activated aluminosilicate concrete.

### 6.1.1 Using fly ash as a portland cement replacement

Eliminating a large portion of CO<sub>2</sub> emissions through the concrete sector requires replacing large quantities of portland cement by a low carbon alternative. Fly ash has been one of the top replacement alternatives with its highly pozzolanic nature for many decades yielding in cost-efficient concrete mixtures with high workability, high ultimate strength, and high durability [19]. The details of pozzolanic reaction is out of scope of this research, and further details on the reaction mechanism can be found in [3,239].

To illustrate how green fly ash concretes are, three representative mixes studied in the lab are briefly discussed below. The chosen mix proportions have varying fly ash contents (0 wt%, 30 wt% and 50 wt%) as portland cement replacement, Table 6-1. Also, all of the chosen mixes have very high workability at a relatively low water-to-binder ratio ( $w/b = 0.35$ ) as seen from their high slump flow diameters  $d_s$ .

**Table 6-1. Concrete mix proportions and the slump flow diameter for each mix [240].**

$(w/b = 0.35)$	Proportions					OPC Content (kg/m <sup>3</sup> )	$d_s$ (mm)
Mix label	OPC	Fly ash F	Fine aggregate	Coarse aggregate	SP (%)		
<b>0 FAF</b>	1.0	-	2.0	2.0	1.43	461	584
<b>30 FAF</b>	0.7	0.3	2.0	2.0	1.43	317	610
<b>50 FAF</b>	0.5	0.5	2.0	2.0	1.14	225	660

\* Keys:  $w/b$  = water-to-binder ratio where binder is (OPC + Fly Ash F); OPC = ordinary portland cement; SP= superplasticizer. Used SP was an entry-level carboxylated polyether-based high-range water reducer (ADVA 140) with a specific gravity of 1.010-1.120.

All of the studied mixes performed very well when strength development was concerned, Figure 6-2a. The early strength development was relatively slower for the mixes with partial cement replacement. At 28 days, the compressive strength of 30 FAF samples caught up the reference concrete samples with no cement replacement. The 50 FAF mix's strength development was much slower. At 28 days, the strength 50 FAF samples were 77% of the reference sample. After 365 days, this ratio increased to 84%. The good strength performance of the FAF mixes was accompanied by their enhanced durability performance. Figure 6-2b shows chloride migration coefficient of these mixes. The reference concrete 0 FAF already shows a good performance, and has a high chloride migration resistance. On the other hand, the mixes with partial cement replacement, shows excellent chloride migration resistance suggesting a longer service life.

There are three main greenhouse gases along with water vapor, carbon dioxide (CO<sub>2</sub>), methane (CH<sub>4</sub>) and nitrous oxide (N<sub>2</sub>O). The CO<sub>2</sub>-eq is calculated based on IPCC guidelines as follows:

$$GWP = 1 \times CO_2 + 21 \times CH_4 + 310 \times N_2O \quad (6.1)$$



The environmental impacts of the concrete mixes were quantified using GreenConcrete LCA, developed by UC Berkeley researchers. The cradle-to-gate LCA tool covers direct and supply-chain global warming potential (GWP) in  $CO_2$ -equivalent ( $CO_2$ -eq) associated with electricity use, fuel use, transportation, and production processes taking place within the concrete production system boundary. The scope of the analysis incorporates extraction of cement raw materials, production of cement, extraction and processing of aggregates, production of superplasticizers, preparation and treatment of fly ash prior to mixing in concrete, extraction and processing of limestone, concrete mixing, and transportation of raw materials and products within the system.

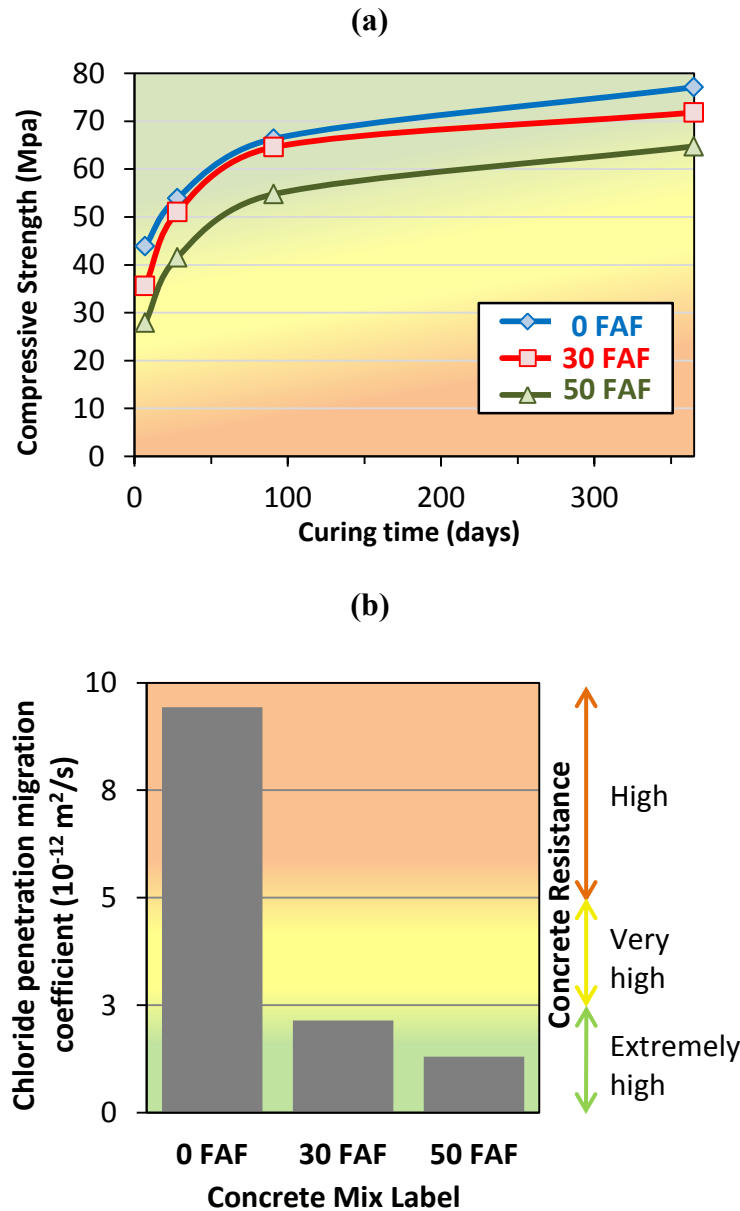


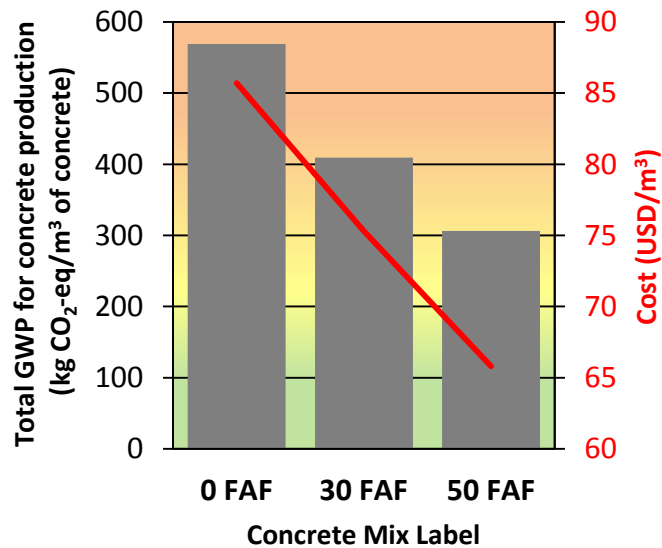
Figure 6-2. (a) Compressive strength development of the high volume fly ash concrete mixes [240]; (b) chloride penetration migration coefficient ( $10^{-12} m^2/s$ ) for the concrete mixes [240].

A basic cost analysis for the mixes is also conducted using the base costs of concrete ingredients per metric ton, Table 6-2.

**Table 6-2. Material cost estimates (USD per metric ton)**

OPC	Fly ash F	Fine aggregate	Coarse aggregate	Water	SP
110.0	44.1 [22]	13.2	8.8	0.386	2205.0

The results of the GWP and cost analysis are summarized in Figure 6-3. The good strength and excellent durability performance of the FAF mixes are followed with not only reduced environmental impact, but also reduced cost. With a total of 569 kg of  $CO_2$ -eq, the reference concrete 0 FAF (in which portland cement is responsible from about 93% of the total GWP) causes the highest amount of GWP. As the cement replacement ratio increases, a dramatic decrease in GWP was seen. The 50 FAF mix has 306 kg of  $CO_2$ -eq per cubic meter of concrete. This is a 46% decrease when compared to reference mix. The cost estimate for the reference mix is around 86\$ per cubic meter. As FAF as cement replacement was introduced, significant cost reductions were observed. At 50% replacement, the cost per cubic meter of concrete is only 66\$, a 27 reduction.



**Figure 6-3. Total GWP of high volume fly ash concrete mixes in terms of kg  $CO_2$ -eq; and cost estimates for each concrete mix [240].**

As illustrated through laboratory mixes, and through many successful projects worldwide, using fly ash as a cement replacement results in highly durable, cost-efficient and green concretes.

### 6.1.2 Using alkali activated fly ash as a binder in concrete

In the past 15 years, significant improvements in alkali-activated aluminosilicates (AAA), often referred as geopolymers, are creating new opportunities in the field of structural and

construction materials. Alkali-activation of aluminosilicates results in a high performance binder that can be an alternative to portland cement based binders at certain applications. Hence, they provide a greener alternative to ordinary portland cement concrete by elimination of a large portion of CO<sub>2</sub> emissions. Also, industrial waste materials rich in aluminosilicates such as fly ash and slag can effectively be utilized as aluminosilicate sources [241].

## 6.2 Characterization of the glass phase in Class F fly ash

Fly ashes from different power plants have different compositions and characteristics. There can be even considerable variations on fly ashes coming from the same source. Having inhomogeneities within a single fly ash particle is also not uncommon; for example, the inner and outer regions of a fly ash particle might have different compositions [242]. In some cases a thin shell of mullite may be present near the surface of the particle [243]. The source of the mullite in fly ash is mainly the kaolinite in raw coal; higher mullite concentration is an indication of high kaolinite content in the feed coal [244]. Needle mullite crystallites on the glass spheres is an indication that mullite crystallized from amorphous aluminosilicate melt during combustion, but not transformed directly from kaolinite [244]. A schematic for fly ash particles is given in Figure 6-4.

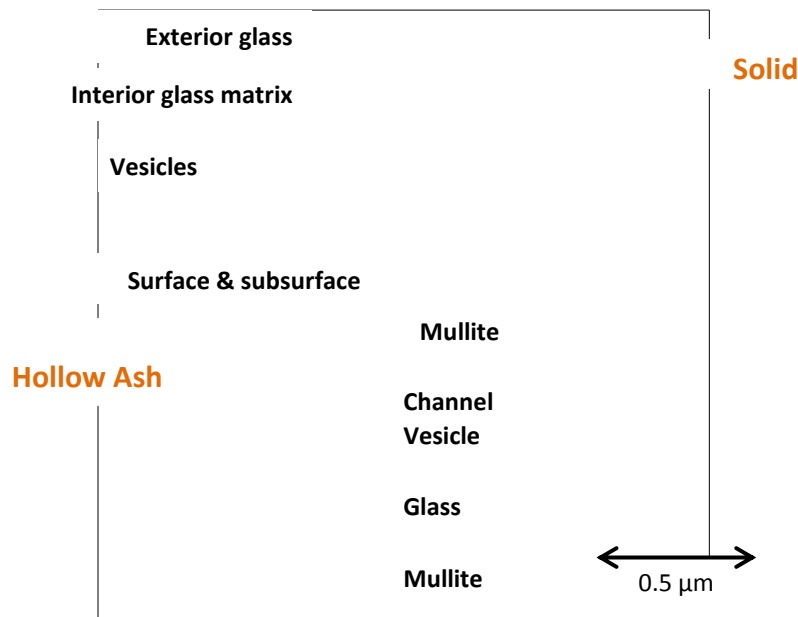


Figure 6-4. Representation of the submicroscopic characteristics of fly ash particles [243].

Similar to the case of amorphous and crystalline silica (see chapter 3), the dissolution rates of amorphous and crystalline SiO<sub>2</sub>/Al<sub>2</sub>O<sub>3</sub> bearing phases within a fly ash differ even under same conditions. The basalt-like glassy phase of a fly ash dissolves the fastest. The rates of quartz, and mullite follows respectively [245]. The glassy phase of fly ash will be the focus of this section, as it is the most reactive and the most abundant phase. For the present work, phase separation of Class F fly ash was done by density difference with the goal of reducing the

crystalline phase concentrations, and having more control on the composition of the glassy ash. The original Class F fly ash was mixed into a mixture solution containing deionized water and 30 ml/l calgon (5% sodium hexametaphosphate,  $(\text{NaPO}_3)_6$  used as deflocculant), in a 2-liter beaker, with a solid-to-liquid ratio of 100 g/l. After settling for 20 minutes, the solution with suspended particles was siphoned out and centrifuged for 20 minutes at 20,000 rpm. After centrifugation, water was removed and the remaining material, mostly consisting of the separated amorphous phase, was dried in an oven at 105 °C. The ash prior to phase separation had particle size distribution ranging from a few percent greater than 100  $\mu\text{m}$ , about 20% concentrated in the sub-micron size and a few percent as small as 0.2  $\mu\text{m}$ . After phase separation the particle size was more homogeneous. The majority of the particles had diameters in the range from 3 to 13  $\mu\text{m}$ ; only few particles were larger than 30  $\mu\text{m}$  and the sub-micron population was reduced to about 10 %: The major oxide composition of the fly ash glass is measured through XRF located at McCone Hall, Berkeley. It is important to note that XRF provides just the bulk composition.

**Table 6-3. Oxide composition of the aluminosilicate glass separated from Class F coal fly ash.**

<b>Oxide Composition</b>		
	<b>(wt. %)</b>	<b>(mol%)</b>
<b>SiO<sub>2</sub></b>	45.10	54.98
<b>Al<sub>2</sub>O<sub>3</sub></b>	21.36	15.34
<b>Fe<sub>2</sub>O<sub>3</sub></b>	4.81	2.21
<b>K<sub>2</sub>O</b>	1.47	1.14
<b>TiO<sub>2</sub></b>	1.02	0.94
<b>CaO</b>	8.74	11.42
<b>Na<sub>2</sub>O</b>	5.19	6.13
<b>P<sub>2</sub>O<sub>5</sub></b>	2.72	1.40
<b>MgO</b>	3.49	6.34
<b>MnO</b>	0.09	0.09
<b>LOI</b>	6.01	-

In order to confirm that the XRF measurements represent the composition of the glassy portion of the fly ash F, EDS spot measurements were used. Figure 6-5a shows the BSE micrograph of a 2 year old 20 wt% OPC – 80 wt% FAF paste. The spherical fly ash particles are easily identifiable. Pozzolanic reaction products grow surrounding the fly ash particles. Characterization of those products is out of scope of this research. Some of the representative major oxide compositions obtained by EDX is summarized in Figure 6-5b. Each fly ash particle has slightly different composition. After comparing the results to the XRF measurement, it is confirmed that the XRF results represent the average composition of the glassy portion of the fly ash.

(a)

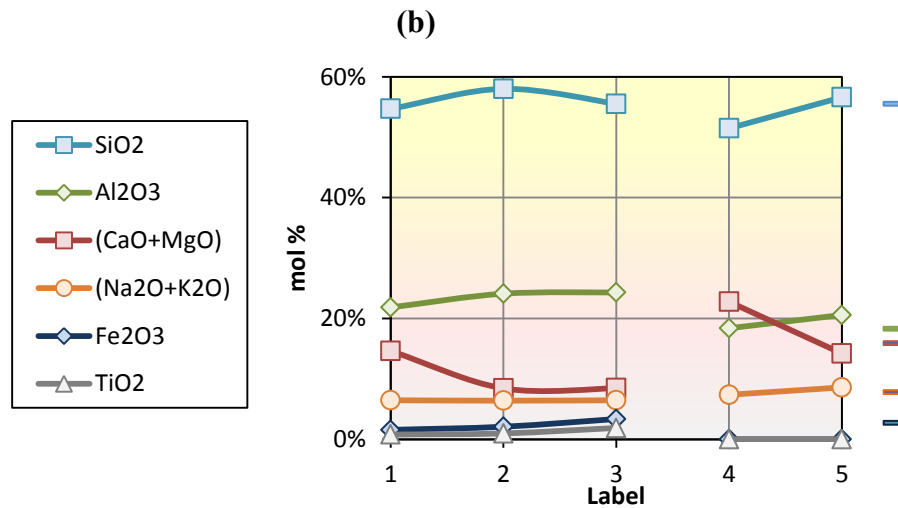
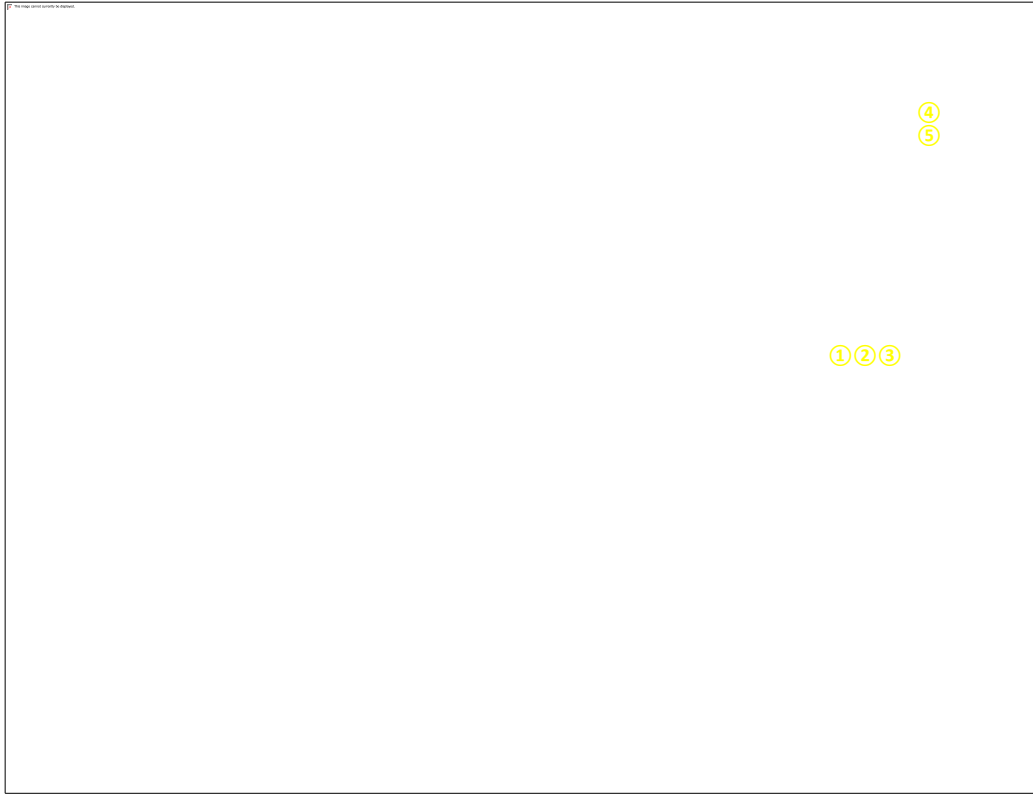


Figure 6-5. (a) BSE micrograph of a 2 year old 20wt% OPC – 90% FAF paste. (b) Composition of the chosen spots obtained by EDX measurements; tick marks on the right represent the XRF measurement. The microscope is located at McCone Hall, Berkeley.

The goal of this chapter is summarizing findings of different characterization techniques used to characterize the fly ash F glass. The methods are chosen to complement each other in order to provide a better characterization. <sup>29</sup>Si and <sup>27</sup>Al MAS NMR are used get information on the local environment of the glass framework. The total scattering investigations provided

information on weighted bond length distribution. The MD modeling resulted in a realistic model that can be used in simulations.

Amorphous aluminosilicates are among the most important binary systems for the earth sciences and materials sciences; therefore, they have been studied in great detail with experiments and computer simulations. This provided reference points to compare the fly ash glass results.

### **6.2.1 Nuclear Magnetic Resonance (NMR) Spectroscopy**

The ordering behavior of framework cations in aluminosilicate glasses have been a relevant topic in geophysics due to its implications for macroscopic thermodynamic and transport properties of magma (*i.e.* heat capacity and viscosity). Unlike the continuous network of SiO<sub>2</sub> tetrahedra, Al<sup>3+</sup> ions on their own do not form a network of AlO<sub>4</sub> tetrahedra. The field strength of Al places it as an intermediate between the high field strength, pure “network former” ions such as SiO<sub>2</sub>, which form low coordinated strongly bonded units, and low field strength “network modifier” ions such as Na, which have a higher coordinated, weaker bound 1<sup>st</sup> coordination shell. The intermediate character of Al is reflected in the dependence of AlO coordination on its chemical environment. For example binary neutron and X-ray diffraction results [246–248] show (La/Ca/Ba)-Al-O, glasses with 50mol% or more Al<sub>2</sub>O<sub>3</sub> have average AlO coordination numbers very close to 4.0(1) [246–248]. This indicates a predominantly tetrahedral Al-O network, with very little 5 or 6 fold species in these glasses. Binary Al-Si-O glasses, and amorphous Al<sub>2</sub>O<sub>3</sub> however, are found to have a higher average AlO coordination, with around half the Al, 4-coordinated, and half 5-coordinated, with minor proportions of (~5%) 6-coordinated AlO [249–253].

Triple quantum <sup>27</sup>Al NMR studies of glass compositions close to that of tested fly ash F glass, include C25-A25-S50 glass [254], and C-N-A-S glass [255] where the abbreviations represent A (Al<sub>2</sub>O<sub>3</sub>), C (CaO), N (Na<sub>2</sub>O). Both these studies find over 90% of the Al to be 4-coordinated, with the remainder being 5-coordinated, and with no 6-coordinated Al. Figure 6-6a shows the <sup>27</sup>Al NMR spectrum of tested fly ash. The fits of the spectrum is summarized in Table 6-4. The spectrum displays one broad component centered around +56.2 ppm associated with tetrahedral aluminum (Al<sub>T</sub>). There are also one small signal located at +29.6 ppm attributed to penta-coordinated (Al<sub>P</sub>) and two located at +9.8 ppm and +1.2 ppm attributed to octahedral aluminum (Al<sub>O</sub>). The octahedral components can be assigned to mullite. The spectrum suggests that the fly ash has 86% of the Al tetrahedrally coordinated. The 5-fold Al can also be explained by tri-clustered 4-fold Al, an AlO<sub>4</sub> tetrahedron in which at least one of the oxygen atoms is coordinated by three TO<sub>4</sub> tetrahedra (T=Al,Si). Figure 6-6b shows the <sup>29</sup>Si NMR spectrum of the fly ash. The wide and rather poorly defined spectrum is an indicative of heterogeneous distribution of the silicon atoms. The deconvolution of this spectrum shows the presence of 8 peaks. Peaks detected at -83, -91.6, -98.8, -103.4 and -108.3 ppm correspond the fly ash glass [256]. The peak at -87.4 assigned to Q3(3Al)Si [256] corresponds to crystalline mullite present in the fly ash. The deconvolution suggests that 4.93% mullite exists in the sample. The peaks beyond -110 ppm (-114 ppm, signals and -123.1 ppm) have been ascribed to the presence of different SiO<sub>2</sub> crystalline phases (Q4(0Al) signals) [256]. The amount of these phases is estimated as 17.96%. Hence, the glassy component of tested fly ash is estimated as 77.11%.

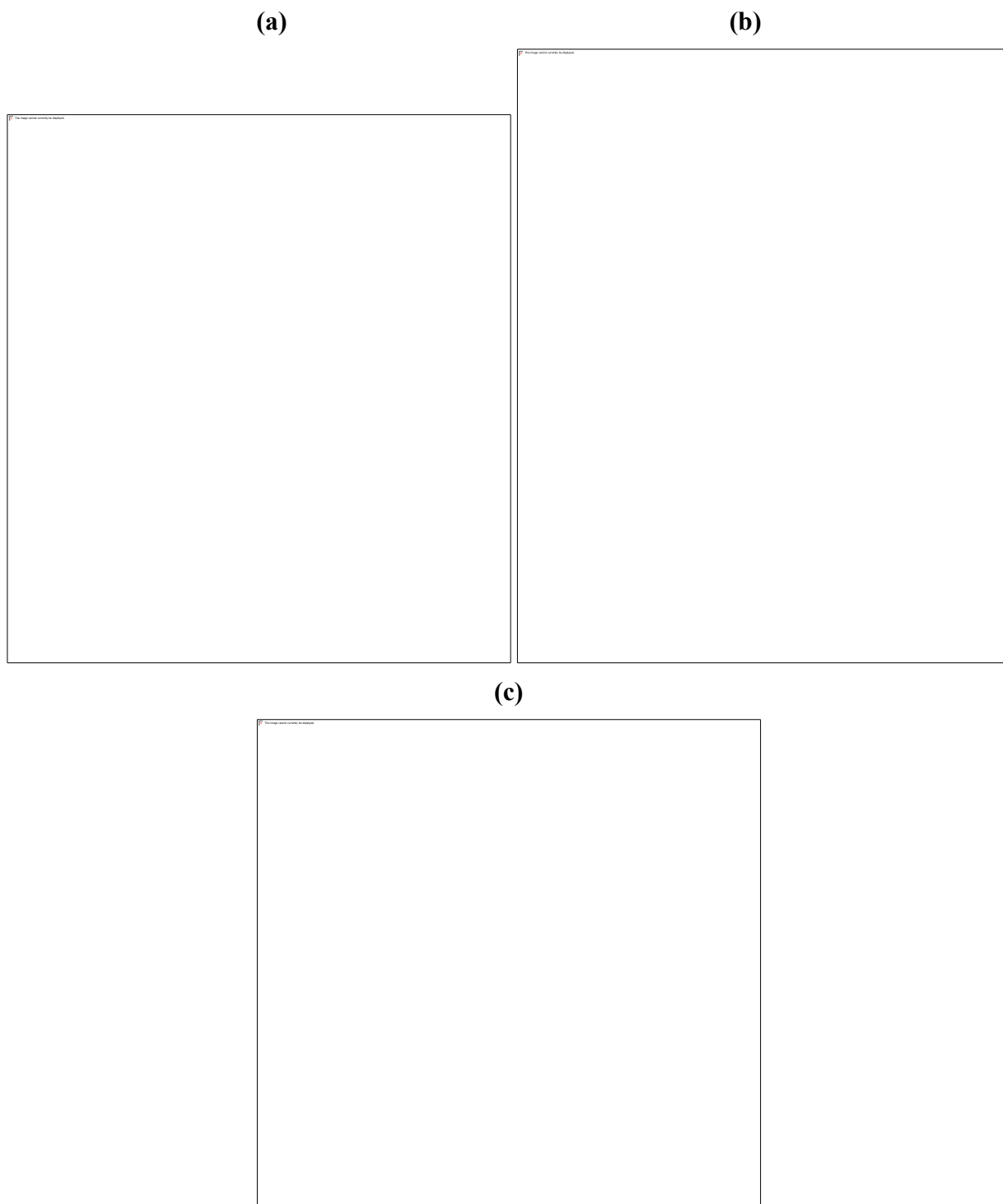


Figure 6-6. Fits to (a)  $^{27}\text{Al}$ , (b)  $^{29}\text{Si}$  and (c)  $^{23}\text{Na}$  MAS-NMR spectra of phase separated fly ash F. The figures include the experimental and fitted spectra (medium: red experimental data, blue: the fitted spectra, green: background), the fitted peaks (bottom), and the residual spectra (top).

Table 6-4. Isotropic chemical shift  $\delta$ , relative integral intensity I for Gaussian lines fitted to the  $^{27}\text{Al}$  MAS NMR spectra for the phase separated fly ash.

$(\text{Al}_2\text{O}_3)/(\text{SiO}_2) = 0.28$	$\delta$ (ppm)	I (%)
Al <sub>O</sub>	+1.2	0.3%
Al <sub>O</sub>	+9.8	7.5%
Al <sub>P</sub>	+29.6	6.2%
Al <sub>T</sub>	+56.2	86.0%

Table 6-5. Isotropic chemical shift  $\delta$ , relative integral intensity I for Gaussian lines fitted to the  $^{27}\text{Al}$  MAS NMR spectra for the phase separated fly ash.

$(\text{Al}_2\text{O}_3)/(\text{SiO}_2) = 0.28$								
$\delta$ (ppm)	-83.0	-87.4	-91.6	-98.8	-103.4	-108.3	-114.0	-123.1
Width	4.9	4.9	4.9	4.9	4.9	4.9	4.9	4.9
Integral (%)	9.59%	4.93%	19.63%	19.49%	7.74%	20.65%	13.49%	4.47%

The typical ranges of  $^{29}\text{Si}$  chemical shifts of Q4(mAl) units in aluminosilicates are given in Figure 6-7.

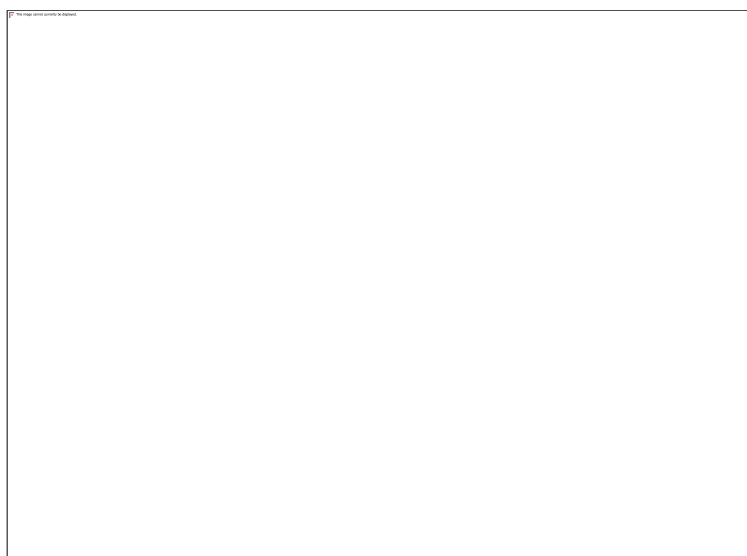


Figure 6-7. Typical ranges of  $^{29}\text{Si}$  chemical shifts of Q4(mAl) units in aluminosilicates [97]

The  $^{23}\text{Na}$  MAS NMR spectrum shown in Figure 6-8 can be difficult to interpret because of the quadrupolar effects and peak overlap. The ash contains a broad single peak located at -16.77 ppm with width of -19 ppm.



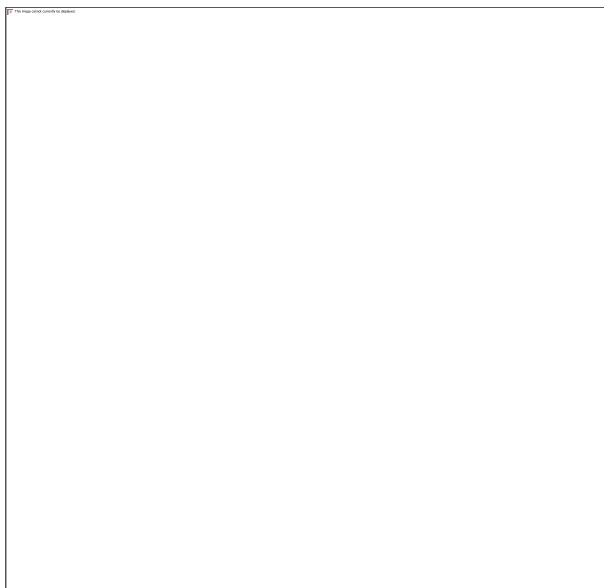


Figure 6-8. Fits to  $^{23}\text{Na}$  MAS-NMR spectra of phase separated fly ash F. The figures include the experimental and fitted spectra (medium: red experimental data, blue: the fitted spectra, green: background), the fitted peaks (bottom), and the residual spectra (top).

### 6.2.2 MD Model

Molecular Dynamics simulations in order to model the glass phase were performed (with the help of Dr. Lawrie Skinner) using the DLpoly classic package [257], with modified Buckingham inter-atomic potentials of the form

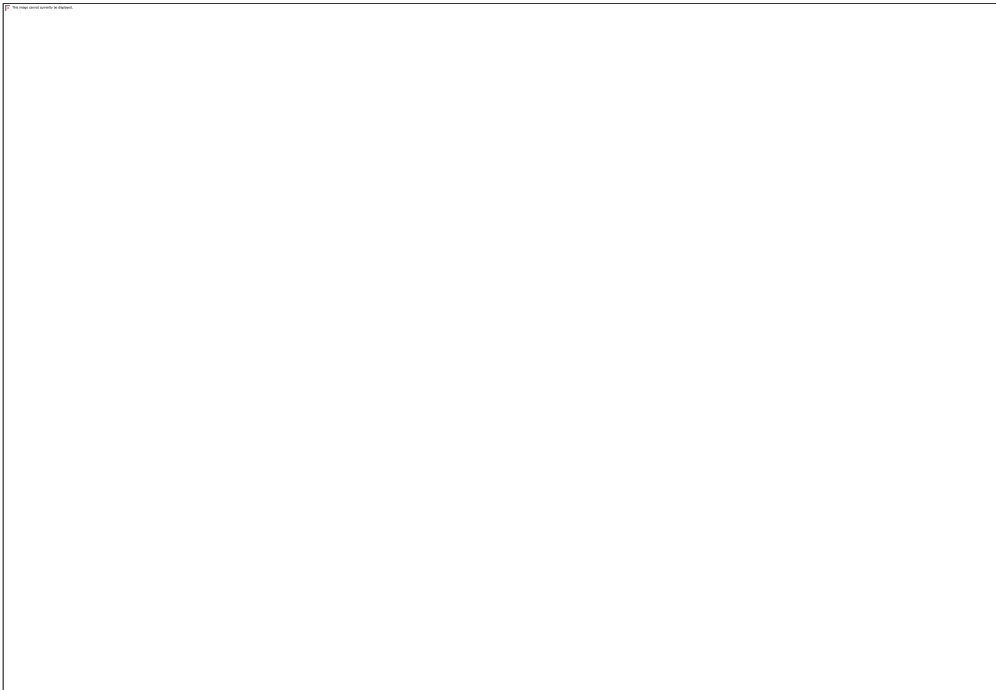
$$V_{ij}(r) = \frac{z_i z_j e^2}{r} + A_{ij} \exp(-B_{ij} r) - C_{ij}/r^6 + D_{ij}/r^{12}$$

In this equation,  $i$  and  $j$  represent different elemental species in the system,  $z_i$  is the charge of species  $i$  and the parameters A-C were calculated in previous work [258–260], and are given in the table below. The  $D/r^{12}$  term was added to correct unphysical attraction of atoms at separations  $< 1\text{\AA}$ . The D parameters were chosen to be the minimum value needed to make the potential and its force derivative positive at low separations.

Table 6-6. Simulation parameters

	A	B	C	D
$\text{Al}^{1.8} - \text{O}^{-1.2}$	12201.42	5.11247	32.0	1
$\text{Si}^{2.4} - \text{O}^{-1.2}$	13702.905	5.15951	54.681	3
$\text{Ca}^{1.2} - \text{O}^{-1.2}$	7750	3.958468	93.1	12
$\text{Na}^{0.6} - \text{O}^{-1.2}$	4383.7555	4.10108	30.70	2
$\text{O}^{-1.2} - \text{O}^{-1.2}$	2029.2204	2.90998	192.58	200

There are five major oxides in the glassy portion of fly ash  $\text{Al}_2\text{O}_3$ ,  $\text{CaO}$ ,  $\text{Na}_2\text{O}$ ,  $\text{SiO}_2$ , and  $\text{MgO}$  as listed in Table 3-1. This composition can be approximated as  $(\text{Na}_2\text{O})_7(\text{Al}_2\text{O}_3)_{15}(\text{SiO}_2)_{60}(\text{CaO})_{18}$ . Even though the Ca-O bond is partially covalent and Mg-O bond is purely ionic, the CaO amount is slightly increased to compensate for MgO. Using this composition, a simulation box with 4680 atoms (450 Al, 270 Ca, 210 Na, 2850 O, and 900 Si) was prepared. The MD was initiated from a random configuration where the atoms had been moved out to be at least 1 Å apart. Then NPT (fixed pressure, variable volume) ensembles, were run at temperature steps of 6000K, 2000K, 1000K, and 300K, where step was held for 50ps. The final configurations were collected from an additional NVT ensemble run at 300K for a further 50ps. A snapshot of the MD model is given in Figure 6-9.



**Figure 6-9. Snapshot for fly ash F- glass model (40 Å x 40 Å). Gold-polyhedra:  $\text{SiO}_4$ , silver-polyhedra:  $\text{AlO}_4$ , red spheres: Ca, blue spheres: Na.**

The glass density depends both on composition and thermal history. The MD model provides an estimate for the fly ash glass,  $2.562 \text{ g/cm}^3$ . This density is reasonable considering glasses with similar composition as listed in Table 6-7. The validity of the MD model is also verified by comparing it with the experimental pair distribution function.

**Table 6-7. Densities of various Ca-Al-Si glass compositions [250]**

Glass composition (mol%)				Density ( $\text{g/cm}^3$ )
$\text{SiO}_2$	$\text{Al}_2\text{O}_3$	$\text{CaO}$	$\text{Na}_2\text{O}$	
40	30	30	-	2.75

50	25	25	-	2.66
60	20	20	-	2.60
<b>60</b>	<b>15</b>	<b>18</b>	<b>7</b>	<b>2.562*</b>
70	15	15	-	2.503
76.5	11.75	11.75	-	2.436

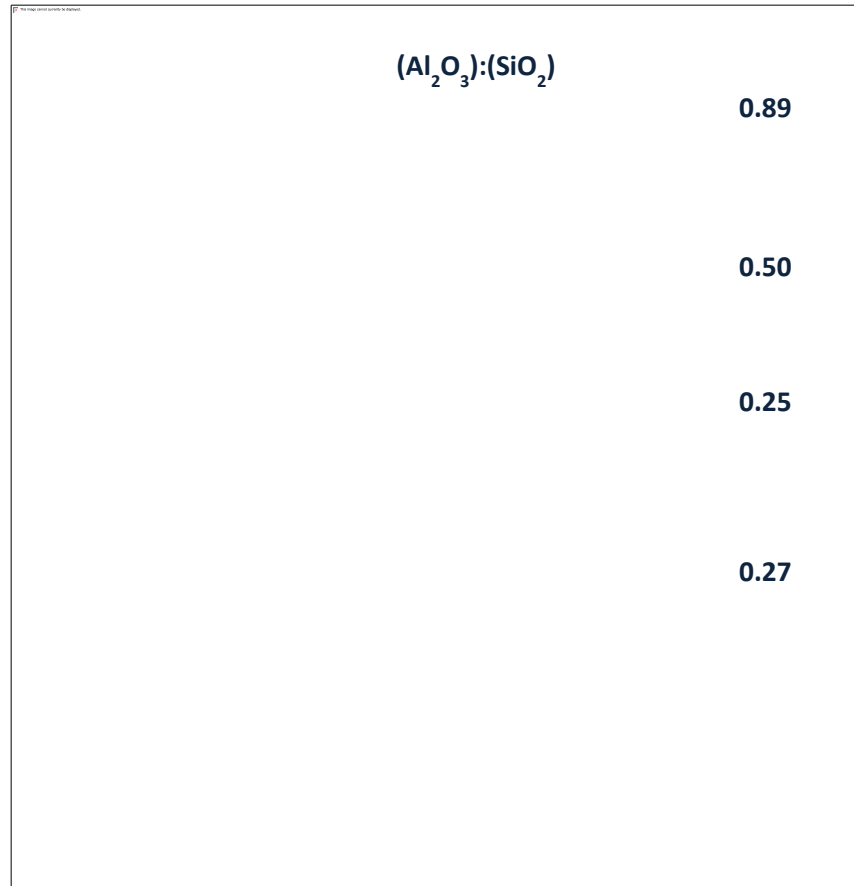
\*The density calculated through the MD model.

### 6.2.3 Total scattering investigations

For total scattering investigations on fly ash glass, the high energy X-ray beamline 11-ID-C located at APS operating at 115 keV described in chapter 2 was used. Powdered samples in 2mm diameter kapton tubes with 0.1mm wall thickness were measured at ambient conditions. An amorphous silicon area detector (Perkin Elmer XRD1621) was placed perpendicular to the incident beam 657 mm behind sample. The data analysis was carried out using Fit2D and PDFgetX2 software packages. First, the momentum transfer scale was calibrated by refining a standard crystalline CeO<sub>2</sub> sample using the FIT2D [109]. Then, the measured intensity was corrected using standard methods in PDFgetX2 [34]. The corrected intensity function was used to calculate the total structure factor,  $S_X(Q)$  which was Fourier transformed to construct the measured pair distribution functions (PDF). In this work two normalizations schemes for the PDF's are plotted first is  $G(r)$ , which is normalized to the estimated macroscopic density of the material such that  $G(r) \rightarrow 1$ , at high- $r$ , and  $G(r)=0$ , means zero probability of finding an atom at that  $r$ -value. Consequently, a negative  $G(r)$  value is unphysical. Alternatively the function  $D(r)=4\pi r \rho [G(r)-1]$ , may be plotted to emphasize higher- $r$  structure, this function oscillates about zero, and the negative slope at low- $r$  values, is related to the macroscopic density of the material. Subscript  $x$  on these functions e.g.  $D_X(r)$  or  $S_X(Q)$  indicates X-ray weighted patterns, whereas multiple letter subscripts identify the pair of atomic species, for un-weighted partial distribution functions (or structure factors). Details of the method can be found in chapter 2.

The measured structure factor for the fly ash (with Al<sub>2</sub>O<sub>3</sub>/SiO<sub>2</sub> molar ratio around 0.27) is given in Figure 6-10. Some small Bragg peaks are observed due to residual mullite and quartz; however, these peaks do not affect the results considerably. One of the key factors affecting the ordering behavior of the aluminosilicate glasses is the field strength of charge balancing cations, in this case Na<sup>+</sup> and Ca<sup>2+</sup>; however, the total structure factor for fly ash glass still resembles that of pure aluminosilicates.

To construct the X-ray weighted structure factor from the MD model, each partial structure factor was calculated from the partial distribution functions, and weighted with the Q-dependent X-ray weighting function obtained from the X-ray form factors and concentrations of each elemental species. The calculated total X-ray structure factor for the MD model compares much better to the experimental measurement on fly ash.

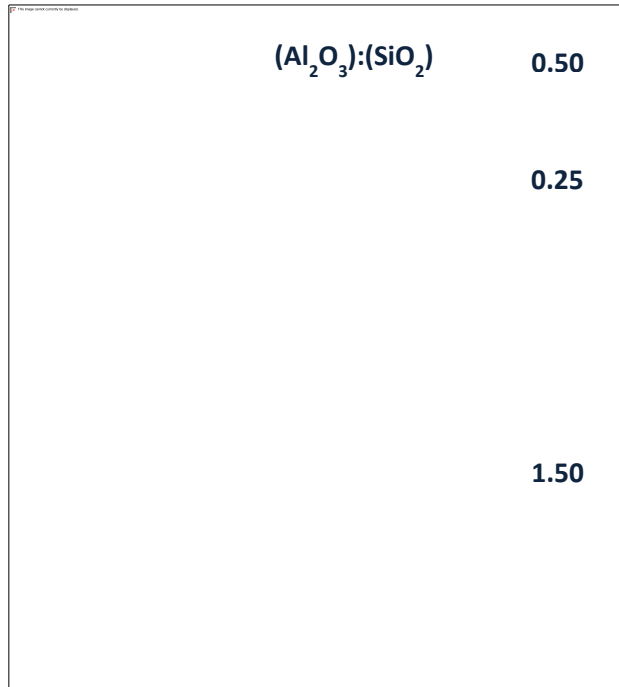


**Figure 6-10. Comparison of the experimental X-ray total structure factor of fly ash F – glass, and the simulated X-ray total structure factors from  $(\text{Al}_2\text{O}_3).2(\text{SiO}_2)$  by Winkler *et al.* [249],  $65(\text{Al}_2\text{O}_3).73(\text{SiO}_2)$  by Pfeleiderer *et al.* [261] and the MD model.**

Hoang *et al.* [251,252,262] deepened the investigations on amorphous  $\text{Al}_2\text{O}_3.2\text{SiO}_2$  in a MD model containing 3025 particles under periodic boundary conditions with the Born-Mayer type pair potentials. The calculated total pair and differential distribution functions for MD models of this study and Hoang's are given in Figure 6-11. Calculated results for mullite are also plotted.

From the Gaussian fits to the first peak of experimental data, the average first nearest-neighbour T-O (T=Al,Si) distance for the fly ash was obtained as 1.65 Å. This peak is asymmetric, as it is formed from contributions from Al-O and Si-O. The average T-O distance of  $\text{SiO}_4$  and  $\text{AlO}_4$  tetrahedra calculated from ionic radii are 1.61 Å and 1.74 Å respectively. For mullite, a much higher T-O peak at 1.79 Å is calculated. This value is higher than the average tetrahedral T-O distances; hence, it indicated the presence of 5- and 6- fold Al atoms. The ordering of Si and Al based frameworks in aluminosilicates is often described in terms of the Al avoidance rule, which rejects the existence of the Al-O-Al linkages. For  $\text{Si}/\text{Al} \geq 1$  (for this fly ash  $\text{Si}/\text{Al} = 1.79$ ), complete Al avoidance is expected such that there can be only Si-O-Al and no Al-O-Al.

(a)



(b)

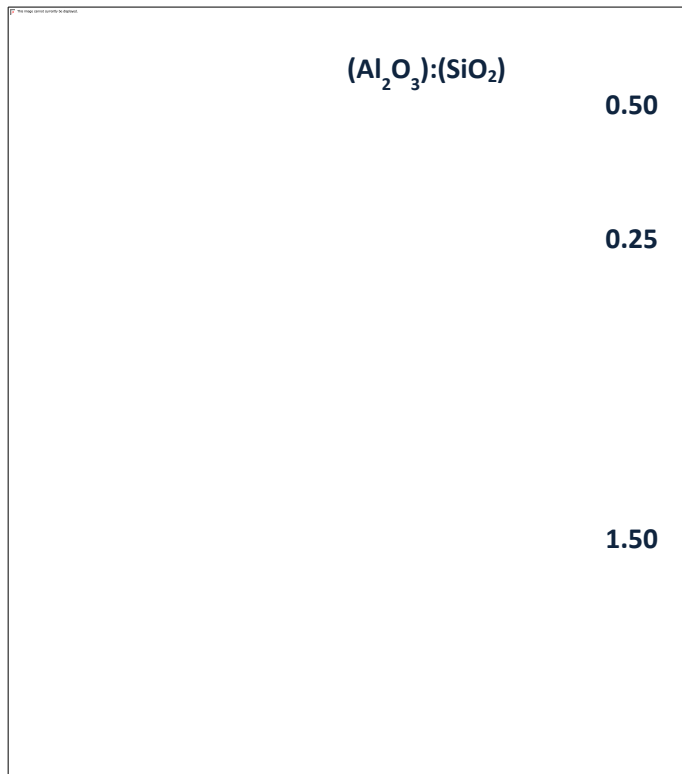
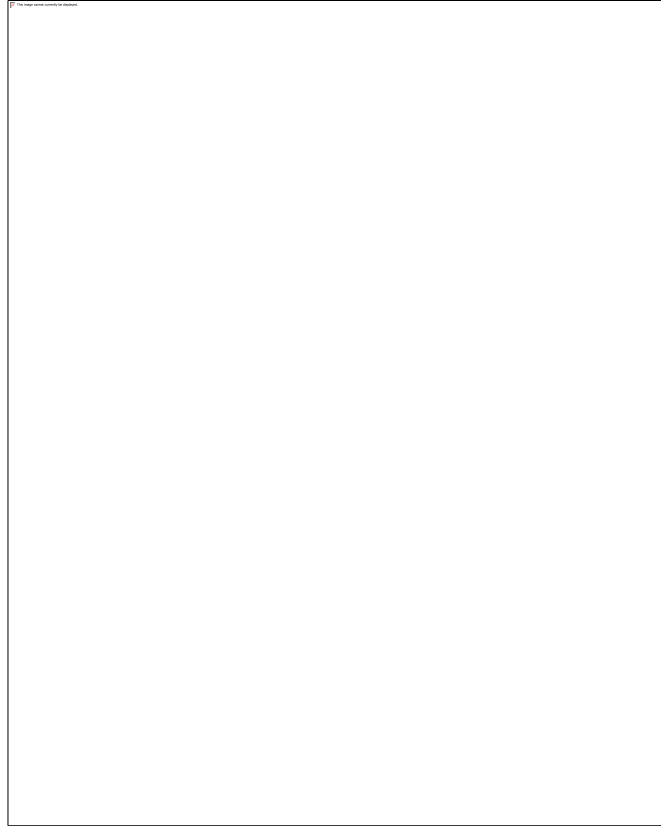


Figure 6-11. The experimental X-ray pair (a) and differential (b) distribution functions for fly ash-F glass compared to this study's and Hoang's (Al<sub>2</sub>O<sub>3</sub>-2(SiO<sub>2</sub>) melt) [252] MD simulations.

The simulations also provide detailed partial pair distribution functions. These partial PDFs can be used to identify the correlations in this fly ash glass. First, let's look at the Hoang's simulation shown in Figure 6-12. As seen from the partials, the 1.51 Å for Si-O and 1.70 Å for Al-O values are significantly underestimated the actual bond lengths.



**Figure 6-12. The atom specific differential distribution factors for Hoang's MD simulation [252].**

Figure 6-13 shows the atom specific X-O partial pair distribution function for the MD model. To make the peaks sharper,  $Q_{\max}$  is used at  $60 \text{ \AA}^{-1}$ . The key distances are summarized in Table 6-8. As seen,  $g_{\text{AlO}}(r)$  is very similar to  $g_{\text{SiO}}(r)$ , but the former has a slightly broader, and weaker, first peak due to the presence of  $\text{AlO}_5$  and  $\text{AlO}_6$ . The Si-O and Al-O bond lengths were identified as 1.607 Å and as 1.774 Å respectively. The Ca-O and Na-O distances are produced as 2.419 Å and 2.484 Å. The O-O distance is identified as 2.637 Å. It is important to note that in crystalline state the local atomic arrangements of modifying cations like Na or Ca vary considerably from one mineral to another [263]. For example, in binary silicates like  $\text{Na}_2\text{SiO}_3$  and  $\text{Na}_2\text{Si}_2\text{O}_5$  the environment consists of a trigonal bipyramid of five oxygens [263]. In crystalline ternary silicates like  $\text{Na}_2\text{CaSiO}_4$  or  $\text{Na}_2\text{Mg}_2\text{Si}_6\text{O}_{15}$ , the Na environment is different with basic structural units is a trigonal antiprism in which Na is coordinated to three oxygens at a bonding distance of 2.3 Å and a further three oxygens at non-bonding distances of around 3 Å [263]. Na in glasses also show a variety of local structures as it does in crystalline systems [263]. For  $\text{Na}_2\text{CaSi}_2\text{O}_{12}$  glasses EXAFS studies revealed that the O shell comprises 5 or 6 atoms, but split into in a similar way like the minerals [263]. For  $\text{Na}_2\text{Si}_2\text{O}_5$  glasses, the O shell is well defined with approximately 5 atoms at 2.3 Å. In contrast to Na, the environments of Ca in crystalline

minerals are extremely distorted [263]. Although the local symmetry is roughly octahedral, the oxygen coordination number varies between 7 and 9. Most oxygens are located around 2.4 Å, but some are at longer distances resulting in a characteristically asymmetric Ca-O pair distribution function [263]. The remaining correlations are given in Figure 6-14.

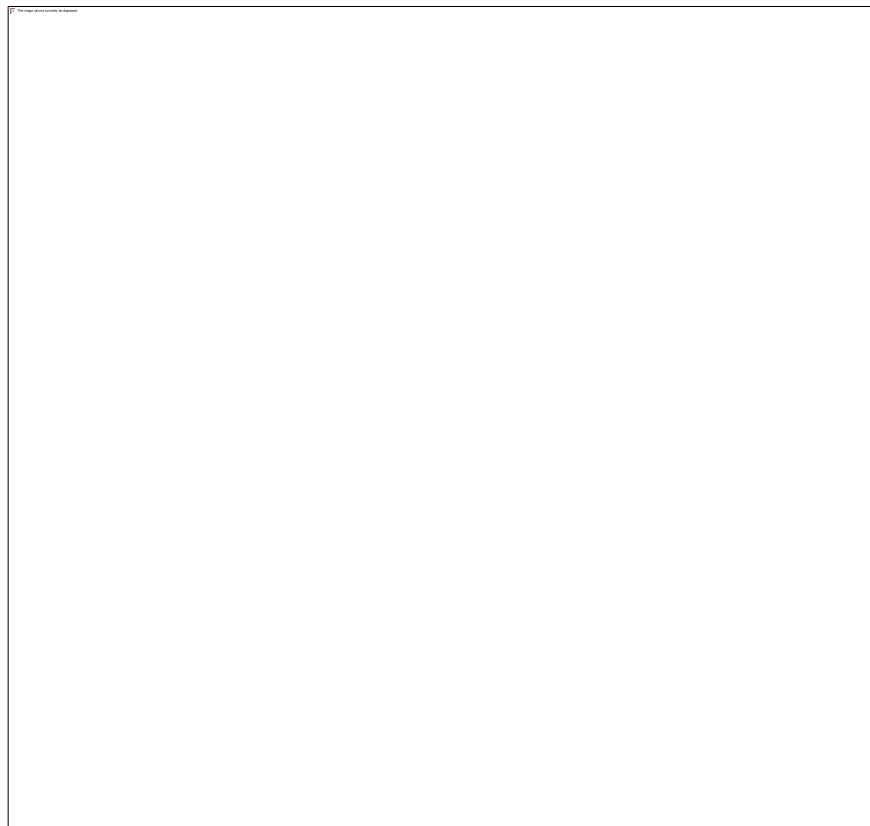


Figure 6-13. The atom specific pair distribution functions of the MD model of this study for X-O [252].

Table 6-8. Key distances (Å) produces from the MD model.

<b>Bond</b>	<b>Distance (Å)</b>
<b>SiO</b>	1.607
<b>AlO</b>	1.774
<b>CaO</b>	2.419
<b>NaO</b>	2.484
<b>OO</b>	2.637



**Figure 6-14. Remaining atom specific pair distribution functions of the MD simulation [252].**

Overall, the obtained MD model resulted in a good with the experimental pair distribution function.

#### ***6.2.4 Scanning Transmission X-ray Microscopy (STXM)***

In this study, the STXM results were collected at beamline 5.3.2.1 at the Advanced Light Source (ALS) described in chapter 2. Two types of samples were prepared for the fine fly ash F-glass powder: in the first case, the powder was dispersed, by blowing, on a silicon nitride membrane window, in the second case, the powder was embedded in epoxy resin and microtomed to approximately 100 nm section and place on a TEM grid. Then, they were placed on a special support and installed into the experimental chamber. The chamber was quickly vacuumed and prepared for the measurements.

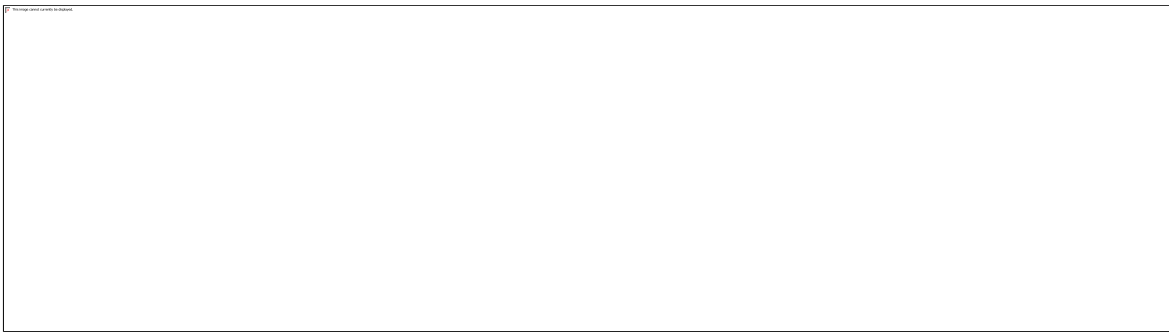
Images-Stacks were performed, which consist on the acquisition of a pile of images on a specific area, over a wide range of energies for the most common elements in cementitious materials (ie., for Na 1065 – 1105 eV for Al 1550 – 1660 eV or for Si 1820 – 1890 eV). There one can select certain regions of interest (ROIs) and extract the related Near Edge X-ray Absorption Fine Structure (NEXAFS) spectra for a specific element. Axis 2000 software



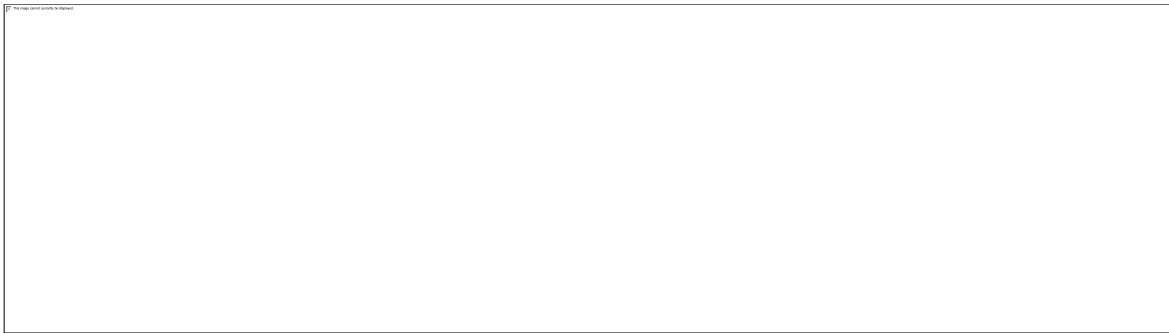
(Version 2.1) [67] is used for the data analysis. Once the Spectra - Image Stack correlation has been processed, elemental maps can be obtained.

Two-Image maps can be obtained by taking a couple of images on the same area or region of interest. One image is taken at a pre-edge energy and one image right at the energy of the peak of interest, for instance, on Silicon the energies can be around 1830 eV and 1849 eV respectively (Figure 6-15a), while on Aluminum can be 1560 eV and 1568 eV respectively (Figure 6-15b). Normalization and background subtraction is performed in order to obtain images where the signal of the element of interest is enhanced. A shift in the peak positions was not observed. However, these scans are conducted on fly ash particles smaller than 1 micron, and they might be too thick for the measurements.

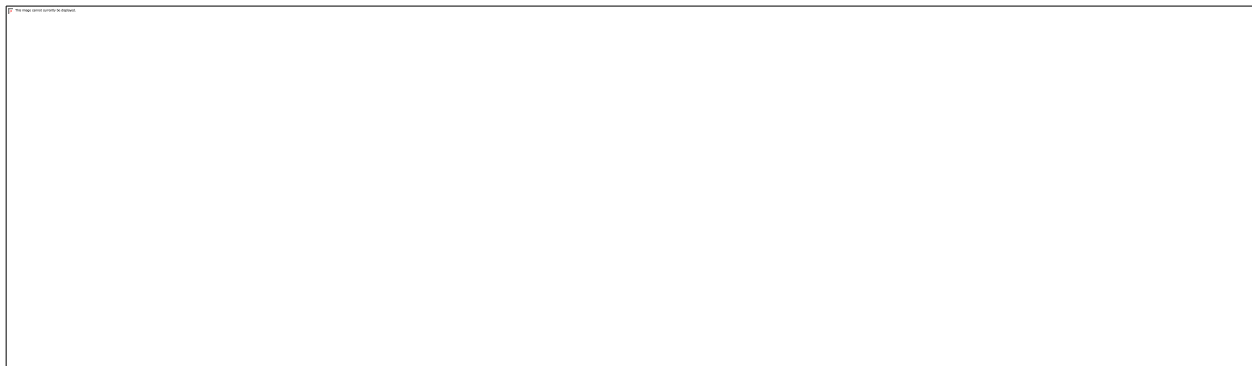
**(a1)**



**(a2)**



**(b)**



**Figure 6-15. (a1-a2) Si K-edge and (b) Al K-edge for fly ash particles both showing a homogeneous surface.**

Then, LineScans were performed to analyze the silicon, aluminum and sodium environments on a microtomed sample, Figure 6-16. This measurement consists on acquiring signal from a single point located on a “horizontal virtual line” placed along the area or particle of interest. From the obtained image, one can “extract” the spectra from specific sub-regions of interest. A significant variation in the Si K-edge peaks was not observed, but only a dependence on thickness. The peak is located 1849 eV. For the samples, the Al K-edge is located at 1568 eV. For particle 3, a small hump located at 1571 eV is observed. The Na spectrum is very noisy therefore a significant observation was not observed.

**(a)**

**(b)**

**(c)**

**(d)**



**(e)**

**(f)**

**(g)**

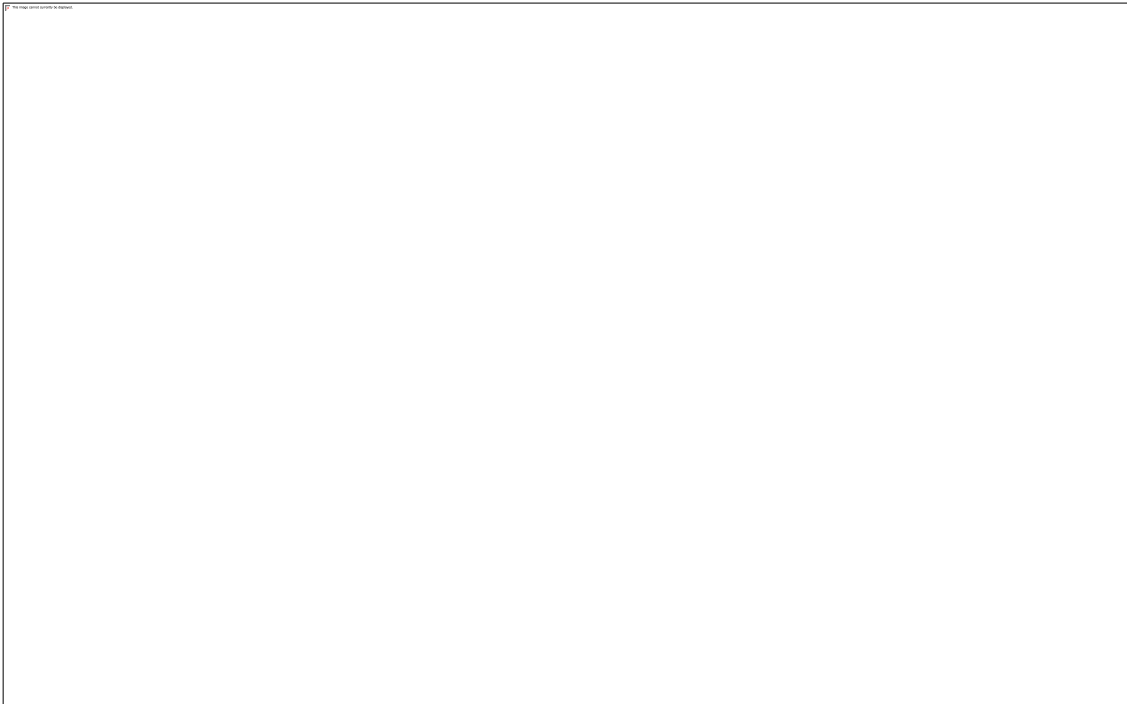


Figure 6-16. (a) The overall image of the microtomed 100nm sample; (b) Si – green line shows where the line scan is conducted, (c) Al and (d) Na K-edge scans of the area marked with yellow box; (e) Si, (f) Al and (g) Na K-edge NEXAFS spectra for the line scan.

## 6.3 Conclusions

Glassy portion of the fly ash is the most reactive part of the ash. However, the information on this glass is limited. In this chapter, several methods complementing each other were used to characterize the glass.  $^{27}\text{Al}$  MAS NMR investigations showed that the Al is mostly tetrahedral coordinated. The  $^{29}\text{Si}$  MAS NMR investigations are used get information on the local environment of the glass framework. The total scattering investigations provided information on weighted bond length distribution. The MD modeling resulted in a realistic model that can be used in simulations.

# 7

## Conclusions

The PDF method is one of the most effective methods to investigate amorphous materials.

Rice husk ash and silica fume, almost pure amorphous silicas commonly used as portland cement replacement, have very different microstructures; however, the PDF results show that they are very similar in short range.

Amorphous and microcrystalline opals, hydrated amorphous silicas, have a variety of microstructures as documented by SEM investigations. Solid state NMR is a powerful technique that could be used in combination with PDF analysis. It is sensitive to local structure in disordered materials and yields information on local symmetry and the speciation distribution of the probe atom [52,53], whereas PDF only gives average coordination numbers. The NMR study on opals show that they are mainly composed of Q3 and Q4 species. The total scattering investigations show that in opals the FSDP shifts towards higher Q indicating an increased characteristic repeat distance when compared to silica glass, silica fume and rice husk ash. This can be explained by presence of water in their structure. The  $Si_1-O_1$  correlations were located at  $\sim 1.61(1)$  Å and the  $O_1-O_1$  correlations were located at  $\sim 2.62(1)$  Å; slightly higher values when compared to that of silica glass. This could be explained by higher amount of non-bridging oxygen atoms in opals. The  $Si_1-Si_2$  correlations were centered slightly lower for opals when compared to that of silica glass at around  $\sim 3.06(2)$  Å, and gave an  $\equiv Si-O-Si \equiv$  bond angle  $\theta \sim 144^\circ$  indicating corner shared connectivity of the tetrahedral, possibly a rather open network in amorphous  $SiO_2$  associated primarily with 5, 6 and 7-membered rings. The correlations of amorphous opal samples got consistently broader and diminished around 12 Å. The correlations for microcrystalline opal samples got weaker; however, continued up to 40 Å consistent with their more ordered structure.

Alkali silica reaction (ASR) is a deleterious interaction within concrete resulting in dissolution of the reactive silica portion of aggregates, and formation of a very hygroscopic amorphous gel. When confined in a matrix, ASR gel can generate high mechanical stresses, eventually leading to cracking. At advanced stages, it may cause loss of structural integrity. The BSE micrographs of concrete samples from Jaguari Dam and Paulo Afonso Dam showed significant aggregate cracking and ASR gel formation that damages the aggregates integrity.

Pulling out the gel for characterization experiments in those samples was difficult. In Furnas Dam and Moxoto Dam the gel formation was so extensive that small pockets of it oozed out from their galleries. These pockets were collected, and were used in the ASR gel characterization experiments.  $^{29}\text{Si}$  NMR analysis showed that ASR gels coming from different sources have similar disordered silicate network structures with different degrees of Q3, Q4 and Q2 connectivity mainly depending on the gels age, and alkali content. The STXM data on Furnas Dam gel showed that  $Na$  and  $K$ , are spatially inversely correlated throughout the gel. For the  $Na$  and  $K$ , there is not different species or coordination environment, suggesting compositionally homogeneous sample with regard to  $Na$  or  $K$  respectively. The INS measurements showed some of the different types of water: free water, hydrogen bound water and  $Na$  or  $K$  bound water, bound water. The SANS analyses showed two evident length scales. The small length scale which is presumably due to voids in the gel, had an estimated spherical radius of  $11\text{\AA}$  for gels at natural state, and  $12\text{\AA}$  for gels deuterated for 1 day. Pair distribution function analysis agreed with previous literature [31] on the persistence of a local amorphous poorly layered alkali-silicate structure. The analysis also confirmed that in the ASR gel, the water molecules mostly resided in pores surrounding alkali-silica fragments. The alkali silica fragments had a periodicity of around  $10.5\text{\AA}$ , but exposing the gels to 100% relative humidity allowed them to soak up even more water, creating sizes with a periodicity of  $\sim 15\text{\AA}$

The most reactive phase of the fly ash is its basalt like glassy portion. However, the information on this glassy phase at atomic level is limited. In this research, several methods complementing each other were used to characterize the glass.  $^{27}\text{Al}$  MAS NMR investigations showed that the Al is mostly tetrahedral coordinated. The  $^{29}\text{Si}$  MAS NMR investigations are used get information on the local environment of the glass framework. The total scattering investigations and pair distribution investigations provided information on weighted average bond length distribution. The MD modeling resulted in a realistic model that can be used in simulations.

# References

- [1] M.A.T.M. Broekmans, Deleterious reactions of aggregate with alkalis in concrete, *Reviews in Mineralogy and Geochemistry*. 74 (2012) 279–364.
- [2] U.S. Geological Survey, Cement statistics and information, Washington, D.C., available at <http://minerals.usgs.gov/minerals/pubs/commodity/cement/mcs-2012-cemen.pdf>, Mineral Commodity Summaries. (2012).
- [3] P.K. Mehta, P.J.M. Monteiro, *Concrete: microstructure, properties, and materials*, 2006.
- [4] P.K. Mehta, Reducing the environmental impact of concrete, *Concrete International*. (2001) 61–66.
- [5] E. Bryant, *Climate process and change*, Cambridge University Press, Cambridge, 1997.
- [6] World Business Council for Sustainable Development, *The Cement Sustainability Initiative, Cement industry energy and CO<sub>2</sub> performance: “Getting the numbers right,”* Washington D.C., 2009.
- [7] E. Worrell, L. Price, N. Martin, Carbon dioxide emissions from the global cement industry, *Annual Review of Energy Environment*. 26 (2001) 303–329.
- [8] G.L. Clark, D.H. Reynolds, Quantitative analysis of mine dusts: An X-Ray diffraction method, *Industrial and Engineering Chemistry*. 8 (1936) 36–40.
- [9] H.M. Rietveld, A profile refinement method for nuclear and magnetic structures, *Journal of Applied Crystallography*. 2 (1969) 65–71.
- [10] R.J. Hill, C.J. Howard, Quantitative phase analysis from neutron powder diffraction data using the Rietveld method, *Journal of Applied Crystallography*. 20 (1987) 467–474.
- [11] G. Le Saoût, V. Kocaba, K. Scrivener, Application of the Rietveld method to the analysis of anhydrous cement, *Cement and Concrete Research*. 41 (2011) 133–148.
- [12] K. Scrivener, Quantitative study of portland cement hydration by X-ray diffraction/Rietveld analysis and independent methods, *Cement and Concrete Research*. 34 (2004) 1541–1547.
- [13] F. Battocchio, P.J.M. Monteiro, H.-R. Wenk, Rietveld refinement of the structures of 1.0 C-S-H and 1.5 C-S-H, *Cement and Concrete Research*. 42 (2012) 1534–1548.
- [14] A.C. Wright, Neutron scattering from vitreous silica. V. The structure of vitreous silica: What have we learned from 60 years of diffraction studies?, *Journal of Non-Crystalline Solids*. 179 (1994) 84–115.

- [15] T. Proffen, S.J.L. Billinge, T. Egami, D. Louca, Structural analysis of complex materials using the atomic pair distribution function — a practical guide, *Zeitschrift Für Kristallographie*. 218 (2003) 132–143.
- [16] T. Egami, S.J.L. Billinge, *Underneath the Bragg peaks: structural analysis of complex materials*, Elsevier Ltd, 2003.
- [17] B. Hammouda, *Probing nanoscale structures - The SANS toolbox*, National Institute of Standards and Technology, 2008.
- [18] J. Ha, S.R. Chae, K.W. Chou, T. Tyliczszak, P.J.M. Monteiro, Scanning transmission X-ray microscopic study of carbonated calcium silicate hydrate, *Transportation Research Record: Journal of the Transportation Research Board*. 2142 (2010) 83–88.
- [19] T.K. Erdem, C. Meral, M. Tokyay, T.Y. Erdogan, Use of perlite as a pozzolanic addition in producing blended cements, *Cement and Concrete Composites*. 29 (2007) 13–21.
- [20] C. Meral, C.J. Benmore, P.J.M. Monteiro, The study of disorder and nanocrystallinity in C–S–H, supplementary cementitious materials and geopolymers using pair distribution function analysis, *Cement and Concrete Research*. 41 (2011) 696–710.
- [21] American Coal Ash Association, *Advancing the management and use of coal combustion products: Coal combustion products production & use statistics*, (2010).
- [22] Transportation Development Association – American Road and Transportation Builder Association, *The economic impacts of prohibiting coal fly ash use in transportation infrastructure construction*, (2011).
- [23] P. Duxson, A. Fernández-Jiménez, J.L. Provis, G.C. Lukey, A. Palomo, J.S.J. van Deventer, Geopolymer technology: the current state of the art, *Journal of Materials Science*. 42 (2006) 2917–2933.
- [24] J. Davisovits, Geopolymers: Inorganic polymeric new materials, *Journal of Thermal Analysis*. 37 (1991) 1633–1656.
- [25] J.L. Provis, G.C. Lukey, J.S.J. van Deventer, Do geopolymers actually contain nanocrystalline zeolites? A reexamination of existing results, *Chem. Mater.* (2005) 3075–3085.
- [26] D.L. Price, Neutron scattering from amorphous, disordered and nanocrystalline materials, in: *Proceedings from the Meeting of the School on Neutron Applications in Materials Science and Engineering Atomic Energy of Canada*, 1994.
- [27] J.A. Seibert, J.M. Boone, X-ray imaging physics for nuclear medicine technologists. Part 2: X-ray interactions and image formation, *Journal of Nuclear Medicine Technology*. 33 (2005) 3–18.

- [28] G.E. Bacon, Neutron Diffraction, Oxford, Clarendon Press, 1975.
- [29] P. Mitchell, S.F. Parker, A.J. Ramirez-Cuesta, J. Tomkinson, Vibrational spectroscopy with neutrons: with applications in chemistry, biology, materials science and catalysis, 2005.
- [30] H.E. Fischer, A.C. Barnes, P.S. Salmon, Neutron and X-ray diffraction studies of liquids and glasses, Reports on Progress in Physics. 69 (2006) 233–299.
- [31] C.J. Benmore, P.J.M. Monteiro, The structure of alkali silicate gel by total scattering methods, Cement and Concrete Research. 40 (2010) 892–897.
- [32] S. Kohara, K. Suzuya, High-energy X-ray diffraction studies of disordered materials, Nuclear Instruments and Methods in Physics Research Section B: Beam Interactions with Materials and Atoms. 199 (2003) 23–28.
- [33] D.A. Keen, A comparison of various commonly used correlation functions for describing total scattering, Journal of Applied Crystallography. 34 (2001) 172–177.
- [34] X. Qiu, J.W. Thompson, S.J.L. Billinge, PDFgetX2: a GUI-driven program to obtain the pair distribution function from X-ray powder diffraction data, Journal of Applied Crystallography. 37 (2004) 678.
- [35] P.A. Egelstaff, Classical fluids, in: D.L. Price, K. Skold (Eds.), Methods of Experimental Physics, Chapter 14, 1987: pp. 405–470.
- [36] N. Cusack, The physics of structurally disordered matter, Philadelphia: Hilger, 1987.
- [37] E. Lorch, Neutron diffraction by germania, silica and radiation-damaged silica glasses, Journal of Physics C: Solid State Physics. 2 (1969) 229–237.
- [38] C.B. Murray, C.R. Kagan, M.G. Bawendi, Synthesis and characterization of monodisperse nanocrystals and closed-packed nanocrystal assemblies, Annual Review of Materials Science. 30 (2000) 545–610.
- [39] M.C. Wilding, M. Wilson, P.F. McMillan, Structural studies and polymorphism in amorphous solids and liquids at high pressure, Chemical Society Reviews. 35 (2006) 964–86.
- [40] B. Warren, H. Krutter, O. Morningstar, Fourier analysis of X-ray patterns of vitreous SiO<sub>2</sub> and B<sub>2</sub>O<sub>3</sub>, Journal of the American Ceramic Society. 19 (1936) 202–206.
- [41] M. Misawa, D. Price, K. Suzuki, The short-range structure of alkali disilicate glasses by pulsed neutron total scattering, Journal of Non-Crystalline Solids. 37 (1980) 85–97.
- [42] Lujan Neutron Scattering Center, Neutron powder diffractometer technical sheet, <http://lansce.lanl.gov/lujan/instruments/NPDFtech.shtml>, (n.d.).



- [43] Q. Mei, C.J. Benmore, R. Sharma, J.L. Yarger, Intermediate range order in vitreous silica from a partial structure factor analysis, *Physical Review B*. 78 (2008) 1–7.
- [44] S.J.L. Billinge, I. Levin, The problem with determining atomic structure at the nanoscale., *Science*. 316 (2007) 561–5.
- [45] R.L. McGreevy, Reverse Monte Carlo modelling, *Journal of Physics: Condensed Matter*. 13 (2001) R877.
- [46] A.K. Soper, Partial structure factors from disordered materials diffraction data: An approach using empirical potential structure refinement, *Physical Review B*. 72 (2005) 1–12.
- [47] I. Bonhoure, I. Baur, E. Wieland, C. Johnson, A. Scheidegger, Uptake of Se(IV/VI) oxyanions by hardened cement paste and cement minerals: An X-ray absorption spectroscopy study, *Cement and Concrete Research*. 36 (2006) 91–98.
- [48] M. Vespa, R. Dähn, D. Grolimund, E. Wieland, A.M. Scheidegger, Co speciation in hardened cement paste: a macro- and micro-spectroscopic investigation, *Environmental Science & Technology*. 41 (2007) 1902–8.
- [49] I. Bonhoure, E. Wieland, A.M. Scheidegger, M. Ochs, D. Kunz, EXAFS study of Sn(IV) immobilization by hardened cement paste and calcium silicate hydrates, *Environmental Science & Technology*. 37 (2003) 2184–91.
- [50] K. Garbev, P. Stemmermann, L. Black, C. Breen, J. Yarwood, B. Gasharova, Structural features of C-S-H(I) and its carbonation in air - A Raman spectroscopic study, Part I: Fresh phases, *Journal of the American Ceramic Society*. 90 (2007) 900–907.
- [51] L. Black, C. Breen, J. Yarwood, K. Garbev, P. Stemmermann, B. Gasharova, Structural features of C-S-H(I) and its carbonation in air - A Raman spectroscopic study, Part II: Carbonated phases, *Journal of the American Ceramic Society*. 90 (2007) 908–917.
- [52] G.M. Bowers, R.J. Kirkpatrick, Natural Abundance  $^{43}\text{Ca}$  NMR spectroscopy of tobermorite and jennite: Model compounds for C-S-H, *Journal of the American Ceramic Society*. 92 (2009) 545–548.
- [53] A.V. Girão, I.G. Richardson, R. Taylor, R.M.D. Brydson, Composition, morphology and nanostructure of C-S-H in 70% white portland cement–30% fly ash blends hydrated at 55°C., *Cement and Concrete Research*. 40 (2010) 1350–1359.
- [54] C.D. Putnam, M. Hammel, G.L. Hura, J.A. Tainer, X-ray solution scattering (SAXS) combined with crystallography and computation: defining accurate macromolecular structures, conformations and assemblies in solution., *Quarterly Reviews of Biophysics*. 40 (2007) 191–285.

- [55] A. Guinier, G. Fournet, C.B. Walker, G.H. Vineyard, Guinier et al. - 1955 - Small-Angle Scattering of X-Rays.pdf, *Physics Today*. 9 (1955).
- [56] D.W. Schaefer, G. Beaucage, D.A. Loy, K.J. Shea, J.S. Lin, Structure of Arylene-Bridged Polysilsesquioxane Xerogels and Aerogels, *Materials Research*. (2004) 1402–1410.
- [57] D.W. Schaefer, K. Keefer, Fractal geometry of silica condensation polymers, *Physical Review Letters*. 53 (1984) 1383–1386.
- [58] D. Mildner, P.L. Hall, Small-angle scattering from porous solids with fractal geometry, *Journal of Physics D: Applied Physics*. 1535 (1986).
- [59] N.A. John Dalton Wright, *Sol-gel materials: chemistry and applications*, CRC, 2001.
- [60] P.A. Seeger, R.P. Hjelm Jr, Small-angle neutron scattering at pulsed spallation sources, *Journal of Applied Crystallography*. 24 (1991) 467–478.
- [61] J.E. Penner-Hahn, X-ray absorption spectroscopy, *Comprehensive Coordination Chemistry II*. (2004) 159–186.
- [62] J.A. Bearden, A.F. Burr, Reevaluation of X-ray atomic energy levels, *Reviews of Modern Physics*. 39 (1967) 125–142.
- [63] G. Principles, L. Ley, *Photoemission in solids I: General principles*, New York. (1978).
- [64] J.C. Fuggle, N. Moartensson, Core-level binding energies in metals, *Journal of Electron Spectroscopy and Related Phenomena*. 21 (1980) 275–281.
- [65] N. Browning, M. Chisholm, S. Pennycook, Atomic-resolution chemical analysis using a scanning transmission electron microscope, *Nature*. (1993).
- [66] E. de Smit, I. Swart, J.F. Creemer, G.H. Hovelings, M.K. Gilles, T. Tyliczszak, et al., Nanoscale chemical imaging of a working catalyst by scanning transmission X-ray microscopy., *Nature*. 456 (2008) 222–5.
- [67] A.P. Hitchcock, aXis2000. <http://unicorn.mcmaster.ca/aXis2000.html>., (n.d.).
- [68] H.E. Bergna, Colloid chemistry of silica : An overview, in: *Colloidal Silica: Fundamentals and Applications*, 2006: pp. 9–35.
- [69] H. Goldsworthy, Z. Min, Mortar Studies Towards the Replication of Roman Concrete, *Archaeometry*. 6 (2008) 932–946.
- [70] N.P. Hasparyk, P.J.M. Monteiro, H. Carasek, Effect of Silica Fume and Rice Husk Ash on Alkali-Silica Reaction, *ACI Materials Journal*. (2001).

- [71] P.K. Mehta, Siliceous ashes and hydraulic cements prepared therefrom, U.S. Patent 4,105,459, 1978.
- [72] P.K. Mehta, Highly durable cement products containing siliceous ashes, U.S. Patent 5,346,548, 1994.
- [73] P.K. Mehta, K.J. Folliard, Rice husk ash - A unique supplementary cementing material: Durability aspects, ACI Special Publications. SP-154 (1995) 531–542.
- [74] H. Hamdan, M. Muhid, S. Endud, E. Listiorini, Z. Ramli, <sup>29</sup>Si MAS NMR, XRD and FESEM studies of rice husk silica for the synthesis of zeolites, *Journal of Non-Crystalline Solids*. 211 (1997) 126–131.
- [75] W. Wang, H. Li, K. Lai, K. Du, Preparation and characterization of mullite whiskers from silica fume by using a low temperature molten salt method, *Journal of Alloys and Compounds*. 510 (2012) 92–96.
- [76] R.F. Abreu, J. Schneider, M.A. Cincotto, Structure and hydration kinetics of silica particles in rice husk ash studied by <sup>29</sup>Si high-resolution nuclear magnetic resonance, *Journal of the American Ceramic Society*. 88 (2005) 1514–1520.
- [77] G.A. Waychunas, H. Zhang, Structure, chemistry, and properties of mineral nanoparticles, *Elements*. 4 (2008) 381–387.
- [78] B.D. Canberra, The origin of precious opal - A new model, *The Australian Gemmologist*. 22 (2004).
- [79] S.V. Filin, A.I. Puzynin, V.N. Samoilov, Some aspects of precious opal synthesis, *The Australian Gemmologist*. 21 (2003) 278–282.
- [80] M. Kastner, J. Keene, J. Gieskes, Diagenesis of siliceous oozes—I. Chemical controls on the rate of opal-A to opal-CT transformation—an experimental study, *Geochimica Et Cosmochimica Acta*. 41 (1977) 1041–1059.
- [81] B.Y. Lynne, K.A. Campbell, Diagenetic transformations (opal-A to quartz) of low-and mid-temperature microbial textures in siliceous hot-spring deposits, Taupo Volcanic Zone, New Zealand, *Canadian Journal of Earth Sciences*. 40 (2003) 1679–1696.
- [82] L.A. Williams, D.A. Crerar, Silica diagenesis: II. General mechanisms, *Journal of Sedimentary Petrology*. 55 (1985) 312–321.
- [83] T.E. Stanton, Expansion of concrete through reaction between cement and aggregate, in: *Proceedings of the ASCE* V.66(10), 1940: pp. 1781–1811.
- [84] D.K. Smith, Opal, cristobalite, and tridymite: noncrystallinity versus crystallinity, nomenclature of the silica minerals and bibliography, *Powder Diffraction*. 13 (1998) 2–19.

- [85] E. Gaillou, E. Fritsch, B. Aguilar-Reyes, B. Rondeau, J. Post, a. Barreau, et al., Common gem opal: An investigation of micro- to nano-structure, *American Mineralogist*. 93 (2008) 1865–1873.
- [86] H. Graetsch, K. Ibel, Small angle neutron scattering by opals, *Physics and Chemistry of Minerals*. 24 (1997) 102–108.
- [87] J.M. Elzea, S.B. Rice, TEM and X-ray diffraction evidence for cristobalite and tridymite stacking sequences in opal, *Clays and Clay Minerals*. 44 (1996) 492–500.
- [88] R. Aines, G.R. Rossman, Water in minerals? A peak in the infrared, *Journal of Geophysical Research*. 89 (1984) 4059–4071.
- [89] E. Stolper, Water in silicate glasses: An infrared spectroscopic study, *Contributions to Mineralogy and Petrology*. 81 (1982) 1–17.
- [90] S.J. Adams, G.E. Hawkes, E.H. Curzon, A solid state  $^{29}\text{Si}$  nuclear magnetic resonance study of opal and other hydrous silicas, *American Mineralogist*. 76 (1991) 1863.
- [91] L.D. Brown, A.S. Ray, P.S. Thomas,  $^{29}\text{Si}$  and  $^{27}\text{Al}$  NMR study of amorphous and paracrystalline opals from Australia, *Journal of Non-Crystalline Solids*. 332 (2003) 242–248.
- [92] J. Elzea, I. Odom, W. Miles, Distinguishing well ordered opal-CT and opal-C from high temperature cristobalite by x-ray diffraction, *Analytica Chimica Acta*. 286 (1994) 107–116.
- [93] S.L. Cady, H. Wenk, K.H. Downing, HRTEM of microcrystalline opal in chert and porcelanite from the Monterey Formation, California, 81 (1996) 1380–1395.
- [94] B.H.W.S. De Jong, J. Van Hoek, W.S. Veeman, D.V. Manson, X-ray diffraction and  $^{29}\text{Si}$  magic-angle-spinning NMR of opals; incoherent long-and short-range order in opal-CT, *American Mineralogist*. 72 (1987) 1195–1203.
- [95] A. Mendes, W.P. Gates, J.G. Sanjayan, F. Collins, NMR, XRD, IR and synchrotron NEXAFS spectroscopic studies of OPC and OPC/slag cement paste hydrates, *Materials and Structures*. 44 (2011) 1773–1791.
- [96] D.C. Maclaren, M.A. White, Products of chemistry cement : Its chemistry and properties, *Journal of Chemical Education*. 80 (2003) 623–635.
- [97] K.K. Unger, Surface structure of amorphous and crystalline porous silicas: status and prospects, in: *Colloidal Silica: Fundamentals and Applications*, 2006: pp. 267–275.
- [98] H. Graetsch, A. Mosset, H. Gies, XRD and  $^{29}\text{Si}$  MAS-NMR study on some non-crystalline silica minerals, *Journal of Non-Crystalline Solids*. 119 (1990) 173–180.

- [99] J. Smith, C. Blackwell, Nuclear magnetic resonance of silica polymorphs, (1983).
- [100] S.J. Kitchin, S.C. Kohn, R. Dupree, C.M.B. Henderson, K. Kihara, In situ  $^{29}\text{Si}$  MAS NMR studies of structural phase transitions of tridymite, *American Mineralogist*. 81 (1996) 550–560.
- [101] H. Graetsch, H. Gies, I. Topalović, NMR, XRD and IR study on microcrystalline opals, *Physics and Chemistry of Minerals*. 21 (1994) 166–175.
- [102] A. Gendron-Badou, T. Coradin, J. Maquet, F. Frohlich, J. Livage, Spectroscopic characterization of biogenic silica, *Journal of Non-Crystalline Solids*. 316 (2003) 331–337.
- [103] M.C. Goryniuk, The reflectance spectra of opal-A (0.5–25  $\mu\text{m}$ ) from the Taupo Volcanic Zone: Spectra that may identify hydrothermal systems on planetary surfaces, *Geophysical Research Letters*. 31 (2004) 4–7.
- [104] M. Schmidt, R. Botz, D. Rickert, G. Bohrmann, Oxygen isotopes of marine diatoms and relations to opal-A maturation, *Geochimica Et Cosmochimica Acta*. 65 (2001) 201–211.
- [105] R. Day, B. Jones, Variations in water content in opal-A and opal-CT from geyser discharge aprons, *Journal of Sedimentary Research*. 78 (2008) 301–315.
- [106] S.D. Rogers, J.G. Dorsey, Chromatographic silanol activity test procedures: the quest for a universal test., *Journal of Chromatography. A*. 892 (2000) 57–65.
- [107] L. Zhuravlev, The surface chemistry of amorphous silica. Zhuravlev model, *Colloids and Surfaces A: Physicochemical and Engineering Aspects*. 173 (2000) 1–38.
- [108] W.H. Zachariasen, The atomic arrangement in glass, *Journal of American Chemical Society*. 54 (1932) 3841–3851.
- [109] A.P. Hammersley, FIT2D V9.129 Reference Manual V3.1, European Synchrotron Radiation Facility, 1998.
- [110] M. Bauchy, Structural, vibrational, and thermal properties of densified silicates: Insights from molecular dynamics, *The Journal of Chemical Physics*. 137 (2012) 044510.
- [111] N. Zotov, H. Keppler, A.C. Hannon, A.K. Soper, The effect of water on the structure of silicate glasses — A neutron diffraction study, *Journal of Non-Crystalline Solids*. 202 (1996) 153–163.
- [112] J. Rino, I. Ebbsjö, R. Kalia, A. Nakano, P. Vashishta, Structure of rings in vitreous  $\text{SiO}_2$ , *Physical Review B*. 47 (1993) 3053–3062.
- [113] F. Galeener, Planar rings in vitreous silica, *Journal of Non-Crystalline Solids*. 49 (1982) 53–62.

- [114] M.B. Boisen, G.V. Gibbs, R.T. Downs, P. D'Arco, The dependence of the SiO bond length on structural parameters in coesite, the silica polymorphs, and the clathrasils, *American Mineralogist*. 75 (1990) 748–754.
- [115] G.V. Gibbs, M.M. Hamil, S.J. Louisnathan, Correlations between Si-O bond length, Si-O-Si angle and bond overlap populations calculated using extended Huckel molecular orbital theory, *American Mineralogist*. 57 (1972) 1578–1613.
- [116] R. Downs, D. Palmer, The pressure behavior of  $\alpha$  cristobalite, *American Mineralogist*. 79 (1994) 9–14.
- [117] J.H. Konnert, D.E. Appleman, The crystal structure of low tridymite, *Acta Crystallographica Section B: Structural Crystallography and Crystal Chemistry*. 34 (1978) 391–403.
- [118] T. Proffen, S.J.L. Billinge, PDFFIT, a program for full profile structural refinement of the atomic pair distribution function, *Journal of Applied Crystallography*. 32 (1999) 572–575.
- [119] K. Kurtis, W. Meyer-Ilse, P.J.M. Monteiro, Soft X-ray spectromicroscopy for in situ study of corrosion, *Corrosion Science*. 42 (2000) 1327–1336.
- [120] K. Kurtis, Transmission soft x-ray microscopy of the alkali-silica reaction, (1998).
- [121] D.W. Hobbs, Alkali-silica reaction in concrete, Thomas Telford Ltd., 1988.
- [122] B. Fournier, M.-A. Bérubé, Alkali-aggregate reaction in concrete: a review of basic concepts and engineering implications, *Canadian Journal of Civil Engineering*. 27 (2000) 167–191.
- [123] K.E. Kurtis, Chemical additives to control expansion of alkali-silica reaction gel: proposed mechanisms of control, 8 (2003) 2027 – 2036.
- [124] K.J. Folliard, M.D.A. Thomas, J.H. Ideker, B. East, B. Fournier, Case studies of treating ASR-affected structures with lithium nitrate, in: *Proc. of the 13th International Conference on Alkali-Aggregate Reaction in Concrete*, 2008: pp. 90–99.
- [125] B. Fournier, M.-A. Berube, K. Folliard, M. Thomas, Report on the diagnosis, prognosis, and mitigation of alkali-silica reaction (ASR) in transportation structures, 2010.
- [126] L.S. Dent Glasser, N. Kataoka, The chemistry of alkali-aggregate reaction, *Cement and Concrete Research*. 11 (1981) 1–9.
- [127] F.-J. Ulm, O. Coussy, L. Kefei, C. Larive, Thermo-chemo-mechanics of ASR expansion in concrete structures, *Journal of Engineering Mechanics*. 126 (2000) 233–242.
- [128] Z. Bazant, Mathematical model for kinetics of alkali-silica reaction in concrete, *Cement and Concrete Research*. 30 (2000) 419–428.

- [129] E. Garcia-Diaz, D. Bulteel, Y. Monnin, P. Degrugilliers, P. Fasseu, ASR pessimum behaviour of siliceous limestone aggregates, *Cement and Concrete Research*. 40 (2010) 546–549.
- [130] L. Khouchaf, J. Verstraete, R.J. Prado, M.H. Tuilier, XANES, EXAFS and RMN contributions to follow the structural revolution induced by alkali silica reaction in SiO<sub>2</sub> aggregate, *Physica Scripta*. 552 (2005) 552.
- [131] B. Fubini, C.O. Arean, Chemical aspects of the toxicity of inhaled mineral dusts, *Chem. Soc. Rev.* 28 (1999) 373–381.
- [132] F. Tielens, C. Gervais, J.F. Lambert, F. Mauri, D. Costa, Ab initio study of the hydroxylated surface of amorphous silica: A representative model, *Chemistry of Materials*. 20 (2008) 3336–3344.
- [133] A.T. Hubbard, *Encyclopedia of Surface and Colloid Science: Por-Z*, CRC Press, 2002.
- [134] A.J. Gratz, S. Manne, P.K. Hansma, Atomic force microscopy of atomic-scale ledges and etch pits formed during dissolution of quartz., *Science (New York, N.Y.)*. 251 (1991) 1343–6.
- [135] A.J. Gratz, P. Bird, Quartz dissolution: Theory of rough and smooth surfaces, *Geochimica Et Cosmochimica Acta*. 57 (1993) 977–989.
- [136] P.M. Dove, N. Han, A.F. Wallace, J.J. De Yoreo, Kinetics of amorphous silica dissolution and the paradox of the silica polymorphs., *Proceedings of the National Academy of Sciences of the United States of America*. 105 (2008) 9903–8.
- [137] W. Stumm, H. Huper, R.L. Champlin, Formation of polysilicates as determined by coagulation effects, *Environmental Science & Technology*. 1 (1967) 221–227.
- [138] R.K. Iler, *The Chemistry of Silica*, Wiley, 1979.
- [139] K. Andersson, L. Dent Glasser, Polymerization and colloid formation in silicate solutions, *Soluble Silicates*, ACS. (1982).
- [140] L.D. Glasser, E. Lachowski, Reactive pigments in inorganic silicate coatings, *Industrial & Engineering Chemistry Product Research and Development*. (1983) 1–5.
- [141] D.N. Furlong, K.S.W. Sing, Parfitt, The precipitation of silica on titanium dioxide surfaces, *Journal of Colloid and Interface Science*. 69 (1978).
- [142] I.L. Svensson, S. Sjoberg, L.-O. Ohman, Polysilicate equilibria in concentrated sodium silicate solutions, *Journal of the Chemical Society, Faraday Transactions 1*. 82 (1986) 3635.

- [143] E.M. Bulewicz, A. Pelc, R. Kozłowski, A. Miciukiewicz, Intumescent silicate-based materials: Mechanism of swelling in contact with fire, *Fire and Materials*. 9 (1985) 171–175.
- [144] P. Dove, D. Crerar, Kinetics of quartz dissolution in electrolyte solutions using a hydrothermal mixed flow reactor, *Geochimica Et Cosmochimica Acta*. 54 (1990) 955–969.
- [145] L.L. Stillings, S.L. Brantley, Feldspar dissolution at 25C and pH 3: Reaction stoichiometry and the effect of cations, *Geochimica Et Cosmochimica Acta*. 59 (1995) 1483–1496.
- [146] A.A. Chernov, Crystal growth and crystallography, *Acta Crystallographica Section A Foundations of Crystallography*. 54 (1998) 859–872.
- [147] P.M. Dove, N. Han, J.J. De Yoreo, Mechanisms of classical crystal growth theory explain quartz and silicate dissolution behavior, *Proceedings of the National Academy of Sciences of the United States of America*. 102 (2005) 15357–62.
- [148] R. Snellings, G. Mertens, J. Elsen, Supplementary cementitious materials, *Reviews in Mineralogy and Geochemistry*. 74 (2012) 211–278.
- [149] P. Juilland, E. Gallucci, R. Flatt, K. Scrivener, Dissolution theory applied to the induction period in alite hydration, *Cement and Concrete Research*. 40 (2010) 831–844.
- [150] S. Brantley, Kinetics of mineral dissolution, in: S.L. Brantley, J. Kubicki, A.F. White (Eds.), *Kinetics of Water-rock Interaction*, New-York, Springer, 2008: pp. 151–210.
- [151] M. Kosmulski, *Chemical Properties of Material Surfaces*, Science, 2001.
- [152] B. Bickmore, J. Wheeler, B. Bates, K. Nagy, D. Eggett, Reaction pathways for quartz dissolution determined by statistical and graphical analysis of macroscopic experimental data, *Geochimica Et Cosmochimica Acta*. 72 (2008) 4521–4536.
- [153] C.C. Perry, T. Keeling-Tucker, Biosilicification: the role of the organic matrix in structure control, *Journal of Biological Inorganic Chemistry*. 5 (2000) 537–550.
- [154] G.A. Icopini, S.L. Brantley, P.J. Heaney, Kinetics of silica oligomerization and nanocolloid formation as a function of pH and ionic strength at 25°C, *Geochimica Et Cosmochimica Acta*. 69 (2005) 293–303.
- [155] L.L. Hench, J.K. West, The sol-gel process, *Chemical Reviews*. 90 (1990) 33–72.
- [156] P. Wijnen, T. Beelen, J. De Haan, L. Van De Ven, R. Van Santen, The structure directing effect of cations in aqueous silicate solutions. A <sup>29</sup>Si-NMR study, *Colloids and Surfaces*. 45 (1990) 255–268.



- [157] C. Gommès, Hybrid silica gels and xerogels: from precursor molecules to porous materials via phase separation and drying Remerciements, Université de Liège, 2006.
- [158] D.W. Schaefer, Polymers, fractals, and ceramic materials, *Science*. 243 (1989) 1023–7.
- [159] C.J. Brinker, Sol-gel processing of silica, in: *Colloidal Silica: Fundamentals and Applications*, 2006: pp. 615–635.
- [160] J. Rarity, Colloids stick to fractal rules, *Nature*. (1989).
- [161] T. Ichikawa, Alkali–silica reaction, pessimum effects and pozzolanic effect, *Cement and Concrete Research*. 39 (2009) 716–726.
- [162] B. Bunker, T. Headley, Gel structures in leached alkali silicate glass, *Mater. Res. Soc. Symp.* 32 (1984) 41–46.
- [163] K.L. Scrivener, P.J.M. Monteiro, The Alkali-Silica Reaction in a Monolithic Opal, *Journal of the American Ceramic Society*. 77 (1994) 2849–2856.
- [164] R.F. Bleszynski, M.D. a. Thomas, Microstructural studies of alkali-silica reaction in fly ash concrete immersed in alkaline solutions, *Advanced Cement Based Materials*. 7 (1998) 66–78.
- [165] L.S. Dent Glasser, N. Kataoka, On the role of calcium in the alkali-aggregate reaction, *Cement and Concrete Research*. 12 (1982) 321–331.
- [166] R. Helmuth, D. Stark, S. Diamond, M. Moranville-Regourd, *Alkali-silica reactivity: An overview of research*, Washington, D.C., 1993.
- [167] X. Hou, L.J. Struble, R.J. Kirkpatrick, Formation of ASR gel and the roles of C-S-H and portlandite, *Cement and Concrete Research*. 34 (2004) 1683–1696.
- [168] S. Hong, F.P. Glasser, Alkali binding in cement pastes Part I. The C-S-H phase, *Cement and Concrete Research*. 29 (2000) 1893–1903.
- [169] S. Urhan, Alkali silica and pozzolanic reactions in concrete. Part 1: Observations on expanded perlite aggregate concretes Interpretation of published results and an hypothesis concerning the mechanism, *Cement and Concrete Research*. 17 (1987) 141–152.
- [170] R. Helmuth, D. Stark, Alkali-silica reactivity mechanisms, *Materials Science of Concrete III*. (1992) 131–208.
- [171] T. Ichikawa, M. Miura, Modified model of alkali-silica reaction, *Cement and Concrete Research*. 37 (2007) 1291–1297.
- [172] M. Kawamura, K. Iwahori, ASR gel composition and expansive pressure in mortars under restraint, *Cement and Concrete Composites*. 26 (2004) 47–56.

- [173] L.J. Struble, S. Diamond, Swelling properties of synthetic alkali silica gels, *Journal of the American Ceramic Society*. 64 (1981) 652–655.
- [174] M.L. Marques, Estudo da reacao alcali-agregado na tomada d'agua da Uhe Jaguari por meio de ensaios laboratoriais, Universidade Estadual Paulista, 2009.
- [175] L. Khouchaf, J. Verstraete, Multi-technique and multi-scale approach applied to study the structural behavior of heterogeneous materials: natural SiO<sub>2</sub> case, *Journal of Materials Science*. 42 (2006) 2455–2462.
- [176] A. Hamoudi, L. Khouchaf, C. Depecker, B. Revel, L. Montagne, P. Cordier, Microstructural evolution of amorphous silica following alkali–silica reaction, *Journal of Non-Crystalline Solids*. 354 (2008) 5074–5078.
- [177] X. Zhao, G. Lu, A. Whittaker, G. Millar, H. Zhu, Comprehensive study of surface chemistry of MCM-41 using <sup>29</sup>Si CP/MAS NMR, FTIR, Pyridine-TPD, and TGA, *The Journal of Physical Chemistry B*. 101 (1997) 6525–6531.
- [178] X. Hou, R.J. Kirkpatrick, L.J. Struble, P.J.M. Monteiro, Structural Investigations of Alkali Silicate Gels, *Journal of the American Ceramic Society*. 88 (2005) 943–949.
- [179] C. Tambelli, J. Schneider, N. Hasparyk, P.J.M. Monteiro, Study of the structure of alkali–silica reaction gel by high-resolution NMR spectroscopy, *Journal of Non-Crystalline Solids*. 352 (2006) 3429–3436.
- [180] J.F. Schneider, N.P. Hasparyk, D. a. Silva, P.J.M. Monteiro, Effect of Lithium Nitrate on the Alkali-Silica Reaction Gel, *Journal of the American Ceramic Society*. 91 (2008) 3370–3374.
- [181] J. Verstraete, L. Khouchaf, D. Bulteel, E. Garcia-Diaz, a. . Flank, M.H. Tuilier, Amorphisation mechanism of a flint aggregate during the alkali–silica reaction: X-ray diffraction and X-ray absorption XANES contributions, *Cement and Concrete Research*. 34 (2004) 581–586.
- [182] D. Li, G. Bancroft, M. Kasrai, M. Fleet, X. Feng, K. Tan, et al., High-resolution Si K-and L<sub>2, 3</sub>-edge XANES of [alpha]-quartz and stishovite, *Solid State Communications*. 87 (1993) 613–617.
- [183] D. Li, G. Bancroft, M. Fleet, X. Feng, Silicon K-edge XANES spectra of silicate minerals, *Physics and Chemistry of Minerals*. 22 (1995) 115–122.
- [184] F. Gaboriaud, D. Chaumont, A. Nonat, B. Hanquet, A. Craevich, Study of the Influence of Alkaline Ions ( Li , Na and K ) on the Structure of the Silicate Entities in Silico Alkaline Sol and on the Formation of the Silico-Calco-Alkaline Gel, *Journal of Sol-Gel Science and Technology*. 358 (1998) 353–358.

- [185] F. Gaboriaud, A. Nonat, D. Chaumont, A. Craievich, B. Hanquet, 29 Si NMR and Small-Angle X-ray Scattering Studies of the Effect of Alkaline Ions (Li + , Na + , and K + ) in Silico-Alkaline Sols, *The Journal of Physical Chemistry B*. 103 (1999) 2091–2099.
- [186] F. Gaboriaud, D. Chaumont, A. Nonat, A. Craievich, Fractal structure of basic silica gels with low Ca content, *Journal of Applied Crystallography*. 33 (2000) 597–599.
- [187] F. Gaboriaud, A. Nonat, D. Chaumont, A. Craievich, Aggregation processes and formation of silico-calco-alkaline gels under high ionic strength., *Journal of Colloid and Interface Science*. 253 (2002) 140–9.
- [188] F. Gaboriaud, a Nonat, D. Chaumont, a Craievich, Structural model of gelation processes of a sodium silicate sol destabilized by calcium ions: combination of SAXS and rheological measurements, *Journal of Non-Crystalline Solids*. 351 (2005) 351–354.
- [189] F. Gaboriaud, A. Nonat, D. Chaumont, A. Craievich, Aggregation and Gel Formation in Basic Silico–Calco–Alkaline Solutions Studied: A SAXS, SANS, and ELS Study, *The Journal of Physical Chemistry B*. 103 (1999) 5775–5781.
- [190] G. Engelhardt, D. Michel, High-resolution solid-state NMR of silicates and zeolites, John Wiley and Sons, New York, NY, 1987.
- [191] N.P. Hasparyk, P.J.M. Monteiro, D.C.C. Dal Molin, AAR in Furnas Dam, Brazil, residual expansion and the effect of lithium, in: *Simposio Sibre Reacao Alkali-agregado Em Estruturas De Concreto*, IBRACON, Rio de Janeiro, 2006: pp. 1–15.
- [192] P.N. Silva, *Reacao alcali-agregado nas usinas hidreletricas do complexo Paulo Afonso*, Universidade de Sao Paulo, 2007.
- [193] L.E. Lopez, Modelagem mecânica e numérica da reação álcali-agregado com aplicação a barragens de concreto, Programa de Pós-Graduação em Engenharia Civil, Universidade Federal do Rio de Janeiro, 2004.
- [194] Z. Johan, G.F. Maglione, Kanemite, a new hydrated sodium silicate, *Bulletin De La Societe Francaise Mineralogie Et De Cristallographie*. 95 (1972) 371–&.
- [195] H. Anhed, L. Fälth, F.J. Lincoln, Crystal structure of synthetic makatite  $\text{Na}_2\text{Si}_4\text{O}_8(\text{OH})_2 \cdot 4\text{H}_2\text{O}$ , *Zeitschrift Für Kristallographie*. (1982) 203–210.
- [196] G.G. Almond, R.K. Harris, K.R. Franklin, A structural consideration of kanemite, octosilicate, magadiite and kenyaite, *Journal of Materials Chemistry*. 7 (1997) 681–687.
- [197] L.A.J. Garvie, B. Devouard, T.L. Groy, F. Camara, P.R. Buseck, Crystal structure of kanemite,  $\text{NaHSi}_2\text{O}_5 \cdot 3\text{H}_2\text{O}$ , from the Aris phonolite , Namibia, 84 (1999) 1170–1175.

- [198] G. Borbely, K.K. Beyer, H. Karge, W. Schwieger, A. Brandt, K.-H. Bergk, Chemical characterization, structural features, and thermal behavior of sodium and hydrogen octosilicate, *Clays and Clay Minerals*. 39 (1991) 490–497.
- [199] G. Brindley, Unit cell of magadiite in air, in vacuo, and under other conditions, *American Mineralogist*. 54 (1969) 1583–1591.
- [200] R.J. Kirkpatrick, A.G. Kalinichev, X. Hou, L. Struble, Experimental and molecular dynamics modeling studies of interlayer swelling: water incorporation in kanemite and ASR gel, *Materials and Structures*. 38 (2005) 449–458.
- [201] S. Hayashi, Solid-state NMR study of locations and dynamics of interlayer cations and water in kanemite, *Journal of Materials Chemistry*. 7 (1997) 1043–1048.
- [202] M.T. Le Bihan, A. Kalt, R. Wey, Étude structurale de  $\text{KHSi}_2\text{O}_5$  et  $\text{H}_2\text{Si}_2\text{O}_5$ , *Bulletin De La Société Française De Minéralogie Et De Cristallographie*. 94 (1971) 15–23.
- [203] W. Wieker, C. Hubert, Alkali–silica reaction—a problem of the insufficient fundamental knowledge of its chemical base, *Materials Science of Concrete*. (1998) 395–408.
- [204] W. Wieker, C. Hubert, Some experiences in chemical modelling of the alkali-silica reaction, in: *11th International Conference on Alkali-aggregate Reaction, 2000*: pp. 119–128.
- [205] M. Prezzi, P.J.M. Monteiro, G. Sposito, The Alkali-Silica Reaction , Part I: Use of the Double-Layer Theory to Explain the Behavior of Reaction-Product Gels, *ACI Materials Journal*. (1997).
- [206] M. Prezzi, P.J.M. Monteiro, G. Sposito, Alkali-Silica Reaction; Part 2: The Effect of Chemical Additives, *ACI Materials Journal*. 95 (1998).
- [207] Y. Huang, Z. Jiang, W. Schwieger, Vibrational spectroscopic studies of layered silicates, *Chemistry of Materials*. (1999) 1210–1217.
- [208] P. McMillan, Structural studies of silicate glasses and melts—applications and limitations of Raman spectroscopy, *American Mineralogist*. 69 (1984) 622–644.
- [209] J. Serra, P. González, S. Liste, C. Serra, S. Chiussi, B. León, et al., FTIR and XPS studies of bioactive silica based glasses, *Journal of Non-Crystalline Solids*. 332 (2003) 20–27.
- [210] F. Feng, K. Balkus, Synthesis of kenyaite, magadiite and octosilicate using poly (ethylene glycol) as a template, *Journal of Porous Materials*. (2003) 5–15.
- [211] H.H.W. Moenke, Silica, the three dimensional silicates, borosilicates and beryllium silicates, in: V.C. Farmer (Ed.), *The Infrared Spectra of Minerals*, Mineral. Soc., London, UK, 1974: pp. 365–382.

- [212] T.W. Dijkstra, R. Duchateau, R.A. Van Santen, A. Meetsma, G.P.A. Yap, Silsesquioxane models for geminal silica surface silanol sites. A spectroscopic investigation of different types of silanols, *Journal of the American Chemical Society*. 124 (2002) 9856–9864.
- [213] R.G. Milkey, Infrared spectra of some tectosilicates, *American Mineralogist*. 45 (1960) 990–1007.
- [214] J. Li, A. Kolesnikov, Neutron spectroscopic investigation of dynamics of water ice, *Journal of Molecular Liquids*. 100 (2002) 1–39.
- [215] A.I. Kolesnikov, J.C. Li, D. Colognesi, Low-energy neutron vibrational spectra of high pressure phases of ice, *Journal of Neutron Research*. 14 (2006) 325–331.
- [216] E. Levy, A.I. Kolesnikov, J. Li, Y. Mastai, Structure of water in mesoporous organosilica by calorimetry and inelastic neutron scattering, *Surface Science*. 603 (2009) 71–77.
- [217] D. Sivia, P. Vorderwisch, R. Silver, Deconvolution of data from the filter difference spectrometer: from hardware to maximum entropy, *Nuclear Instruments and Methods in Physics Research Section A: Accelerators, Spectrometers, Detectors and Associated Equipment*. 290 (1990) 492–498.
- [218] C.M.B. Line, G.J. Kearley, An inelastic incoherent neutron scattering study of water in small-pored zeolites and other water-bearing minerals, *The Journal of Chemical Physics*. 112 (2000) 9058–9067.
- [219] M. Hartl, L. Daemen, G. Muhrer, Water trapped in silica microspheres, *Microporous and Mesoporous Materials*. 161 (2012) 7–13.
- [220] V.G. Engelhardt, D. Zeigan, H. Jancke, W. Wieker,  $^{29}\text{Si}$ -NMR Spectroscopy of Silicate Solutions. 2. On the Dependence of the structure of Silicate anions in Water Solutions from the Na : Si Ratio, *Zeitschrift Für Anorganische Und Allgemeine Chemie*. 418 (1975) 17–28.
- [221] H. Maekawa, T. Maekawa, K. Kawamura, T. Yokokawa, The structural groups of alkali silicate glasses determined from  $^{29}\text{Si}$  MAS-NMR, *Journal of Non-crystalline Solids*. 127 (1991) 53–64.
- [222] P. Yu, R.J. Kirkpatrick, B. Poe, P.F. McMillan, X. Cong, Structure of Calcium Silicate Hydrate (C-S-H): Near-, Mid-, and Far-Infrared Spectroscopy, *Journal of the American Ceramic Society*. 82 (1999) 742–748.
- [223] J. Tossell, Quantum mechanical calculation of  $^{23}\text{Na}$  NMR shieldings in silicates and aluminosilicates, *Physics and Chemistry of Minerals*. (1999) 70–80.
- [224] X. Xue, J.F. Stebbins,  $^{23}\text{Na}$  NMR Chemical Shifts and Local Na Coordination Environments in Silicate Crystals, Melts and Glasses, *Phys Chem Minerals*. (1993) 297–307.

- [225] M.R. Rowles, J.V. Hanna, K.J. Pike, M.E. Smith, B.H. O'Connor,  $^{29}\text{Si}$ ,  $^{27}\text{Al}$ ,  $^1\text{H}$  and  $^{23}\text{Na}$  MAS NMR Study of the Bonding Character in Aluminosilicate Inorganic Polymers, *Applied Magnetic Resonance*. 32 (2007) 663–689.
- [226] H. Koller, G. Engelhardt, A.P.M. Kentgens, J. Sauer,  $^{23}\text{Na}$  NMR Spectroscopy of Solids: Interpretation of Quadrupole Interaction Parameters and Chemical Shifts, *The Journal of Physical Chemistry*. 98 (1994) 1544–1551.
- [227] F. Angeli, J.-M. Delaye, T. Charpentier, J.-C. Petit, D. Ghaleb, P. Faucon, Influence of glass chemical composition on the Na–O bond distance: a  $^{23}\text{Na}$  3Q-MAS NMR and molecular dynamics study, *Journal of Non-Crystalline Solids*. 276 (2000) 132–144.
- [228] C. Bronnimann, R. Zeigler, G. Maciel, Proton NMR study of dehydration of the silica gel surface, *Journal of the American Chemical Society*. 110 (1988) 2023–2026.
- [229] B.L. Phillips, H.E. Mason, S. Guggenheim, Hydrogen bonded silanols in the 10 Å phase: Evidence from NMR spectroscopy, *American Mineralogist*. 92 (2007) 1474–1485.
- [230] Y. Li, H. Ishida, Concentration-dependent conformation of alkyl tail in the nanoconfined space: Hexadecylamine in the silicate galleries, *Langmuir*. 48 (2003) 2479–2484.
- [231] W. Ching, S. Mo, Y. Chen, Calculation of XANES/ELNES spectra of all edges in  $\text{Si}_3\text{N}_4$  and  $\text{Si}_2\text{N}_2\text{O}$ , *Journal of the American Ceramic Society*. 15 (2002) 11–15.
- [232] J. Du, L. Corrales, Compositional dependence of the first sharp diffraction peaks in alkali silicate glasses: A molecular dynamics study, *Journal of Non-Crystalline Solids*. 352 (2006) 3255–3269.
- [233] S.R. Elliott, Origin of the first sharp diffraction peak in the structure factor of covalent glasses and liquids, *Journal of Physics: Condensed Matter*. 4 (1992) 7661–7678.
- [234] P.S. Salmon, R. a Martin, P.E. Mason, G.J. Cuello, Topological versus chemical ordering in network glasses at intermediate and extended length scales., *Nature*. 435 (2005) 75–8.
- [235] R.D. Shannon, C.T. Prewitt, Effective ionic radii in oxides and fluorides, *Acta Crystallographica Section B: Structural Crystallography and Crystal Chemistry*. 25 (1969) 925–946.
- [236] K. Celik, M. Jackson, M. Mancio, C. Meral, A. Emwas, K. Mehta, et al., High-volume natural volcanic pozzolan and limestone powder as partial replacements for portland cement in self-compacting and sustainable concrete, *Cement and Concrete Composites*. (n.d.).
- [237] H.J. Feuerborn, Coal ash utilisation over the world and in Europe, in: *Workshop on Environmental and Health Aspects of Coal Ah Utilization*, Israel, 2005.

- [238] D. Cao, E. Selic, J.-D. Herbell, Utilization of fly ash from coal-fired power plants in China, *Journal of Zhejiang University-Science A*. (2008) 681–687.
- [239] V.M. Malhotra, High-performance high-volume fly ash concrete, *Concrete International*. 24 (2002) 30–34.
- [240] K. Celik, C. Meral, A. Stack, M. Mancio, P. Gursel, A. Horvath, et al., Development of low-cost, environmentally-friendly self-consolidating concrete mixtures with high-volumes of fly ash and limestone powder, Unpublished Data. (2012).
- [241] P. Duxson, A. Fernández-Jiménez, J.L. Provis, G.C. Lukey, A. Palomo, J.S.J. Deventer, Geopolymer technology: the current state of the art, *Journal of Materials Science*. 42 (2007) 2917–2933.
- [242] H. Brouwers, R.V. Eijk, Fly ash reactivity: extension and application of a shrinking core model and thermodynamic approach, *Journal of Materials Science*. 7 (2002) 2129–2141.
- [243] M.J. Dudas, C.J. Warren, Submicroscopic model of fly ash particles, *Geoderma*. 40 (1987) 101–114.
- [244] S. Dai, L. Zhao, S. Peng, C.-L. Chou, X. Wang, Y. Zhang, et al., Abundances and distribution of minerals and elements in high-alumina coal fly ash from the Jungar Power Plant, Inner Mongolia, China, *International Journal of Coal Geology*. 81 (2010) 320–332.
- [245] X. Querol, N. Moreno, J. Umana, A. Alastuey, Synthesis of zeolites from coal fly ash: an overview, *Journal of Coal Geology*. 50 (2002) 413–423.
- [246] L. Skinner, A. Barnes, P. Salmon, H. Fischer, J.W. Drewitt, V. Honkimäki, Structure and triclustering in Ba-Al-O glass, *Physical Review B*. 85 (2012) 1–12.
- [247] C.J. Benmore, J.K.R. Weber, S. Sampath, J. Siewenie, J. Urquidi, J.A. Tangeman, A neutron and x-ray diffraction study of calcium aluminate glasses, *Journal of Physics: Condensed Matter*. 15 (2003) S2413–S2423.
- [248] R. Weber, C.J. Benmore, J. Siewenie, J. Urquidi, T.S. Key, Structure and bonding in single- and two-phase alumina-based glasses, *Physical Chemistry Chemical Physics*. 6 (2004) 2480.
- [249] A. Winkler, J. Horbach, W. Kob, K. Binder, Structure and diffusion in amorphous aluminum silicate: a molecular dynamics computer simulation, *The Journal of Chemical Physics*. 120 (2004) 384–93.
- [250] R.J. Loucks, J.C. Mauro, A. Tandia, N.T. Timofeev, Semi-Empirical Technique for Computation of Glass Density, *Journal of the American Ceramic Society*. 90 (2007) 4020–4022.

- [251] V.V. Hoang, N.N. Linh, N.H. Hung, Structure and dynamics of liquid and amorphous  $\text{Al}_2\text{O}_3 \cdot 2\text{SiO}_2$ , *The European Physical Journal Applied Physics*. 37 (2007) 111–118.
- [252] V.V. Hoang, Composition dependence of static and dynamic heterogeneities in simulated liquid aluminum silicates, *Physical Review B*. 75 (2007) 1–15.
- [253] S. Lee, S. Park, Y. Yi, C. Ahn, Structure of Amorphous Aluminum Oxide, *Physical Review Letters*. 103 (2009) 4–7.
- [254] J.F. Stebbins, E.V. Dubinsky, K. Kanehashi, K.E. Kelsey, Temperature effects on non-bridging oxygen and aluminum coordination number in calcium aluminosilicate glasses and melts, *Geochimica Et Cosmochimica Acta*. 72 (2008) 910–925.
- [255] S.K. Lee, G.D. Cody, B.O. Mysen, Structure and the extent of disorder in quaternary (Ca-Mg and Ca-Na) aluminosilicate glasses and melts, *American Mineralogist*. 90 (2005) 1393–1401.
- [256] Á. Palomo, S. Alonso, A. Fernandez-Jiménez, I. Sobrados, J. Sanz, Alkaline activation of fly ashes: NMR study of the reaction products, *Journal of the American Ceramic Society*. 87 (2004) 1141–1145.
- [257] W. Smith, T.R. Forester, DL\_POLY\_2.0: A general-purpose parallel molecular dynamics simulation package Overall design, *Journal of Molecular Graphics*. 14 (1996) 136–141.
- [258] C.J. Benmore, J. Weber, M. Wilding, Temperature-dependent structural heterogeneity in calcium silicate liquids, *Physical Review B*. 82 (2010) 224202.
- [259] J. Du, A. Cormack, The medium range structure of sodium silicate glasses: a molecular dynamics simulation, *Journal of Non-Crystalline Solids*. 349 (2004) 66–79.
- [260] J. Du, L. René Corrales, Understanding lanthanum aluminate glass structure by correlating molecular dynamics simulation results with neutron and X-ray scattering data, *Journal of Non-Crystalline Solids*. 353 (2007) 210–214.
- [261] P. Pfleiderer, J. Horbach, K. Binder, Structure and transport properties of amorphous aluminium silicates: Computer simulation studies, *Chemical Geology*. 229 (2006) 186–197.
- [262] N.N. Linh, V.V. Hoang, Structural properties of simulated liquid and amorphous aluminium silicates, *Physica Scripta*. 76 (2007) 165–172.
- [263] G.N. Greaves, Exafs and the structure of glass, *Journal of Non-Crystalline Solids*. 71 (1985) 203–217.